Journal of METALS

APRIL 1957

TRANSACTIONS SECTION

VOL. 9, NO. 4, IN TWO SECTIONS—SECTION TWO

Electron Probe Microanalyzer and Its Application to Ferrous Metallurgy — R. Castaing, J. Philibert, and C. Crussard — 389

Oxidation of Zirconium Between 400° and 800°C — E. A. Gulbransen and K. F. Andrew — 394

Prot Fatigue Study of an Aircraft Steel in the Ultra High Strength Range — P. W. Ramsey and D. P. Kedzie — 401

Effect of Dissolved Oxygen on the Grain Size of Annealed Pure Copper and Cu-Al Alloys — D. L. Wood — 406

Some Properties of Certain High-Conductivity Copper-Base Alloys — W. Hodge — 408

Habit Planes of Martensite in Chrome-Carbon Steel — H. M. Otte and T. A. Read — 412

Effects of Solid Solution Alloying on Creep Deformation of Aluminum — G. D. Gemmell and N. J. Grant — 417

Stepped Austenitizing Treatment for 4340 Steel — E. P. Klier, V. Weiss, and G. Sachs — 424

Central Region of the Mg-Zn Phase Diagram — J. B. Clark and F. N. Rhines — 425

Electron Diffraction Study of Flake Graphite Extracted from Molten Pig Iron — K. Niwa and G. Shimaoka — 430

Some Estimates of the Thermal Stability of Dispersion-Hardened Alloys — A. W. Cochardt — 434

Grain Growth of Titanium Carbide in Nickel — L. P. Skolnick — 438

Strength of Silver Brazed Joints in Mild Steel — W. G. Moffatt and J. Wulff — 442

Flaking of Heavy Alloy Steel Sections — C. R. Garr and A. R. Troiano — 445

Nucleation of Dislocation Loops by Cracks in Crystals — J. J. Gilman — 449

Strain Induced Transformation in Beta Brass — T. B. Massalski and C. S. Barrett — 455

High-Strength Zirconium Alloy: Zr-4 Wt Pct Sn-1.6 Wt Pct Mo — W. Chubb — 461

Effect of Small Amounts of Alloying Elements on the Ductility of Cast Molybdenum — L. E. Olds and G. W. P. Rengstorff — 468

Table of Contents Continued

Structural Changes Associated with Strain-Induced Grain Boundary Migration in Si-Fe — K. T. Aust and C. G. Dunn — 472

Zone Purification of Reactive Metals — R. L. Smith and J. L. Rutherford — 478

Compounds in the Titanium-Rich Region of the Ti-Al System — E. Ence and H. Margolin — 484

Crack Propagation in the Hydrogen-Induced Brittle Fracture of Steel — W. J. Barnett and A. R. Troiano — 486

Cleavage Steps and the Cleavage Plane in Chemically Embrittled Cu-Au Single Crystals — R. Bakish — 494

Deformation of Magnesium Single Crystals by Nonbasal Slip — R. E. Reed-Hill and W. D. Robertson — 496

Effect of Temperature on the Flow Stress and Strain-Hardening Coefficient of Magnesium Single Crystals — H. Conrad and W. D. Robertson — 503

Comparison of the Strength of Sintered Carbides — J. Gurland — 512

Action of Vibration on Solidifying Aluminum Alloys — P. D. Southgate — 514

Discussion—Institute of Metals Division — 518

The Transactions papers appearing in the Journal of Metals during 1957 will subsequently appear in AIME Transactions Volume 209, and may be permanently referenced to that volume.

Electron Probe Microanalyzer and Its Application To Ferrous Metallurgy

by R. Castaing, J. Philibert, and C. Crussard

APPARATUS described in this paper uses the properties of X-radiation, emitted by substances under electron bombardment, as a means of rapid chemical point analysis. The method is based upon the principles of emission X-ray spectrography pioneered by Moseley in 1913.

A very finely focused beam of electrons—the *electron probe*—is projected on the surface of a sample, which has a very large area compared with the beam diameter, at the point where it is desired to know the chemical composition. The minute volume of the sample which is thus irradiated emits a complex X-ray spectrum consisting principally of the characteristic radiations of the elements present in the volume. Measurement of the wavelength and intensity of each component of this spectrum thus affords a simple method of determining the chemical identity and concentration of these elements.

The volume of sample which is analyzed at each position of the beam is limited by the diffusion of electrons in the sample. For an accelerating potential of the electron beam of about 30 kv, which is a convenient value for producing the characteristic radiation, this diffusion extends over a diameter of about 1 μ normal to the beam, and about 2 μ in the direction of the beam. Thus a beam of 1 μ in diameter leads to a volume of about 2 μ in diameter being irradiated. The limits of the analyzed region are thus considerably smaller than those obtained by using spark or arc emission spectrometry, which must extend to about 50 μ at right angles to the beam, and those obtained in X-ray fluorescence analysis, where the penetration of the specimen is considerably greater.

The apparatus itself consists of three main parts: an electron optical system, an X-ray spectrograph and an optical microscope. The electron optical system consists of a tungsten cathode emitting the electrons, and a pair of magnetic lenses which focus the electron beam on the specimen to be analyzed. The specimen is prepared in the usual way, as in optical micrography. The X-radiation, emitted at the focal spot where the electrons strike the sample, is analyzed with a curved crystal, Geiger-Müller counter, vacuum spectrograph. The light microscope, designed to observe the surface of the sample in the region to be analyzed, is provided with a reflecting objective placed on the axis of the second magnetic lens. Its magnification is X450.

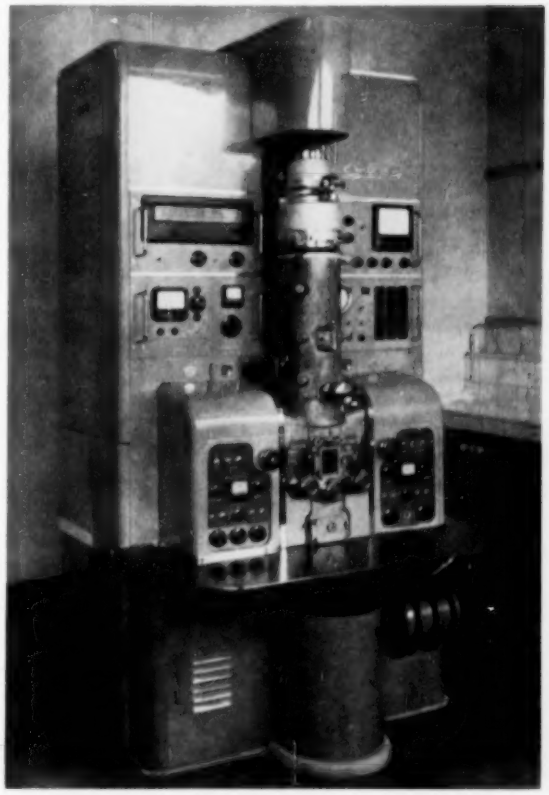

Fig. 1—General layout of the electron probe microanalyzer.

The quantitative determination of an element A in the analyzed region is made by measuring the intensity I, of a strong characteristic line of the element, as emitted from the sample, and then the intensity $I(A)$ of this same line as emitted from a

R. CASTAING is Professor, Faculté des Sciences, Université de Toulouse, Toulouse, France. C. CRUSSARD and J. PHILIBERT are Director of the Laboratories and Staff Member, respectively, Institut de Recherches de la Sidérurgie, Saint-Germain-en-Laye, France.

TP 4404E. Manuscript, June 26, 1956. New Orleans Meeting, February 1957.

Copyright 1957 by American Institute of Mining, Metallurgical, and Petroleum Engineers, Inc. Printed in U. S. A.

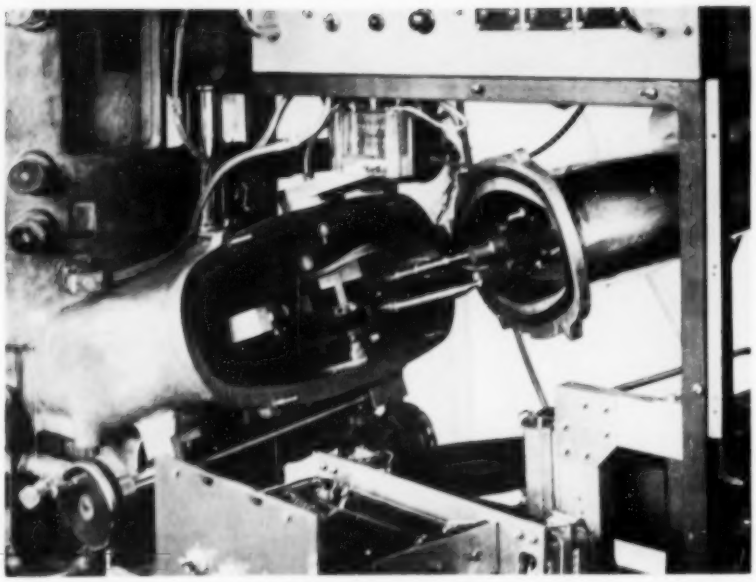

Fig. 2—View of the open spectrometer.

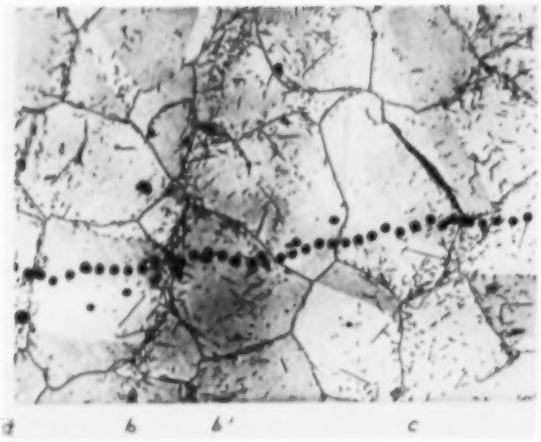

Fig. 3—Hadfield steel with segregation bands, annealed 2 hr at 850°C. Note that the impact spots are smaller than the black dots, due to a spreading of the contamination around the impact. Etched with nital. X450. Reduced approximately 35 pct for reproduction.

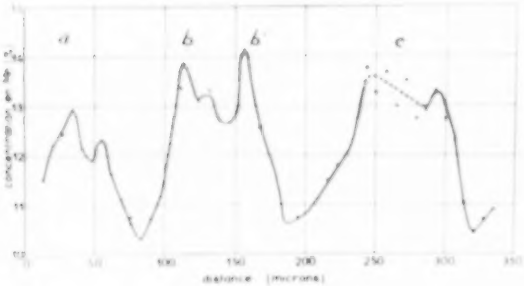

Fig. 4—Manganese segregation in Hadfield steel. Zones of high manganese content (a, b, b', and c) correspond to the carbide containing bands, see Fig. 3.

piece of pure element A mounted near the sample. It can be shown, and this is one of the greatest advantages of this technique, that the ratio $I_x/I(A)$ is to a first approximation equal to the concentration of element A in the sample. The comparison of these intensities of radiation of the same wavelength makes the method absolute, and avoids the use of standard alloys of composition covering a range of composition including that of the specimen. This factor is of prime importance if the method is to be of any practical use, since it would be impossible to make a series of standards which would be homogeneous on the small scale required for this technique.

An exact analysis requires that corrections for self-absorption in the specimen and fluorescence radiation be made. Graphs and equations giving these corrections have been established and, after due allowance, it is possible to obtain a precision of about 1 pct for chemical analyses.

The equipment described here, called hereafter a *microanalyzer*, enables the determination to be made of all the elements of atomic number greater than that of chlorine. It may be possible, by the use of special counters, to extend this limit downward in atomic number to include aluminium and magnesium. The analysis for very light elements, such as carbon, whose characteristic radiation is extremely soft, raises problems of technique which might make the method unsuitable for industrial use.

This method of rapid chemical analysis has already found many uses in the field of metallography, and may also be extended to the study of non-conductors, providing these are first coated with a very thin metallic layer (about 3 mμ thick), which makes the surface conductive. Thus an important field of application is opened up in mineralogy. The study of certain elements in marine sediments has already been successfully carried out with this equipment.

It must be pointed out that the limit of resolution, normal to the beam, so far obtained (about 2 μ), is not inherent in the method itself, but results from the use of relatively thick samples. If very thin samples were used, such as can be obtained by ionic bombardment through which the beam could pass

without scattering, this limit could be decreased still further without the technique becoming significantly more complicated.

Construction of the Apparatus and Preliminary Trials

Two microanalyzers have been constructed at the Office National d'Etudes et Recherches Aéronautiques (ONERA) to the design of one of the authors.[1,2] The cost of construction was borne by ONERA and IRSID (Institut de Recherches de la Sidérurgie), each of which now has one complete model in operation. The layout of the apparatus is shown in Figs. 1 and 2.

The remainder of this paper is devoted to a description of some preliminary tests which have been made at IRSID to establish some possible applications in metallurgy. These were confined to studies of segregation, diffusion, identification and analysis of metallic phases and, finally, the microanalysis of minerals.

Segregation of Manganese—Although manganese is reputed not to show major segregation, it has long been known from microradiographic studies that minor segregation occurs.[3] A typical case of this is to be found in the banded structure of steels that contain a rather high percentage of manganese. Quantitative information on the degree of manganese segregation can be obtained with the equipment described. For the purposes of illustration two steels have been chosen.

Tire Steel: The tire steel analyzed as follows: C, 0.55 pct; Mn, 1.05 pct; S, 0.026 pct; Si, 0.3 pct; P, 0.020 pct.

The Comstock etch, which reveals the segregation of phosphorus, showed the typical structure of the bands of segregation. It is interesting here to note the presence of sulfides in the high phosphorus zones. Table I shows the results of the authors' analyses for manganese and iron at different locations.

These results show that, besides the regions of high manganese content resulting from the presence of sulfides, there is a considerable increase of manganese in the metallic matrix in the regions where phosphorus segregates.

Hadfield Steel (12 Pct Mn, 1.28 Pct C): A thorough investigation of the decomposition of austenite in this steel[4,5] has led to the conclusion that manganese segregation should be important in this steel. For that purpose, sections parallel to the axis of the rod have been examined by conventional micrography and with the microanalyzer. The banded structure is revealed markedly after an annealing at 850°C for 2 hr by carbides precipitated along some bands, as shown in Fig. 3.

A row of black dots seen in the same figure represents the successive impacts of the electron probe, when the sample has been analyzed in the apparatus. These impacts are due to contamination by an electron beam of increased intensity.

Segregation has been observed along that line, Fig. 4. Zones of high manganese content correspond to the carbide-containing bands, but it should be noted that the reported manganese content corresponds to that of the matrix, and *not* to that of the carbides, which are richer in manganese.

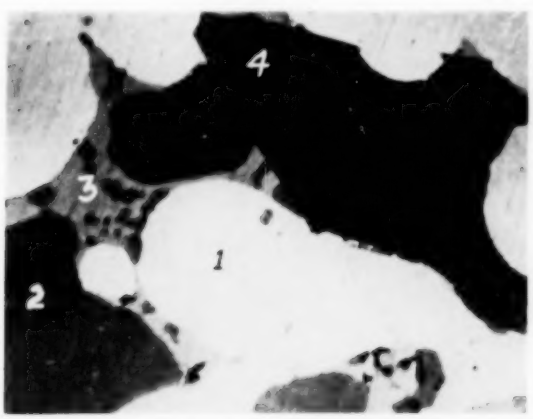

Fig. 5—Open-hearth steel scale; mechanical polishing. 1) metal; 2) FeO, ash grey; 3) FeS, yellowish grey; and 4) dark grey silicate. X1200. Reduced approximately 30 pct for reproduction.

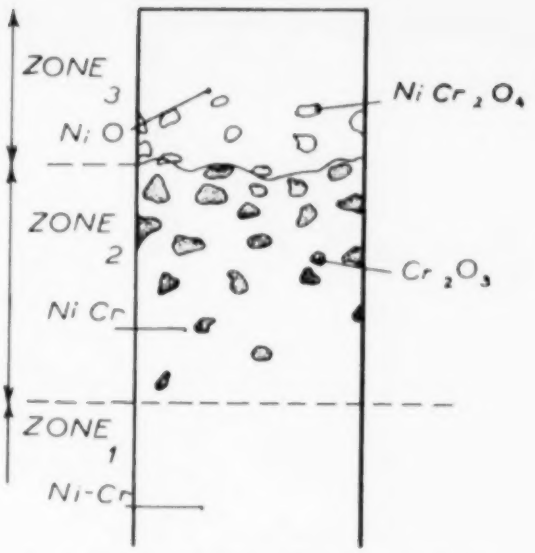

Fig. 6—Schematic diagram of oxidation of a Ni-Cr alloy.

Table I. Manganese and Iron Contents

Analyzed Region	Pct Mn	Pct Fe
High phosphorus	1.4	
Medium phosphorus	0.9 to 1.1	
Low phosphorus	0.7	
Sulfide	42.5	20.5

Selective Oxidation During Scaling—*Scaling:* Billets heated in an oil-fired furnace are coated with complex scales. With the microanalyzer, the various constituents can be studied, using a micrographic section. The photomicrograph of the interior of this scale, as found on a typical open-hearth billet (0.4 pct C, 0.6 pct Mn, 0.31 pct Si, 0.22 pct Ni, 0.14 pct Cu), shows the existence of four phases, Fig. 5. The results of the analyses, shown in Table II, enable the phases from the iron (+ manganese) content to be identified, the approximate composition of the phases being known in advance. The identifications are given in the last column of the table.

Considerable enrichment of nickel has been observed in the metal which is surrounded by oxides, sulfides, and silicates, whereas those phases themselves contain no trace of nickel. An increase in the copper content has been found in the sulfide, while

Table II. Results of Analyses

Analyzed Region	Pct Fe	Pct Mn	Pct Si	Pct Cu	Total of Metals	Identification
1—White	98	0	3	0.75	100	Metal
2—Ash grey	77	~0.5	0	0	77 to 77.5	Oxide:FeO
3—Yellowish grey	62	~0.5	0	0.8	63 to 63.5	Sulfide:FeS
4—Dark grey	52	1 to 1.5	0	0	53	Silicate

none was observable in the oxide or in the silicate. Finally, manganese was found in the silicate.

Internal Oxidation of Ni-Cr Alloys: In the field of studies of the oxidation mechanism of binary alloys of iron, nickel, or chromium,[7] analyses have been made of the products of oxidation of a Ni-Cr alloy (4.6 pct Cr). A section, perpendicular to the surface, shows three distinct zones: 1) metal, 2) metal + precipitates of Cr_2O_3, and 3) dense oxide, Fig. 6.

From the analysis of zone 2 it has been verified that the only metal in the precipitates is chromium. In the metallic matrix the percentage of nickel varies progressively from 95 pct near zone 1 to 99 or 99.5 pct near the oxide zone 3, which corresponds to a decrease in chromium due to Cr_2O_3 precipitation.

Identifying and Studying the Phase-Equilibrium Diagrams—It has been shown above, in the study of the scaling of billets, that the microanalyzer can be used for identifying phases of nearly stoichiometric compounds. Further examples of this will be given for various substances, e.g., sulfides and carbides. It should be noted here that the microanalysis of two phases in equilibrium makes the establishment of the equilibrium diagram possible with considerably fewer samples than with any previous method.

Sulfides: Microanalyses have been made of two types of sulfides encountered in cast iron. The yellowish grey sulfides, the so-called *iron-sulfides*, contain 60 to 61 pct Fe and 2 to 3 pct Mn. The ash grey sulfides, or *manganese-sulfides*, contain 43 to 25.5 pct Mn and 20 to 37.5 pct Fe. In both cases the total metal content is always about 63 pct. It is important to note that the iron-sulfide contains hardly any manganese, while the manganese-sulfide often has a higher percentage of iron than of manganese.

Carbides: In high-alloy steels the microanalyzer can be used to follow the growth of carbides during high-temperature heat treatment.

A. High Speed Steel. Analyses have been made of samples used (by J. Papier) in a study of high-speed steel of the type 18-4-2.[8] The analysis of this steel gave, in weight percent: C, 0.8; W, 18.8; Cr, 4.4; and V, 1.9.

Here again a direct study of the metallic matrix was made whereas, in the usual method, which uses electrolytic extraction of carbides, the composition of the matrix has to be determined by difference.

The samples have been treated in two ways: annealing at 1300° and at 1050°C. In the first case, the carbides were relatively large (about 5 μ), while in the second case their dimensions were as small as the limit of resolution of the microanalyzer. Three elements, iron, tungsten, and chromium, have been determined, and analyses for vanadium will be carried out shortly.

Table III. Results of Analyses

Temperature of Heat Treatment	Phase	Pct Fe	Pct W	Pct Cr	Total
1300°C	Matrix	84.5	8.5	5	98
	Carbide	31.5	60	3	94.5
1050°C	Matrix	87.5	5.5	5	98
	Carbide	31.5	56	3	90.5

The results in Table III refer to the complex carbides of tungsten and to the matrix, excluding the small carbides (of vanadium).

B. Austenitic Steel for Turbine Blades. Small precipitates were observed on a micrographic specimen of an austenitic steel (for turbine blades) containing nickel, chromium, and cobalt, and a small percentage of molybdenum, tungsten, and columbium; these were carbides of columbium, this element being found in the precipitates only and not in the matrix. It was immediately verified that this was columbium and not tantalum.

Fe-Cr Alloys: The results of G. Pomey on the α-transformation of Fe-Cr alloys[9,10] show that for a 45 pct pure chromium alloy the percentage of iron and chromium in the α and σ-phases (σ formed by cold-working) are equal. These results have been confirmed. Thus, the transformation takes place without diffusion.

By maintaining the temperature at 1050°C and using impure alloys, complex carbides of iron and of chromium can be formed, which redissolve only above 1200°C. For a 30 pct Cr alloy, annealed at 1050°C, Fig. 7, it was found that the matrix was only slightly impoverished (28.5 pct Cr) but, within 4 to 5 μ of the carbides, the percentage of chromium

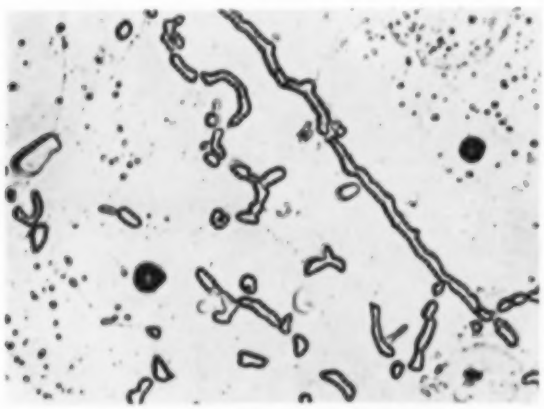

Fig. 7—Fe 30 pct Cr alloy annealed at 1050°C. Ferrite and carbides; electrolytic polishing. X700. Reduced approximately 30 pct for reproduction.

went down to 26 pct. The analysis gave the following composition for the carbide: 59 pct Cr and 31 pct Fe, which probably corresponds to the carbide M_7C_3.

Studies of Diffusion—The microanalyzer is especially useful in studying the interdiffusion between two metals, or alloys, at high temperature. With this apparatus, the penetration curves can be traced rapidly and with a high degree of accuracy. Two studies are now being pursued: one concerning the diffusion couple Fe-Cu; the other, in collaboration with the Atomic Energy Commission, concerning the couple U-Zr. From these curves the diffusion coefficients, their variation with concentration, the activation energy, and (for diffusion in multiple phases) the limits of solubility, can be obtained.

Both concentration penetration curves are given here in order to indicate the high degree of precision the method can yield.

1) For a general study of U-Zr diffusion, U-Zr couples formed by welding at 600°C under a high pressure have been utilized, and diffusion curves obtained in the temperature range where γ-uranium dissolves in all proportions in β-zirconium.[10]

Fig. 8 shows the penetration curve studied after a diffusion treatment of 4 hr at 1000°C. For these measurements, the K_α rays of zirconium and L_α rays of uranium were chosen. The diffusion coefficient was observed to vary considerably with the atomic concentration C of zirconium. The values of the diffusion coefficient at $C = 10$ pct and $C = 95$ pct are 3.2×10^{-7} sq cm per sec and 8.0×10^{-10} sq cm per sec, respectively; the diffusion coefficient is also seen to pass through a minimum of 4.3×10^{-10} sq cm per sec at $c = 80$ pct, Fig. 9.

2) The Fe-Cu couples were made by vacuum melting pure copper in pure iron crucibles above the temperature at which ε-phase is formed, i.e., above 1094°C.[11]

The diffusion of copper in iron was seen to proceed mainly along grain boundaries. After quenching and etching, each grain is seen to be surrounded by a succession of differently colored rings. The copper concentration in these aureoles have been measured from the interface Fe-Cu or from grain boundaries to the interior of the grains. Fig. 10 shows the results obtained by a diffusion treatment of 64 hr at 1100°C. The solubility limit of copper in iron, measured very near the $\gamma/\gamma + \text{liquid}$ interface, is seen to be 10 pct (in weight).

The penetration of copper in iron indicated in the graph is measured along a direction in the plane of observation, but this plane is oblique to the plane of the interface.

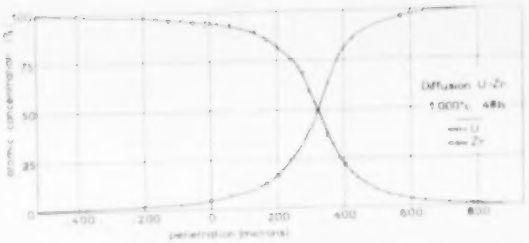

Fig. 8—Concentration-penetration curve of U-Zr diffusion for 48 hr at 1000°C.

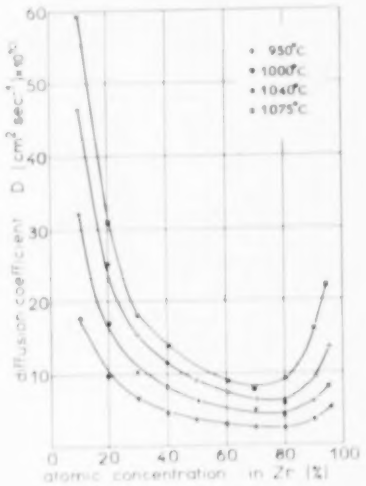

Fig. 9—Variation of the diffusion coefficient with atomic concentration in zirconium.

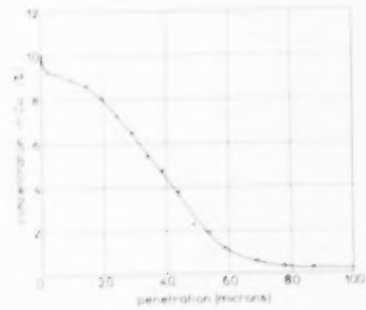

Fig. 10—Concentration-penetration curve of Cu-Fe, diffusion for 64 hr at 1100°C.

Table IV. Results of Oolite Analysis

Iron Ore	Analyzed Region	Fe, Pct
First oolite	Central nucleus	50.5
	Black zones	43.5 to 44.5
	White zones	48.5 to 49.5
	Grey zones	45.5 to 46.5
Second oolite	Central nucleus	52.5
	Black zones	42.5
	Dark grey zones	45.5 to 46.5
	White zones	48 to 49

Studies of Iron Ore—It is possible to study nonconductors as well as metals, provided they receive a special preparation such as metallizing.

Oolites, extracted from a Lorraine ore, were studied in this manner. These were first embedded in plastic, and mechanically polished, Fig. 11. Analyses of the iron contents were made of the nucleus and the various concentric layers of the oolite, Table IV. The percentage of manganese in oolite is too low to permit precise measurements; however, it seems that the zones which are richest in iron are also the richest in manganese.

Conclusion

This short survey of the first results obtained with the fine-focus emission spectrometer demonstrates the great variety of its applications. It is possible to carry out local analyses of non-conductors (such as ores) as well as metals or alloys of one or more phases and, further, to measure all the variations of composition within one phase such as a segregate. The very light elements cannot be determined, as has been stated in the introduction. The microanalyzer has also been used to find the

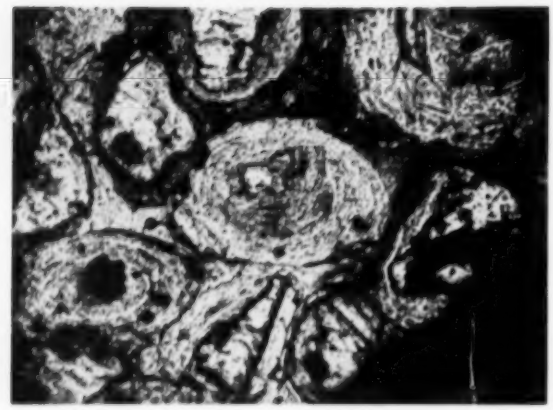

Fig. 11—Oolite from the ore of Sainte Barbe, embedded in plastic and mechanically polished. X150. Reduced approximately 25 pct for reproduction.

composition of non-metallic inclusions, of sulfides, carbides, and oxides formed by internal or surface oxidation. By analyzing the surrounding matrix, the distribution coefficient of various elements between precipitates and matrix is automatically obtained. If the precipitates have been obtained by prolonged annealing at a fixed temperature, it is easy to establish the equilibrium diagram.

Experience has shown that the accuracy of these analyses is excellent. The relative error is about 1 pct for percentages which are not too low. The detection threshold of an element seems to be at concentrations of about 0.2 to 0.3 pct.

References

[1] R. Castaing: Thesis, 1951. ONERA Publication No. 55.

[2] R. Castaing and J. Descamps: *Le Journal de Physique et le Radium*, 1955, vol. 16, p. 304.

[3] W. Betteridge and R. S. Sharpe: *Journal* Iron and Steel Inst., London, 1948, vol. 158, p. 185.

[4] A. Kohn, J. Plateau, and G. Pomey: *Comptes Rendus*, 1956, vol. 242, p. 256.

[5] G. Collette, C. Crussard, A. Kohn, J. Plateau, G. Pomey, and M. Weisz: Communication to *Journée d'automne de la Sté Francaise de Metallurgie*, 1956.

[6] J. Moreau and J. Benard: *Comptes Rendus*, 1953, vol. 237, p. 1417.

[7] J. Papier: *Revue de Metallurgie*, 1954, vol. 51, p. 723.

[8] G. Pomey and P. Bastien: *Revue de Metallurgie*, 1956, vol. 53, p. 147.

[9] G. Pomey: Thesis, 1955. IRSID Publication No. A117.

[10] Y. Adda and J. Philibert: *Comptes Rendus*, 1956, vol. 242, p. 3081; vol. 243, p. 1115.

[11] M. Zamcer and F. Sirca: *Rudarsko Metalurski Zbornik*, 1951, No. 1, p. 25.

Discussion of this paper sent (2 copies) to AIME by June 1, 1957 will appear in AIME *Transactions* Vol. 209, 1957, and in JOURNAL OF METALS, October 1957.

Oxidation of Zirconium Between 400° and 800°C

The vacuum microbalance method is used to study the oxidation reaction for two surface preparations over the temperature range of 400° to 800°C. The results fit in well with the authors previous work at temperatures of 200° to 425°C and with the work of other groups at higher temperatures. An analysis of the rate data shows that the cubic rate law fits the experimental data best for the abraded specimens. However, the parabolic rate law can be fitted to the data if an initial deviation is disregarded. With chemically polished specimens, a good fit is obtained with the parabolic rate law. The parabolic rate law constant *A* gives two straight lines when plotted as log *A* vs 1/*T*. For the temperature range of 200° to 525°C an energy of activation of 18,200 cal per mol is calculated while a value of 28,600 cal per mol is calculated for the temperature range of 525° to 750°C. The results of this work bring together the previously determined high-temperature oxidation studies of Cubicciotti with the early low-temperature studies of Gulbransen and Andrew.

by Earl A. Gulbransen and Kenneth F. Andrew

DRY oxidation of zirconium has been studied by several groups.[1-3] The present work extends our early study[1] to the high-temperature studies of Cubicciotti[2] and Belle and Mallett.[3] Gulbransen and Andrew[1] showed that the parabolic rate law fitted the 2-hr experiments between 200° and 425°C after an initial deviation. An energy of activation of 18,200 cal per mol was calculated. Cubicciotti,[2] in a study between 593° and 880°C, showed that the parabolic rate law fitted the data and an energy of activation of 32,000 cal per mol was calculated. In contrast to these studies on sheet specimens, Belle and Mallett[3] studied the oxidation reaction on rod specimens and found a cubic rate law to fit the data.

E. A. GULBRANSEN, Member AIME, and K. F. ANDREW are associated with the Research Laboratories, Westinghouse Electric Corp., Pittsburgh.

TP 4376E. Manuscript, July 9, 1956. New Orleans Meeting, February 1957.

In view of the growing importance of zirconium and its alloys as metallurgical materials, this work was undertaken with three purposes in view: 1) to study the reaction between 400° and 800°C to ascertain if a change occurs in the reaction mechanism between 400° and 600°C; 2) to test the application of the cubic and parabolic rate laws to the data for long-time oxidations and for specimens of varying surface preparation; and 3) to test the mechanism of the reaction by the use of theoretical rate expressions.

Experimental

The vacuum microbalance method was used in this work.[5,6] To extend the range of our earlier work, smaller specimens were used together with a specially constructed low-sensitivity microbalance. The balance had a sensitivity of 0.21 × 10^{-4} cm per μg weight change. Weight changes were estimated to 1.5 μg.

A gas-tight mullite furnace tube was used to enclose the sample.[7] This tube was sealed directly to the all-glass vacuum system. Pressures of less than 10^{-4} mm Hg could be achieved in the system.[8]

To minimize reaction of zirconium with the gases present in the vacuum system during the heat-up period, the specimen and furnace tube were evacuated at room temperature for 16 hr at pressures of less than 10^{-4} mm Hg. After raising the furnace around the furnace tube, purified oxygen[9] was added as soon as thermal equilibrium was established.

Table I shows the spectrographic analyses of the hafnium-free grade of zirconium.

Three specimen sizes were used. The 0.5000-g specimens had surface areas of 11.3 to 12 sq cm and a thickness of 0.0127 cm, the 0.2500-g specimens had surface areas of about 6.5 sq cm, and the 0.1000-g specimens had surface areas of 2.5 sq cm. The samples were abraded and cleaned following procedures used in earlier studies.[1]

Some of the specimens were chemically polished in a special acid bath having a composition 45 pct HNO_3, 10 pct HF, and 45 pct H_2O.

Results and Discussion

Figs. 1 to 3 show the results of the oxidation experiments. In these figures the weight gain in micrograms per square centimeter is plotted as a function of the time in minutes. An oxygen pressure of 7.6 cm Hg and oxidation times of 6 hr are used for all of the experiments.

To convert the weight gain in micrograms per square centimeter to thickness in Angstrom units, a factor of 61.5 is used. This factor is calculated from the crystal structure of the oxide,[7] assuming a surface roughness ratio of unity. The reproducibility of the data is 10 to 25 pct below 500°C and 5 to 10 pct above 500°C.

Abraded Surface Treatment—Fig. 1 shows weight gain curves for the temperature range of 450° to 750°C. A rapid initial rate of reaction occurs with the rate of reaction decreasing as the oxide thickens. Table II shows a summary of the thickness data after 6 hr of reaction, together with the color of the oxide film. All of the oxide films adhered to the metal on cooling. At 750°C the oxide grew to a thickness of 125,000Å in 6 hr. This corresponds to 20 pct reaction of the specimen.

At 800°C an extremely rapid reaction occurred. Before an observation could be made on the weight gain after adding oxygen, the specimen and supporting wire melted and fell to the bottom of the

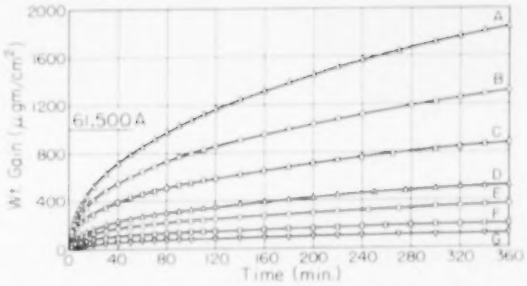

Fig. 1—Reaction of zirconium with oxygen at 450° to 750°C; 7.6 cm of Hg of O_2, abraded through 4/0. *A*, 750°; *B*, 700°; *C*, 650°; *D*, 600°; *E*, 550°; *F*, 500°; and *G*, 450°C.

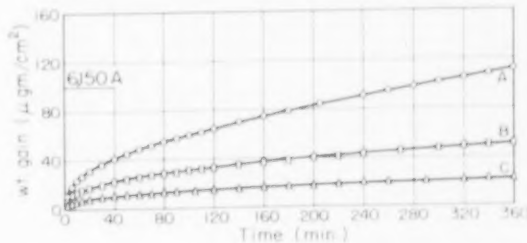

Fig. 2—Effect of temperature on oxidation of chemically polished zirconium; 7.6 cm of Hg of O_2. *A*, 500°; *B*, 450°; and *C*, 400°C.

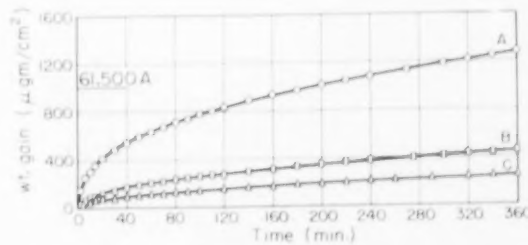

Fig. 3—Effect of temperature on oxidation of chemically polished zirconium; 7.6 cm of Hg of O_2. *A*, 700°; *B*, 600°; and *C*, 550°C.

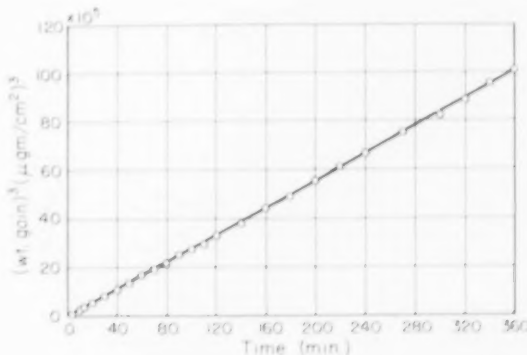

Fig. 4—Oxidation of zirconium (cubic plot) at 500°C; 7.6 cm of Hg of O_2, abraded through 4/0.

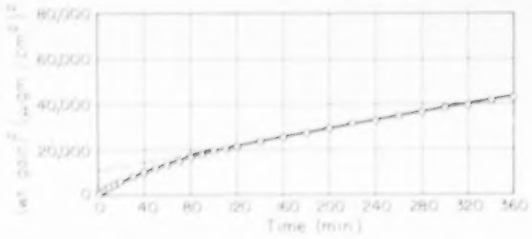

Fig. 5—Oxidation of zirconium (parabolic plot) at 500°C, 7.6 cm of Hg of O_2, abraded through 4/0. A equals 1.48×10^{-13} (g per sq cm)^2 per sec.

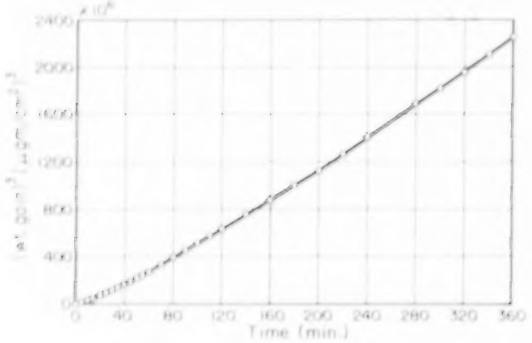

Fig. 6—Oxidation of zirconium (cubic plot) at 700°C, 7.6 cm of Hg O_2, abraded through 4/0.

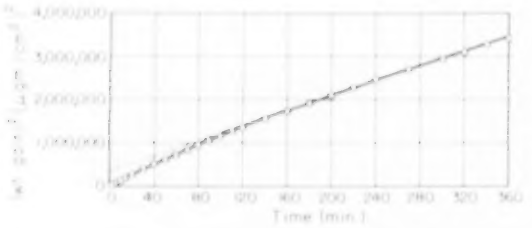

Fig. 7—Oxidation of zirconium (parabolic plot) at 750°C, 7.6 cm of Hg of O_2, abraded through 4/0. A equals 1.42×10^{-12} (g per sq cm)^2 per sec.

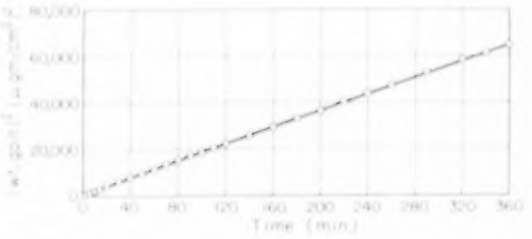

Fig. 8—Oxidation of chemically polished zirconium (parabolic plot) at 550°C, 7.6 cm of Hg of O_2. A equals 2.89×10^{-13} (g per sq cm)^2 per sec.

furnace tube. This type of spontaneous ignition of zirconium has been reported by Hayes and Roberson[18] using thicker specimens at 1000°C.

Spontaneous ignition results from the rapid rate of oxidation, the high heat of formation of the oxide,[11] and the high surface-to-mass ratio for 5-mil-strip specimens.

Chemically Polished Specimens—Figs. 2 and 3 show weight gain curves for the temperature ranges of 400° to 500°C and 550° to 700°C, respectively. Typical oxidation curves are obtained. However, the rates of oxidation are smaller than those obtained on abraded specimens for the same temperatures. We attribute the lower rates of oxidation to the smoother surfaces formed by chemical polishing and to the presence of a passive oxide film formed in the chemical polishing process.[19]

Table II summarizes the 6-hr oxide film thickness data and the color of the oxide film for the chemically polished specimens.

Rate Law Correlation—Both the cubic rate law and the parabolic rate law have been used to explain the oxidation rate data on zirconium.[1-6] The cubic rate law states

$$W^3 = A't + C'.$$

Here A' and C' are constants, t is the time, and W is the weight gain. Mott and Cabrera[16] derived this law from physical principles for a limited thickness range. No general derivation for a wide range of film thicknesses has been given.

The parabolic rate law states

$$W^2 = At + C.$$

Here A and C are constants and the other symbols have the same meaning as in the previous equation.

Table I. Spectrographic Analyses of Zirconium

Element	Wt Pct
Si	0.002
Fe	0.015
Al	0.007
Hf	0.009
Cu	0.0006
Ti	0.001
Ca	<0.05
Mn	<0.001
Mg	<0.001
Pb	0.002
Mo	<0.001
Ni	0.002
Cr	0.001
Sn	<0.001
Co	<0.0005
B	0.00005
Cd	<0.00005

Wagner and Grünewald[17] and later Mott[16] derived this equation from fundamental physical principles.

Two points of view may be taken in applying rate laws to the experimental data. First, from a practical point of view one may be interested in finding the best empirical rate law. Second, from a theoretical point of view one may be interested in interpreting the mechanism of the reaction. In the latter case it is essential to realize that the properties of the oxide and the surface depend upon the initial pre-treatment and the amount of reaction. Thus, it is difficult to interpret theoretically the initial stage of oxidation in terms of the physical and chemical properties of thicker oxide films.

At least five factors may affect the initial stages of the reaction. 1) The surface area exposed to the reacting gas decreases as oxidation proceeds. 2) The

surface temperature may vary due to the rapid initial reaction. 3) Certain impurities may concentrate in the oxide during the initial stages of the reaction. 4) The crystallite size of the oxide changes rapidly during the initial stages of the reaction. 5) The metal may be covered with an oxide film of variable thickness and properties.

To test the fit of the two rate laws, plots are made of the experimental data. Fig. 4 shows a plot to test the cubic rate law. Here the weight gain cubed is plotted against time. Fig. 5 shows a test of the parabolic rate law. Here the weight gain squared is plotted against time. These figures and Table II show that the cubic rate law gives a better fit to the data for the experiments on abraded specimens between 400° and 650°C.

Figs. 6 and 7 show cubic and parabolic rate law plots for the 700°C oxidation of abraded specimens. An initial deviation is found for the parabolic rate law plot while the cubic rate law plot shows a steadily increasing slope. Similar deviations of the rate laws are found for the 750°C experiment.

Table II. Thickness and Color of the Oxide Films Formed on Zirconium

Temperature, °C	Oxide Thickness*		Color	Rate Law
	μG per Sq Cm	A		
Abraded				
450	126	7,750	Blue-black	Cubic
475	160	9,840	Blue-black	Cubic
500	207	12,730	Blue-black	Cubic
525	264	16,240	Blue-black	Cubic
550	361	22,200	Blue-black	Cubic
600	530	32,600	Blue-black	Both cubic and parabolic laws show deviations
650	880	54,100	Blue-black	
700	1310	80,570	Blue-black	
750	1850	113,800	Black	
800	Runaway reaction; specimen melted.			
Chemically Polished				
400	22.6	1,390	Green-pink	Parabolic
450	51.2	3,150	Metal gray	Parabolic
450	59.1	3,630	Metal gray	Parabolic
500	112	6,890	Metal gray	Parabolic
550	254	15,600	Metal gray	Parabolic
600	449	27,600	Metal gray	Parabolic
700	1270	78,100	Metal gray	Both cubic and parabolic laws show deviations

* For 6-hr experiments.

We conclude that for practical predictions the cubic rate law gives the best correlation.

For the chemically polished specimens, Table II summarizes the fit of the two rate laws. Figs. 8 and 9 shows the parabolic rate law plots for the 550° and 700°C experiments. An excellent fit is found for the 550°C experiment. At 700°C the data only fit the rate law after a reaction time of 140 min.

The good fit to the parabolic rate law below 600°C for these specimens is probably due to the lower surface roughness of the specimen and to the presence of a passive film which limits the initial rate of reaction. Mathematically, the parabolic rate law predicts a slower initial rate of reaction than the cubic rate law. It would be expected, therefore, that the parabolic rate law would explain the oxidation of chemically polished specimens, with the cubic rate law giving a better fit for the abraded specimens.

Temperature Coefficient—Table III shows a summary of the parabolic rate law constants for the two surface preparations, while Fig. 10 shows a plot of the logarithm of the rate law constant against 1/T. The results of the present study are shown together with the results of our earlier work[1] and those of Cubicciotti.[7] The figure shows that the abraded and chemically polished specimens oxidize at nearly the same rate for temperatures of 600°C and higher. At lower temperatures, the chemically polished specimens react at a much lower rate. The high temperature results are in fair agreement with those of Cubicciotti,[7] considering the fact that a different quality of zirconium was used as well as a different experimental method.

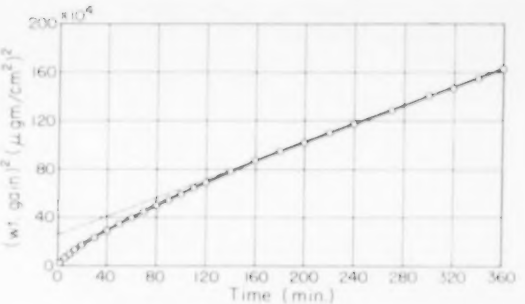

Fig. 9—Oxidation of chemically polished zirconium (parabolic plot) at 700°C, 7.6 cm of Hg of O_2, abraded through 4/0. A equals 6.2×10^{-11} (g per sq cm)^2 per sec.

The results on the abraded specimens of Fig. 10 are explained by two straight lines. Below 525°C a heat of activation of 18,200 cal per mol is calculated while a heat of activation of 28,600 cal is calculated for the data between 525° and 750°C. The reason for the break in the plot at 525°C is not understood.

Theoretical

One method to establish the mechanism of the oxidation reaction is to apply theoretical rate laws to the data and test the agreement. In our earlier paper[1] we applied the transition state theory of oxidation[10] to interpret the parabolic rate laws. Using the experimental value of 18,200 cal per mol for the heat of activation an entropy of activation of −25.6 cal per mol per °C was calculated. The negative entropy of activation was interpreted in terms of diffusion occurring at oxide grain boundaries rather than through the oxide lattice.

With the restatement of the classical theory of diffusion by Zener,[11] it has been possible to clarify the processes involved in oxidation and diffusion and to interpret the entropies and heats of activation experimentally observed in terms of assumed models.

Two types of processes are involved in oxidation: thermodynamic processes which involve the free energy of formation of a vacancy or interstitial defect ΔF, and rate processes which involve a free energy of activation of diffusion ΔF^*. For oxidation reactions where the parabolic rate law has been found to fit the data, it is possible to set down several mechanisms for the reaction depending upon the details of forming defects by which reactions occur.

Mechanisms for the Oxidation—Four mechanisms have been proposed for the oxidation of metals. These are: 1) migration of anions via anion vacancies, 2) migration of cations via cation vacancies, 3) migration of anions via interstitial sites, and

4) migration of cations via interstitial sites. Mechanism 1 has been proposed to be rate controlling with the vacancies being formed at the metal-oxide interface. Before discussing these mechanisms further, it is important to consider the crystal structure of ZrO_2.

Structure of ZrO_2, Vacancies, and Intersitial Holes—Electron diffraction studies by Hickman and Gulbransen[7] have shown the formation of monoclinic ZrO_2 when zirconium is oxidized. The monoclinic lattice is a distorted form of the fluorite structure. The oxygen ions in ZrO_2 are in a close-packed arrangement with oxygen spacings of 2.6 to 2.7A. Every other distorted cube of eight oxygen ions contains a zirconium ion.

Since the oxygen ions are in a close-packed arrangement, it would be extremely difficult for another oxygen ion or atom to occupy the center of this close-packed group. From a structural viewpoint, the migration of anions interstially is rather improbable.

The evidence to support the existence and diffusion of anion vacancies is the fact that inert markers placed on the metal surface remain on the surface during oxidation[8] and to the fact that the oxide may contain less oxygen (or more metal) than the stoichiometric amount. To maintain electrical neutrality, two zirconium ions near the anion vacancy must assume a charge of +3 instead of +4.

In the fluorite structure, the interstitial sites for cation diffusion are the same as those discussed for interstitial oxygen ion diffusion. The six adjacent distorted cubes of oxygen ions to a Zr^{++} ion are vacant. The thermodynamic evidence suggests that the Zr^{++} ion is strongly bonded to the neighboring oxygen ions.

Cation vacancies are formed by solution of oxygen in the lattice and the removal of a Zr^{++} ion. To maintain electrical neutrality, four neighboring $O^{=}$ ions may give up an electron forming O^{-}.

To simplify the use of rate theory in evaluating the mechanism of oxidation, we will consider the details of two most probable oxidation mechanisms: 1) anion diffusion via anion vacancies, and 2) cation diffusion via cation vacancies. Cation diffusion via interstitial sites can be classed with mechanism 1 since the entropy of the formation of an interstitial ion is probably small. In contrast, mechanism 2 involves a rather large entropy change for the formation of defects.

Fig. 11 shows the two possible mechanisms considered here for the oxidation of zirconium and the defect equations.

Table III. Parabolic Rate Law Constants Abraded and Chemical Polished Surfaces (New Data)

Temperature, °C	Chemically Polished, A (G per Sq cm)^2 per Sec	Abraded, A (G per Sq Cm)^2 per Sec
400	2.11×10^{-14}	—
450	1.41×10^{-13}	5.60×10^{-13}
	1.08×10^{-13}	9.55×10^{-13}
475		8.94×10^{-13}
500	5.70×10^{-13}	1.48×10^{-12}
525		2.70×10^{-12}
550	2.89×10^{-12}	4.88×10^{-12}
600	8.44×10^{-12}	1.08×10^{-11}
650		3.01×10^{-11}
700	6.20×10^{-11}	6.80×10^{-11}
750	—	1.42×10^{-10}
800	—	Ignited

Parabolic Rate Law Equations—Using the classical theory of oxidation and diffusion,[9] we can derive theoretical expressions for the parabolic rate law constant A.

Assuming anion diffusion with the vacancies formed by mechanism A of Fig. 11, we have the following expression based on 1 g atom of oxygen reacting with the metal.

$$A = 1.26\Omega N\nu a^2\gamma \exp\left[\frac{(\Delta S^v/3 + \Delta S^*)}{R}\right] \exp\left[\frac{-(\Delta H^v/3 + \Delta H^*)}{RT}\right] \quad [1]$$

Assuming cation diffusion with vacancies formed by mechanism B of Fig. 11, we have the following expression based on 1 g atom of oxygen reacting with the metal.

$$A = 0.66\Omega N\nu a^2\gamma \exp\left[\frac{(\Delta S^v/2.5 + \Delta S^*)}{R}\right] \exp\left[\frac{-(\Delta H^v/2.5 + \Delta H^*)}{RT}\right] \cdot P_{O_2}^{1/4} \quad [2]$$

Here Ω is the volume of oxide formed per ion diffusing through the lattice, P is the pressure of O_2, N is the number of anion or cation sites per cubic centimeter, ν is the frequency of vibration along the reaction path, a is the distance between diffusing sites, γ is a constant determined by the geometry of the jump processes and ΔS^* and ΔH^* are the entropy and heat of activation of diffusion. ΔS^v and ΔH^v are the entropy and heat of formation of 1 g atom of oxide following mechanisms A and B of Fig. 9. The factors 3 and 2.5 by which ΔS^v and ΔH^v are divided arise from the number of defects formed per gram atom of oxide formed.

Except for numerical constants and the pressure of oxygen in equation 2, these expressions are similar.

In the discussion that follows we shall estimate the entropy of defect formation for the two processes. The other quantities in the rate expressions are determined from the structure of the oxide. Since the heat of formation of defects plus the heat of activation of diffusion are determined experi-

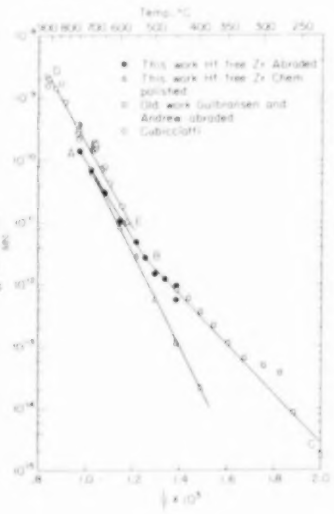
Temp., °C
This work Hf free Zr Abraded
This work Hf free Zr Chem polished
Old work Gulbransen and Andrew abraded
Cubicciotti

Fig. 10—Log A vs $1/T$ oxidation of zirconium. $\Delta H_{a,p}$ = 28,600 cal per mol; $\Delta H_{a,c}$ = 18,200 cal per mol; and $\Delta H_{a,x}$ = 32,000 cal per mol, according to Cubicciotti.[2]

mentally, the only undetermined quantity is the entropy of activation of diffusion. This can be calculated experimentally from the rate expression. According to the Zener picture of diffusion,[17] the entropy of activation of diffusion must take on positive values for normal diffusion processes.

Calculation of Absolute Rate of Oxidation of Zirconium—The following steps are used to evaluate the parabolic rate law constant A.

1) The frequency ν is evaluated from the Debye temperature θ_D by the equation

$$\nu_{max} = \theta_D \cdot \frac{k}{h}.$$

Here k is Planck's constant and h is Boltzman's constant. Appendix 1 shows the calculation.

2) γ, a, Ω and N are determined from the structure of ZrO_2.

3) $\Delta H^\circ + \Delta H^*$ are determined as a sum from the experimental plot of log A vs $1/T$. Fig. 10 shows two values of $\Delta H^\circ + \Delta H^*$. These are 18,200 cal per mol for the temperature range of 200° to 550°C and 28,600 cal per mol for the temperature range of 550° to 750°C.

4) ΔS° can be estimated from two considerations: a) entropy change assuming no distortion of the ZrO_2 lattice; or b) entropy change of distortion of the ZrO_2 due to the formation of the vacancy and other lattice defects. Gulbransen and Andrew have made these calculations in detail for NiO.[18] Appendix 2 shows the calculation of ΔS° for the two processes of forming vacancies.

5) ΔS^*, the entropy of activation of diffusion has been shown by Zener to take on positive values for lattice diffusion. ΔS^* may be evaluated theoretically.[17, 19] However, the accuracy of the experimental data does not warrant the calculation. We judge a mechanism as a probable one if a small positive value is obtained for ΔS^*.

Correlation with Theory—Table IV summarizes the experimental and calculated values for the parabolic rate law constants, the heats, entropies, and free energies of activation as evaluated from the theoretical rate expressions. The results for the two mechanisms are given for the temperature range of 525° to 750°C.

Table V summarizes the results of the calculations on ΔS° and ΔS^* for the two processes. Since our criterion of a fit of the mechanism is a positive value for ΔS^*, the cation diffusion process gives the best agreement with the data. This result is surprising since previous work has suggested anion diffusion as the rate controlling mechanism.[20]

The results at 200° to 525°C are difficult to interpret on the basis of lattice diffusion. The negative values of ΔS^* may be interpreted on the basis of diffusion at grain boundaries or other short circuiting paths in the oxide. This has been discussed in an earlier paper.[21]

Summary

The oxidation of zirconium has been studied over the temperature range of 400° to 800°C. The results on abraded specimens can be fitted best to the cubic rate law. However, the results on chemically polished specimens can be fitted to the parabolic rate law. The temperature dependence of the parabolic rate law leads to an energy of activation of 18,200 cal per mol between 200° and 525°C. Above this temperature the calculated energy of activation is 28,600 cal per mol.

The oxide film adheres to the surface up to a temperature of 800°C where spontaneous ignition occurred. In general, the specimens given a chemically polished treatment reacted at a slower rate with oxygen than the abraded specimens.

The classical theory of oxidation and diffusion is applied to the data assuming two mechanisms of reactions. A fit is obtained with a mechanism based on the diffusion of zirconium ions in cation vacancies.

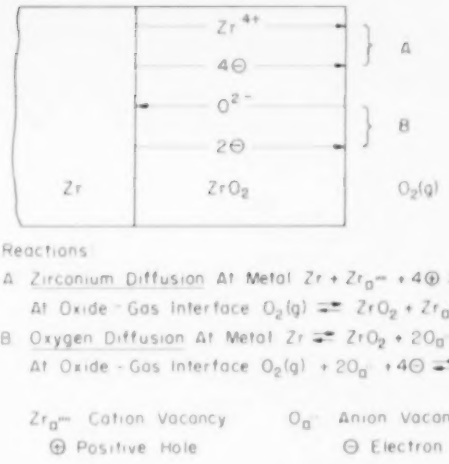

Fig. 11—Two mechanisms of oxdiation of zirconium.

Appendix 1—Frequency of Vibration of $O^{\cdot}$-$O^{\cdot}$ and $Zr^{\cdots}$-$Zr^{\cdots}$ Bonds in ZrO_2

Let us assume that the atoms in ZrO_2 are acting as harmonic oscillators and that Hooke's law governs the interactions. It is necessary to assume that the calculated frequency is characteristic of the movement of $O^{\cdot}$ ions and $Zr^{\cdots}$ ions in the lattice. The assumption of harmonic oscillators is a reasonable one as the atoms spend the great bulk of their time in these energy states.

The value of the frequency ν_{max} is calculated from the characteristic Debye temperature θ_D,

$$\theta_D = \frac{h\,\nu_{max}}{k}.$$

Here k is Boltzman's constant and h is Planck's constant. For ZrO_2, θ_D is 345,[22] which gives a value of ν_{max} of 7.25×10^{12} vibrations per sec.

Appendix 2—Entropy of Vacancy Formation

Cation Vacancies—According to the model of Fig. 11, the vacancies are formed by the defect equation

$$\tfrac{1}{2}\,O_2\,(g) \rightleftharpoons \tfrac{1}{2}\,ZrO_2 + \tfrac{1}{2}\,Zr\,(x) + 2\,(y).$$

Here $Zr\,(x)$ refers to cation vacancy and (y) is a positive hole. Since zirconium has only four valence electrons, the positive hole may be associated with an $O^{\cdot}$ site giving $O^{\times}$.

The entropy of ZrO_2[23, 24] at 873°K is 22.94 cal per mol per °C. The entropy of the $2O^{\cdot}$ in ZrO_2 is assumed to be two thirds of 22.94 or 15.30 cal per mol

Table IV. Parabolic Rate Law Constants, Entropies, Heats and Free Energies of Activation As Calculated by the Two Mechanisms in Abraded Specimens

Temperature, °C	A, Sq Cm per Sec	$\frac{\Delta H^{\circ} + \Delta H^{*}}{2.5}$ Cal per Mol	$\frac{\Delta S^{\circ} + \Delta S^{*}}{2.5}$ Cal per Mol per °C	$\frac{-T(\Delta S^{\circ} + \Delta S^{*})}{2.5}$ Cal per Mol	ΔF, Cal per Mol
Anion diffusion					
525	1.00×10^{-9}	28,600	−9.1	7260	35,860
550	1.82×10^{-9}	28,600	−8.7	7160	35,760
600	4.02×10^{-9}	28,600	−9.3	8120	36,720
650	1.12×10^{-8}	28,600	−8.8	8120	36,720
700	2.53×10^{-8}	28,600	−9.1	8850	37,450
750	5.28×10^{-8}	28,600	−9.1	8310	37,910

Temperature, °C	A, Sq Cm per Sec	$\frac{\Delta H^{\circ} + \Delta H^{*}}{3}$ Cal per Mol	$\frac{\Delta S^{\circ} + \Delta S^{*}}{3}$ Cal per Mol per °C	$\frac{-T(\Delta S^{\circ} + \Delta S^{*})}{3}$ Cal per Mol	ΔF, Cal per Mol
Cation diffusion					
525	1.00×10^{-9}	28,600	−6.9	5510	34,110
550	1.82×10^{-9}	28,600	−6.5	5350	33,950
600	4.02×10^{-9}	28,600	−7.1	6200	34,800
650	1.12×10^{-8}	28,600	−6.4	5910	34,510
700	2.53×10^{-8}	28,600	−6.9	6710	35,310
750	5.28×10^{-8}	28,600	−6.9	7060	35,660

per °C. On the basis of 1 g atom of oxygen ions, this is 7.65 cal per °C.

The entropy of 1 g atom of oxygen[7] at 873°K is 28.55 cal per °C. For the above reaction the entropy change is −20.9 cal per g atom per °C.

The total entropy change is made up of two terms: 1) the entropy change without lattice distortion, and 2) the entropy change associated with the two types of distortion. For solution of 1 g atom of oxygen in NiO the authors have shown that this entropy term amounts to −2.3 cal per mol. We shall assume the same value for the zirconium reaction. Since 2.5 defects are involved, the effect of the distortion entropy term on the calculation is minor. If we assume this value for the distortion effect the total entropy change associated with 1 g atom of oxygen is −20.9 + (−2.3) or −23.2 cal per °C. The entropy change per mol of defects is −9.3 cal per °C.

Table V. Summary of Oxidation Data

	Anion Diffusion		Cation Diffusion	
	700° to 525°C	525° to 750°C	700° to 525°C	525° to 750°C
$(\Delta H^{\circ} + \Delta H^{*})$ / 3 (experimental) cal per mol	18,200	28,600	—	—
(0.4 $\Delta H^{\circ} + \Delta H^{*}$) (experimental) cal per mol	—	—	18,200	28,600
$(\Delta S^{\circ} + \Delta S^{*})$ / 3 (experimental) cal per mol per °C	−21.9	−9.0	—	—
(0.4 $\Delta S^{\circ} + \Delta S^{*}$) (experimental) cal per mol per °C	—	—	19.6	−6.7
ΔS° (theory) / 3	−0.6	−0.6	—	—
(0.4 ΔS° (theory)	—	—	9.3	−9.3
ΔS^{*} (experimental)	−21.3	−8.4	10.3	+2.6

Anion Vacancies—The entropy of $\frac{1}{2}$ g atom of the metal is 8.2 cal per °C, while the entropy of 1 g atom of zirconium in ZrO_2 is 7.65 cal per °C, assuming that the zirconium ions contribute one third of the entropy in ZrO_2. We assume the entropy associated with the quasi-free electron to be small. The entropy change for the reaction above without distortion is −0.55 cal per °C. Adding the entropy change of −1.3 cal per g atom per °C for the formation of an anion defect, assuming the value to be similar to that for a cation defect, we have −1.9 cal for the above reaction. Since three defects are involved, the entropy change per g atom of defects is −0.6 entropy units. This calculation is very approximate. However, the entropy change associated with this particular mechanism is small.

References

[1] E. A. Gulbransen and K. F. Andrew: *AIME Trans.*, 1949, vol. 185, p. 515; JOURNAL OF METALS, August 1949.
[2] D. Cubicciotti: *Journal* Amer. Chemical Soc., 1950, vol. 72, p. 4138.
[3] J. Belle and M. W. Mallett: *Journal* Electrochemical Soc., 1954, vol. 101, p. 339.
[4] E. Gulbransen: *Metallurgy of Zirconium*, Ed. by Lustman and Kerze, pp. 555-608. McGraw-Hill Pub. Co. New York, 1955.
[5] *Reactor Handbook. Materials.* U. S. Atomic Energy Commission. McGraw-Hill Pub. Co. New York, 1955.
[6] E. A. Gulbransen: *Trans.* Electrochemical Soc., 1942, vol. 81, p. 187.
[7] E. A. Gulbransen: *Review of Scientific Instruments*, 1944, vol. 15, p. 201.
[8] E. A. Gulbransen and K. F. Andrew: *Industrial and Engineering Chemistry*, 1949, vol. 41, p. 2762.
[9] J. W. Hickman and E. A. Gulbransen: *Journal of Analytical Chemistry*, 1948, vol. 20, p. 158.
[10] E. T. Hayes and A. H. Roberson: *Trans.* Electrochemical Soc., 1949, vol. 96, p. 142.
[11] G. L. Humphrey: *Journal* Amer. Chemical Soc., 1954, vol. 76, p. 978.
[12] K. F. Andrew: Unpublished results.
[13] N. F. Mott and N. Cabrera: *Reports on Progress in Physics*, 1948-1949, vol. 12, p. 163.
[14] C. Wagner and K. Grünewald: *Ztsch. für Physikalische Chemie*, 1938, vol. B40, p. 455.
[15] N. F. Mott: *Trans.* Faraday Soc., 1940, vol. 36, p. 472.
[16] E. A. Gulbransen: *Trans.* Electrochemical Soc., 1943, vol. 83, p. 301.
[17] C. Zener: *Journal of Applied Physics*, 1951, vol. 22, p. 372.
[18] D. E. Thomas: *Metallurgy of Zirconium*, Ed. by Lustman and Kerze, p. 635. McGraw-Hill Pub. Co. New York, 1955.
[19] E. A. Gulbransen: *Annals of the New York Academy of Science*, 1954, vol. 58, p. 830.
[20] E. A. Gulbransen and K. F. Andrew: *Journal* Electrochemical Soc., 1954, vol. 101, p. 128.
[21] K. K. Kelley: *Industrial and Engineering Chemistry*, 1944, vol. 36, pp. 377-378.
[22] K. K. Kelley: *Metallurgy of Zirconium*, Ed. by Lustman and Kerze, p. 60. McGraw-Hill Pub. Co. New York, 1955.
[23] J. P. Coughlin and E. G. King: *Journal* Amer. Chemical Soc., 1950, vol. 72, p. 2262.
[24] Selected Values of Chemical Thermodynamic Properties. Circular No. 500. National Bureau of Standards. Washington, D. C., 1952.
[25] E. A. Gulbransen: *Proceedings of International Symposium on the Reactivity of Solids*, p. 899. Gothenburg, 1954.

Discussion of this paper sent (2 copies) to AIME by June 1, 1957 will appear in AIME *Transactions* Vol. 209, 1957, and in JOURNAL OF METALS, October 1957.

Prot Fatigue Study of an Aircraft Steel in The Ultra High Strength Range

Fatigue properties were determined, using the Prot method, for a Ni-Cr-Mo-V steel (AMS-6434) in the ultra high tensile strength range up to 280 ksi. A useful increase in fatigue strength of carefully ground specimens was found up to about 240 ksi tensile strength with an endurance ratio of from 0.40 to 0.42. Above this level the fatigue strength appeared to level off, or drop slightly. Comparison with the Wohler method showed worthwhile savings in specimens and test time through use of the Prot *progressively increasing load* method. Some trend for failure stress to decrease as inclusion size increased was noted.

by P. W. Ramsey and D. P. Kedzie

INCREASING demand for improved strength-weight ratios made on aircraft structures has resulted in a gradual increase in the tensile strength requirements for steels used in such applications. As the cyclic loads often are more critical than static loads, and the fatigue properties are generally the design criteria, the question arises as to whether an improvement in fatigue properties accompanies the increased tensile strength.

The present investigation was undertaken to determine the relationship between fatigue and tensile properties for an aircraft quality steel in the 155 to 280 ksi (1000 psi) tensile strength range, using the Prot method of fatigue testing.

Procedure and Results

After preliminary work to establish proper heat treating procedures for this heat of aircraft quality electric furnace steel (a Ni-Cr-Mo-V steel,* AMS-6434), about 100 flexure fatigue specimens were prepared at tensile strength levels of 155, 180, 195, 225, 240, 260 and 280 ksi.

The specimens were tested individually at their resonant frequency, using an electromagnetic vibration exciter. Prot progressively increasing load fatigue tests were made of all tensile strength levels, and a Wohler conventional S-N fatigue test was made of the 195 ksi level.

In addition, tensile and hardness tests were made, as well as microstructure and inclusion studies.

* Aeronautical Material Specification (SAE) 6434: 0.31 to 0.38 pct C, 0.60 to 0.80 pct Mn, 1.65 to 2.00 pct Ni, 0.65 to 0.90 pct Cr, 0.30 to 0.40 pct Mo, 0.17 to 0.23 pct V, 0.20 to 0.35 pct Si, 0.040 pct maximum P, and 0.040 pct maximum S.

P. W. RAMSEY, Member AIME, and D. P. KEDZIE, Junior Member AIME, are with the Metallurgical Research Dept., A. O. Smith Corp., Milwaukee, Wisc.

TP 4395E. Manuscript, Apr. 16, 1956. Cleveland Meeting, October 1956.

Prot Fatigue Testing Method—The determination of the endurance limit by the conventional Wohler method can be time-consuming and easily require 20 specimens when statistical variance is to be established. This is also true when endurance limit loads are determined on actual parts or subassemblies, and the desirability of a reliable *accelerated* method has been evident for some time.

The primary advantage of the Prot method of fatigue testing is in reducing the number of specimens and the time required for each test. Unlike the Wohler method, every Prot specimen tested contributes to the determination of the endurance limit, and the authors have been able to duplicate Wohler results obtained with 20 specimens with only half the specimens and a fourth of the total cycles.

Table I. Summary of Prot Endurance Limit Data for AMS-6434 Steel

Tensile Strength, Ksi	No. of Specimens*	Prot Endurance Limit, Ksi: Median Value	95 Pct Confidence Range	Endurance Ratio	Slope, Ksi/$\alpha^{0.5}$	Correlation Coefficient, r
155	10	80.9	75.5 to 88.4	0.52	55.0	+0.86
180	8	90.4	80.0 to 100.7	0.50	57.5	+0.72
195	19	76.1	71.2 to 81.0	0.39	72.4	+0.84
225	10	91.0	80.8 to 101.3	0.40	58.8	+0.71
240	9	101.2	92.3 to 110.1	0.42	34.6	+0.61
260	7	94.8	89.7 to 99.9	0.36	63.9	+0.95
280	10	100.1	88.5 to 111.8	0.36	43.3	+0.53

* Specimens that failed outside of test area are not included.

This new technique for defining the endurance limit was proposed in 1948[1] by Marcel Prot and consists of progressively increasing cyclic stress until fatigue failure occurs. By varying the load rate, α, a useful relationship is found to exist with failure stress, so that for steel the failure stress appears to

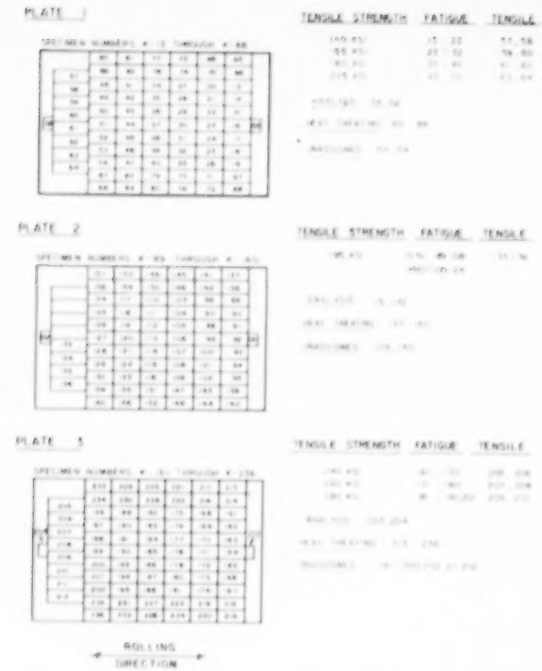

Fig. 1—Specimen blank layout for three 9/16 x 15 1/16 x 66 in. plates of AMS 6434 steel.

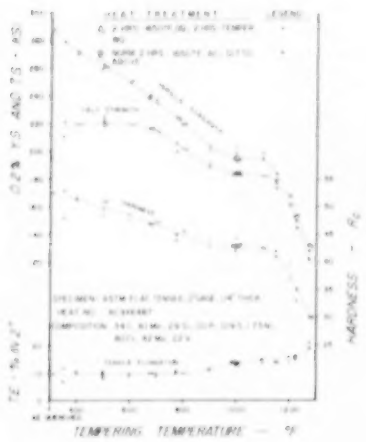

Fig. 2—Mechanical properties of AMS-6434 vs tempering temperature.

be a linear function of $\alpha^{1/2}$. By extrapolating this line to the ordinate, a value of failure stress, called the Prot endurance limit, is obtained. This can also be considered the failure stress for an infinitely slow loading rate, which corresponds to Wohler test conditions ($\alpha = 0$).

The Prot method has limitations for nonferrous materials which do not show well-defined endurance limits at room temperatures, as well as for ferrous materials that are affected by cyclic stressing below the endurance limit.[5] In a later report,[6] Prot indicated that the function may not be linear for all metals.

Material—Three plates of hot rolled AMS-6434 steel, 9/16 x 15 1/16 x 66 in., were used for this investigation. The chemical composition of these plates is covered by the following ranges: 0.32 to 0.36 pct C, 0.60 to 0.65 pct Mn, 0.28 to 0.29 pct Si, 1.72 to 1.83 pct Ni, 0.79 to 0.80 pct Cr, 0.42 to 0.43 pct Mo, 0.20 to 0.23 pct V, 0.011 to 0.012 pct P, and 0.019 pct S.

The arrangement and identification of specimen blanks on the three plates are shown in Fig. 1. The fatigue and tensile specimens were confined to the central portion of each plate to avoid possible edge effects, while the edge material was assigned to tensile specimens for the preliminary heat treating tests.

In carrying out the program, the 140 ksi tensile strength group was not tested in fatigue, although it was included in the tensile tests.

Heat Treatment and Properties—Preliminary tests performed to determine the heat treating characteristics of a particular heat of AMS-6434 steel (U. S. Steel Corp. Heat No. AC9X6487) consisted of austenitizing 2 hr at 1650°F, oil quenching, tempering 2 hr at temperature and water quenching. Tempering temperatures ranged from 400° to 1200°F in 100° increments. After heat treating, duplicate ASTM flat tensile specimens having a 2 in. gage length, ½ in. gage width, and ¼ in. thickness were prepared. The tensile specimens were ground to final dimensions after heat treatment to remove any decarburized layer.

Following this survey, heat treating procedures were then specified for the desired tensile strength levels. The remaining specimen blanks were first normalized for 2 hr at 1650°F, air cooled, and then heat treated as before, using predetermined tempering temperatures of 350°, 500°, 675°, 775°, 1000°, 1150°, 1225° and 1275°F. Tensile specimen blanks were heat treated along with each group of fatigue specimen blanks so that tensile properties as well as hardness values could be checked. The results of the tensile and hardness tests for both the preliminary and final heat treatment series have been combined and are shown in Fig. 2. Yield strength values were determined at 0.2 pct offset from strain gage data.

Poisson's ratio was measured, using strain gages mounted transversely and longitudinally on a fatigue specimen (K-103) having 195 ksi tensile strength. Baldwin CD-7 gages were used for the dynamic determination, and A-7 gages for the static determination. The ratio was 0.303 under dynamic bending, and 0.293 under static tension.

With this information, a strain gage could be mounted transversely on a fatigue specimen and its output converted to longitudinal strain. In this way very high longitudinal stresses could be measured without fatigue failure of the strain gage.

Fatigue Specimen Preparation—The flexure fatigue specimens were flat bars, 0.250±0.001 x 1.000 ±0.001 x 8±¼ in., with a radius of 1/32 in. on the longitudinal edges. In rough machining the blanks, an equal amount of material was removed from each side to within 0.050 in. of the final size. To remove any decarburization an equal amount of material was ground from each side of the fatigue specimens after heat treatment, using light passes and a coolant. The final passes were on the order of 0.002 in. or less, to attain the Profilometer roughness specification of 7 μ in. RMS (maximum), measured perpendicular to the grinding marks. All grinding marks were parallel to the length of the specimens.

In order to minimize failures due to clamping stresses during fatigue testing, it was found neces-

sary to shot peen the ends of the specimens. The center 1½ in. of each specimen was masked off and the peening done with nominal 0.007 in. heat treated steel shot (SAE Shot No. 70) to produce an arc height of 0.004 to 0.006 in. on a *peening intensity* test strip (SAE designation: 0.004 to 0.006A).

Fatigue Testing—Testing was done with an electromagnetic vibration exciter at the resonant frequency of the specimen. The exciter is powered by a motor-generator set which supplies alternating current of controllable frequency (5 to 500 cps) to the driver coil, causing it to move in a magnetic field. The driver coil is attached to a movable table which in turn transmits motion to the test fixture. Both displacement and frequency of the movable table can be controlled. The exciter is designed to withstand 50 times the force of gravity and has a rated force output of 200 lb. Maximum peak to peak displacement is 1.0 in.

A typical test setup is shown in Fig. 3. The specimen is shown under vibration, with weights added which permit an increase in outer fiber stress. The weights were only necessary for the Prot tests and were not used for the Wohler tests. A filar micrometer microscope was used to observe specimen displacement, a velocity pickup to measure the displacement or acceleration of the exciter, and a Baldwin CD-7 strain gage on special calibration specimens to determine maximum strain. The strain gage signal was fed into a bridge-amplifier circuit, and then displayed on an electronic voltmeter and cathode ray oscillograph. The dynamic strain gage signal was then measured by means of a calibrated

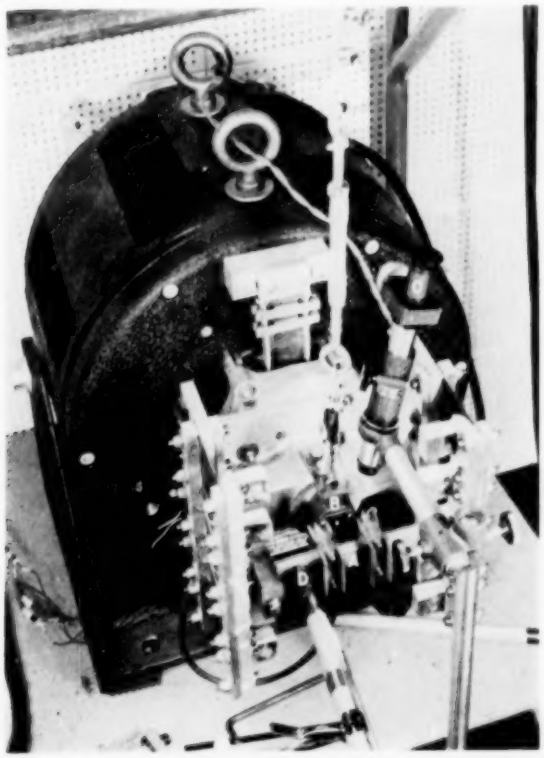

Fig. 3—MB electromagnetic vibration exciter with flat fatigue specimen under test. *A*, specimen (blurred because of motion); *B*, velocity pickup, attached to exciter table; *C*, filar micrometer microscope; and *D*, inductive pickup, automatic frequency controller.

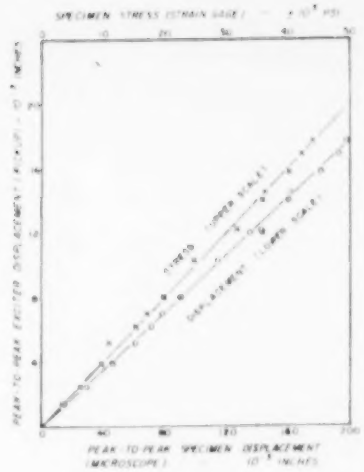

Fig. 4—Calibration curves for fatigue specimen No. K-40 with CD-7 type strain gage, mounted transversely.

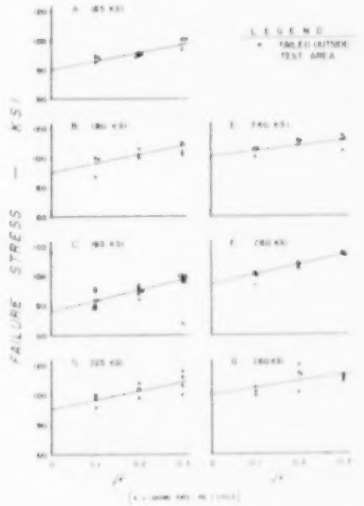

Fig. 5—Prot fatigue data on AMS-6434 steel of various tensile strengths.

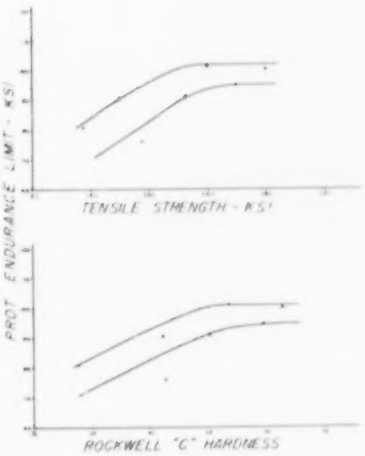

Fig. 6—Prot endurance limit vs strength and hardness of AMS-6434 steel.

potentiometer in the bridge-amplifier circuit using a *chop* line on the oscillograph.

Calibration tests were run over a stress range so that velocity pickup signals could be correlated to maximum specimen strain or displacement. During fatigue tests, the velocity pickup signal was used

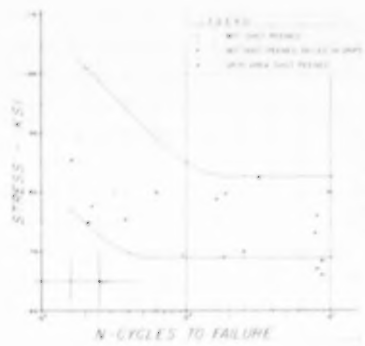

Fig. 7—S-N curve for AMS 6434 steel at 195 ksi tensile strength.

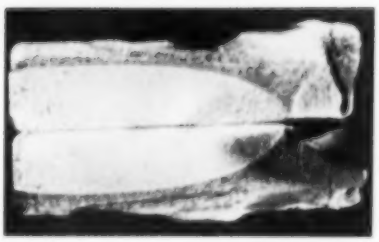

Fig. 8—Macrograph of typical fracture of AMS 6434 fatigue specimen No. K-32, with a tensile strength of 155 ksi, which failed at 90 ksi, 1.2×10^7 cycles. Prot testing rate was 0.04 psi per cycle. Unetched specimen. X2.

for controlling and monitoring. A typical calibration curve, shown in Fig. 4, demonstrates good linearity. The calibration constants were then used to relate specimen stress to pickup signal. As a further check, a calibration at one displacement was made with the micrometer microscope on each individual specimen prior to fatigue test.

Specimens were tested singly to permit better control of stress level, although the test fixture was designed to accommodate up to five specimens. During constant stress Wohler tests, the exciter was first adjusted to the natural frequency of the specimen, and the desired stress level was attained by increasing the power input to the driver coil manually. Minor adjustments were required in some tests to maintain the stress level.

Frequency was held at resonance by means of an automatic controller which utilized a phase angle relationship between specimen displacement and driver coil voltage (displacement). The phase angle was adjusted with manual controls, and then maintained automatically by the controller, which increased or decreased the frequency as necessary. The test was monitored continuously, and at the first indication of a drop in natural frequency, as shown by an electronic counter, the power was turned off. In this manner failures could be detected before fracture had progressed very far. The number of cycles to failure was measured by multiplying the testing time by the average natural frequency. If no failure occurred in eight million cycles, the test was discontinued and the specimen considered to have *run out*.

During Prot testing, the specimen was initially stressed at a level approximating 25 pct of its tensile stress. At predetermined cycle increments the stress level was increased 2 ksi, held at the new level for another cycle increment, and the process repeated until failure occurred. Three cycle increments were used, so that loading rates of 0.01, 0.04 and 0.09 psi per cycle were obtained in a stepwise manner. The increments were 200, 50 and 22.2 kilocycles, respectively. In other respects, these tests were conducted as were the constant stress level Wohler tests.

The data indicate that the authors' discontinuous method of varying the stress gives the same linear relationship as does the continuous loading method. The Prot data for each tensile strength were analyzed, using a card-programmed calculator, to determine the line of best fit as determined by the least-squares method. Specimens which failed outside the 1½ in. long test areas were plotted, but not included in the least-squares calculation.

The individual Prot curves for seven tensile strength levels are shown in Fig. 5. A summary curve, Fig. 6, plotting the extrapolated average Prot endurance limits as a function of tensile strength, shows the leveling off at higher tensile strength levels, indicating that no useful increase in fatigue strength for carefully ground specimens is realized above 240 ksi tensile level. The trend shown appears clear and confirms the general conclusion of other investigators in this ultra high tensile strength range.[1,3]

Due to the statistical nature of fatigue properties, there is much scatter in the data and Table I shows the 95 pct confidence limits[5] for the extrapolated Prot endurance limit, the correlation coefficient* and other pertinent information. The confidence limits define the range that can be expected to include the line of best fit (least-squares method) through these data. The limits are actually curves that diverge and are wider at the extrapolated value of failure stress than in the test range.

* Indicates the extent of correlation between two variables. Values under 0.2 indicate slight correlation; 0.2 to 0.4, low; 0.4 to 0.7, moderate; 0.7 to 0.9, high; and over 0.9, very high correlation. The sign indicates whether the relationship is direct (+) or inverse (−).

A comparison of Prot endurance limits with specimen hardness averaged from four readings, measured in the polished test section but away from the fatigue crack, is also shown in Fig. 6. Again the trend is similar with a leveling off above a hardness of approximately Rc 47.

The anomalous fatigue behavior of the 195 ksi tensile strength group is difficult to explain. At this strength level a drop in fatigue strength occurred. Microstructure gave no clue as to the reason for this difference, although the tempering curve, Fig. 2, indicates that the 195 ksi group was tempered in the 1000°F region, where so-called *secondary hardening* occurs. This is an age-hardening process associated with the nucleation and growth of alloy carbides.[7] It is also possible that this drop is associated with the temper brittleness phenomenon. More work would be required to determine if this is indeed an unfavorable tempering region with regard to the fatigue properties.

To compare Prot endurance limits with conventional, but time-consuming Wohler tests, 20 specimens of 195 ksi tensile strength were tested at constant stress levels between 65 and 100 ksi until failure occurred, or until at least eight million cycles were withstood. Results are plotted as an S-N curve in Fig. 7, where a minimum endurance limit of about 70 ksi was found. Some run-outs, however, occurred at stresses as high as 80 ksi. The data agree reasonably well with those from the Prot test, Figure 5c, where an endurance limit of about 75 ksi was found.

Inclusions—Fatigue fracture surfaces from the 155, 180, 225 and 280 ksi tensile strength level specimens were examined under plane polarized light to

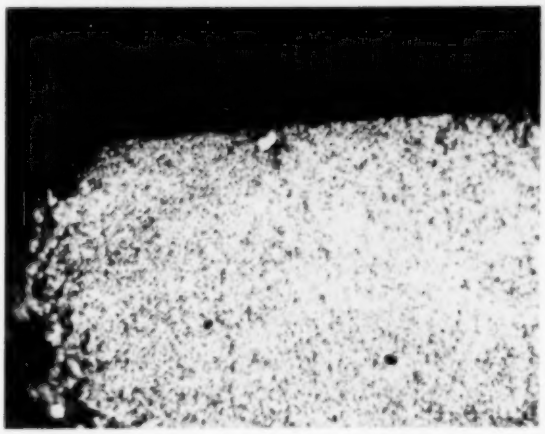

Specimen No. K-49, with a tensile strength of 225 ksi; inclusion size, 2.5 mil. X50. Reduced approximately 15 pct for reproduction.

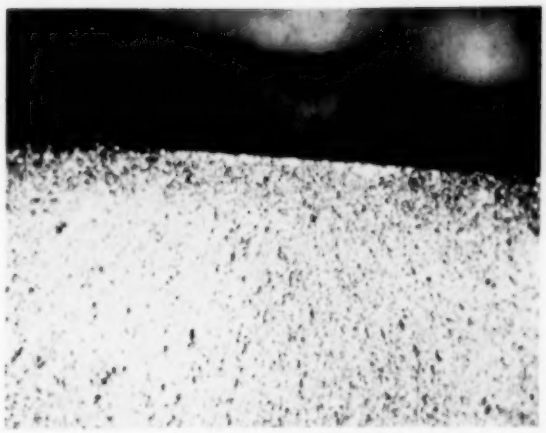

Specimen No. K-184, with a tensile strength of 280 ksi; inclusion size, 1.2 mil. X50. Reduced approximately 20 pct for reproduction.

Fig. 9—Typical nonmetallic inclusions found on fracture surfaces of AMS-6434 fatigue specimens. Micrographs taken with plane polarized light.

determine the origin of fracture and the relationship between inclusion size and failure stress.

Practically without exception, failure was found to have started at nonmetallic inclusions on the surface of the specimen. Radial lines on the fracture surface centered at the point of origin. A macrograph of a typical fracture is shown in Fig. 8. In some of the higher tensile strength specimens where the radial lines defined an area rather than a single source, the largest inclusion occurring in the area was measured.

The inclusions found on the unetched fracture surfaces, as shown in Fig. 9, were essentially spherical in shape, which is typical of alumina-type inclusions not malleable at steel rolling temperatures. The fracture surfaces were examined at X50, and photographed with plane polarized light to increase the contrast between parent stock and inclusion.

An inclusion rating was also made of specimen K-191 from Plate 3, see Fig. 1, on an unetched polished section cut parallel to the rolling plane. The rating was 0-0-C, according to ASTM practice E45, with sulfide stringers predominating. Apparently these were not as damaging to the fatigue properties as alumina types.

As the specimens had been tested at various loading rates, the data were grouped in that manner, and an analysis of variance made. To eliminate differences due to tempering treatment, the median fatigue failure strength was picked for each tensile strength group, as shown in Table II, so the data could be combined for variance study.

Inclusion size was averaged in the case of elliptical shapes by taking the square root of the product of the length and thickness. The correlation coefficient was then determined for *equivalent inclusion diameter* vs *deviation from median failure stress*. A plot of these variables for the three loading rates is shown in Fig. 10. The lines of best fit were determined, using the least-squares method. In addition, the correlation coefficient was determined for each set of data. For the 0.01 and 0.09 psi per cycle groups, a marginal correlation was found, but for the 0.04 psi per cycle group, complete randomness is indicated. It was concluded that there seems to be a trend for failure stress to decrease as the inclusion size increased, but this tendency can easily be obscured by other variables.

This trend is in agreement with the work of Ransom,[7] in which the transverse endurance limit of an inclusion-free, vacuum-melted forging of SAE 4340 steel was found to be 50 pct higher than that obtained from commercial SAE 4340 steel forging. It was concluded that nonmetallic inclusions were the major source of fatigue weakness in many forged machine elements. Epremian and Mehl[8] show also

Table II. Inclusion Size Vs Prot Failure Stress for AMS-6434 Steel at Various Tensile Strength Levels

Specimen No. K-	Loading Rate, Psi per Cycle	Failure Stress, Ksi	Deviation From Median, Failure Stress, Ksi	Inclusion Size, 10^{-3} In.		
				Length	Thickness	$(L \times T)^{1/2}$
155 Ksi Tensile Strength						
23	0.01	88.6	+1.4	1.5	1.0	1.23
26	0.01	85.3	−1.9	1.6	1.5	1.55
29	0.01	89.0	+1.8	1.0	1.3	1.14
24	0.04	89.9	−0.3	1.5	1.5	1.50
27	0.04	88.7	−1.8	2.0	2.0	2.00
30	0.04	91.7	+1.5	1.7	1.7	1.70
32	0.04	90.3	+0.1	2.0	1.5	1.73
25	0.09	94.2	−3.4	1.9	1.9	1.99
28	0.09	100.9	+3.3	1.4	1.2	1.30
31	0.09	100.8	+3.2	1.6	1.0	1.60
180 Ksi Tensile Strength						
33	0.01	100.0	+6.3	1.0	1.0	1.00
36	0.01	99.8	+6.1	1.8	1.5	1.64
39	0.01	87.3	−6.4	3.0	2.0	2.45
34	0.04	100.0	−3.0	1.5	1.0	1.23
37	0.04	106.1	+3.1	2.0	1.5	1.73
41	0.04	102.0	−1.0	3.0	3.0	3.00
35	0.09	102.0	−4.0	3.0	2.0	2.45
38	0.09	104.0	−2.0	2.0	1.5	1.73
42	0.09	110.0	+4.0	2.0	1.0	1.41
225 Ksi Tensile Strength						
43	0.01	92.0	−7.0	—	—	—
46	0.01	100.0	+1.0	1.0	1.0	1.00
49	0.01	98.0	−1.0	2.5	2.5	2.50
44	0.04	104.0	+1.0	2.0	1.5	1.73
47	0.04	108.0	+5.0	1.0	1.0	1.00
50	0.04	98.0	−5.0	1.0	1.0	1.00
45	0.09	112.0	+4.0	1.0	1.0	1.00
48	0.09	116.0	+8.0	1.0	1.0	1.00
51	0.09	100.0	−8.0	2.0	1.5	1.73
52	0.09	106.0	−2.0	1.2	1.0	1.10
280 Ksi Tensile Strength						
181	0.01	105.0	+2.8	1.5	1.5	1.50
184	0.01	102.0	−0.2	1.2	1.2	1.20
201	0.01	99.4	−2.8	1.5	1.5	1.50
182	0.04	114.4	+3.7	3.0	2.0	2.45
185	0.04	101.4	−9.3	1.0	1.0	1.00
188	0.04	113.5	+2.8	1.2	1.0	1.12
190	0.04	119.9	−9.2	1.0	1.0	1.00
183	0.09	112.7	−2.1	1.5	1.0	1.23
186	0.09	111.2	−0.6	1.3	1.3	1.30
189	0.09	108.5	−2.1	1.0	1.0	1.00

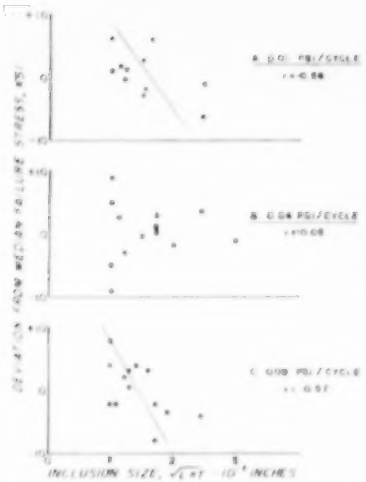

Fig. 10—Inclusion size vs failure stress for AMS 6434 Prot fatigue specimens at various loading rates.

that "two SAE 4340 heats of identical chemical composition but with different inclusion ratings have correspondingly different dispersions in fatigue life; large variability being associated with high inclusion rating." Further confirmation is found in Stulen's[9] comment that "in carefully prepared specimens, the origin of failure is almost always at a microscopic non-metallic inclusion which is open to the surface or only slightly subsurface."

Conclusions

1) There is a useful increase in fatigue strength of carefully ground specimens of AMS-6434 steel accompanying higher tensile strengths up to about the 240 ksi tensile level with an endurance ratio of 0.40 to 0.42. Above this tensile strength the fatigue strength appears to level off, or even drop slightly.

2) Almost every fatigue failure initiated at a non-metallic inclusion, pointing up the importance of cleanliness of microstructure in fatigue applications. Some trend for failure stress to decrease as inclusion size increased was noted.

3) The Prot method appears to be a useful fatigue testing technique for high strength aircraft steels, and correlated well with the Wohler method at the 195 ksi tensile strength level. By means of Prot testing, endurance limits were determined with half the specimens and a fourth of the test cycles required with the Wohler method.

Acknowledgments

The authors wish to acknowledge the assistance and guidance given to them by Merrill A. Scheil, Director of Metallurgical Research, A. O. Smith Corp., and the help of Lloyd K. Purnell in the test program and in the preparation of the figures. They are also indebted to the A. O. Smith Corp. for permission to publish the results.

This paper is based upon a portion of a thesis submitted by the authors to the University of Wisconsin in partial fulfillment of the requirements for the degree of Master of Science.

References

[1] E. M. Prot: Fatigue Testing Under Progressive Loading. *Revue de Metallurgie*, 1948, vol. 45, pp. 481-489.

[2] H. T. Corten, T. Dimoff, T. J. Dolan, and M. Sugi: An Appraisal of the Prot Method of Fatigue Testing, Part II. Technical Report No. 35, Project No. NR-D 31-005, Office of Naval Research, University of Illinois, June 1953.

[3] E. M. Prot: Results of Fatigue Tests Under Progressive Loading. *Revue de Metallurgie*, 1951, vol. 48, pp. 822-824.

[4] Battelle Memorial Institute: *Prevention of Failure of Metals Under Repeated Stress*. John Wiley & Sons Inc. New York, 1941.

[5] H. J. Grover, S. A. Gordon, and L. R. Jackson: Fatigue of Metals and Structures. Battelle Memorial Institute, Nav. Aer. No. 00-25-534, 1954.

[6] W. J. Dixon and F. J. Massey, Jr.: *Introduction to Statistical Analysis*, chap. 11, section 4. McGraw-Hill Pub. Co. New York, 1951.

[7] E. C. Bain: *Functions of the Alloying Elements in Steel*, pp. 271-273. Amer. Soc. for Metals. Cleveland, 1939.

[8] J. T. Ransom: The Effect of Inclusions on the Fatigue Strength of SAE 4340 Steels. *ASM Trans.*, 1954, vol. 46, pp. 1254-1269.

[9] E. Epremian and R. F. Mehl: Investigations of Statistical Nature of Fatigue Properties. NACA TN 2719, 1952.

[10] F. B. Stulen: On the Statistical Nature of Fatigue. ASTM Symposium on Statistical Aspects of Fatigue, STP No. 121, 1951.

Discussion of this paper sent (2 copies) to AIME by June 1, 1957 will appear in AIME *Transactions* Vol. 209, 1957, and in JOURNAL OF METALS, October 1957.

Effect of Dissolved Oxygen on the Grain Size Of Annealed Pure Copper and Cu-Al Alloys

The grain growth restraint which occurs far in advance of the aluminum oxide front during the internal oxidation of Cu-Al alloys is shown to be a result of oxygen in solid solution. Studies show that oxygen in solid solution in pure copper restrains grain growth.

by D. L. Wood

INTERNAL oxidation[1] is a process in which oxygen, diffused into a suitable alloy, causes precipitation of solute oxide particles as the oxidation front moves inward. During an investigation of internal oxidation now in progress it was observed that the grain size is relatively small in thin strip specimens that have been internally oxidized in the as-rolled condition. This may be due to the restraint of grain growth by the precipitated oxide particles. It was observed also that the grain size in unoxidized portions of partially oxidized specimens was

D. L. WOOD is with the Metallurgy & Ceramics Research Dept. Research Laboratory, General Electric Co., Schenectady.

TP 4407E. Manuscript, May 22, 1956. New Orleans Meeting, February 1957.

somewhat smaller than the grain size in specimens given identical thermal treatment in the absence of oxygen. The structures shown in Fig. 1 are those resulting from a 1 hr anneal at 1000°C of copper + 0.84 wt pct Al cold rolled 92 pct to 0.040 in. The sample shown in Fig. 1a was annealed in argon in a quartz tube containing titanium chips. That shown in Fig. 1b was annealed in an air tight copper tube containing a mixture of cuprous oxide and copper to supply oxygen at a partial pressure equal to the decomposition pressure of cuprous oxide. The darker zones show the extent of internal oxidation. The inner portion, in which no aluminum oxide has yet been formed, is finer grained than the specimen in Fig. 1a, which has undergone similar annealing, but in the absence of oxygen.

A possible cause of this grain growth restraint could be the precipitated oxides of some impurity element in the Cu-Al alloy. The growth restraint occurs far in advance of the aluminum oxide front. If precipitation on an impurity oxide is responsible, this oxide must form at a lower oxygen concentration than does aluminum oxide. Barring tremendous differences in nucleation requirements, this oxide must then be more stable than aluminum oxide. In order to determine the relative stabilities of aluminum oxide and the hypothesized grain growth retarding particles, specimens were annealed in argon with titanium chips after partial internal oxidation. Fig. 2 shows that the grain size in the aluminum oxide region remained unaltered, while the grain growth restraint was removed in the center. Therefore, the central region must not contain oxide particles even as stable as aluminum oxide, and the grain growth inhibition cannot be attributed to oxide particles.

The formation of aluminum oxide at the oxidation front does not reduce the concentration of dissolved oxygen to zero but only to some minimum concentration that is necessary for the oxidation reaction to occur. If the grain growth restraint is due to dissolved oxygen ahead of the oxidation front, then a similar effect should also be evident in pure copper.

To investigate this possibility vacuum remelted OFHC copper was cold rolled 92 pct to 0.040 in. and annealed at 1000°C in argon with titanium chips or in a cuprous oxide-copper pack. The grain sizes resulting after various times are shown in Fig. 3. After 5 min the grain size in the two differently treated specimens is similar, but at longer annealing times the difference becomes appreciable. The chemical analysis of copper annealed for 30 min in argon at 1000°C in the presence of titanium gave 0.0009 ± 0.0003 pct O; copper annealed for 30 min in the cup-

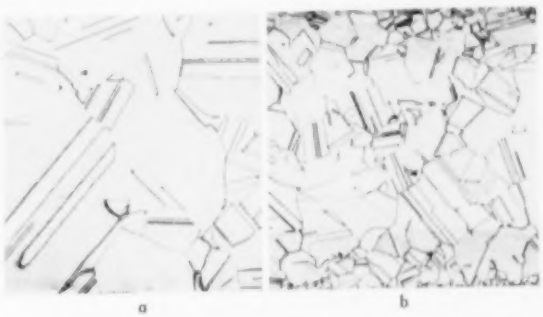

Fig. 1—Cu 0.84 pct Al annealed 1 hr at 1000°C in a) argon with titanium chips, and b) a cuprous oxide-copper pack. X50. Reduced approximately 15 pct for reproduction.

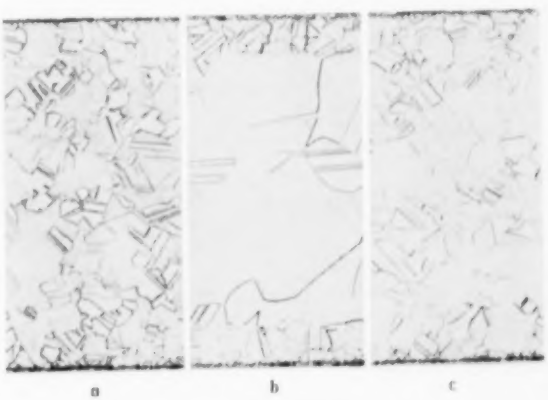

Fig. 2—Cu 0.84 pct Al rolled 92 pct to 0.040 in. and then a) annealed in a cuprous oxide-copper pack for 20 min at 1000°C, b) treated as in 2a, plus 10 min at 1000°C in argon with titanium, and c) annealed in a cuprous oxide-copper pack for 30 min at 1000°C. Specimens were nickel-plated. X100. Reduced approximately 30 pct for reproduction.

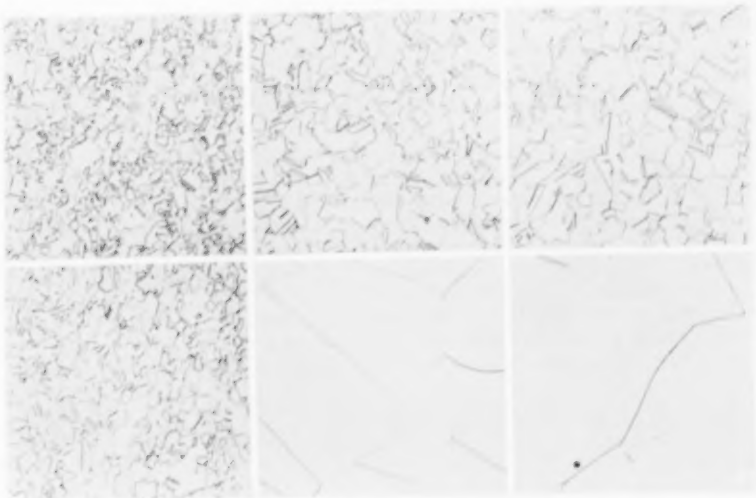

Fig. 3—Pure copper rolled 92 pct to 0.040 in. and annealed for various times at 1000°C in: TOP ROW, cuprous oxide-copper pack; and BOTTOM ROW, argon with titanium. LEFT, 5 min; CENTER, 15 min; and RIGHT, 30 min. X100. Reduced approximately 30 pct for reproduction.

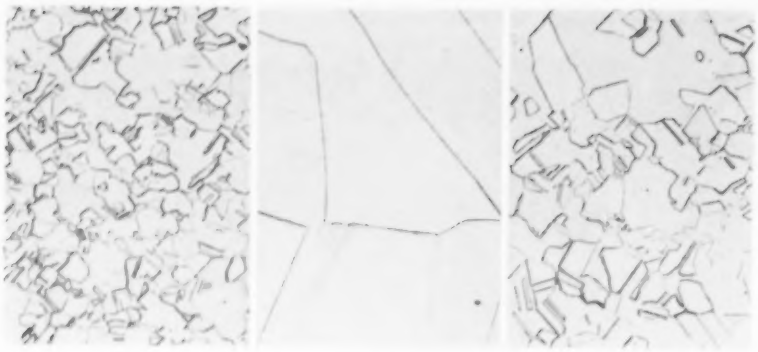

a b c

Fig. 4—Pure copper, 92 pct deformation, annealed at 1000°C for a) 1 hr in cuprous oxide-copper pack, b) same as 4a plus 1 hr in argon with titanium, and c) 2 hr in cuprous oxide-copper pack. X100. Reduced approximately 35 pct for reproduction.

rous oxide-copper pack contained 0.0108 ± 0.0009 pct O.

The removal of the oxygen from specimens initially annealed in cuprous oxide-copper packs can be accomplished by a subsequent anneal in argon with titanium. Such removal of oxygen allows grain growth to resume in a normal manner, as shown in Fig. 4.

Summary

During internal oxidation of Cu-Al alloys there is a grain growth restraint far ahead of the internal oxidation front. Relative stabilities of this restraint and aluminum oxide have shown that the restraint is not due to the precipitated oxides of an impurity element. The grain growth restraint in partially internally oxidized specimens is removed by annealing at lower oxygen pressure. Studies of pure copper indicate that the grain growth restraint is due to oxygen in solid solution.

Acknowledgment

The author is indebted to R. L. Fullman for helpful discussion of this report.

Reference

[1] F. N. Rhines: A Metallographic Study of Internal Oxidation in the Alpha Solid Solutions of Copper. *AIME Trans.*, 1940, vol. 137, p. 246; METALS TECHNOLOGY, February 1940.

Discussion of this paper sent (2 copies) to AIME by June 1, 1957 will appear in AIME *Transactions* Vol. 209, 1957, and in JOURNAL OF METALS, October 1957.

Some Properties of Certain High-Conductivity Copper-Base Alloys

by Webster Hodge

SMALL generators and motors are required to operate, in some critical applications, at temperatures where cold-worked silver-bearing copper recrystallizes. Copper containing up to 30 oz Ag per ton has been used for many years to build the highest grades of commutators and slip rings. With failure of commutators impending because silver-bearing copper cannot withstand the stresses imposed at these higher temperatures, Cr-Cu was tried as a substitute with varying degrees of success. Cr-Cu proved difficult to fabricate because a critical heat treatment was necessary to obtain sufficient ductility. Besides, its rupture strength was shown to be low at operating temperatures, its electrical conductivity lower than desired, and its cost high. Furthermore, it often contained hidden flaws.

The Nippert Electric Products Co. set out to find a better material by undertaking a research project with the stated objective of providing a material suitable for commutators that would have 1) a softening temperature above 750°F (400°C), 2) a minimum electrical conductivity of 90 pct of that of pure copper, 3) a strength not less that that of cold-worked silver-bearing copper, and 4) a materials cost of not over 1.5 times the cost of copper containing 25 to 30 oz Ag per ton. No commercial alloy met these specifications. However, it was found that copper containing from 0.18 to 0.35 pct Zr could be produced quite easily in the laboratory, and promised to fulfill the major requirements noted above. Interest naturally centered in the lower part of this composition range, since such alloys gave somewhat better electrical conductivities, and were lower in

W. HODGE, Member AIME, is Consultant, Nonferrous Metallurgy Division, Battelle Memorial Institute, Columbus, Ohio.

TP 4405E. Manuscript, Nov. 16, 1955. New Orleans Meeting, February 1957.

materials cost. Later, a 0.25 pct Zr alloy was made commercially.

This paper describes and compares some properties of Zr-Cu, important to commutator manufacture, with similar properties of silver-bearing copper and of Cr-Cu. Specifically, these properties are electrical conductivity, softening temperature upon long-term exposure, hot hardness, tensile properties at room and elevated temperature, and stress-rupture properties on notched and unnotched specimens and on specimens representing the longitudinal and transverse direction to rolling during fabrication.

Materials

The approximate compositions of the three commercial alloys used are shown in Table I. The variation from the analysis shown in Table I for the commercial Zr-Cu was ±0.02 pct.

All specimens not otherwise described were cut parallel to the rolling direction. The Zr-Cu specimens were obtained from a standard wire bar rolled in a commercial mill. The material had been cast from oxygen-free copper with zirconium added. Specimens taken in the transverse to rolling direction of Zr-Cu and of silver-bearing copper were obtained from a wire bar of each material that had been rolled lengthwise to form flat plates about 5 in. wide. Transverse specimens of Cr-Cu were cut from an 8-in.-wide flat plate supplied by the same commercial source as the Cr-Cu wire bar from which the longitudinal specimens were taken. Spectrographic analysis of these two Cr-Cu alloys showed that they were practically identical in composition. Some of the properties of Zr-Cu were determined on alloys cast and rolled in the laboratory. Wherever materials produced in the laboratory were used, the actual analysis is shown to distinguish these results from those obtained on the material from a commercial source.

Softening Temperature and Electrical Conductivity

Experiments showed that the addition to copper of zirconium in amounts less than 0.12 pct had little effect on the softening temperature, while larger additions caused the softening temperature of the alloy, cold rolled to 50 pct reduction, to rise rapidly from about 570°F (300°C) with 0.12 pct Zr to 930°F (500°C) with 0.18 pct Zr. These determinations were made after ½-hr exposure to temperature. Still larger additions of zirconium produced only a minor increase in the short-time softening temperature. The room-temperature hardness of Zr-Cu and of silver-bearing copper, after limited exposure to elevated temperatures, is shown in Fig. 1. It is apparent that the softening temperature is markedly higher for the Zr-Cu even though the testing conditions were different for the two alloys. The softening temperature of nominal 0.35 pct Cr-Cu, cold rolled and aged to RB 82, was found to be slightly above 930°F (500°C) after a 30 min exposure to temperature. The softening temperature of the 0.8 pct Cr-Cu alloy is believed to be about the same.

Age-hardening treatments had a slight effect on the mechanical properties of Zr-Cu alloys with from 0.20 to 0.27 pct Zr that were produced in the laboratory. Solution-annealing temperature, however, did have an effect on the ability of the cold-rolled alloy to resist continued exposure to elevated temperature. Fig. 2 shows the hardness and electrical conductivity of the nominal 0.25 pct Zr alloy, cold rolled 60 pct

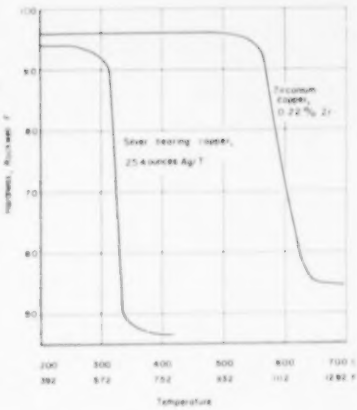

Fig. 1—Softening temperature of silver-bearing copper and Zr-Cu alloys. The silver-bearing copper was annealed for ½ hr at 850°F (455°C), cold rolled to RB 62, and held 1 hr at temperature shown. The Zr-Cu was annealed for ½ hr at 1700°F (925°C), water quenched, cold rolled, and aged 10 min at 750°F (400°C). Final hardness, RB 66.

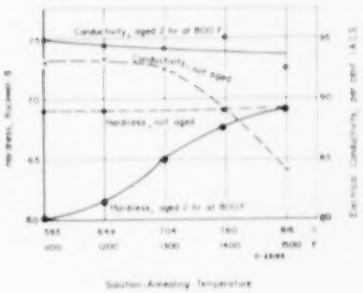

Fig. 2—Hardness and electrical conductivity of nominal 0.25 pct Zr-Cu solution annealed at temperatures shown, then cold rolled 60 pct.

and aged for 2 hr at 800°F (425°C) after solution annealing at various temperatures. These data show that the zirconium alloy that had been solution annealed at temperatures below 1500°F (815°C) became softer upon aging at 800°F (425°C) for short periods. The electrical conductivity of the alloy solution annealed, but not aged, decreased with increasing solution temperature above 1300°F (705°C). The decrease in conductivity indicates that more zirconium entered into solid solution as the annealing temperature increased. When the alloy, after solution annealing at temperatures from 1300°F (705°C) to 1500°F (815°C) was, however, reheated to 800°F (425°C) for 2 hr, the electrical conductivity was again high. This gain in conductivity is the most notable effect that can be obtained by aging treatments.

Table I. Composition of Commercial Alloys

Alloy Type	Nominal Content
Zr-Cu	0.25 Wt Pct Zr
Cr-Cu	0.8 Wt Pct Cr
Silver-bearing copper	25 to 30 Oz Ag per Ton*

* Longitudinal specimen—25.4 oz Ag per ton, by analysis.

The electrical conductivity measurements shown in Fig. 2 were made on wire specimens that underwent the same percentage reductions by drawing that the hardness specimens underwent by rolling. Microhardnesses of the strip and wire were almost identical. Wire and strip were heat treated together. Precision measurements on rolled strip produced the somewhat higher electrical conductivity values noted in Table II.

The temperature coefficient of resistivity, α, of a 0.21 pct Zr alloy wire, solution annealed at 1700°F

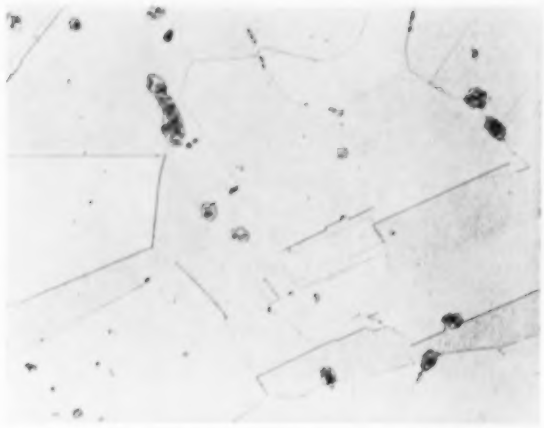

Fig. 3—Microstructure of 0.21 pct Zr-Cu alloy solution annealed 45 min at 1700°F (925°C). Etchant: potassium dichromate. X500. Reduced approximately 30 pct for reproduction.

(925°C) for 45 min, cold drawn to 50 pct reduction, and aged at 770°F (410°C) for 30 min in a salt bath, was 0.00363 per °C over the range from 32° to 482°F (0° to 250°C).

Alloys with 0.21 and 0.52 pct Zr that were reheated for 500 hr at 750°F (400°C), after solution annealing at 1700°F (925°C), increased in hardness from 98 to 100 RF, and from 98 to 101 RF, respectively, after an initial rapid increase (the alloys had been aged for 10 min at 770°F (410°C) before this test was started). Alloys with less than 0.18 pct Zr softened after exposures of less than 100 hr at 750°F (400°C).

Resistance of the Zr-Cu alloy to softening during continued exposures to elevated temperatures requires solution-annealing temperatures of at least 1300°F. Resistance to softening probably increases slightly with the amount of zirconium taken into solid solution. When the 0.21 pct Zr-Cu was solution annealed at 1700°F (925°C) for 45 min, some zirconium remained out of solution, see Fig. 3. With all the zirconium in solution, the properties of this alloy were not appreciably altered. This confirmed the observation already mentioned that, above a certain amount, larger additions of zirconium have little effect on the softening temperature.

Fig. 4 shows the change in hot hardness of the three types of alloys during short exposures to elevated temperature. The hardness measurements were made at intervals during the heating and cooling of the specimens. Silver-bearing copper was permanently softened at temperatures slightly over 500°F (260°C). Cr-Cu and Zr-Cu showed no permanent change in hardness characteristics after heating to 800°F. Cr-Cu showed the highest hardness at 550°F (288°C) and above.

Tensile Properties

Table III shows the usual tensile properties of the three types of alloys studied, both at room temperature and at 550°F (288°C). The silver-bearing copper, both strip (longitudinal) and plate (transverse) specimens, was cold rolled to RB 61 after annealing at 850°F (405°C). The Cr-Cu was annealed at 1830°F (1000°C) for 15 min, cold rolled to about RB 70, and aged at 830°F (445°C) for 16 hr. The Zr-Cu was annealed at 1300°F (705°C) for about 20 min, cold rolled to about RB 65, and aged at 800°F (425°C) for 1 hr. After identical treatment, the final hardness of the longitudinal and transverse Cr-Cu specimens was RB 82 and RB 78, respectively. Similarly, the hardness of the longitudinal and transverse Zr-Cu specimens was RB 64 and RB 66, respectively. These differences in the hardness values of similar materials after identical heat treatments may have been caused by slight differences in composition, since the longitudinal and transverse specimens originated in separate melts. Table III also shows room-temperature properties of Zr-Cu prepared in the same way, except that aging preceded cold rolling. The final hardness of these specimens was RB 68.

The tests on silver-bearing copper indicated little anisotropy at 550°F, although there was lower ductility in the specimens taken in the direction transverse to rolling. Cr-Cu, on the other hand, showed a considerable decrease in strength and elongation in specimens taken in the transverse to rolling direction as compared with those taken in the longitudinal direction. Ductility of this alloy, measured in either direction, was markedly lower when the temperature was increased to 550°F. Specimens of Zr-Cu taken in the transverse direction were slightly stronger than those in the longitudinal direction. The ductility was about the same in each direction. The loss in ductility upon heating to 550°F was much less than for the Cr-Cu.

Stress-Rupture Data

A commutator segment is subjected to severe compressional stresses in the parallel to rolling direction. These stresses are exerted by the locking mechanism. The segments are notched at each end and, in service, centrifugal stresses are set up across the notches (i.e., in the transverse to rolling direction). These centrifugal forces are relatively small, but the stress they develop is augmented by the compression forces that develop in the lengthwise direction in the segment as a result of thermal expansion as the commutator temperature rises.

On the test stands, when the generators were subjected to unusually high temperatures over extended periods, commutators of silver-bearing copper failed by deformation and displacement. The alloy had softened permanently. Under similar conditions, some segments of Cr-Cu failed by cracking. All of the cracks originated at the root of the locking

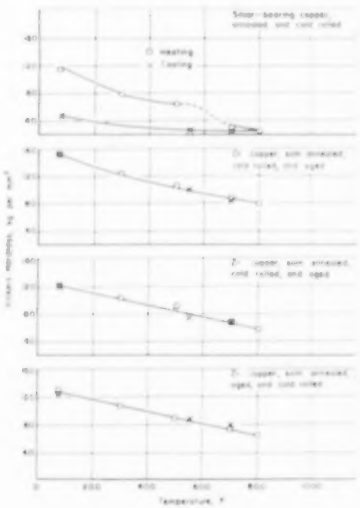

Fig. 4—Hot hardness of the three different copper-base alloys studied.

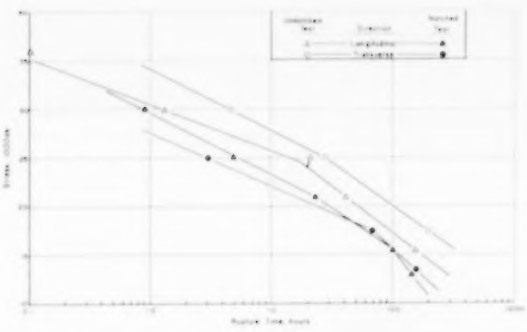

Fig. 5—Stress-rupture strength of the silver-bearing copper tested in the notched and unnotched conditions at 550°F (288°C).

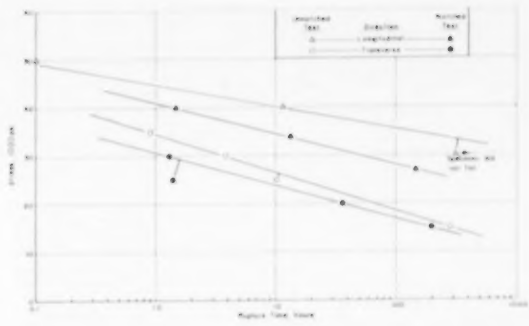

Fig. 6—Stress-rupture strength of the Cr-Cu tested in notched and unnotched conditions at 550°F (288°C).

notch. The cracks appeared to be tensile failures. Segments of Zr-Cu in commutators, on the other hand, did not fail either by displacement or by cracking.

This service behavior of the three alloys cannot be explained readily by results of short-time tensile tests at the maximum operating temperature. However, stress-rupture tests at 550°F (288°C) of notched specimens loaded in the transverse to rolling direction make the observed behavior understandable. Fig. 5 shows the results of stress-rupture tests at 550°F on specimens of silver-bearing copper in both the notched and unnotched conditions loaded either parallel or transversely to the rolling direction. Sharp changes in direction in three of the curves after about 25 hr and in the fourth curve after 70 hr are believed to mark the beginning of recrystallization and permanent softening. After 150 hr, the hardness at room temperature of three of the specimens had dropped from RB 61 to about RB 17. The hardness of the fourth specimen, which was unnotched and taken in direction transverse to rolling, was RB 24 after 195 hr. The strength of notched specimens was consistently lower than the strength of unnotched specimens.

Table II. Electrical Resistivity and Conductivity of Zr-Cu and Cr-Cu at 68°F (20°C)

Sample Number	1*	2†	3‡	4§	5¶
Resistivity, Ohm-Cm x 10^{-6}	1.78	1.82	1.80	1.79	2.07
Conductivity, Pct IACS	96.9	94.7	95.8	96.3	83.3

* Zr-Cu—0.259 in. thick, solution annealed at 1300°F (705°C) for 20 min, water quenched, RF 56.
† Zr-Cu—0.259 in. thick, solution annealed at 1300°F (705°C) for 20 min, water quenched, aged 1 hr at 800°F (425°C), cold rolled to RB 68, 0.097 in. thick.
‡ Zr-Cu—0.259 in. thick, solution annealed at 1300°F (705°C) for 20 min, water quenched, cold rolled to RB 66, 0.126 in. thick; aged 1 hr at 800°F (425°C), RB 64.
§ Zr-Cu—0.259 in. thick, solution annealed at 1300°F (705°C) for 20 min, water quenched, aged 1 hr at 800°F (425°C), RF 58.
¶ Cr-Cu—0.259 in. thick, solution annealed at 1830°F (1000°C) for 15 min, water quenched, cold rolled at RB 68, 0.096 in. thick; aged 16 hr at 830°F (445°C), RB 82.

Results of similar stress-rupture tests on Cr-Cu are shown in Fig. 6. The original hardness of these specimens ranged from RB 78 to RB 82. At the conclusion of the tests the room-temperature hardness varied from RB 71 to RB 78. However, the strength of notched and unnotched specimens taken in direction transverse to rolling dropped to 15,000 psi after 196 and 286 hr, respectively. Strengths measured in the longitudinal to rolling direction were consistently higher than those in the transverse direction. In the unnotched condition, the strength of the longitudinal specimen decreased only to 30,000 psi after 305 hr under load.

The results of stress-rupture tests on Zr-Cu, Fig. 7, were notably different from those on the other alloys examined, in that the notched specimens taken in either direction to rolling were stronger than corresponding unnotched specimens. The strength in the direction transverse to rolling for both notched and unnotched specimens was appreciably higher than in the direction longitudinal to rolling. After a period of 328 to 353 hr at 550°F, the room-temperature hardness had dropped from RB 66-64 to RB 59-58. Although the rate of loss of strength and hardness of the notched specimens was somewhat greater than for the unnotched specimens, the data indicate the probability that the resistance of a notched, transverse specimen to a load of 25,000 psi at 550°F would be high. One specimen of Cr-Cu failed under this load after 1.4 hr. Fig. 6 indicates that similar Cr-Cu specimens would be expected to fail after about 10 hr under the same conditions.

Machinability of the three different alloys was not measured. However, no difference in speed of cutting or of tool life was noted after the substitution on the production line of Zr-Cu for silver-bearing copper. Cr-Cu, because of the hard particles of undissolved chromium it contains, often caused damage to cutting tools.

Conclusions

Properties of a Zr-Cu alloy were determined and compared with those of silver-bearing copper and Cr-Cu alloys that are used to make commutator seg-

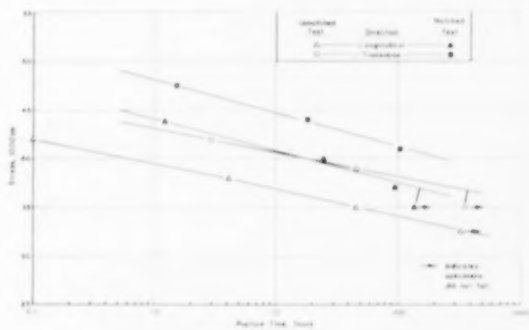

Fig. 7—Stress-rupture strength of the Zr-Cu tested in the notched and unnotched conditions at 550°F (288°C).

ments. The Zr-Cu (0.25 pct Zr) alloy showed some important advantages.

1) After aging, its electrical conductivity was about 95 pct IACS. This was almost as high as the conductivity of silver-bearing copper and much higher than that of Cr-Cu.

2) Its softening temperature and that of Cr-Cu was about 930°F (500°C) or above. Silver-bearing copper softened at a much lower temperature.

Table III. Tensile Properties of Three Copper-Base Alloys*

Testing Temperature	Rolling Direction	Yield Strength, 0.2 Pct Offset, Psi	Ultimate Strength, Psi	Elongation, Pct in 2 In.	Reduction in Area, Pct
Silver-Bearing Copper; Cold Rolled					
Room temperature	Parallel	47,000	50,000	8.5	51.3
550°F	Parallel	28,000	35,000	12.1	42.7
550°F	Transverse	31,000	36,500	8.2	25.7
Cr-Cu; Solution Annealed, Quenched, Cold Rolled, Aged					
Room temperature	Parallel	64,000	71,000	16.0	43.4
550°F	Parallel	46,000	50,000	4.2	7.2
550°F	Transverse	41,000	47,000	2.7	5.8
Zr-Cu; Solution Annealed, Quenched, Cold Rolled, Aged					
Room temperature	Parallel	50,500	53,000	10.1	54.3
550°F	Parallel	40,500	42,000	7.5	37.6
550°F	Transverse	42,000	44,200	6.5	43.6
Zr-Cu (Special); Rolled After Aging					
Room temperature	Parallel	56,000	59,000	6.4	61.3

* Average from tests on two specimens. See text for heat treatments and hardness of these alloys.

3) Its room-temperature tensile strength, processed to the hardness level preferred for the manufacture of commutator segments, was slightly greater than the strength of silver-bearing copper. The tensile strength of Cr-Cu was much higher than that of either of the other alloys. The same order of merit in strength of the three alloys persisted in short-time tensile tests at 550°F (288°C). In the elevated temperature tests there was little difference in strength between Cr-Cu and Zr-Cu, when determined on specimens taken transverse to rolling.

4) Its electrical conductivity, after a solution and aging treatment, was high.

5) Upon extended exposure under load to a temperature of 550°F (288°C), its room-temperature hardness was not impaired. Cr-Cu also resisted softening, but the silver-bearing copper was permanently softened.

6) Its tensile strength increased when notched, whereas Cr-Cu and the silver-bearing alloy were greatly weakened by a notch.

7) Its rupture strength at 550°F (288°C) for notched and unnotched specimens was greater in the direction transverse to rolling than in the direction longitudinal to rolling. In the notched condition and at the same temperature, the rupture strengths of both Cr-Cu and silver-bearing copper were lowest in the direction transverse to rolling.

From all of these tests, and from limited experience with practical applications, it was concluded that Zr-Cu containing 0.18 pct or more zirconium is a superior material for commutator manufacture. The superiority of Zr-Cu over silver-bearing copper would be expected to be most evident when these alloys are used as commutators subjected to greater than normal temperature rise, greater than normal speed of rotation, or both.

Zr-Cu should be useful in all applications requiring high electrical conductivity and retention of strength at elevated temperatures.

Acknowledgments

The author wishes to thank P. W. Nippert of The Nippert Electric Products Co. for permission to publish this work. Special thanks are due to B. W. Gonser of Battelle Memorial Institute for his encouragement and advice throughout the experimental program. Thanks are also due to the many colleagues at Battelle Memorial Institute who carried out the experimental work, and to J. G. Kura for careful review of this manuscript.

Discussion of this paper sent (2 copies) to AIME by June 1, 1957 will appear in AIME *Transactions* Vol. 209, 1957, and in JOURNAL OF METALS, October 1957.

Habit Planes of Martensite In Chrome-Carbon Steel

Observations are reported on the scatter of the habit planes of martensite in a 2.8 pct Cr, 1.5 pct C steel. Only a small amount of the scatter is actually due to experimental error; most of it is real. Possible reasons for the real scatter are proposed and examined.

by H. M. Otte and T. A. Read

H. M. OTTE, formerly Research Associate, University of Illinois, is now at Birmingham University, Birmingham, England. T. A. READ, Member AIME, is Head, Dept. of Mining and Metallurgical Engineering, University of Illinois, Urbana, Ill.

TP 4388E. Manuscript, May 31, 1956. New Orleans Meeting, February 1957.

THEORETICAL analysis by Wechsler, Lieberman and Read[1] of the crystallography of martensite formation has shown that the requirement for the existence of a macroscopically undistorted plane between austenite and martensite permits a calculation of the indices of the habit plane of the marten-

site. Their calculations are based on the experimental observation that the distortion involved in the formation of martensite is inhomogeneous on a microscopic or submicroscopic scale. The inhomogeneous character of the transformation distortion can be expressed as a simple shear superimposed on the homogeneous distortion required to bring about the change in structure. Since it does not affect the crystal structure, the simple shear must correspond to a slip or twinning distortion.

The analysis has also shown that if the simple shear referred to above occurs on a unique plane in a unique direction, then for given initial and final structures the habit plane indices must have a unique value. Successful predictions have been made in a number of systems.[1-4] An extension[3] of the analysis to include a number of possible modes of inhomogeneous deformation indicated that the habit planes in iron alloys were restricted to certain ranges of values. The extent of each range depended on the range of permissible lattice parameters. Similar analyses have been published during the past few years and have been reviewed recently.[5]

The most reliable data[6] now available show, however, an appreciable distribution in the observed values of the habit plane indices in a single steel. If this distribution is real, it must mean that even within a single austenite grain different planes and/or directions of simple shear are involved in the formation of the individual martensite plates.

It is one of the purposes of the present work to determine to what extent this distribution of values is real and not the result of experimental scatter.

The alloy chosen as being most suitable for this investigation was one with 2.8 pct Cr, 1.50 pct C (28Cr150) because it had an M_s temperature conveniently below room temperature.

Experimental Methods

In this section particular attention will be given to those parts of the experimental procedure which may be sources of error and thus contribute to the scatter in the observations.

Preparation of Specimens—The alloy was prepared by melting a 120 g ingot under a helium atmosphere using high purity materials. Negligible melting losses were encountered and the nominal composition was therefore assumed to be approximately the actual composition. A specimen, about $\frac{1}{4} \times \frac{1}{4} \times \frac{1}{2}$ in., was cut from the ingot and austenitized for 50 hr at 1200°C in dry helium gas (containing 8 pct H_2). By placing the specimen in a small graphite container, direct contact with which was prevented by wrapping wolfram wire around the specimen, a perfectly neutral atmosphere was obtained. The specimen was neither carburized nor decarburized. Test samples showed that after the first few hours at 1200°C little further increase in grain size occurred, but the additional time was given to ensure homogeneity of the specimen (judged by the distribution of martensite plates throughout the specimen on cooling a little below M_s). Homogeneity was important since the habit plane appears to vary somewhat with composition.[6] The M_s temperature of the present alloy was a little below −35°C so that at room temperature the specimen was fully austenitic after water quenching from 1200°C. The largest austenite grains were about 1 mm in diam.

Determination of the Habit Plane—Unlike the case of single interface transformations, where the habit plane can be precisely measured as the interface plane, in steels measurements have to be made on very small martensite plates embedded in the austenite matrix. Consequently, the habit plane is frequently ill-defined. Two definitions of the habit plane are possible: 1) the plane of the mid-rib or 2) the plane parallel to the martensite plate. In the literature difficulties are avoided by assuming these two planes parallel. This is not necessarily always so. Fig. 1 shows a martensite crystal in which the mid-rib runs out of the plate before the plate reaches the edge of the specimen. Experimental determination of the mid-rib plane by a two surface analysis of such martensite crystals would yield a polemical interpretation of the habit plane, since the significance of the mid-rib is not known at the moment and to assign to it the role of the interface may be misleading. In addition, the mid-rib was frequently found to have a slight curvature. For the present work, therefore, definition 2 seemed more acceptable. Hence, measurements were made along the length of the martensite plate. These measurements were considered to give the most probable value of the true interface; namely, the interface which would be observed if the transformation could be induced to proceed in a single crystal by the movement of a single interface, as in certain other systems.[7,8]

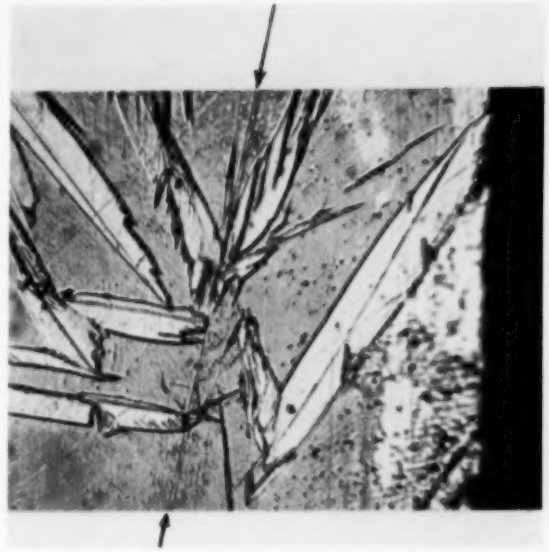

Fig. 1—Edge of specimen with surface mechanically polished; etched with Nital. Arrows indicate twin plane. X1400. Reduced approximately 10 pct for reproduction.

Table I. Rotation as a Result of Slip in Austenite

Deformation of Specimen, Pct True Strain in Compression	Angle Made with Austenite Slip Lines by Martensite	
	Plate *A*	Plate *B*
0	56°	57°
2.2	55°	56°
4.4	54½°	54½°

Measurements of the same martensite plate were made on two adjacent faces and the traces plotted on a 30 cm diam stereographic net. The angle (which was close to 90°) between the two adjacent faces was measured on a two-circle optical goniometer.

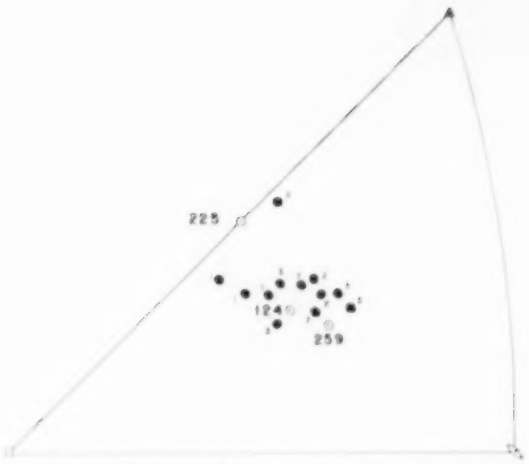

Fig. 2—Distribution of habit planes of martensite plates formed at the surface of the specimen.

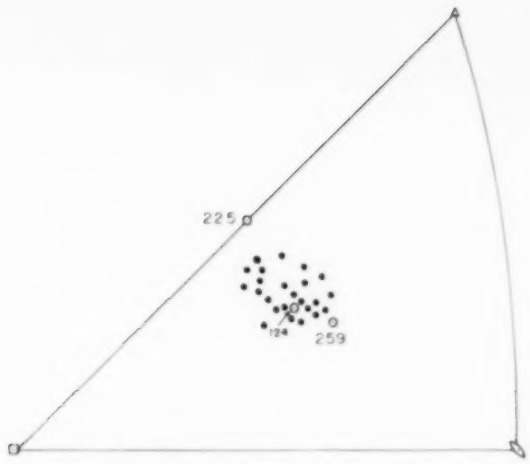

Fig. 3—Distribution of habit planes of martensite plates formed in grains 0.05 in. below the surface.

The orientation of the austenite was determined by the usual Laue back-reflection technique, using a 3 cm specimen to film distance and a 0.020 in. collimator with tungsten radiation. To prevent excessive background blackening of the film due to fluorescent radiation from the iron, two photographic films, placed on top of each other, were employed, one serving the purpose of a filter;[5] this proved a little more effective and convenient than aluminum foil. The films were measured on a Greninger net[6] and all results plotted on a 30 cm stereographic net.

For the two-surface analysis the specimen had to be mechanically polished in a clamp so that a sharp edge could be preserved between the two adjacent faces. The mechanical polishing, however carefully performed, always produced sufficient cold-working of the surface of the austenite to prevent really good Laue patterns being obtained. For these, therefore, the specimens were electrolytically polished (with a 2:1 acetic anhydride: perchloric acid solution). To reveal the grain boundaries, the polished specimen was etched for several minutes in a 2 pct Nital solution. No tempering treatment was given, since it was found that after such treatment the austenite grains could not be persuaded to show up in the presence of martensite.

Results and Discussion

Accuracy of Measurement—In order to determine the precision with which measurements could be made, a number of twins were analyzed. As shown in Fig. 1, the twin plane was extremely straight and could be measured to any desirable degree of accuracy. The position of the poles of the twin planes agreed to within $\pm\frac{1}{2}°$ with the Laue orientation, and this was taken to represent the experimental error under the present conditions.

Martensite plates, however, unlike twin planes, always show a finite width and, in addition, are only a fraction of the length of the twin trace, Fig.1. Furthermore, the martensite crystals rarely exhibited a straightness such as observed for the twin plane. All these factors contributed to a slight uncertainty involved in tracing a well-defined straight line through a martensite plate. For the plates on which measurements were made, however, it was estimated that this uncertainty rarely exceeded $\pm\frac{1}{2}°$. Overall reproducibility of results may therefore be placed at $\pm1°$.

Magnitude of Scatter—The poles of twelve martensite plates formed in three austenite grains at the surface of the specimen on quenching to −52°C were measured and the results, after plotting, ro-

a b c

Fig. 4—Surface relief on specimen electropolished at room temperature, then quenched to −23°C: a) undeformed, b) deformed 2.2 pct at room temperature, and c) deformed 4.4 pct at room temperature. X350. Reduced approximately 20 pct for reproduction.

tated into one stereographic triangle as shown in Fig. 2. The grain to which each pole belongs has been marked in the figure. Each pole in Fig. 2 represents a different variant of the habit plane in the given grain. As only a relatively small number of martensite plates were formed, not many of the same variant were observed. When observed, those which were adjacent were generally found to be parallel to within 1° or less. Those separated by plates of a different variant (in the same austenite grain) were identical to within 2° or 3°, though one result gave a somewhat larger difference. In Fig. 2, all poles, with one exception, fall within a cone of semi-angle of approximately 5°. This represents a scatter outside experimental error.

In the first theoretical treatment referred to earlier, any constraints resulting from the fact that the martensite plates are embedded in the austenite crystal were considered as minor effects and not taken into consideration. The constraints result from the interference with: 1) the volume expansion of the martensite and 2) the macroscopic average shear of the plate. These become vanishingly small as the plate is made increasingly thinner compared with its lateral dimensions. Actual martensite plates do, however, have a finite thickness and consequently the constraints must be accommodated in some manner. Adjustments can take place in either the austenite or the martensite or both. A reason for the scatter was therefore sought in these adjustments by attempting to evaluate the nature of the distortions in the austenite and the martensite and the extent of their influence on the scatter of the results. This proved fairly successful for the austenite, but less so for the martensite. The role of deformation was first examined by considering the constraints at a free surface and within the material.

The constraints at a free surface may differently affect the separate variants of the habit plane and produce a slight scatter. If deformation (of the austenite or martensite, or both) plays an appreciable role in causing this scatter, then its magnitude would most likely be less at the surface than inside the material, where the constraints are larger. The possibility that a larger scatter might be found when observations were made on plates formed well within the specimen was investigated as follows.

Fig. 5—Surface relief on specimen electropolished at room temperature, then quenched to —23°C, deformed 4.4 pct at room temperature. X700. Reduced approximately 10 pct for reproduction.

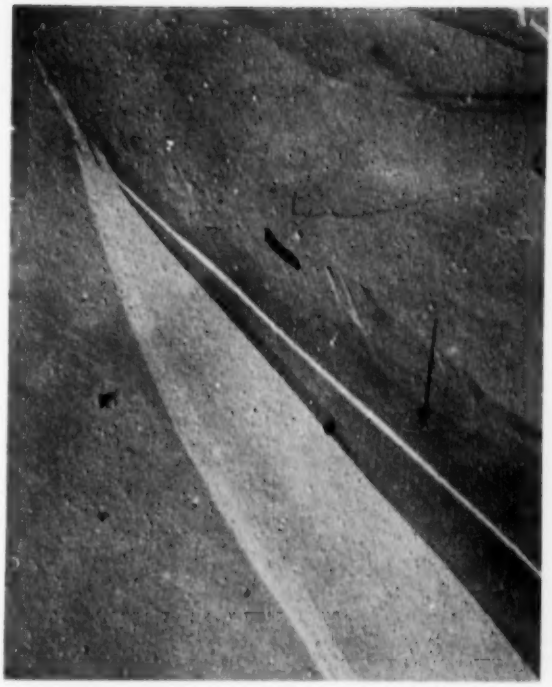

Fig. 6—Electron micrograph of surface relief on Fe-32 pct Ni. Arrow indicates direction of striations. X10,000. Reduced approximately 55 pct for reproduction.

By careful grinding on a wet belt, 1⅓ mm (0.05 in.) were removed from the two adjacent faces of the specimen examined above. The removal of 1¼ mm ensured that any grain exposed at the surface would be completely removed, as even the largest grain did not exceed 1 mm. The poles of 24 martensite plates were determined in four of the new grains revealed by this procedure, and are given in Fig. 3. No change in the amount of scatter resulted. It must thus be concluded that if the free surface has any effect on the habit, it is outside the observable range and (within the same limits) that deformation is not a factor producing the scatter. This conclusion also found support from the subsequent observations on the nature of the deformation in the austenite and martensite described in the remainder of this paper.

Deformation of the Austenite—The slip in the austenite which frequently accompanies the formation of martensite is readily seen in the surface relief of the polished specimen shown in Fig. 4a.* The slip lines are easily identified by comparison with Figs. 4b and 4c which were obtained from the same specimen after light mechanical deformation. Profuse slip in the austenite as a result of the additional mechanical deformation is visible and the position of the martensite plates is affected. Though the direction of the externally applied stress naturally governs the choice of the particular slip plane variant which becomes operative in the austenite, Fig. 5 shows that after 4.4 pct deformation slip will also occur on other variants in the vicinity of the martensite plate. Table I gives numerical values for the

* Figs. 4, 5, 8 and 9 are actually from an 8.8 pct Cr, 1.0 pct C steel austenitized 23 hr in vacuum at 1225°C and water quenched into a 10 pct NaOH solution at 15°C. M_s temperature of alloy was about —10°C.

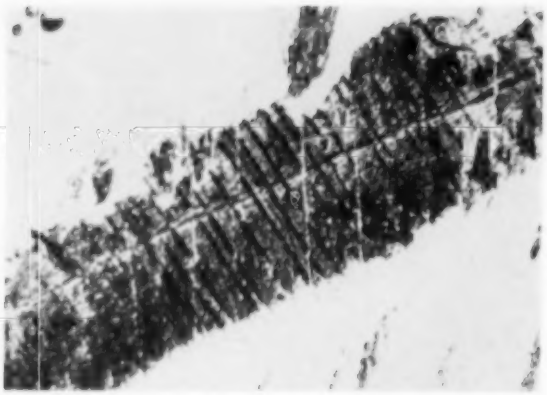

Fig. 7—Specimen deformed 4.4 pct at room temperature, tempered 30 sec at 425°C, electropolished and etched with Vilella reagent. X1500. Reduced approximately 15 pct for reproduction.

amount of rotation of two almost parallel martensite plates (*A* and *B*, Fig. 4a), as a result of slip in the austenite. The initial positions of the two plates differ slightly, probably because plate *A* has several other martensite plates attached to it while around plate *B* mainly slip in the austenite can be detected. Table I shows that an appreciable amount of slip in the austenite seems necessary in order to make a measurable difference to the position of the habit plane, and thus merely confirms the conclusion reached above, viz., that deformation may be eliminated as a factor producing scatter. This would not be expected if the formation of martensite consisted of two successive stages in which the production of the new structure (first stage) was followed by slip in the parent (or product) phase (second stage), as has been suggested.[9]

Deformation of the Martensite—Martensite plates freshly formed in relief show a perfectly smooth surface under the optical microscope even at the highest magnifications examined (about X3,000). Under the electron microscope, however, striations were observed at X10,000, as shown in Fig. 6,* taken from an Fe-32 pct Ni alloy. (This photograph was the best of several obtained from both the Fe-32 pct Ni and the 23Cr150 alloy.) These striations could be interpreted as thin twins or as clusters of slip lines. A clear choice between the two does not seem possible at the moment, but they can be discussed with a view to selecting the more probable one.

* Obtained by shadow-casting with an Au-20 pct Cr alloy the carbon replica of surface relief of an electrolytically polished and transformed specimen. Surfaces in the shadow—lighter on the photographs—thus show no detail. Contrast depends on the relative position of the replica with respect to the angle of shadow-casting.

Twinning: Transformation twins are known to occur in pure iron,[10] though there is little evidence at the moment of their existence in martensite. X-ray back-reflection Laue observations of a single martensite plate in a special case[11] did not yield any suggestion of twins. If martensite were a twinned product, then the ratio of the twin thicknesses should, according to theory 1, be 2:1, whereas the electron microscope photograph (Fig. 6), suggests a ratio more in the neighborhood of 10:1.

Transformation twins thus appear to be absent in martensite, but observations on the behavior of martensite during deformation suggest that martensite is at least capable of twinning mechanically. Evidence for this may be obtained from the deformed martensite shown in Figs. 4 and 5. Visible in relief on the martensite and lying approximately perpendicular to the length of the plate are straight narrow ridges. They may be seen as dark etching bands running across the plate after tempering, polishing and etching the specimen. These bands, shown in Fig. 7, appeared to be twins, since they could be easily detected in an untempered specimen as well. This is illlustrated in Fig. 8, obtained after electropolishing.* Note that the slip lines in the austenite do not show up. Fig. 7 shows twins in martensite which bear great resemblance to those reported by Greninger and Troiano[11] in martensite mechanically polished.

* This also causes partial etching of the specimen.

It would thus appear that if martensite were a twinned product, metallographic observation of this would be possible.

Slip: Suppose that slip of only one interatomic distance in the $[111]_\alpha$ direction on any given $(211)_\alpha$ plane were to occur in the martensite during its formation, then theory[7] predicts that approximately every sixth plane would have to slip in order to preserve an invariant interface plane. The scale of this would be too fine to be seen by the electron microscope (which has an optimum resolution of about 50Å under favorable conditions). If, however, sufficiently large and widely separated clusters of slip occurred, they could be detected by the electron microscope. The observations in Fig. 6 interpreted on such a basis indicate that the clusters of slip planes would be about 100Å thick and separated by a distance of approximately 1000 to 1500Å. This implies slip by more than one interatomic distance on most of the planes in the cluster. Scatter in the habit planes could then arise from slight variations in the amount of slip on these planes as a result of external constraints during the formation of a martensite plate. External constraints could be accommodated by small deviations from the position of the theoretical strain-free interface.

In the foregoing discussion it has been assumed that the striations were traces from $\{211\}_\alpha$ planes. This may not be so. The choice of a crystallographically different slip plane leads, in the extended theoretical treatment to different habit planes—pro-

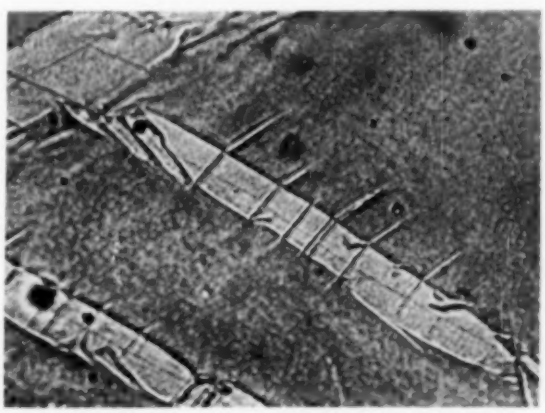

Fig. 8—Specimen deformed at room temperature and electropolished only (untempered and unetched). X700. Reduced approximately 15 pct for reproduction.

viding that it is,[4] possible to satisfy the criterion of an unstrained interface at all. Thus, the fact that body-centered-cubic crystals exhibit a diversity of slip planes suggests that the habit planes could also be associated with some variation in the effective slip plane from one martensite plate to another.

Consideration of the general diffuseness of X-ray diffractions from martensite[11-13] would indicate that, if simple slip is to be associated with the formation of a martensite crystal, it must be accompanied by a considerable number of defects in the martensite lattice. These defects may form a rather complicated pattern and further speculation at this stage seems premature.

Conclusions

The observed scatter in the habit planes of martensite in steel has been found to be greater than the experimental error and must therefore be considered real. A small amount of the real scatter results from an inherent inability to define the interface plane precisely enough. The remainder is a consequence of the constraints arising during transformation. These give rise to two effects. One seems fairly well established and may be assigned to slip in the austenite accompanying the transformation. The contribution of this to the scatter appears to be small. The other is of an undetermined nature and is to be associated with the rather imperfect structure of the martensite. It is suggested that slip in the martensite is involved.

Acknowledgments

This work was supported by the Air Research and Development Command under Contract No. AF 18(600)-1311. The authors wish to thank T. S. Noggle and A. E. Vatter for their cooperation in obtaining the electron microscope photographs.

References

[1] M. S. Wechsler, D. S. Lieberman, and T. A. Read: *AIME Trans.*, 1953, vol. 197, p. 1503; JOURNAL OF METALS, November 1953.
[2] M. W. Burkart and T. A. Read: *AIME Trans.*, 1953, vol. 197, p. 1516; JOURNAL OF METALS, November 1953.
[3] D. S. Lieberman, M. S. Wechsler, and T. A. Read: *Journal of Applied Physics*, 1955, vol. 26, p. 473.
[4] M. S. Wechsler and T. A. Read: Unpublished work.
[5] B. A. Bilby and J. W. Christian: *Monograph and Report Series No. 18* Inst. of Metals, 1956, p. 121.
[6] A. B. Greninger and A. R. Troiano: *AIME Trans.*, 1940, vol. 140, p. 307; METALS TECHNOLOGY, August 1940.
[7] A. Kelly: *Proceedings* Physical Soc., 1953, vol. 66, p. 403.
[8] A. B. Greninger: *AIME Trans.*, 1935, vol. 117, p. 61.
[9] A. H. Geisler: *Acta Metallurgica*, 1953, vol. 1, p. 260.
[10] A. B. Greninger: *AIME Trans.*, 1936, vol. 120, p. 293.
[11] A. B. Greninger and A. R. Troiano: *AIME Trans.*, 1949, vol. 185, p. 590; JOURNAL OF METALS, September 1949.
[12] J. A. Wheeler and M. A. Jaswon: *Journal* Iron and Steel Inst., London, 1947, vol. 157, p. 161.
[13] R. A. Smith: *Journal* Iron and Steel Inst., London, 1953, vol. 173, p. 147.

Discussion of this paper sent (2 copies) to AIME by June 1, 1957 will appear in AIME *Transactions* Vol. 209, 1957, and in JOURNAL OF METALS, October 1957.

Effects of Solid Solution Alloying On Creep Deformation of Aluminum

The effects of solid solution alloying on the creep-rupture properties, deformation characteristics, ductility, and fracture of pure aluminum were studied by means of creep-rupture tests on polished specimens of three alloys each of Al-Cu (0.24, 0.79, and 2.05 pct Cu), Al-Zn (4.93, 9.89, and 19.78 pct Zn), and Al-Mg (0.94, 1.92, and 5.10 pct Mg) at 500°, 700°, and 900°F.

by Gordon D. Gemmell and Nicholas J. Grant

CREEP rupture characteristics of high purity Al-Mg solid solution alloys were studied by Mullendore and Grant[1] to investigate solid solution strengthening of pure aluminum and the accompanying effects on deformation and fracture characteristics. This paper presents the results of an extension of that work to Al-Cu and Al-Zn alloys to permit a comparison of the relative effects of the three solute elements on the high temperature strength and on the deformation and fracture characteristics.

G. D. GEMMELL, formerly Fellowship Student, Department of Metallurgy, Massachusetts Institute of Technology, is now with E. I. DuPont Co., Wilmington, Delaware. N. J. GRANT, Member AIME, is Professor of Metallurgy, Massachusetts Institute of Technology, Cambridge, Mass.

TP 4416E. Manuscript, July 23, 1956. New Orleans Meeting, February 1957.

Experimental Procedure

A total of nine alloys was studied. They were all made of ultra high purity aluminum alloyed with high purity copper, zinc and magnesium. The com-

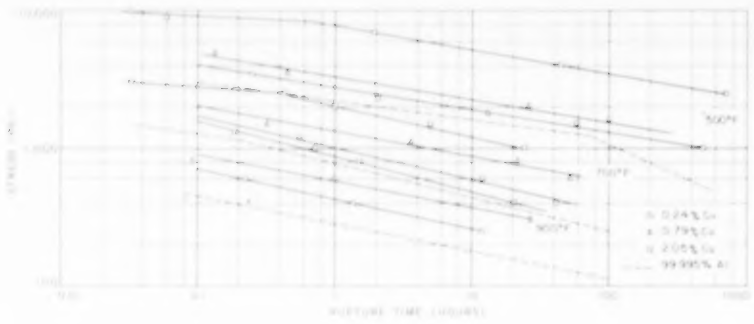

Fig. 1a—Log stress, log rupture time plot at 500°, 700°, and 900°F for Al-Cu solid solution alloys, compared with high purity aluminum.[2] The 0.79 pct Cu alloy is two phase at 500°, and the 2.05 pct Cu alloy is two phase at 500° and 700°F.

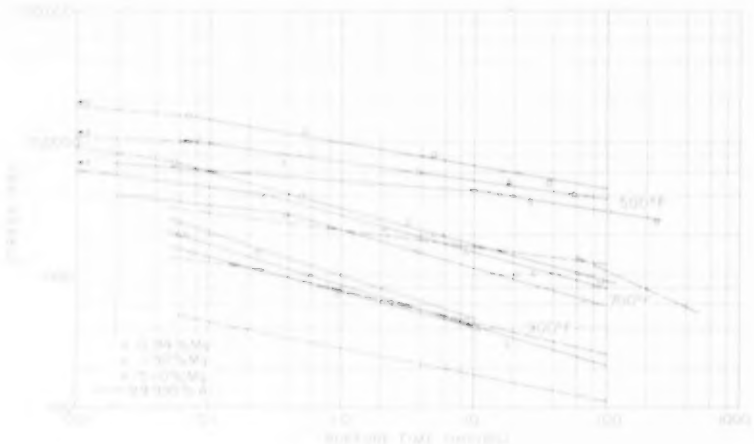

Fig. 1b—Log stress, log rupture time plot at 500°, 700°, and 900°F for Al-Mg solid solution alloys, compared with high purity aluminum.[2]

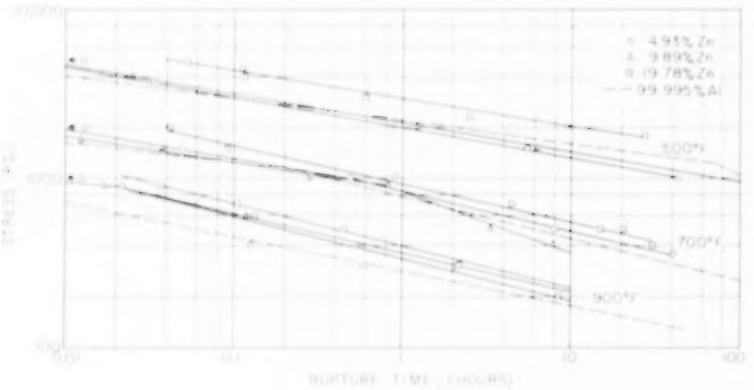

Fig. 1c—Log stress, log rupture time plot at 500°, 700°, and 900°F for Al-Zn solid solution alloys, compared with high purity aluminum.[2]

positions are listed in Table I. Constant stress creep rupture tests were made on electrolytically polished (Jacquet's solution) specimens of each alloy at 500°, 700°, and 900°F. All specimens were annealed at 1000°F for a time necessary to produce the desired grain size of approximately 1 mm average diameter. The constant stress testing apparatus has been described previously.[5]

The test conditions permitted testing in the solid solution region of each binary phase diagram, with the exception of the 0.79 pct Cu alloy at 500°F and the 2.05 pct Cu alloy at 500° and 700°F, which were two-phase alloys. These two-phase alloys were included to permit an examination of strength and deformation changes in going from the single phase field into the two-phase field to facilitate extension of the current work to other two-phase alloys.

The limits of solubility for the three alloy systems are shown in Table II.

The Al-Mg alloys are the same as those studied by Mullendore and Grant.[1] However, whereas they used constant load tests, it was found advantageous to perform the present work at constant stress to permit easier comparison of creep rates and ductilities.

Results

Creep-Rupture Properties—Figs. 1a, b, and c show the total creep-rupture results plotted as log stress vs log rupture time for each of the three alloy series. Curves for high purity aluminum from the work of Servi and Grant[2] are included in each of the figures for purposes of comparison. The data for pure aluminum shown in other figures are from the same source. Similar plots were obtained of log

stress vs log minimum creep rate; the results simply confirmed the observations made from Fig. 1, which are discussed below, and are accordingly not presented.

Fig. 1 is based on the plotting convention of drawing the best straight line through the experimental points, with a break in slope to indicate and emphasize a region of material instability with respect to the test conditions.[2] Such instabilities were confirmed by metallographic examination or other evidence. For the alloys in this series the slope changes which are shown are associated with the incidence of active grain boundary sliding and/or intercrystalline cracking; the metallographic as well as normal visual observation clearly showed the start of such grain boundary deformation and intercrystalline cracking.[1] Marked decreases in ductility at fracture support these observations of intercrystalline cracking and simplify the detection of these regions of equicohesion.

With reference to Fig. 1a, it was observed that the 2.05 pct Cu alloy underwent intercrystalline cracking at 500° and at 700°F. Regarding Fig. 1b, intercrystalline cracking was noted for the 5.10 pct Mg alloy at 500°F, and at high strain rates at 700°F. Some intercrystalline cracking was also observed in the 1.92 pct Mg alloy at 500°F. However, the fracture was mostly transgranular due to the increased strain rates as a result of a decreased cross section resulting from the intercrystalline cracks. In general, the results observed on the Al-Mg alloys at constant stress are in close agreement with the tests performed on the same alloys at constant load.[1] Extensive intercrystalline cracking and fracture also occurred in the 19.78 pct Zn alloy at 500°F.

In the lower alloy content compositions of all the solid solution alloys other than those noted above, there was a marked tendency at 500°F for some intercrystalline cracking to occur, as evidenced by the heavy and highly restricted deformation along the grain boundaries, with restricted or no evidence of grain boundary migration. However, intercrystalline cracking occurred only in localized regions. On the other hand, at 700°F there was extensive grain boundary migration and freedom from intercrystalline cracking except as noted above. This trend was completed at 900°F in that not one of the nine alloys showed any evidence of intercrystalline cracking, but all showed extensive grain boundary sliding and migration.

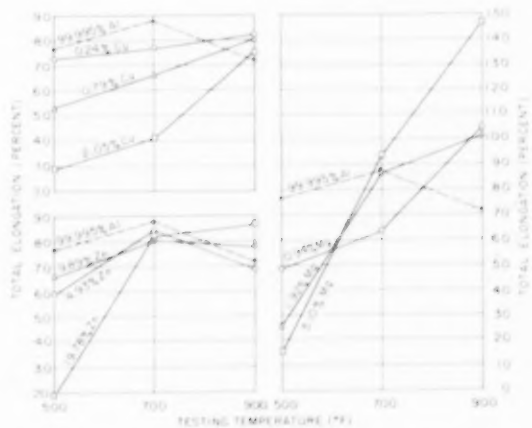

Fig. 2—Total elongation vs test temperature. Each value is the average of all tests at that temperature for each alloy.

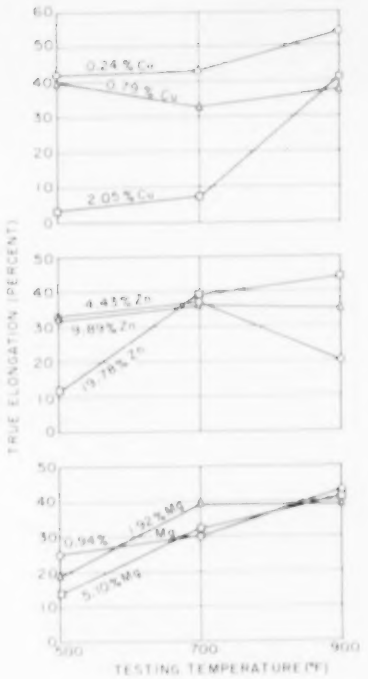

Fig. 3—Second stage (true) elongation vs test temperature. Each value is the average of all tests at that temperature for each alloy.

Ductility Observations—Since it has been observed in the past that elongation at the end of second stage of creep (and sometimes total elongation) is a good indicator of intercrystalline cracking,[1,2] considerable attention was given to measurements of both elongation values. Some small error exists in that an exact value of strain on loading was not obtainable with the existing equipment, but the interpretation of the data was not complicated by this.

Fig. 2 shows the average total elongation at fracture for each alloy for all of the specimens tested at a given temperature plotted against the test temperature. The comparative values for pure aluminum are also shown.[1] At 500°F, where intercrystalline cracking was observed, it will be noted that with one minor exception (9.89 pct Zn alloy), as the alloy content increased the elongation decreased. Further, the 5.10 pct Mg and the 19.78 pct Zn alloys, which showed the most severe intercrystalline cracking, also showed the most severe embrittlement. As recovery processes are enhanced with increasing temperature of test above 500°F, and intercrystalline cracking is largely or wholly eliminated, elongation values increased sharply at 700°F, and continued to increase up to 900°F. In fact, at 900°F most of the aluminum alloys show greater elongation than pure aluminum. Of particular interest is the high ductility of the 5 pct Mg alloy, which not only exhibits the highest values of stress for rupture at all three test temperatures, but is also the most ductile at 700° and 900°F. In fact, the 5.1 pct Mg alloy, a solid solution alloy, is stronger at all three temperatures than the 2.05 pct Cu alloy, which is a two-phase alloy at 500° and 700°F (although no effort was made to produce a structure to yield optimum strength).

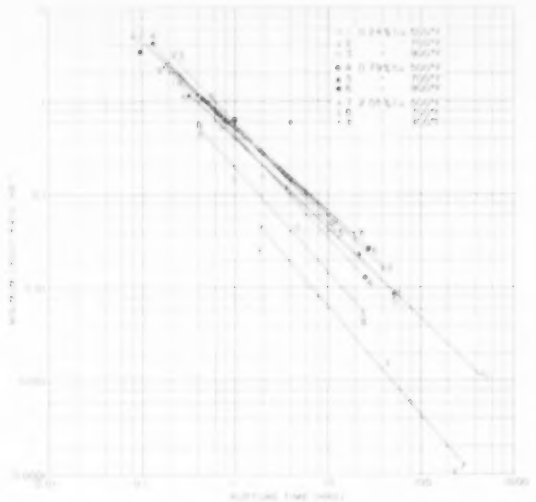

Fig. 4a—Log-log plot of minimum creep rate vs rupture time for Al-Cu alloys.

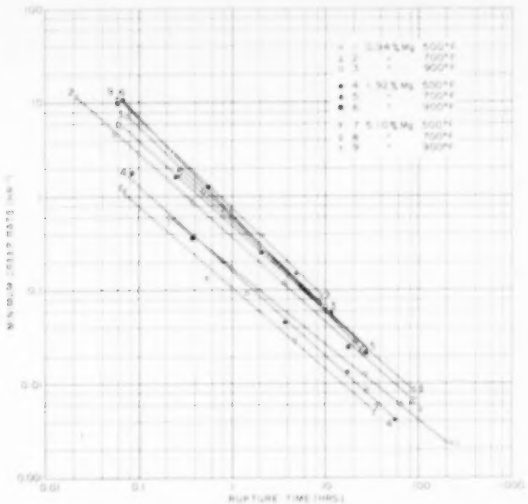

Fig. 4b—Log-log plot of minimum creep rate vs rupture time for Al-Mg alloys.

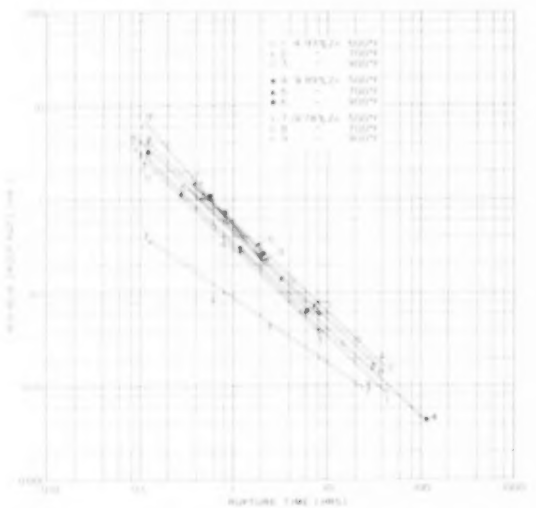

Fig. 4c—Log-log plot of minimum creep rate vs rupture time for Al-Zn alloys.

The *true elongation* (elongation at end of second stage creep), because it presents a somewhat different ductility picture, is worth examining, and is shown in Fig. 3. Again, at 500°F, due to slow recovery processes with attendant intercrystalline cracking, there is in all instances a decrease in elongation with increasing alloy content. In this case the two-phase copper alloy (2.05 pct) shows a sharp drop in elongation. At 700°F, where recovery is enhanced, there is a significant gain in ductility by those alloys which showed low values at 500°F. The change in second stage elongation from 700° to 900°F is small in all instances except for the 2 pct Cu alloy, which becomes a single phase alloy above 700°F. These results indicate that those alloys which had very limited intercrystalline cracking or none at all at 500°F do not show an important change in elongation at the end of second stage creep in the entire 500° to 900°F temperature range. Where recovery processes, as evidenced by grain boundary migration, prevent intercrystalline cracking, large gains in elongation at the end of second stage creep result, as compared to the 500°F values.

Furthermore, by comparing Figs. 2 and 3, these results indicate that large amounts of third stage deformation were possessed by these alloys at 700° and 900°F. This is especially the case for the solid solution magnesium alloys of aluminum.

In Figs. 4a, b, and c, plots of log rupture time vs log minimum creep rate are shown for all the alloys, with all alloys of one type being plotted on a common graph, independent of temperature. In most cases, a straight line may be drawn for each alloy composition in each alloy system at each temperature which is only slightly displaced from the rest of the curves. These curves can be represented by the following equations

$$\log \dot{\epsilon} = \log E_o - \log t_r$$

or

$$\dot{\epsilon} = \frac{E_o}{t_r}$$

where $\dot{\epsilon}$ is the minimum creep rate, E_o is a constant and t_r is the rupture time. E_o had an average value of 0.316 for high purity aluminum, and 0.350 for 2S aluminum.

Fig. 4 shows that for each alloy system almost all of the points can be represented by a narrow band of slope (−1). Points or lines which fall outside (i.e., below) the main band correspond to tests which failed with low ductility. These alloys are the following: 2.05 pct Cu alloy at 500° and 700°F; 0.94, 1.92, and 5.10 pct Mg alloys at 500°F; and 19.78 pct Zn alloy at 500°F.

It will be seen from Figs. 2 and 3 and the discussion above that these are the low ductility tests in which the specimens failed by or showed intercrystalline cracking.

The main bands, which include most of the lines, can be represented by the relationship

$$\dot{\epsilon} = 0.5\, t_r^{-1.0}.$$

E_o varies inappreciably for these alloys with increasing alloy content or with change in temperature,

except insofar as a combination of these variables results in low ductility at fracture.

Solid Solution Strengthening at Elevated Temperatures—In order to determine the relative strengthening effects of the three alloying elements, a comparison was made using the ratio $\frac{\sigma_{alloy}-\sigma_{Al}}{\sigma_{Al}}$ where σ_{Al} is the stress which gives a 10 hr rupture life for pure aluminum at a given temperature, and σ_{alloy} is the stress for 10 hr rupture time of the alloy at the same temperature. This ratio gives the fractional increase or decrease in strength of the alloy compared to pure aluminum.

Because little is known regarding the basis of high temperature solid solution strengthening, a number of variables were examined. Fig. 5 shows the variation of the strength ratio plotted against the concentration, in atomic pct, of the solute element, including the two-phase copper alloys. Copper and magnesium have similar strengthening effects, copper having a slightly greater effect on a per atomic pct basis, but magnesium having the greater effect within the solubility limits. Zinc, on the other hand, shows either a very small strengthening effect at 900°F or a weakening effect at 500° and 700°F. Similar weakening effects for zinc in solution on the creep resistance of aluminum have been reported by Robinson, Tietz, and Dorn,[7] and by McLean and Farmer.[8]

To observe the strengthening by each solute element as a function of the degree of saturation, the same strength ratio has been plotted vs fraction of saturation of the solute element (c/c$_s$). It was observed that per fraction of saturation, magnesium, which is more soluble than copper in aluminum, has the greater strengthening effect. On this basis, strengthening with magnesium is greater at the lower temperatures, but appears inferior to copper at the higher temperatures. It should be pointed out, however, that at 900°F the limit of saturation of the magnesium alloys is the α plus liquid field whereas the limit of saturation of the copper alloys is the α plus CuAl$_2$ field, giving a different and imperfect basis of comparison of the saturation fraction.

Lattice strain is a factor in solid solution strengthening, and the variations of lattice parameter with

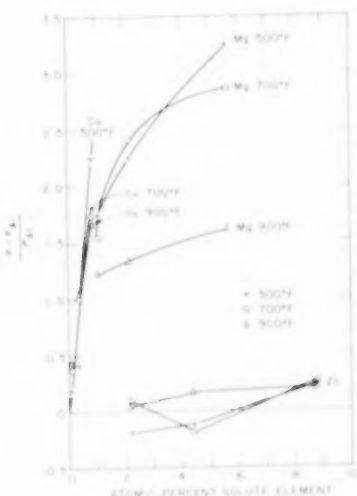

Fig. 5—Strength parameter vs atomic pct solute element for copper, zinc, and magnesium in aluminum; σ is the stress required to give a 10 hr rupture life.

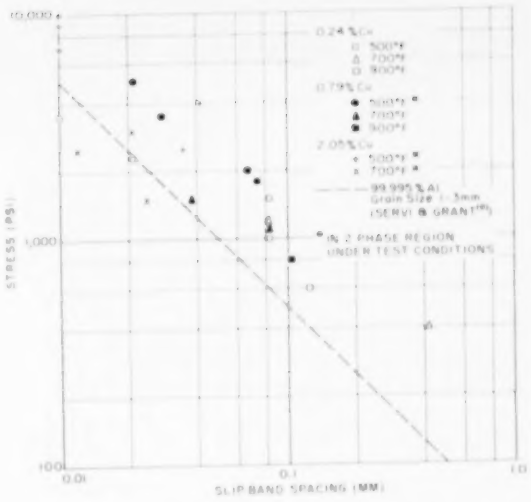

Fig. 6a—Stress vs slip band spacing for Al-Cu alloys.

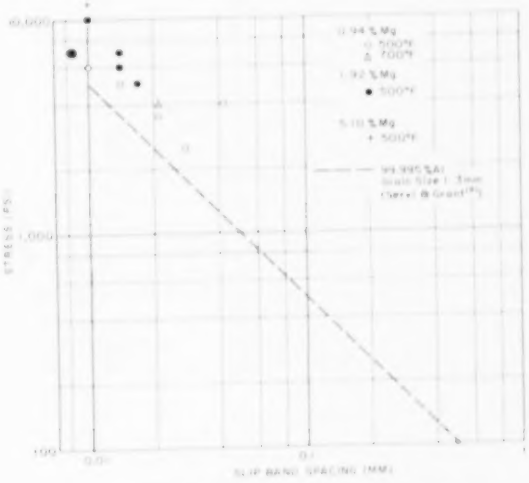

Fig. 6b—Stress vs slip band spacing for Al-Mg alloys.

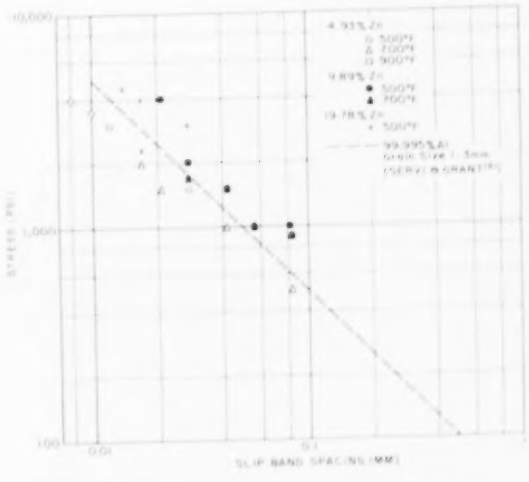

Fig. 6c—Stress vs slip band spacing for Al-Zn alloys.

Fig. 7—Al-19.78 pct Zn alloy. Creep rupture tested at 500°F and 4500 psi. X150. Reduced approximately 35 pct for reproduction.

Fig. 8—Al-19.78 pct Zn alloy. Creep rupture tested at 700°F and 1500 psi. X100. Reduced approximately 35 pct for reproduction.

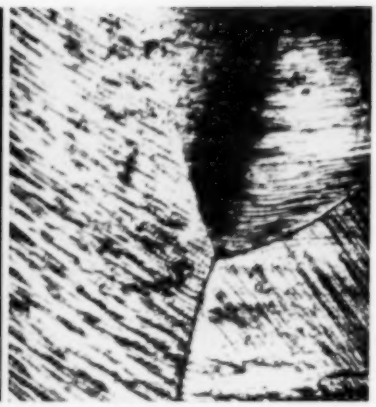

Fig. 9—Al-0.79 pct Cu alloy. Creep rupture tested at 500°F and 5000 psi. X100. Reduced approximately 35 pct for reproduction.

concentrations of copper, zinc, and magnesium in aluminum, as determined by Axon and Hume-Rothery,[5] were considered. While the effect of zinc, per atomic pct of addition, is small, nevertheless the contribution to the solid solution strengthening at high temperatures for large additions is not proportional to the lattice change as compared to either copper or magnesium. Copper additions, on the other hand, appear to have the most profound effects per atomic pct of solute addition.

On the assumption that the density of slip band spacing would change with increasing alloy content, measurements of average slip band spacing at fracture were made on all specimens in which slip was observed. According to Orowan, the slip band spacing at maximum strain is inversely proportional to the applied stress.[7] This was confirmed by Servi and Grant[8] for pure aluminum and was shown to be independent of temperature. Their values are shown in Figs. 6a, b, and c as a basis of comparison for the solid solution alloys. The values for the alloys also fit into a band of slope of approximately (—1). In the case of the copper and the magnesium alloys, the values are above the curve for pure aluminum with only occasional exceptions, suggesting that a higher stress is required to achieve the same density of slip bands at fracture as compared to pure aluminum. In the case of the zinc alloys, the points are distributed equally about the curve for pure aluminum, lending support from a deformation point of view to the observation that zinc does not significantly strengthen aluminum in hot creep as a solute element.

Metallographic Observations—The deformation mechanisms which occur in hot creep of pure aluminum[9,10] and in solid solution alloys of magnesium in aluminum[1] have been reported. The observations on the three magnesium alloys of aluminum reported by Mullendore and Grant[1] were substantiated in the present work, and only a few brief observations on the effects of copper and zinc will be made.

Table I. Compositions of Alloys*

Alloy No.	Atomic Pct	Elements, Wt Pct					Lattice Spacing† at 25°C, kX
		Cu	Fe	Ni	Mg	Zn	
1	0.10 Cu	0.24	0.002	0.005	0.008	0.000	4.0408
2	0.34 Cu‡	0.79	0.001	0.002	0.000	0.000	4.0397
3	0.88 Cu§	2.05	0.001	0.001	0.001	0.000	4.0372
4	2.09 Zn	0.005	0.002	0.002	0.000	4.93	4.0400
5	4.33 Zn	0.004	0.002	0.001	0.000	9.89	4.0383
6	9.23 Zn	0.005	0.004	0.001	0.000	19.78	4.0335
7	1.04 Mn	0.002	0.007	0.004	0.94	0.000	4.0445
8	2.12 Mn	0.002	0.003	0.002	1.92	0.000	4.0495
9	5.65 Mn	0.002	0.002	0.004	5.10	0.000	4.0630

* All the alloys and their analyses were furnished by the Aluminum Co. of America.
† By interpolation or extrapolation from data by H. G. Axon and W. Hume-Rothery.[5]
‡ Two phase at 500°F.
§ Two phase at 500° and 700°F.

As in the case of alloying with magnesium, alloying with copper and zinc also resulted in the incidence of intercrystalline cracking at 500°F in those alloys in which recovery processes were too slow at sufficiently high strain rates to permit strain accommodation and migration of grain boundaries to new unstrained positions. An increase of test temperatures to 700° or 900°F enhanced recovery processes, particularly boundary migration, resulting in the avoidance of intercrystalline cracking (except at 700°F at very high strain rates in the case of the highest magnesium and copper alloys).

Fig. 7 shows some of the deformation characteristics observed for the 19.78 pct Zn alloy tested at

Fig. 10—Al-0.79 pct Cu alloy. Creep rupture tested at 500°F and 1400 psi. Reduced approximately 25 pct for reproduction.

500°F and 4500 psi, which failed by intercrystalline means. At the high strain rate of this test some slip is evident in a number of grains. A sharp but small offset at the triple point is also observed which is associated with the broad fold in the grain into which the offset took place. Fig. 8 shows the same alloy tested at 700°F and 1500 psi; little or no slip is evident and a sharp intercrystalline crack is noted along two of the grain boundaries. At lower stresses (longer time tests) at 700°F this alloy failed with increasing ductility and by transcrystalline means as recovery processes were enhanced and grain boundary migration became increasingly prevalent.

In the Cu-Al alloys only the 2.05 pct composition showed complete intercrystalline failures at 500°F. Nevertheless, there was a marked change in the deformation characteristics in going from 500° to 700°F or with changing strain rate at 500°F. This is shown in Figs. 9 and 10, for the 0.79 pct Cu alloy at 500°F. Fig. 9 shows the high strain rate structure with extensive slip and absence of significant boundary sliding. Fig. 10 shows the low strain rate structure, with extensive boundary sliding and a fold plainly evident in grain *C*. A few intercrystalline cracks were discernible but the fracture was transcrystalline. This same type of transition in deformation was observable in all the alloys to a greater or lesser extent at about 500°F, the sharpness of the change being associated with the extent of intercrystalline cracking or fracture.

Table II. Concentration Limits of the α Phase

	Atomic Pct		
	500°F	700°F	900°F
Cu in Al	0.13	0.47	1.53
Zn in Al	12.0	66.0	28.0 (above eutectic)
Mg in Al	6.0	10.0	14.5 (above eutectic)

Summary

Both copper and magnesium in solid solution are highly effective in improving creep resistance and rupture life of aluminum, although a clear-cut criterion for strengthening was not found and is not warranted on the basis of only the three alloy systems studied in this program. The largest benefits occur with the first small additions of solute element. Significant strength improvements over pure aluminum occur at all temperatures from 500° to 900°F.

Zinc in solid solution has little or no effect on the high temperature creep resistance of aluminum, and for certain test conditions appears to have a weakening effect. An explanation of this behavior is not yet available but should make an important contribution to some of the theories of hot strengthening.

At 500°F at certain strain rates all alloys undergo a marked change in the deformation mechanism, changing from slip predominantly to high temperature processes, such as grain boundary sliding and fold formation. As alloying content increases in the solid solution range the change is considerably more marked. When recovery processes are slowed sufficiently so that grain boundary migration is highly restricted, and accommodation of strains across grain boundaries cannot be achieved, extensive intercrystalline cracking occurs with large loss of ductility. At longer times (lower strain rates) at 500°F, grain boundary sliding and migration and fold formation become more active and result in a resumption of transcrystalline failures. This effect was, of course, much more evident at 700° where intercrystalline cracking was present only in the most highly alloyed metals at high strain rates, and was completely absent at 900°F. Above 500°F large gains in ductility were noted with the advent of extensive grain boundary sliding and migration and fold formation.

Thus, in three alloy systems based on aluminum, in which the alloys were maintained at ultra high purity levels, it has been observed that intercrystalline cracking takes place when boundary deformation processes (sliding) begin to take place but cannot be fully accommodated because of the high recovery temperatures of the grains due to the increased alloy content. Under these circumstances continuity of strains cannot be transmitted across grain boundaries due to lack of fold formation, grain boundary migration, slip, etc., and brittle intercrystalline fracture occurs. With increased test temperature or time at test, recovery processes, especially migration, become operative and prevent intercrystalline cracking. Impurities such as oxygen, nitrogen, or carbon, or certain tramp elements are not necessary therefore to initiate or cause intercrystalline cracking, but if present would of course make intercrystalline cracking easier, more severe, and less subject to elimination by increases in temperature or decreases in strain rate.

None of the modes of deformation noted for pure aluminum at these same temperatures was eliminated by solid solution alloying, but there were definite changes in the extent of their participation in deformation. For example, as noted above, grain boundary migration is often reduced by alloying, and folds become shorter and broader with increasing alloy content. Average slip band spacing, measured at fracture, remained inversely proportional to the stress, but there appeared to be a wider spacing of slip bands for a given stress with alloying. Kinks and subgrains were noted but were not studied in detail in this instance.

Acknowledgments

The authors wish to express their appreciation to the Aeronautical Research Laboratory, Wright Air Development Center, for support of this program; and to the Aluminum Co. of America for its support of a fellowship and for furnishing the alloys and chemistries.

References

[1] A. W. Mullendore and N. J. Grant: *AIME Trans.*, 1954, vol. 200, p. 973; Journal of Metals, September 1954.

[2] I. S. Servi and N. J. Grant: *AIME Trans.*, 1951, vol. 191, p. 909; Journal of Metals, October 1951.

[3] N. J. Grant and A. G. Bucklin: *ASM Trans.*, 1950, vol. 42, p. 720.

[4] A. T. Robinson, T. E. Tietz, and G. E. Dorn: *ASM Trans.*, 1952, vol. 44, p. 896.

[5] D. McLean and M. H. Farmer: *Journal* Inst. of Metals, 1954-1955, vol. 83, p. 1.

[6] H. G. Axon and W. Hume-Rothery: *Proceedings* Royal Soc., London, 1948, vol. 193A, p. 1.

[7] E. Orowan: *Nature*, 1941, vol. 147, p. 452.

[8] I. S. Servi and N. J. Grant: *AIME Trans.*, 1951, vol. 191, p. 917; Journal of Metals, October 1951.

[9] H. C. Chang and N. J. Grant: *AIME Trans.*, 1952, vol. 194, p. 619; Journal of Metals, June 1952.

[10] H. C. Chang and N. J. Grant: *AIME Trans.*, 1953, vol. 197, p. 395; Journal of Metals, February 1953.

Discussion of this paper sent (2 copies) to AIME by June 1, 1957 will appear in AIME *Transactions* Vol. 209, 1957, and in Journal of Metals, October 1957.

Technical Note

Stepped Austenitizing Treatment for 4340 Steel

by E. P. Klier, Volker Weiss, and George Sachs

IT has been shown that the isothermal transformation of austenite in a special steel can be modified by isothermal holding in the high subcritical transformation range.[1] Since this treatment potentially leads to increased hardenability, limited testing has been completed to determine if the stabilization effects observed with this treatment can be used to advantage in the heat-treating of 4340 steel. As an index of the effects of the several austenitizing treatments on the hardenability of the steel, Jominy-type hardenability tests were completed for specimens 2.5 in. in diameter and 8 in. long.

Since the steel studied is to be used at strength levels where notch sensitivity is of major concern, notch sensitivity after selected austenitizing treatments has been evaluated by notch tensile tests for several specimen sizes.

The steel composition and the austenitizing treatments are given in Table I. The test specimens are presented in Fig. 1. The hardenability data are given in Fig. 2 and the notch tensile properties are presented in Fig. 3.

The hardenability of the steel investigated when determined by use of the standard Jominy test specimen[2] was high and remained essentially unchanged for the different austenitizing treatments. For the larger test specimen, as has been shown by other investigations,[3,4] the characteristic hardenability indexes are changed and it becomes possible to isolate austenitizing treatments which promote maximum hardenability. The stepped austenitizing treatment promotes higher hardenability as is indicated in Fig. 2.

The evaluation of notch sensitivity for very high strength steels is best accomplished by means of the notch tensile test. The experimental conditions of the test, however, modify the notch strengths measured, and in the present experimentation an effort was made to achieve a limiting notch condition by fixing the notch root radius at 0.001 in. while the specimen diameter was allowed to increase from 0.3 to 1.1 in.* For this root radius the notch strength, i.e. the average fracture stress on the cross section under the notch, was measured at room temperature as indicated in Fig. 3 for the different specimens as the tempering temperature was raised from 400° to 1000°F.

The trend of the notch strength vs tempering temperature has been established earlier[5] for the 0.3-in.-diam specimen, and this trend differs from that for the larger specimens. At the highest tempering temperatures the 1.1-in.-diam specimens yield comparable results for the austenitizing treatments compared. However, as the tempering temperature is progressively lowered below 800°F, em-

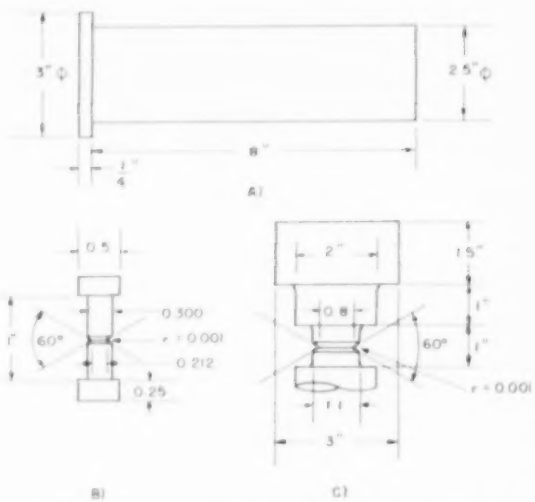

Fig. 1—Test specimens: a) hardenability specimen, b) 0.3-in.-diam notch tensile specimen, and c) 1.1-in.-diam notch tensile specimen.

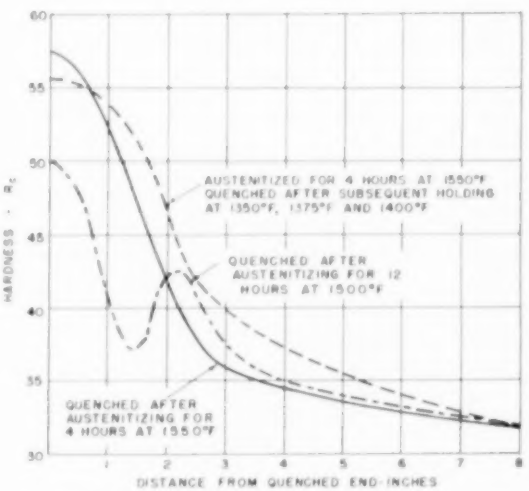
HARDNESS - Rc
DISTANCE FROM QUENCHED END-INCHES
AUSTENITIZED FOR 4 HOURS AT 1550°F QUENCHED AFTER SUBSEQUENT HOLDING AT 1350°F, 1375°F AND 1400°F
QUENCHED AFTER AUSTENITIZING FOR 12 HOURS AT 1500°F
QUENCHED AFTER AUSTENITIZING FOR 4 HOURS AT 1550°F

Fig. 2—Hardenability of 4340 steel after selected austenitizing schedules; end-quench test of 2.5-in.-diam x 8-in. long Jominy-type specimens.

* The section-size effect which modifies the notch test results will be treated in a later publication. It is important to note that as the test section is suitably increased both the tensile and notch tensile properties are markedly reduced.

E. P. KLIER, Member AIME, is Professor of Metallurgy, V. WEISS is Research Associate, and G. SACHS, Member AIME, is Associate Director of Research, Research Institute, Syracuse University, Syracuse, N. Y.

TN 383E. Manuscript, Dec. 30, 1955.

brittlement or notch sensitivity progressively increases. Further, in contrast to results obtained with the impact test, the notch strength for the large specimens does not reveal a *500°F embrittlement* range.

The notch sensitivity as determined with the 0.3-in. specimen of 4340 steel given the stepped austenitizing treatment has been discussed elsewhere.[5] This quantity as measured for the 1.1-in.-diam notch tensile test and given in Fig. 3, is taken to signify that reduced notch sensitivity is encountered in the 600° to 800°F tempering range for specimens given the stepped austenitizing treatment.

The stepped austenitizing treatment may, therefore, be of use in promoting deeper hardenability for a 4340 steel while at the same time giving reduced notch sensitivity in the high-strength range in which this steel is now being used.

Table I. Composition and Heat Treatments

Composition of 4340 Steel, Pct

C	Mn	P	S	Si	Cr	N	Mo
0.43	0.73	0.012	0.022	0.26	0.78	1.9	0.24

Heat Treatments

No.	Temperature, °F	Holding Time, Hr	Cooling Procedure*
1	1550	4†	O.Q. or J.Q.
2	1550	4†	F.C. to and hold for 1 hr at 1325°—O.Q.
3	1550	4	F.C. to and hold for 1 hr at 1350°—J.Q.
4	1550	4	F.C. to and hold for 1 hr at 1375°—J.Q.
5	1550	4	F.C. to and hold for 1 hr at 1400°—J.Q.
6	1500	12	J.Q.
7	1625	2	A.C.
	1525	2	O.Q.

* O.Q. refers to oil quench; A.C., air cool; F.C., furnace cool; and J.Q., Jominy quench.
† For the 0.300-in.-diam notch tensile specimens this holding time was 1 hr.

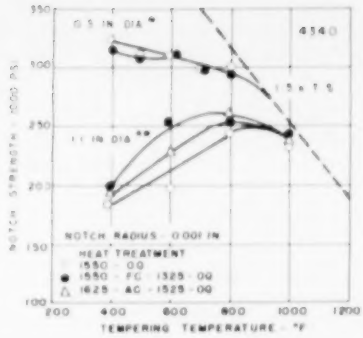
0.5 IN. DIA *
1.1 IN. DIA **
4340
1.5 x T.S.
NOTCH STRENGTH, 1000 PSI
NOTCH RADIUS = 0.001 IN.
HEAT TREATMENT
1550 - OQ
1550 - FC - 1325 - OQ
1625 - AC - 1525 - OQ
TEMPERING TEMPERATURE - °F

Fig. 3—Effect of heat treatment and section size on the notch strength of 4340 steel. Single asterisk refers to 1 hr austenitizing time; double asterisk, 4 hr austenitizing time.

Acknowledgments

The work reported was supported by the U. S. Navy Bureau of Aeronautics. The authors are indebted to the Bureau of Aeronautics for granting permission to publish results of this research and to N. E. Promisel, H. Hessing, and J. Maltz for their interest.

References

[1] E. P. Klier and V. Weiss: Discussion to R. F. Hehemann and A. R. Troiano, Stabilization of the Bainite Reaction, *AIME Trans.*, 1955, vol. 203, p. 707; JOURNAL OF METALS, May 1955.
[2] E. P. Klier, V. Weiss, and G. Sachs: Hardenability Studies on 4340 Steel, Syracuse University Research Institute, Final Report No. 1, Contract No. NOas 54-424-c to U. S. Navy, Bureau of Aeronautics, October 1954.
[3] C. M. Carman and D. F. Armiento: Effect of Specimen Size on the Jominy Hardenability, Frankford Arsenal Report No. R-1164, September 1954.
[4] J. Vajda and P. E. Busby: Effect of Composition on Transverse Properties of Slack-Quenched Steel, *ASM Trans.*, 1955, vol. 47, p. 408.
[5] A. R. Troiano and L. J. Klinger: Limitations of the End-Quench Hardenability Test, *ASM Trans.*, 1952, vol. 44, p. 775.
[6] G. Sachs, V. Weiss, and E. P. Klier: Effect of a Number of Heat Treating and Testing Variables on the Notch Strength of 4340 Steel, ASTM Preprint No. 71, 1956.

Central Region of the Mg-Zn Phase Diagram

The phase equilibria in the Mg-Zn system from 0 to 85 wt pct Zn and from 335° to 93°C have been redetermined. In this region four intermetallic phases, Mg_3Zn_{11}, MgZn, Mg_2Zn_3, and $MgZn_2$, exist. Below 325°C, the Mg_3Zn_{11} phase decomposes eutectoidally to magnesium solid solution + MgZn. The MgZn phase is stable over the temperature range from 335°C to 93°C; below 325°C, it is in equilibrium with the magnesium solid solution.

by J. B. Clark and F. N. Rhines

J. B. CLARK, Junior Member AIME, is associated with the Metallurgical Laboratories, Dow Chemical Co., Midland, Mich., and F. N. RHINES, Member AIME, is Aluminum Co. of America Professor of Light Metals, Dept. of Metallurgical Engineering, Carnegie Institute of Technology, Pittsburgh.

TP 4365E. Manuscript, Jan. 16, 1956. Cleveland Meeting, October 1956.

THE most recent phase diagram of the Mg-Zn system is that of Köster and Müller,[*] Fig. 1. Certain diffusion studies, that will be described in a future paper, led to the conclusion that this phase diagram is incorrect in indicating that the MgZn phase decomposes by a eutectoid reaction at 340°C, instead of persisting to low temperature. Accord-

ingly, that portion of the MgZn diagram lying between 0 and 85 wt pct Zn and between 93° and 335°C has been re-examined and a revised phase diagram is presented.

Preparation of Alloys

The alloy compositions prepared for this study are listed in Table I. These alloys were prepared by melting, singly, sublimed magnesium and high-purity zinc under a chloride flux in a graphite crucible. The magnesium was melted first and the zinc addition was stirred into the molten magnesium with a carbon rod until alloyed. The alloy melt was stirred vigorously at about 700°C for 15 min and chill cast into a rod form.

All the alloys were studied in the cast condition except the 20 and 35 wt pct Zn alloys which were extruded. For a given composition and heat treatment, the phases present in the cast and extruded condition were identical.

Heat Treatment

Samples of each of these alloys were homogenized by annealing first at 335°C for 10 days. Subsequently, samples of each alloy were annealed at 320°, 260°, 204°, 149°, and 93°C respectively, for periods up to 1000 hr, followed by a rapid air cooling, or an ice water quench. No difference was observed between the structures of water-quenched specimens and air-cooled specimens. In addition, some diffusion couples composed of a disk of pure magnesium welded to a disk of the MgZn phase were diffused at 335°C and were examined to verify the existence of the Mg_2Zn_3 phase field at 335°C. During these treatments the alloy samples were protected from deterioration in Pyrex vials containing an argon atmosphere. The heat treatments were carried out in an electric furnace which maintained the temperature within ±1.5°C. No surface attack or depletion of zinc or magnesium was observed metallographically.

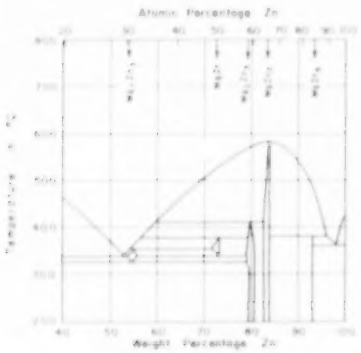

Fig. 1—Mg-Zn phase diagram according to Köster and Muller.[6]

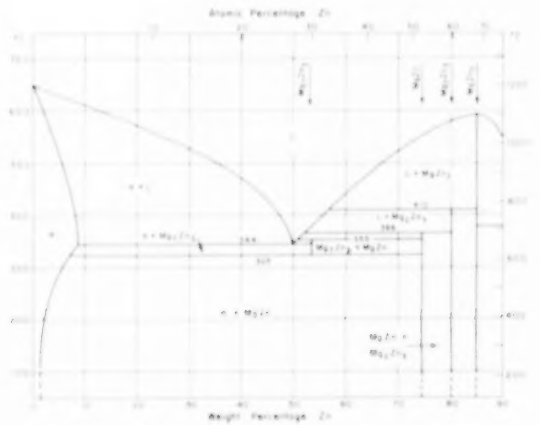

Fig. 2—Equilibria in the central region of the Mg-Zn phase diagram as determined by the authors.

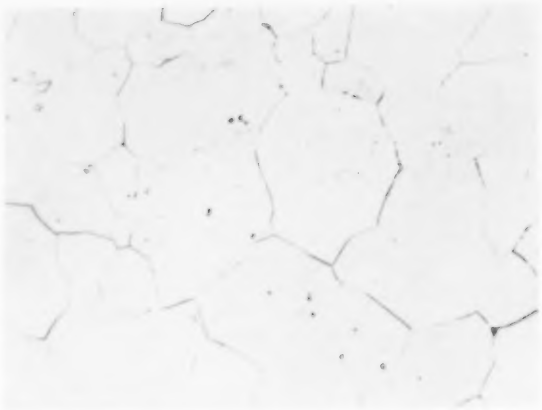

Fig. 3—74.5 wt pct Zn alloy after a 139-hr anneal at 335°C, followed by a water quench. Glycol etch. X500. Reduced approximately 20 pct for reproduction.

Table I. Alloy Compositions

Nominal Composition, Wt Pct Zn	Composition by Analysis, Wt Pct Zn
10	10.2
20	20.4
30	30.8
35	35.3
40	39.8
50	49.9
60	59.17
70	70.5
71	72.0
72	72.6
73	73.42
75	76.2
77	76.5
53 (Mg_2Zn_3)	52.9
74 (MgZn)	74.5
80 (Mg_2Zn_3)	79.0
84 ($MgZn_2$)	85.1

Method of Analysis

The heat-treated alloy specimens were analyzed by metallographic examination and powder X-ray diffraction. The alloys were polished and etched using standard procedures for magnesium. Table II lists the main etchants used in the study, and outlines the procedure used to distinguish metallographically between Mg_2Zn_3 and MgZn.

Powder X-ray diffraction was performed on a 143.2-mm-diam camera with nickel-filtered copper radiation. Powder patterns of homogenized alloys of MgZn, Mg_2Zn_{11} and Mg_2Zn_3 were prepared and used as standards for phase identification in other alloys. The *d*-values for these phases are listed in Table III.

Discussion of Results

Those regions of the revised diagram, shown in Fig. 2, that were not re-investigated by the authors, are taken from the literature. The liquidus curves, the temperatures of the eutectic and of the peritectics associated with the formation of MgZn and

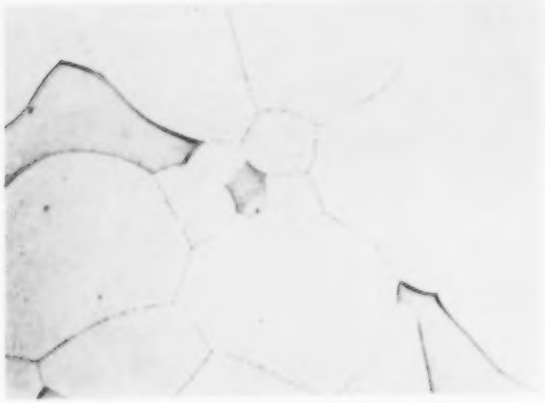

Fig. 4—73 wt pct Zn alloy after a 5-day anneal at 335°C. A small amount of Mg_2Zn_3 (darker gray) is shown in a matrix of MgZn. Glycol etch. X1500. Reduced approximately 10 pct for reproduction.

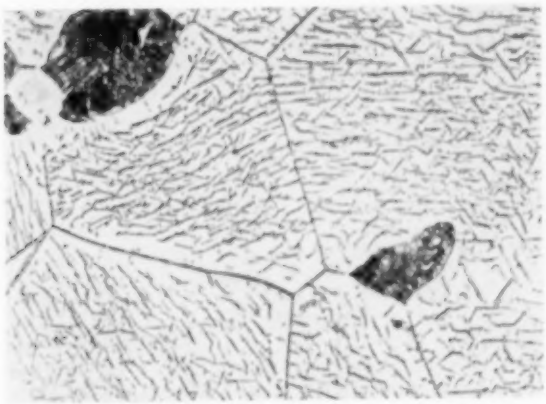

Fig. 5—73 wt pct Zn alloy with initially the structure shown in Fig. 4 after an 83-hr anneal at 149°C. The Mg_2Zn_3 has decomposed, leaving a fine dark eutectoid structure. Precipitation has occurred in the MgZn matrix. Glycol etch. X1500. Reduced approximately 15 pct for reproduction.

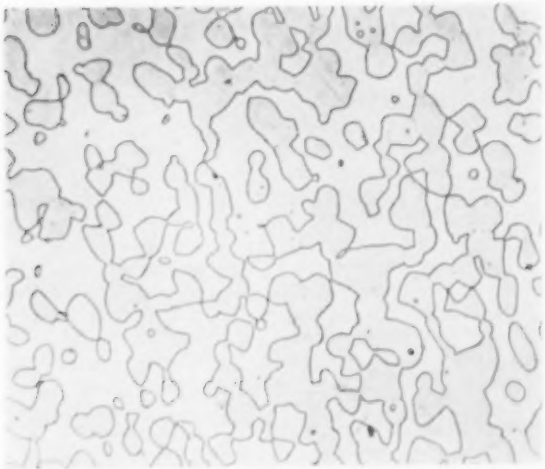

Fig. 6—35 wt pct Zn alloy after a 5-day anneal at 335°C. Magnesium solid solution (outlined, darker gray) is shown in a matrix of Mg_2Zn_3. Glycol etch. X500. Reduced approximately 5 pct for reproduction.

Fig. 7—53 wt pct Zn alloy after a 5-day anneal at 320°C. Nodules composed of lamellae of magnesium solid solution (dark) and MgZn (gray) are shown impinging in a matrix of Mg_2Zn_3. Glycol etch. X200. Reduced approximately 10 pct for reproduction.

Fig. 8—Cross section of a couple of magnesium and the MgZn phase after diffusion for 1000 hr at 335°C, showing the diffusion layer of Mg_2Zn_3. Glycol etch. X75. Reduced approximately 30 pct for reproduction.

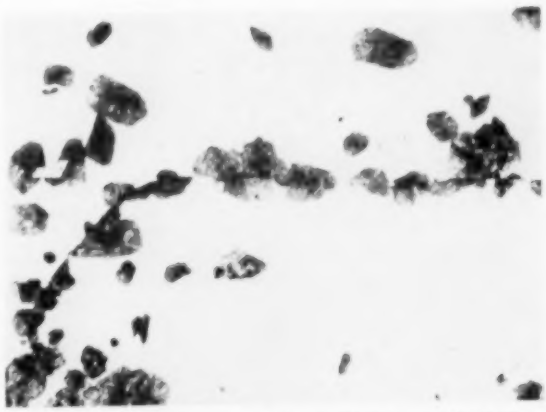

Fig. 9—Decomposition of the Mg_2Zn_3 phase along the interface of the Mg/MgZn diffusion couple. Unetched. X250. Reduced approximately 10 pct for reproduction.

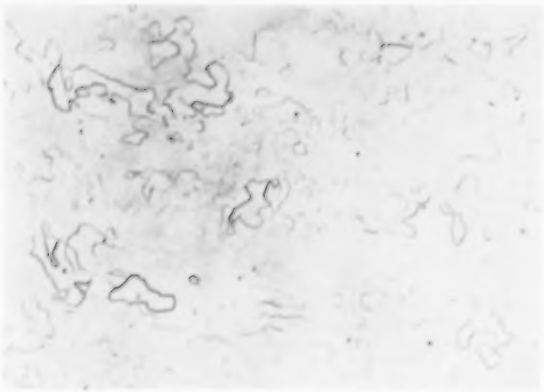

Fig. 10—80 wt pct Zn alloy after a 10 day anneal at 260°C. The structure consists entirely of the Mg_2Zn_{11} phase. Glycol etch. X500. Reduced approximately 10 pct for reproduction.

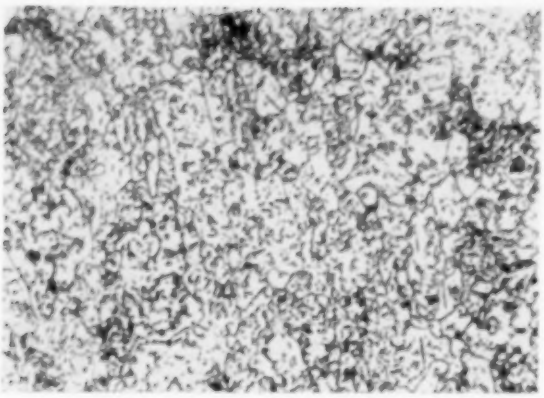

Fig. 11—80 wt pct Zn alloy after 24 hr anneal at 149°C. Glycol etch. X500. Enlarged approximately 30 pct for reproduction.

Mg_2Zn_{11}, and the short vertical line representing the limited existence of the phase Mg_2Zn_3 are taken from the data of Urazov and coworkers.[7] The magnesium-rich solidus is taken from the diagram reported by Adenstedt and Burns[5] and the corresponding solvus from the diagram reported by Hess.[6] The peritectic temperature of the Mg_2Zn_3 phase is taken from the diagram reported by Laves,[1] as are the vertical lines representing the range of existence of the phases MgZn, and Mg_2Zn_3.

It was found that the phase field of the MgZn compound lies at 74.5 wt pct Zn, as evidenced by the single-phase alloy shown in Fig. 3, rather than at 72.9 wt pct Zn, as predicted from the stoichiometry of the MgZn compound. That the phase MgZn is stable down to low temperature, as indicated in Fig. 2 by a vertical line at 74.5 wt pct Zn, extending from 366°C to the base of the diagram, has been demonstrated in several ways. All alloys up to and

Table II. Etchants and Procedure Used to Distinguish Between the MgZn and Mg_2Zn_3 Phases

Phase	Etchant Used*	Time of Specimen Immersion, Sec	Reaction
Mg_2Zn_3	3†	10	Roughened, pitted
MgZn	3†	10	Remained relatively unattacked
Mg_2Zn_3	1	2	Slightly attacked
MgZn	1	2	Severely attacked

* Etchants used were composed of: No. 1, 50 g Cr_2O_3, 4 g Na_2SO_4, and 1000 cu cm water; No. 2, 75 cu cm ethylene glycol, 24 cu cm distilled water, 1 cu cm concentrated HNO_3, and No. 3, 1.5 cu cm HCl, 2.5 cu cm HNO_3, 0.5 cu cm HF, and 95.5 cu cm water.
† Diluted 100 times with water.

including 60 wt pct Zn, which had been stabilized at 320°C and below, were found to be composed of the two phases, magnesium-rich solid solution and MgZn, and exclusively these. The phase identification was made positive by the analysis of the corresponding X-ray diffraction spectra.

Above 320°C, the 73 wt pct Zn alloy was found to be made up almost entirely of MgZn, with a small amount of Mg_2Zn_3 (see Fig. 4). Upon annealing at lower temperature, the MgZn phase remained untransformed except for the appearance of a Widmanstätten precipitate (Fig. 5). This precipitate has not yet been identified, although it seems most probable that it is magnesium-rich solid solution. In any case it is evident that MgZn is stable throughout the temperature range examined, and that it must have some, though perhaps a small, composition range of existence.

The studies by Köster[2] show clearly that the phase Mg_2Zn_3 is not stable at low temperature; rather it undergoes eutectoid decomposition at a temperature not far from that of the eutectic. This temperature has been found in the present research to lie between 335°C and 320°C, probably close to 325°C, as shown in Fig. 2. The evidence derives from both equilibrium and diffusion-couple experiments. All alloys containing up to 49.9 wt pct Zn, when annealed at 335°C, were found to be composed of magnesium-rich solid solution and Mg_2Zn_3. See, for example, Fig. 6. Those alloys from 59.17 to 73.42 wt pct Zn, stabilized at the same temperature, were composed of MgZn and Mg_2Zn_3, as has been shown in Fig. 4. Both series of alloys, upon slow cooling or stabilization at 320°C and below, undergo the eutectoid decomposition of Mg_2Zn_3 to a more or less well developed lamellar constituent of magnesium-rich solid solution and MgZn. This can be seen in a zinc-rich alloy, Fig. 5, and in the partly transformed alloy of Mg_2Zn_3 composition shown in Fig. 7. Accordingly, a eutectoid horizontal has been drawn in Fig. 2, at 325°C, connecting the phases: magnesium-rich solid solution at 8 wt pct Zn, Mg_2Zn_3 at 53 wt pct Zn, and MgZn at 74.5 wt pct Zn.

As a final check upon the correctness of these deductions, an alloy couple that was made up of a disk of pure magnesium and a disk of the 73.42 wt pct Zn alloy (MgZn) was diffused 1000 hr at 335°C. In accordance with expectation, a new layer corresponding to Mg_2Zn_3 developed between the magnesium and the MgZn layers (see Fig. 8).

Upon air cooling, over a period of 10 min, decomposition of the Mg_2Zn_3 progresses by the nucleation and growth of eutectoid nodules. A state of partial decomposition is illustrated in Fig. 9; preferential nucleation upon the oxide film of the original interface is to be noted. X-ray diffraction studies upon Mg_2Zn_3, transformed isothermally, indicate that the change proceeds in two steps. The MgZn first appears in an unstable transition form, which subsequently changes to the stable state. At temperatures below 204°C, the unstable form has been observed to persist in the diffraction pattern for more than 1000 hr. Table III includes a list of

Table III. Main Reflections of Phases Studied

Mg_2Zn_3		MgZn		$MgZn_2$		Metastable Structure of MgZn	
d, A	*I/I*$_1$	*d*, A	*I/I*$_1$	*d*, A	*I/I*$_1$	*d*, A	*I/I*$_1$,*
10.0	23	12.9	43	15.0	6	4.55	4
7.0	17	7.5	43	13.0	6	4.25	4
		6.4	8	10.9	6	2.33	4
5.8	23	6.0	25	6.3	4	2.23 to 2.18	15
5.1	17	5.6	20	5.4	4	2.08	3
		4.85	13	5.2	4	2.00	3
4.58	5	4.40	13	4.90	25	1.77	3
4.44	20	4.28	50	4.73	50	1.42	2
		4.07	13	4.69	50	1.24	2
4.10	7	3.80	3	4.38	38	1.112	2
3.78	23	3.62	8	4.23	75		
		3.57	8	4.09	25		
3.51	9	3.30	5	3.99	6		
3.37	1	3.20	3	3.65	4		
		3.11	5	3.58	4		
3.22	1.5	2.70	1	3.41	6		
3.17	1.5	2.65	1	2.61	6		
		2.58	1	2.50	63		
3.04	1	2.56	3	2.39	6		
2.75	7	2.47	31	2.36	75		
		2.44	8	2.35	75		
2.69	1.5	2.34	63	2.31	6		
2.64	3	2.31	63	2.29	6		
		2.25	100	2.25	75		
2.57	13	2.23	38	2.23	100		
2.53	3	2.20	3	2.20	100		
		2.16	43	2.16	75		
2.46	10	2.11	13	2.12	13		
2.43	23	2.06	13	2.11	25		
		2.05	50	2.07	25		
2.41	10	2.00	15	2.04	13		
2.33	23	1.98	3	2.03	19		
		1.95	5	1.98	6		
2.29	100	1.92	25	1.93	6		
2.22	8	1.87	5	1.915	6		
		1.83	20	1.904	6		
2.19	1.5	1.805	10	1.87	13		
2.17	1.5	1.78	5	1.835	13		
		1.74	8	1.80	6		
2.13	1.5	1.725	8	1.77	25		
2.07	3	1.70	3	1.73	6		
		1.675	3	1.70	6		
1.99	9	1.615	1	1.69	6		
1.95	1.5	1.60	3	1.67	6		
		1.55	18	1.499	6		
1.91	5	1.50	1	1.484	13		
1.895	3	1.450	15	1.459	13		
		1.424	75	1.450	13		
1.85	3	1.416	38	1.431	13		
1.78	1.5	1.393	50	1.429	38		
		1.373	8	1.405	6		
1.75	3	1.360	15	1.398	13		
1.70	1.5	1.343	43	1.390	13		
		1.320	3	1.374	6		
1.68	1.5	1.312	1	1.366	6		
1.64	1.5	1.304	15	1.350	63		
		1.261	23	1.335	6		
1.59	1.5	1.231	18	1.320	6		
1.480	3	1.229	10	1.305	38		
		1.217	0.5	1.300	6		
1.446	5	1.208	5	1.287	6		
1.426	13	1.199	23	1.280	6		
		1.184	8	1.276	6		
1.420	13	1.170	15	1.268	6		
1.404	5	1.151	3	1.258	13		
		1.139	3	1.245	38		
1.395	5	1.120	13	1.192	6		
1.370	4	1.104	10	1.181	13		
		1.095	18	1.170	6		
1.250	1.5			1.160	6		
1.214	4			1.153	6		
				1.140	6		
				1.135	6		
				1.121	25		
				1.110	6		
				1.096	13		
				1.080	6		
				1.071	6		
				1.060	6		
				1.050	6		

* The intensity values are relative to those of the matrix of magnesium solid solution.

the main Debye-Scherrer reflections identified with the transition state, in addition to those of the stable crystal forms.

A comparison of the microstructures of samples of the 80 wt pct Zn alloy stabilized at various lower temperatures after prior homogenization at 335°C shows a precipitation of a second phase with decreasing temperature; compare, for example, Figs. 10 and 11. Evidently there is a finite range of composition over which Mg_2Zn_3 can exist. In the absence of a measure of the width of this range, no attempt has been made to display it upon the phase diagram.

Summary

1) The phase equilibria in the Mg-Zn system from 0 to 85 wt pct Zn between 335° and 93°C have been redetermined.

2) The phase MgZn is stable at least over the temperature range 93° to 335°C.

3) The temperature of eutectoid decomposition of Mg_2Zn_3 is near 325°C.

4) The phases MgZn and Mg_2Zn_3 both have some, though probably small, composition ranges of existence at elevated temperature.

Acknowledgments

The authors wish to express their appreciation to the Titanium Alloys Mfg. Corp. and the Office of Naval Research for financial support of this research. This paper is a portion of a thesis by J. B. Clark

submitted in partial fulfilment of the requirements for the degree of Doctor of Philosophy in Metallurgical Engineering to the Graduate Faculty of the Carnegie Institute of Technology.

References

1. F. Laves: *Naturwissenschaften*, 1939, vol. 27, p. 454.
2. W. Köster: *Ztsch. für Metallkunde*, 1950, vol. 41, p. 37.
3. W. Köster and F. Müller: *Ztsch. für Metallkunde*, 1948, vol. 39, p. 352.
4. G. G. Urazov, N. A. Filin, and A. V. Shashin: *Metallurg*, 1940, vol. 15, No. 6, pp. 3-11.
5. H. Adenstedt and J. Burns: *ASM Trans.*, 1951, vol. 43, p. 873.
6. J. B. Hess: *ASM Handbook*, p. 1227. ASM, Cleveland, 1948.

Discussion of this paper sent (2 copies) to AIME by Mar. 1, 1957 will appear in AIME *Transactions* Vol. 209, 1957, and in JOURNAL OF METALS, October 1957.

Electron Diffraction Study of Flake Graphite Extracted from Molten Pig Iron

Single graphite flakes segregated from molten carbon or silicon-rich iron at 1200° to 1500°C were subjected to electron diffraction experiments. The results indicated that the well developed thick flakes are composed of one single crystal, while the thin almost colorless flakes consist of two or three single crystals oriented with the basal plane parallel to the flake surface and rotated at an angle of 15°, 18°, 22°, 25° or 28° about the C-axis. The stacking of the atomic layers in each single crystal indicates that they are α and β-type, or a more disordered structure, at each instant. Double diffraction evidence and additional electron microdiffraction observations showed that the thin single flake has an aggregate structure with two close-packed single crystals.

by Kichizo Niwa and Goro Shimaoka

IN the past, the crystalline states of graphite in cast iron have been studied by many investigators. Recently several authors[1-4] have published interesting information on the crystal texture of the individual graphite grain, especially spherulites in nodular cast iron.

In regard to the crystal structure of graphite, Lipson and Stokes[5] showed by powder X-ray analysis that most of the crystals contain about 14 pct rhombohedral structure (β-form) which differs from the hexagonal structure (α-form) in the sequence of layer stacking. Hoerni[6] confirmed the existence of the β-form in a single crystal with electron diffraction by Kossel-Moellenstedt's method. Furthermore, Hoerni and Weigle[7] found extra reflections in electron diffraction patterns, which are given by a unit cell twice as large as the usual one in the basal plane. Recently, Lukesh[8] observed graphite twinning and satellite reflections in his X-ray work and considered them as evidence for the existence of an orthorhombic superstructure.

Owen and Street[9] and Matuyama[10] studied the structures of graphite crystals in several types of cast iron, using the X-ray powder method, and they showed that the graphite crystal contains a certain amount of the β-form, an amount which varies with the sources of the cast iron used.

K. NIWA is Professor of Chemistry, Faculty of Science, Hokkaido University, Sapporo, Japan, and Visiting Professor, Massachusetts Institute of Technology, Cambridge, Mass. G. SHIMAOKA is Research Assistant, Hokkaido University.

TP 4392E. Manuscript, Aug. 24, 1955. New Orleans Meeting, February 1957.

The present study was made in order to secure structural information on graphitization in cast iron. Electron diffraction studies on the structure of single graphite flakes segregated from molten carbon or silicon-rich iron at 1200° to 1500°C are reported.

Experimental

Honkeiko pig iron (4.05 pct C, 1.59 pct Si, and 0.65 pct Mn) was used as the solvent of carbon or silicon. The pig iron was melted in an open furnace and a small quantity of metallic silicon was added to the melt at 1300°C. The melt was heated to 1500°C, and then retort black carbon or metallic silicon was added little by little. The components added to the bath contained approximately 5.0 pct C and 2.0 pct Si in the carbon-rich material, and 3.8 pct C and 5.4 pct Si in the silicon-rich iron. These two types were held at 1500°C and then cooled without graphitizing by cutting the heat sup-

Table I. Classification of Segregated Graphite Specimens

Specimen*	Temperature, °C
C 1	1480 to 1310
C 2	1310 to 1240
C 3†	1240 to 1220
Si 1	1500 to 1290
Si 2	1290 to 1220
Si 3†	1220 to 1200

* Specimens C 1, C 2, and C 3 were extracted from carbon-rich iron; Si 1, Si 2, and Si 3 were extracted from silicon-rich iron.
† The residue in the crucible after casting.

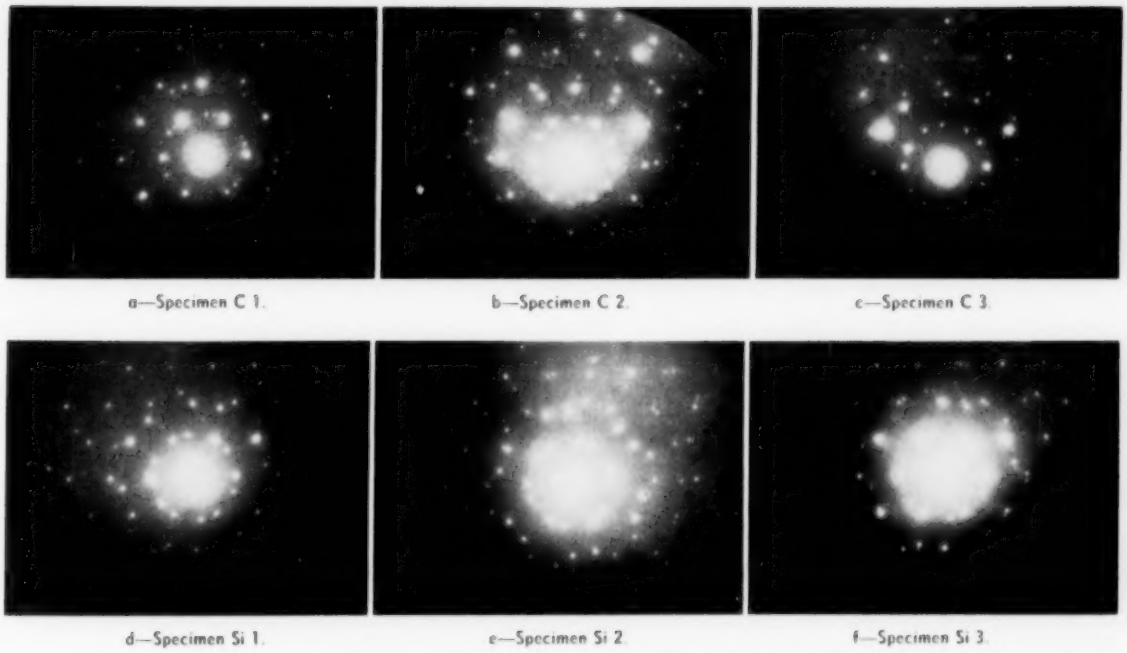

a—Specimen C 1. b—Specimen C 2. c—Specimen C 3.

d—Specimen Si 1. e—Specimen Si 2. f—Specimen Si 3.

Fig. 1—Transmission patterns of thin single graphite flakes. $L\lambda$ = 30 cm. Specimens C 1, C 2, and C 3, and Si 1, Si 2, and Si 3 were extracted from carbon and silicon-rich iron, respectively.

ply from the furnace. As the temperature fell, graphite precipitates came to the surface of the molten iron at successive intervals. Graphite specimens were segregated by blowing air against the surface in the temperature ranges shown in Table I.

Various sizes and thicknesses of the single flake graphite were obtained. The thin almost colorless flakes were suitable for electron diffraction transmission study. Relatively large crystals were studied both by cleavage and powder method. For the purpose of cleavage, chisels ground from sharp points of steel needles were used. Powder specimens were prepared by drying, on 200-mesh brass gauze, a suspension of graphite flakes that had been ground down in an agate-mortar.

Most electron diffraction experiments were carried out by the transmission method. The accelerating potential was about 45 kv, the specimen-to-plate distance, L, was approximately 30 or 50 cm, and the $L\lambda$ value was calculated from the diffraction pattern of an evaporated film of pure silver.

Table II. Electron Diffraction Data from Fig. 1

Specimen*	d_{0002}, A†	ψ_{0002}, Degrees†
C 1	2.13	15, 25
C 2	2.13	28
C 3	2.12	25
Si 1	2.12	22
Si 2	2.12	18
Si 3	2.12	22

* Specimens C 1, C 2, and C 3 were extracted from carbon-rich iron; Si 1, Si 2, and Si 3 were extracted from silicon-rich iron.
† d is interplanar spacing; ψ is the rotation angle between two N-patterns.

Results

Thin Single Graphite Flake—Typical diffraction patterns from thin single graphite flakes normal to the electron beam are shown in Fig. 1. Each pattern consists of two or three sets of N-pattern, arrayed as regular triangles rotating at an angle about the center. The interplanar spacings, d, and the rotation angles, ϕ, obtained with these patterns are given in Table II.

The structure assigned to graphite by X-ray is hexagonal in the α-form with the dimensions: a = 2.456A and c = 6.696A;[1] the structure was hexagonal in β-form with the dimensions: a = 2.456A and c = 3/2 × 6.696 = 10.044A.[2] The unit of the reciprocal lattice corresponds in the α-form to:

$$\begin{cases} 1/a^* = a\cos 30^\circ = 2.127\text{A} = d_{10\bar{1}0} \\ 1/c^* = c = 6.696\text{A} = d_{0002} \end{cases}$$

and in the β-form to:

$$\begin{cases} 1/a^* = 2.127\text{A} = d_{10\bar{1}0} \\ 1/c^* = 10.044\text{A} = d_{0002} \end{cases}$$

Observed spacings $d_{obs.}$ = 2.12 to 2.13A agree with $d_{10\bar{1}0}$ in both the α and β-structure. It is evident therefore that each specimen consists of two or three single crystals oriented with the (0001) planes parallel to the flake surface, and rotated at an angle of ϕ about the [0001] axis.

However, if the patterns in Fig. 1 are examined more closely, the following will be seen: For example, in the pattern of Fig. 1b, a number of faint spots occur all over the pattern. In Fig. 1f each spot is broken up into several minute bits. It seems that there is some relation either to impurities or to irregularities in the graphite structure. These points will be discussed later.

Diffraction patterns from the flakes inclined obliquely to the beam gave information about the layer arrangement in the graphite lattice and such an oblique photograph is shown in Fig. 2. The spacings and the intensities corresponding to the diffraction

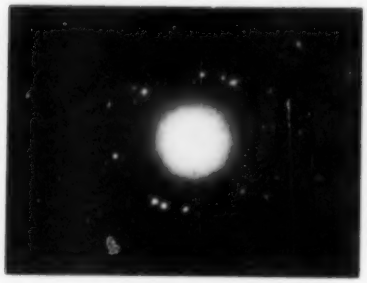

Fig. 2—Oblique photograph of thin single graphite flake. The film was inclined at 45° to the beam. l = 50 cm.

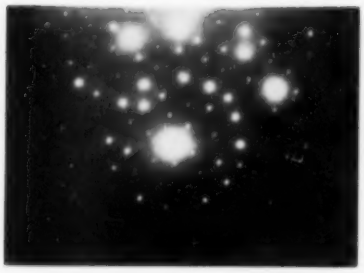

Fig. 3a—Double diffraction pattern of thin single graphite flake. l = 50 cm.

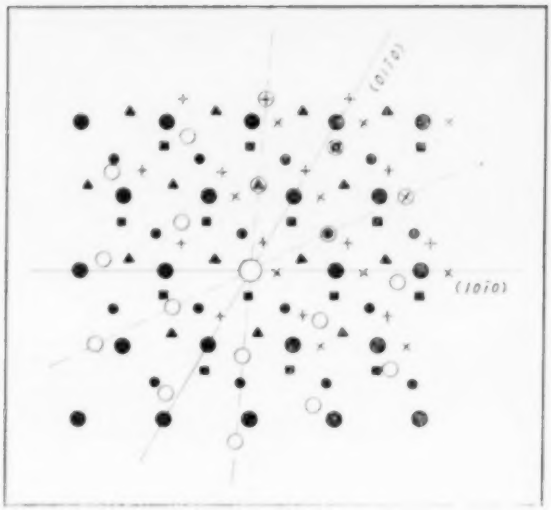

Fig. 3b—Diagrammatic representation of double diffraction. Large circles represent spots given by primary scattering and small symbols indicate spots arising from secondary elastic scattering.

spots are given in Table III. By comparing the present data with calculated spacings from the α-structure, it was observed that the pattern contained several *extra* spots which could not be explained on the basis of simple α-structure. Among these spots, those indexed (10$\bar{1}$2/3), (10$\bar{1}$3/5), and (10$\bar{1}$4/5) must be due to β-structure, but unassigned and unaccountable spots, e.g., (10$\bar{1}$5/4) or (10$\bar{1}$4/3) and (10$\bar{1}$3/4), are present. The oblique photographs

Table III. Electron Diffraction Data from Fig. 2

Observed		α-Structure		β-Structure
Pair of Spots, Intensity*	d, A	$hkil$	d_{hkil}, A	$hkil$
1 (vvs)	3.85	—	—	—
1 (s)	2.124	1010	2.127	1010
1 (ms)	2.088	(10$\bar{1}$2/3)	2.081	1011
1 (m)	2.067	(10$\bar{1}$3/4)	2.069	—
		(10$\bar{1}$4/5)	2.062	—
2 (s)	2.032	1011	2.027	—
1 (m)	1.986	(10$\bar{1}$5/4)	1.977	—
1 (ms)	1.961	(10$\bar{1}$4/3)	1.959	1012
$\frac{1}{2}$ (ms), $\frac{1}{2}$ (ms)	1.948	—	—	—
2 (m)	1.791	1012	1.795	1013
$\frac{1}{2}$ (m)	1.748	—	—	—
$\frac{1}{2}$ (vw)	1.627	(10$\bar{1}$8/3)	1.623	1014
$\frac{1}{2}$ (s)	1.537	1013	1.540	—
1 (m)	1.313	1014	1.315	1016
3 (ms)	1.227	1120	1.228	1120
1 (vw)	1.209	11$\bar{2}$1	1.208	—
8 (ms)	1.154	1122	1.153	1123
$\frac{1}{2}$ (s)	1.081	1123	1.076	—
1 (m)	1.058	2020	1.063	2020
2 (m)	1.014	2022	1.013	2023

* Relative intensity abbreviations represent: (vs), strong; (ms), medium strong; (m), medium; (w), weak; and (vw), very weak.
† Forbidden reflection of structure factor.

obtained with the other five specimens also indicated the existence of similar *extra* spots.

Thin curved graphite flakes gave more complicated patterns which contained many extra diffraction patterns that did not conform to the α or β-structures. Furthermore it appeared that a complete analysis of these extra spots was almost impossible. Except for weak irregular spots, however, strongly paired spots symmetrically disposed about the incident spot belonged mostly to the α and β-structures.

An abnormal pattern obtained with the flake normal to the beam is shown in Fig. 3a and the pattern consists of a normal graphite pattern with a rotation angle of $\phi = 25°$, and many extra spots asymmetrically disposed about the central spot. These extra spots cannot be ascribed to impurities but might be explained as follows:

When the electron beam passes through the composite film of two single crystals, the primary beam will reveal the spot pattern of the first crystal. The transmitted beam and the diffracted beams nearly parallel to the primary beam will reveal the other spot patterns formed by the underlying crystal. In electron diffraction, the Ewald sphere of reflection is so large that the sphere may be considered as a plane normal to the incident beam. If the two single crystals are tightly bound in a thin film, a resemblance to the actual pattern can be expected from a pattern constructed by translating the origin of one reciprocal lattice, on the Ewald sphere, to each point of the other reciprocal lattice. A schematic diagram of a pattern constructed around a rotation axis of $\phi = 25°$ is given in Fig. 3b and is in good agreement with the observed pattern, Fig. 3a.

Thus, it was concluded that the extra spots were the result of double diffraction, formed by two single crystals of a close-packed aggregate. Accordingly, a similar effect in case of the specimens with other ϕ values would also be expected.

Further electron microdiffraction studies were made to investigate the binding state of two single crystals forming a single flake. Electron microscope shadow images and patterns of very small areas of the specimen, limited with masking plate, were observed without changing the specimen position. It was found that the flake specimen consisted of small portions of varying thicknesses and types of diffrac-

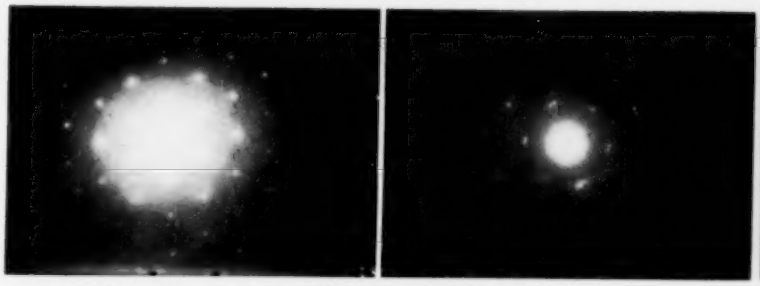

Fig. 4—Diffraction patterns of slightly thick single graphite flakes. l = 30 cm; a—one single crystal, and b—aggregate of several single crystals.

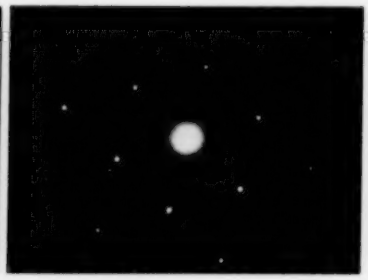

Fig. 5—N-pattern of thin flake cleaved from a relatively large graphite flake. l = 50 cm.

tion patterns, e.g., Kikuchi lines, Laue zones, N-patterns, and mixtures of these. It was also observed that jagged portions near the edge of the flake usually gave complicated spot patterns, while even continuously flat portions in the flake often gave the double sets of N-patterns, shown in Fig. 1. These results may be taken to indicate that thin single graphite flakes consist of two single crystals of a close-packed aggregate. Therefore, it is suggested that such a binding state has a close relationship to growth of graphite crystals in molten pig iron.

Slightly Thick Single Graphite Flakes—As the thickness of the specimen increases, the contrast between the diffraction pattern and the continuous background, given by inelastic scattering, becomes indistinct, in such a way that clear patterns can not be observed. However, several types of diffraction patterns (e.g., one or two sets of N-patterns, faint Kikuchi lines and bands, and background without diffraction pattern) were observed, to the extent that the electron beam penetrated the specimen. Some specimens gave nearly complete N-patterns with a single crystal arrangement, Fig. 4a, but many of them showed an aggregate of several single crystals with a common [0001] axis rotated within a few degrees of 2° to 3° about the [0001] axis, Fig. 4b. Although quantitative measurements of the thickness of these specimens were not performed, it would appear that the thicker films would have a structure that is closer to that of the single type.

Thick Single Graphite Flakes—If cleavage proceeded smoothly, thin films cut from well developed, relatively large graphite flakes showed a complete N-pattern, Fig. 5, and the slightly thicker films a Kikuchi line pattern. On the other hand, films damaged during cleavage and thick graphite flake powder specimens showed diffraction rings—indicating a mixture of α and β-structure—and several extra diffractions, such as $(10\bar{1}^{3}/_{4})$ or $(10\bar{1}^{1}/_{2})$ and $(10\bar{1}^{1}/_{4})$.

From these results, it may be concluded that the well developed relatively large flakes are composed of one single crystal in which the stacking sequence of each atomic layer is not completely regular.

In addition to those flake types already described, there were some cases where an entirely different powder pattern was observed. This pattern consisted of rather diffuse continuous rings next to the spot-bearing graphite rings, indicating that the extra rings might be due to impurities. The origin of these impurities will be discussed elsewhere.

Discussion

Lipson and Stokes[5] showed that the structure of β-graphite consists of a repeating unit of three hexagonal layers—$a\ b\ c, a\ b\ c\ \ldots$, Fig. 6—and has a unit cell* in which the c-axis is 3/2 times as long as that for α-graphite, with a periodic repetition of $a\ b, a\ b, a\ b\ \ldots$. This structure explains why the occurrence of the reflections of l-indices are multiples of 2/3. However, if it is assumed that the α and β-structure coexist in one crystal, various relations may be considered between these two phases—$a\ b, a\ b, a\ b\ c, a\ b\ c\ \ldots$; $a\ b, a\ b, a\ b\ c, b\ c, b\ c\ \ldots$; $a\ b, a\ b, a\ b\ c, a\ c, a\ c\ \ldots$; etc. Such disorder in atomic layer stacking may result in the formation of a larger unit cell in which the c-axis is $n/2$ times as long as the α-graphite cell, where n is an integer. In the present experiment, in addition to the reflections of l-indices being multiples of 2/3, fairly strong reflections of the other fractional l-values—such as l = 4/5 (= 2 × 2/5) or 3/4 (= 3 × 1/4) and 5/4 (= 5 × 1/4)—were observed, Table III. Finch and Wilman[10] observed similar reflections of fractional l-indices in electron diffraction of Ceylon graphite (using thin films about 20A thick) and called them secondary reflections, equivalent to fractional orders of normal Laue indices, which they thought was the result of the thinness of the crystal. However, the specimens used in the present experiment were confirmed by electron microscopic method to be much thicker. Furthermore, since similar reflections were observed in the powder pattern, which gave little evidence of abnormal diffraction, it may be concluded that the single graphite flakes consist of α and β-type or a more disordered structure.

* This structure is really rhombohedral with a = 3.635A and α = 39.49°.

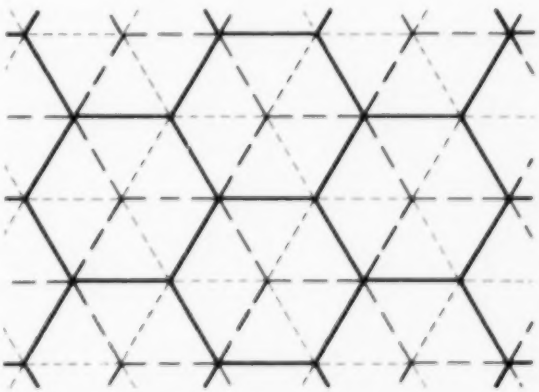

Fig. 6—Arrangement of atomic layers in β-graphite. Lines represent: solid, layer a; medium dashed, layer b; and light dashed, layer c.

On the other hand, the reflection of (1/2 0 0) or (1/2 1/2 0) indices, reported by Hoerni and Weigle,[7] was not observed when irregularities in the hexagonal basal plane existed. Some of the specimens gave the satellite reflections that were observed by Lukesh,[8] and some showed an aggregate structure in which the basal planes rotated at small angles about the c-axis, Figs. 1f and 4b. Furthermore, from the results already described, considerable disorder in the basal plane may be expected. Further study of these points is desirable.

Summary

The structure of single graphite flakes extracted from molten carbon or silicon-rich iron at 1200° to 1500°C has been studied by the electron diffraction transmission.

It has been found that well developed relatively large flakes are composed of one single crystal. Thin almost colorless flakes consist of two or three single crystals oriented with the (0001) planes parallel to the flake surface and rotated at an angle of 15°, 18°, 22°, 25°, or 28° about the [0001] axis.

The arrangement of the atomic layers in each single crystal is of the α and β-types or of a more disordered structure in each instant.

In the diffraction pattern of thin single graphite flakes, new spots have been discovered which can be regarded as *forbidden* reflections resulting from the structure. It has been explained (and confirmed by electron microdiffraction study) that these new spots are the result of double diffraction which occurs in two single crystals of a close-packed aggregate.

Acknowledgments

The authors wish to express their gratitude to Shizuya Maekawa of The Muroran Works, Japan Steel Works Ltd., who provided the facilities for preparation of the graphite specimens used. The authors also thank Taro Takeyama, Faculty of Technology, Hokkaido University, for his assistance in the electron microdiffraction work.

References

[1] H. Grober and H. Haneman: Archiv für Eisenhüttenwesen, 1937, vol. 11, p. 199.

[2] H. Morrogh and W. J. Williams: *Journal*, Iron and Steel Inst., 1947, vol. 155, p. 321; 1948, vol. 158, p. 306.

[3] H. E. Stauss, F. W. von Batchelder, and E. I. Salkovitz: *AIME Trans.*, 1951, vol. 191, p. 249; JOURNAL OF METALS, March 1951.

[4] R. Kusakawa, H. Tsuchikura, and T. Okumoto: *Journal*, Japanese Inst. of Metals, 1951, vol. A-15, p. 424.

[5] H. Lipson and A. R. Stokes: *Proceedings*, Royal Soc., 1942, vol. A181, p. 101.

[6] J. Hoerni: *Nature*, 1949, vol. 164, p. 1045.

[7] J. Hoerni and J. Weigle: *Nature*, 1949, vol. 164, p. 1088.

[8] J. S. Lukesh: *Physical Review*, 1950, vol. 80, p. 226.

[9] W. S. Owen and B. G. Street: *Journal*, Iron and Steel Inst., 1951, vol. 167, p. 113.

[10] E. Matuyama: *Journal*, Japanese Inst. of Metals, 1952, vol. 16, p. 198; 1953, vol. 17, pp. 17, 557.

[11] W. Trzebiatowski: *Roczn. Chem.*, 1937, vol. 17, p. 73; *Chemical Abstracts*, vol. 31, p. 4177.

[12] G. I. Finch and H. Wilman: *Proceedings*, Royal Soc., 1936, vol. A155, p. 345.

Discussion of this paper sent (2 copies) to AIME by June 1, 1957 will appear in AIME *Transactions* Vol. 209, 1957, and in JOURNAL OF METALS, October 1957.

Some Estimates of the Thermal Stability Of Dispersion-Hardened Alloys

The mechanism of overaging is explained, and the time is estimated in which structural changes should occur in alloys hardened with Ni_3Al, Al_2O_3, Fe_3C, TiC, and TiN. It is found that particles of the intermetallic, carbide, or nitride of 200Å radius would dissolve at 1340°F in a nickel-base matrix within minutes or hours while the size of the oxide particle would not change appreciably within several hundred years.

by A. W. Cochardt

A. W. COCHARDT, Junior Member AIME, is Advisory Engineer, Westinghouse Electric Corp., East Pittsburgh, Pa.

TP 4415E. Manuscript, July 16, 1956. New Orleans Meeting, February 1957.

MOST of the current high temperature materials are precipitation-hardened alloys. These alloys are usually soft when quenched from a solution heat-treatment temperature, but become harder

Table I. Results of the Calculation

Hardener	Matrix	Temperature, °K	Element	$-\log D$	$-\log u_\infty$	$\log t$
Ni_3Al	Ni-4 pct Al	1000	Al	10	2	2
Al_2O_3	Ni-4 pct Al	1000	O	7	14	11
Al_2O_3	Ni-8 pct Al	1500	O	5	11	6
Fe_3C	Fe-0.025 pct C	995	C	6	4	0
TiC	Ni-0.1 pct C	1000	C	8	4	2
TiN	Ni	1000	N	7	7	4

when aged at a temperature at which precipitation takes place. If the aging treatment is continued further, the distance between the precipitated particles increases above a critical value and the alloy becomes soft again, a process which is called over-aging.

Mott and Nabarro[1] have explained this phenomenon on the basis of dislocation theory. The alloys are relatively soft in the quenched and in the over-aged condition, because the distance between the dispersed particles is either too small or too large to impede the dislocation motion effectively. However, if the distance between the particles is of the order of 50 atomic spacings, the alloy should be relatively hard according to this theory, since moving dislocations are then most effectively stopped by the precipitate.

The service temperatures of existing precipitation-hardened high temperature alloys are often in the range where over-aging and structural changes can take place. As a result, the strength of such alloys may be initially high, but often decreases rather rapidly at longer periods of time. This is probably one of the reasons for the relatively short high temperature life of such alloys. Thus, the question of the thermal stability of dispersion-hardened alloys is of great practical importance. It is the object of the present paper to describe the factors that govern this process. Also, an attempt is made to estimate the time in which over-aging should occur with some of the most common hardeners of existing nickel and iron-base high temperature alloys and with Al_2O_3 as a hardener.

Mechanism of Over-Aging

To explain the mechanism of over-aging, a precipitate of the intermetallic compound Ni_3Al, which is the principal hardener[2] in such alloys as Inconel X 550, Inconel 700, and Superior Waspaloy, will be used as an example. When the alloy is aged to maximum hardness, the distance between the dispersed particles is probably of the order of 50 atomic spacings and the diameter of the particle, therefore, probably of the order of 25 atomic spacings, since the hardener content is generally of the order of a few per cent by volume. A certain fraction of each particle dissociates into nickel and aluminum atoms which dissolve in the nickel-base matrix. Since the matrix solubility for aluminum increases with decreasing Ni_3Al particle size, there is a concentration gradient between smaller and larger particles. As a result, aluminum atoms diffuse through the matrix from a small particle to a larger one and combine with the larger particle provided the temperature is high so that diffusion can occur readily. In this manner the smaller Ni_3Al particles slowly dissolve while larger particles grow, and the alloy finally over-ages. It is assumed that the rate controlling process is the diffusion of the element (in this case aluminum) which has the lowest diffusivity.

The time required for solution of the smaller particle can be estimated in the following way. Let a in Fig. 1 be the radius of a small, spherical particle of initial radius a_o; c, the radius of a larger one, of initial radius c_o; and b, the distance from the center of the small particle to the surface of the larger particle. According to the Thomson-Freundlich relation,[3] the concentration u of the diffusing element at a is then

$$\ln \frac{u(a)}{u_\infty} = \frac{\alpha}{a} \qquad [1]$$

in which u_∞ is the concentration of the diffusing element in equilibrium with a particle of infinite radius and

$$\alpha = \frac{2M\gamma}{RT\rho} \qquad [2]$$

The γ is the interfacial energy per unit area between the particle and the matrix; M is the molecular weight and ρ, the density of the particle; R, the gas constant; and T, the absolute temperature. Similarly, the concentration $u(b)$ at b is

$$\ln \frac{u(b)}{u_\infty} = \frac{\alpha}{c} \qquad [3]$$

Since atoms should generally diffuse radially from a small particle to larger ones that surround it, we shall use the spherical diffusion equation

$$\frac{\partial u}{\partial t} = D\left(\frac{\partial^2 u}{\partial r^2} + \frac{2}{r}\frac{\partial u}{\partial r}\right)$$

rather than the linear one, although the order of magnitude of the results is the same in both cases. D is the diffusion coefficient; r, the distance from the center of the small particle, Fig. 1; and t, the time.

The total time t, in seconds, in which a small particle dissolves, is usually large compared to the diffusion times b^2/D. We can, therefore, use the steady state solution of the diffusion equation.

$$u(r) = A + \frac{B}{r}$$

where the constants A and B are determined from the boundary conditions, Eqs. 1 and 3.

$$A = \frac{b\,u(b) - a\,u(a)}{b - a}$$

$$B = \frac{u(a) - u(b)}{b - a}\,a\,b\,.$$

The u-r relationship is indicated in Fig 1 on the assumption that the matrix concentration of the

diffusing element near the larger particles is nearly equal to the average matrix concentration.

The amount of material that is transported through the surface $4\pi a^2$ per sec is $4\pi a^2 D \frac{\partial u}{\partial r}$ for $r = a$. This amount must be equal to $-\rho 4\pi a^2 \frac{da}{dt}$, which is the amount of material that has disappeared from the small particle in that time. This then leads to

$$\frac{da}{dt} = -\frac{D}{\rho}\frac{b}{a}\left(\frac{u_a - u_b}{b - a}\right). \qquad [4]$$

In order to simplify the integration of this differential equation, we shall approximate the Thomson-Freundlich relation, Eqs. 1 and 3, for the range of interest $a < a < a_0$ by the functions

$$u'(a) = u_\infty\left(1 + \frac{a'}{a}\right)$$

$$u'(b) = u_\infty\left(1 + \frac{a'}{c}\right)$$

where we define a' through the relation

$$u'(a) = u(a)$$

which leads to $a' = (e-1)\,a$. Functions u and u' differ by not more than 13 pct in the range of interest $a < a < a_0$.

By replacing in Eq. 4 the two u functions by the two u' functions, by substituting Eq. 2 for a, and by integrating Eq. 4 from $a = a_0$ to $a = 0$, we find the total time t in which the small particle dissolves

$$t = \frac{\rho' RT a_0^3}{3.6 M \gamma D u_\infty} f. \qquad [5]$$

The f is a function which depends on the relative initial particle size $c^* = \frac{c_0}{a_0}$ and the relative diffusion distance $b^* = \frac{b}{a_0}$

$$f = \frac{c^*}{b^*}\left[\frac{1}{3} + (b^* - c^*)\left(c^{*2}\ln\frac{c^*}{c^*-1} - c^* - \frac{1}{2}\right)\right].$$

The f is of the order of one for c^* larger than about 1.01 and for hardener concentrations of a few volume percent.

Discussion of Results

The actual over-aging process is much more complicated than the simple case that was considered. Particles which have first grown at the expense of smaller particles may themselves later disappear. The actual times in which particles grow until they can be resolved with the light microscope will be longer than the time t, Eq. 5, since the actual time will be a sum of such expressions. Nevertheless, the time t is a measure of the thermal stability of an alloy. If t were infinite, the structure of the alloy would not change; whereas if t were small, the particles would grow rapidly.

It is noticed from Eq. 5 that the time required for solution of a particle depends very markedly on its initial size. It is found, after substituting values for all the constants, that Ni_3Al particles with radii of the order of 50A will probably be dissolved quite rapidly, while it takes a much longer time to dissolve a particle of the order of a few hundred A. The average particle size will, therefore, increase quite rapidly during the first stages of aging and at a much slower rate whenever the average particle size reaches a value of $a_0 >> a$.

Table I lists some of the hardeners of current high temperature alloys plus aluminum oxide as a hardener. The time, in seconds, in which a particle of $a_0 = 200$A dissolves when surrounded by particles of $c_0 = 220$A at a distance of about 1000A (2 pct hardener by volume) has been estimated for all these hardeners. The interfacial energy γ between the particle and the matrix is in all cases assumed to be 710 erg per sq cm, a value which has been determined for cementite in α-iron.[5] The error introduced by this assumption is not large because the interfacial energy values for most substances probably lie between 300 and 1500 erg per sq cm. The diffusion coefficients D, in units of sq cm per sec for the element that controls the rate of the process, are estimated in those cases where they have not been reported.[4]

Probably the most important factor in Eq. 5 is the solubility u_∞. The values of u_∞ for Ni_3Al and Fe_3C were taken from the phase diagrams. In the other cases, they were derived from the free energies of formation of the compounds, which have been reported;[7] and from values for the free energy of solution, which were estimated. The procedure used for Al_2O_3 at 1000°K is explained in detail in the Appendix.

It is seen from the log t-values in Table I that cementite is the least stable hardener of those listed. Ni_3Al, TiC, and TiN are more stable. However, particles of these compounds, under the stated assumptions, would dissolve in a matter of minutes or hours, while an Al_2O_3 particle of the same size would last more than a thousand years. It is further noticed in Table I that the alloy hardened with Al_2O_3 is even more stable at 1500°K (2240°F) than the other alloys at 1000°K (1340°F). This difference in stability is due to the low solubility of oxygen in the matrix in equilibrium with the oxide, and the low solubility in turn is mainly due to the much higher free energy of formation of the oxide compared to that of Ni_3Al, TiC, and TiN. Generally, alloys hardened with a stable oxide are more stable at high temperature than alloys hardened with intermetallics, carbides, and nitrides, since the free energy of formation of a stable oxide is generally much higher than the free energy of formation of the most stable intermetallics, carbides, and nitrides. However, some practical difficulties have to be overcome before oxide hardened nickel base alloys can be prepared.

Appendix

The solubility of oxygen u_∞ in a Ni-4 pct Al matrix at 1000°K in equilibrium with Al_2O_3 is derived

from the standard free energy change ΔF_1° of the reaction

$$\frac{2}{3}\,Al_2O_3 = \frac{4}{3}\,\underline{Al} + 2\underline{O} \qquad [6]$$

As is ordinarily done when writing such reactions, the symbols of elements in solution are underlined, and the standard state of the solute is taken as 1 wt pct.

The ΔF_1° can be derived from the free energy ΔF_2° of the reaction

$$\frac{2}{3}\,Al_2O_3 = \frac{4}{3}\,Al + O_2 \qquad [7]$$

which has been reported[4] to be $\Delta F_2^\circ = 220$ kcal at 1000°K and from the free energies of solutions of aluminum and oxygen in nickel. The free energy ΔF_3° of the reaction

$$\frac{4}{3}\,Ni_3Al = 4Ni + \frac{4}{3}\,Al \qquad [8]$$

can be estimated[5] from the measured heat of formation:[6] $\Delta F_3^\circ = 49 \pm 5$ kcal at 1000°K. ΔF_4° of the reaction

$$\frac{4}{3}\,Ni_3Al = 4\underline{Ni} + \frac{4}{3}\,\underline{Al} \qquad [9]$$

at 1000°K is taken from the Ni-Al phase diagram using the relation

$$\Delta F_4^\circ = \frac{4}{3}\,RT \ln a_{Al} = \frac{4}{3}\,RT \ln c_{Al} = -3.7 \text{ kcal.}$$

The error introduced by substituting the activity of aluminum in solution in nickel a_{Al} by the weight percentage of aluminum c_{Al} is small since the solubility of aluminum at 1000°K is only 4 wt pct and since the standard state was taken as 1 wt pct. The free energy ΔF_5° of the reaction

$$\frac{4}{3}\,Al = \frac{4}{3}\,\underline{Al} \qquad [10]$$

is then found by subtracting reaction 9 from reaction 8.

$$\Delta F_5^\circ = -53 \pm 5 \text{ kcal.}$$

The free energy of solution of oxygen in nickel is derived in a similar manner. The ΔF_6° of the reaction

$$2NiO = 2Ni + O_2 \qquad [11]$$

has been reported[4] to be $\Delta F_6^\circ = 70$ kcal at 1000°K. The ΔF_7° of the reaction

$$2NiO = 2\underline{Ni} + 2\underline{O} \qquad [12]$$

is taken from the Ni-O phase diagram, again using the relation

$$\Delta F_7^\circ = RT \ln a_O = RT \ln c_O = 15 \text{ kcal.}$$

The error in the derived ΔF_7° is small, since the oxygen concentration c_o is low. Subtracting reaction 12 from reaction 11, the reaction

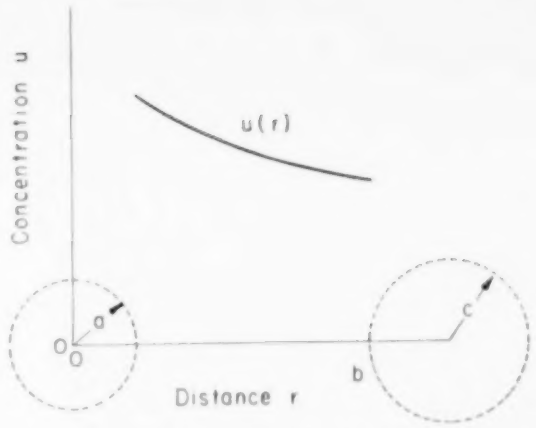

Fig. 1—Concentration as a function of distance between a small and a larger particle.

$$O_2 = 2\underline{O} \qquad [13]$$

is obtained, and $\Delta F_8^\circ = -55$ kcal. Finally, ΔF_1° is found by adding reactions 7, 10, and 13: $\Delta F_1^\circ = 112 \pm 5$ kcal.

The equilibrium constant of reaction 6 is

$$K = \frac{(a_{Al})^{\frac{4}{3}}\,(a_O)^2}{(a_{Al_2O_3})^{\frac{2}{3}}}.$$

The Al_2O_3 is of substantially constant composition, and its activity may be taken as unity. The activity of aluminum in solution in nickel is of the order of unity, since the standard state was taken as 1 wt pct, and since the solubility of aluminum is of the order of 1 pct. As the oxygen concentration is low, the activity of oxygen may safely be taken as equal to the weight percentage. Hence, $K = u_o^2 \times 10^4$ or $\log u_o = -14$ if the relation

$$\log K = -\frac{\Delta F_1^\circ}{4.575}$$

is used. It is not likely that the derived u_o is off by more than a factor of 10 from the actual value. Such an error is negligibly small since it would change the total time t by only an extremely small fraction.

Acknowledgments

The author wishes to thank his associates at the Research Laboratories, Westinghouse Electric Corp., particularly H. Wiedersich and C. W. Helstrom, for several stimulating discussions.

References

[4] N. F. Mott and F. R. N. Nabarro: Report on Strength of Solids, p. 1. Physical Society, 1948. London.

[5] R. F. Wilde and N. J. Grant: Aging in Complex Commercial Nickel-Chromium Alloys Hardened with Titanium and Aluminum. To be published.

[6] B. S. Lement, B. L. Averbach, and M. Cohen: Further Study of Microstructural Changes on Tempering Iron Carbon Alloys. *ASM Trans.*, 1955, vol. 47, p. 291.

[4] C. J. Smithells: *Metals Reference Book*, vol. 2, pp. 546-618. Interscience Publishers Inc. New York, 1955.

[5] P. A. Flinn: Private communication.

Discussion of this paper sent (2 copies) to AIME by June 1, 1957 will appear in AIME *Transactions* Vol. 209, 1957, and in JOURNAL OF METALS, October 1957.

Grain Growth of Titanium Carbide in Nickel

The infiltration technique was employed to study the grain growth of titanium carbide in liquid nickel. Three successive stages of growth were observed; formation of idiomorphic grains, spheroidization accompanied by rapid growth, and a period of coalescence and closer packing of the carbide grains. The primary mode of grain growth appears to be by dissolution of high energy surfaces, transport of carbide through the liquid phase and isothermal redeposition.

by Leonard P. Skolnick

PROPERTIES of materials containing a hard constituent dispersed in a metallic matrix are dependent on the distribution of the hard phase.[1-3] The grain growth of titanium carbide in liquid nickel was studied in order to understand microstructural development in this and similar systems.

Smith[4] has examined the influence of surface energy on the distribution of phases in alloys. The grain growth of tungsten carbide in cobalt has been the subject of many conflicting theories. Those prior to 1950 have been summarized by Goetzel.[5] Recently, Gurland and Norton[6] and Gurland[7] have indicated that growth occurs primarily by diffusion through the liquid phase in order to lower the interfacial energy between the carbide and the liquid metal. In the development of the Ti-C-Ni ternary phase diagram, Stover and Wulff[8] have shown that both eutectiferous dendritic titanium carbide, and primary titanium carbide which had developed crystals of cubic symmetry, were rounded by heating below the solidus, and that if primary carbide was already present the typical eutectic decomposition products were not formed.

Experimental Procedure

The infiltration technique was used to study the grain growth of titanium carbide in nickel. In contrast to sintering, infiltration more readily assures uniform dispersion of the two phases, and the problems associated with mixing by milling; i.e., mill contamination, breakdown of original carbide size in the operation, development of interfering surface films, etc., are avoided. In addition, the complicating effect of densification by shrinkage is eliminated.

The titanium carbides used were commercial grades. Their chemical analyses, size distributions and shapes are summarized in Table I. Size analysis was conducted by microscopic count on a minimum

L. P. SKOLNICK, Member AIME, is Research Assistant, Dept. of Metallurgy, Massachusetts Institute of Technology, Cambridge, Mass.

TP 4406E. Manuscript, Apr. 13, 1956. New York Meeting, February 1956.

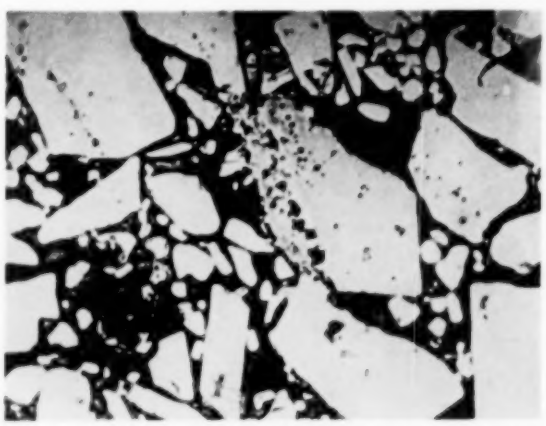

Fig. 1—Micrograph of grade 1 titanium carbide infiltrated with nickel for 1 min; etched with Marble's reagent. X750. Reduced approximately 30 pct for reproduction.

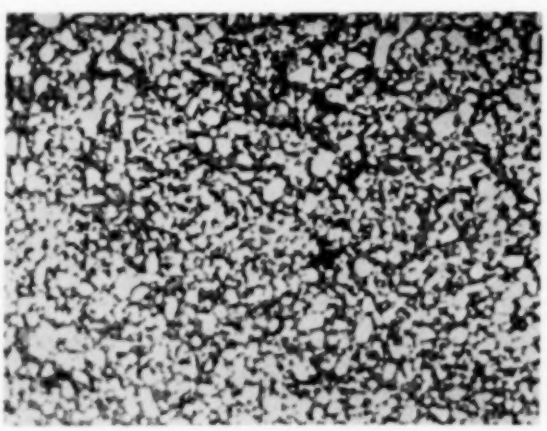

Fig. 2—Micrograph of grade 2 titanium carbide infiltrated with nickel for 1 min; etched with Marble's reagent. X750. Reduced approximately 30 pct for reproduction.

of 5000 particles. Chemical analysis was conducted by the laboratories of the Titanium Alloys Mfg. Div., National Lead Co. Titanium carbide powder grade Nos. 1, 2 and 3 were prepared by the arc melting of pigment grade rutile with an excess of carbon, crushing the product to —325 mesh, leaching to remove iron and other contaminants and finally lowering the free carbon content by a flotation process. Grade 1 powder was the as-received product from which grades 2 and 3 were derived. These finer particle distributions were obtained by a simple laboratory sedimentation to remove the coarser fractions, followed by a drying operation at 60°C. Grade 4 powder was presumably manufactured in a menstruum type process and was used in the as-received condition. This powder was almost spherical in shape and it was hoped that despite the variation in manufacturing technique some information on the effect of particle shape on the rate of grain growth might be ascertained.

A skeleton body of each of the titanium carbides was made by pressing the powder without binder or lubricant in a tungsten carbide lined die 2½ x ¼ x ¼ in. at a pressure of 1 ton per sq in. and sintering at 1400°C for 1 hr in a carbon tube induction furnace at a vacuum of about 10^{-4} mm. Each of these specimens was then cut into ¼ in. cubes for infiltration. This specimen size was chosen as the smallest that could conveniently be examined metallographically. The small size was employed to minimize any temperature gradient and time lag due to penetration rate of the infiltrant. As far as could be detected, the infiltrated structures were uniform throughout the section.

The infiltration was conducted in a furnace similar to that used for sintering at a vacuum of less than 100 μ Hg. The titanium carbide body was placed on a beryllia support plate and the infiltrant allotment, in the form of cuttings of electrolytic nickel sheet, was placed on top of the porous carbide skeleton. The infiltrant allotment was selected so that the ratio of carbide to nickel was about 50 pct by weight. The entire assembly was heated up to the melting point of nickel within a period of 15 min. The temperature was measured optically. Melting occurred in all cases at 1450° to 1460°C. Temperature was controlled at the level of incipient melting within ±5°C.

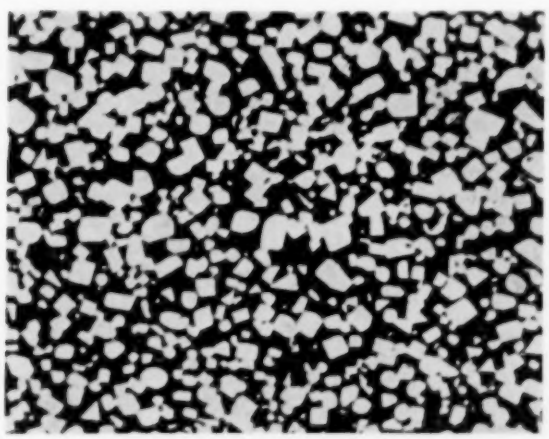

Fig. 3—Micrograph of grade 2 titanium carbide infiltrated with nickel for 10 min; etched with Marble's reagent. X750. Reduced approximately 25 pct for reproduction.

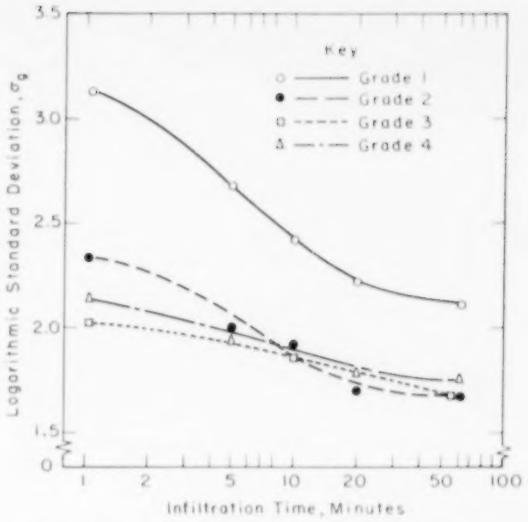

Fig. 4—Effect of time of infiltration with nickel upon the standard deviation of the grain size distribution of titanium carbide.

Metallographic preparation of the nickel-infiltrated carbide specimens was made by sectioning, mounting in Bakelite, grinding and polishing through 0 to 3 μ diamond paste.

Representative X500 micrographs were used to make the statistical measurements to describe the changes in microstructure that occurred. The exact analytical methods are discussed in a variety of references[10] and will not be detailed here.

Four basic parameters were chosen to describe the structure of the titanium carbide phase in terms of quantitative mathematical values:

1) A statistical measure of average grain diameter. The statistical size employed was that derived for uniform spherical particles by Fullman[10] and used by Gurland and Norton.[9]

2) The logarithmic standard deviation of the distribution of particle sizes (i.e., particle diameters).

3) A coefficient describing the shape of the particle. A factor of spheroidity was used which was the ratio of the surface area of the carbide grains to the surface area calculated for spherical grains of equivalent diameter.

4) The volume fraction of carbide phase present, simply derived from the principle of equality of point, line, area and volume fractions.

Experimental Results

The grain growth of titanium carbide in nickel can be described in three successive stages:

1) **Tendency toward Idiomorphism**—This period is evidenced in several ways. Fig. 1 shows the grade 1 carbide after 1 min in contact with molten nickel. The grain in the center of the micrograph is typical of many grains of the same type in the specimen. This rather coarse carbide contains some typically rugged crushed surfaces and some idiomorphic faces which are a result of intercrystalline cleavage in crushing of the titanium carbide melt. It is apparent that solution of the noncrystalline surfaces is occurring preferentially.

On the other hand, the finer carbide powder fraction has virtually no crystalline faces remaining, as evidenced by powder examination before proc-

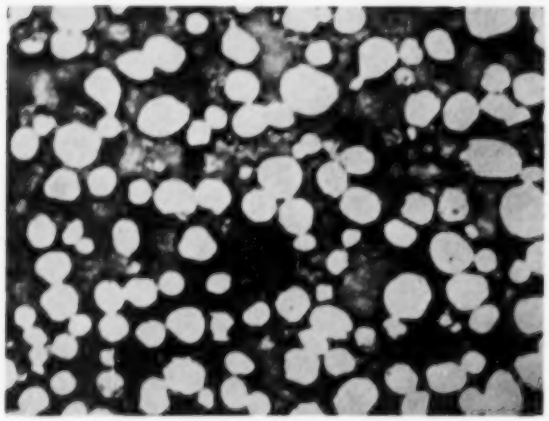

Fig. 5—Micrograph of grade 2 titanium carbide infiltrated with nickel for 20 min; etched with Marble's reagent. X750. Reduced approximately 30 pct for reproduction.

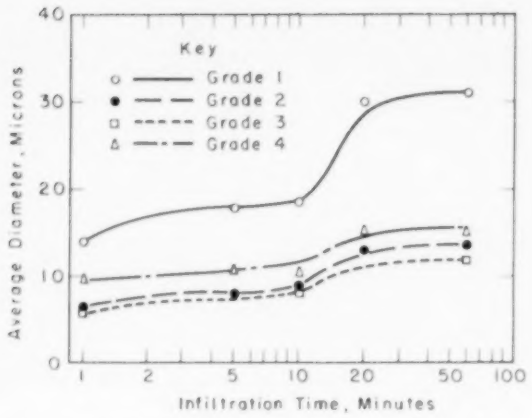

Fig. 6—Effect of time of infiltration with nickel upon grain size of titanium carbide.

essing, and in Fig. 2 which shows the grade 2 carbide after 1 min of infiltration. The marked formation of idiomorphic grains after 10 min of infiltration can be seen in Fig. 3.

During this stage, as well as the succeeding one, a narrowing of the particle size distribution occurs. This can be seen in Fig. 4 where the logarithmic standard deviation of the carbide grain size is plotted against time of infiltration. The major decrease in the spread seems to occur within this initial period. This trend is clear in the case of the materials with the widest initial distribution, that is, grades 1 and 2; see Table I. It is also apparent that the broader the starting size distribution, the more pronounced the change in the standard deviation.

2) **Rounding and Growth Period**—This stage, which takes place between 10 and 20 min of infiltration at these temperatures, is characterized by spheroidization accompanied by rapid growth. The typical changes that occur are illustrated by comparison between Figs. 3 and 5, showing the structure of a grade 2 nickel-infiltrated specimen after 10 and 20 min of infiltration, respectively. Fig. 6 shows the increase in average size during infiltration for all the carbide grades. The major increase in size occurs during the period of spheroidization.

Table I. Analysis of Titanium Carbide Grades

	Carbide Grade			
	1, Arc Melted	2, Arc Melted	3, Arc Melted	4, Menstruum
Chemical Composition				
Titanium	79.10	79.10	79.10	80.07
Combined Carbon	19.07	19.07	19.07	19.46
Free Carbon	0.30	0.30	0.30	0.13
Iron	0.05	0.05	0.05	0.02
Balance	1.58	1.58	1.58	0.32
Size Analysis, Pct by Count				
1μ	32.2	56.3	65.5	5.3
1 to 4μ	18.1	31.9	28.9	28.5
4 to 7μ	10.9	11.1	5.5	53.2
7 to 10μ	19.4	0.6	0.1	12.6
10 to 20μ	13.6	0.1	—	0.4
20 to 50μ	5.8	—	—	—

The coefficient of spheroidity, mentioned in the experimental method, is plotted vs time of infiltration in Fig. 7. The curves for grades 1 and 2 show a typical steep increase in the 10 to 20 min period. These carbides also show a small increase in the spheroidity coefficient initially, as the rugged as-crushed surfaces become idiomorphic and thus have lower surface area. In view of the similarity of grade 3 carbide a curve of similar shape was drawn for it, although only three experimental points were obtained.

The curve for the grade 4 carbide shows interesting characteristics relating to the stage of idiomorphic grain formation, as well as the rounding and growth period. The starting carbide material in this case consisted of substantially spherical particles which after 1 min in contact with molten nickel had already undergone considerable changes and become more angular. With continuing infiltration time up to 10 min the coefficient of spheroidity decreases as the grains tend to become idiomorphic, thus illustrating that the surface energy can be lowered despite an increase in interfacial area. Continued grain growth finally results in spheroidization again as in the case of the other carbides.

3) **Period of Increasing Carbide Concentration**—After the second stage, growth of the carbide comes virtually to a standstill as can be seen in comparing Fig. 8, which shows the grade 2 material after 1 hr in contact with molten nickel; with Fig. 5, which shows the same material after 20 min. Measurement of the carbide structure revealed an increase in carbide concentration of about 8 pct in grades 1, 2 and 4 during the period of from 20 to 60 min of infiltration.

Discussion

Three modes of grain growth for tungsten carbide in cobalt have been suggested[7] and, in view of the similarities in the phase diagram of the titanium carbide-nickel pseudo-binary diagram[9] with the above system,[13] it seems reasonable to discuss the phenomena observed in light of these mechanisms: 1) grain growth by isothermal dissolution and redeposition, 2) solution and reprecipitation in cooling, and 3) growth by coalescence of adjoining carbide grains.

For the most part, grain growth of titanium carbide infiltrated with nickel occurs by the mechanism of dissolution of high energy surfaces, transport of the carbide through the liquid phase and redeposition on existing grains to realize a condition of lower interfacial energy. This phenomenon is manifested initially by preferred dissolution of non-idiomorphic surfaces and the formation of grains

tending toward cubic or rectangular shapes. During this phase little grain growth occurs.

It is plausible that the formation of idiomorphic grains does not take place by growth, but occurs by solution of the highest energy regions until the binder becomes saturated. This hypothesis is partly substantiated by the fact that grain growth is limited during this stage. Furthermore, the size of the idiomorphic grains seems to be closely related to the maximum starting size. Thus those materials with the widest starting size distributions appear to *grow* the most during the first stage since the average size increases. For example, the grade 4 carbide, which had a very narrow initial distribution, experienced essentially no growth during the formation of idiomorphic grains, while grade 1, with the widest size distribution, had a rather substantial increase in average size. It seems reasonable to assume, then, that this stage is a dissolution phenomena and is in keeping with the Gibbs-Thomson surface energy relationship.

The second stage of rounding and growth to form the spheroidized structure typical of these compositions can be explained as an attempt to lower the interfacial energy by a minimization of surface area. It occurs in the liquid phase sintering of most cubic metals.[12]

This stage of growth represents a significant departure from the behavior typical of cobalt cemented tungsten carbide. Gurland[9] has shown that in the latter system isothermal dissolution and redeposition is the primary mode of grain growth, just as this investigation has indicated for titanium carbide-nickel. The difference in the behavior of the two systems can be explained in terms of the crystal structure of the carbide phase. Tungsten carbide is a simple hexagonal structure and therefore might be expected to be strongly anisotropic. In this case interfacial energy cannot be minimized by lowering the interfacial area, since the unit interfacial energy of the few densely packed low index planes is much lower than that of the other crystal planes. On the other hand, the less anisotropic cubic titanium carbide possesses more uniform surface energy from plane to plane and therefore rounding can occur. The *round* grains need not be round, in the sense of possessing vicinal faces, but may consist of submicroscopic steps of relatively low index faces.[13] Thus the minimum interfacial energy is realized in the two systems by the formation of different structures.

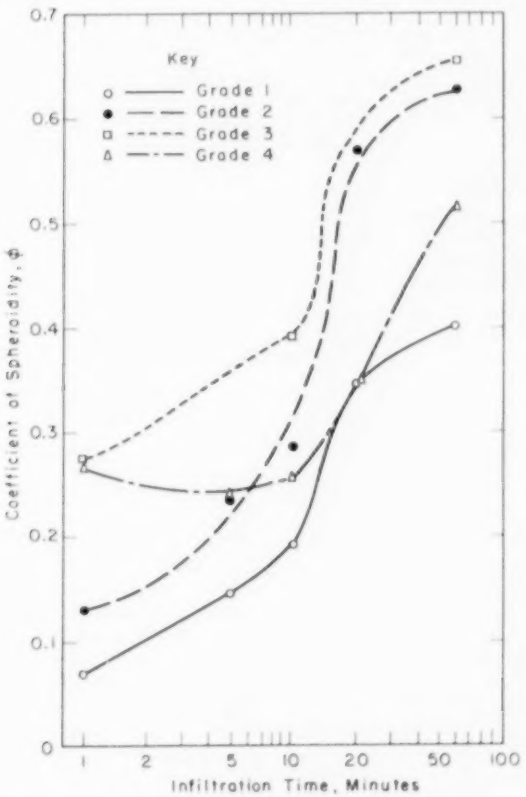

Fig. 7—Effect of time of infiltration with nickel upon rounding of the titanium carbide grades.

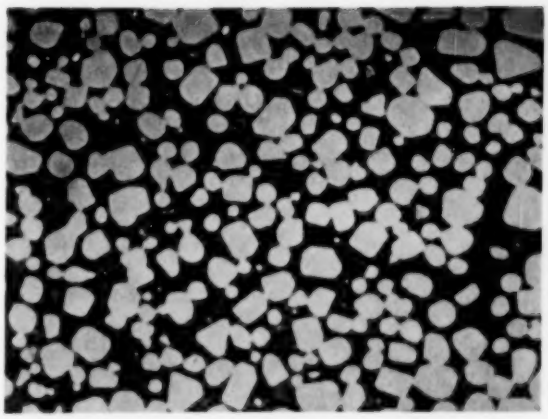

Fig. 8—Micrograph of grade 2 titanium carbide infiltrated with nickel for 60 min; etched with Marble's reagent. X750. Reduced approximately 30 pct for reproduction.

The third stage, in which the titanium carbide grains become more closely packed, is a result of the surface tension forces. This has been used to explain the shrinkage in sintering of tungsten carbide. The reasons for densification of the titanium carbide plane in nickel is somewhat different since no voids were present. Silverman[14] has also observed a similar effect in infiltration of titanium carbide with certain cobalt alloys.

During this stage certain grains favorably oriented to one another undergo coalescence, Fig. 8. During the coalescence period grain growth proceeds very slowly, indicating that this mode of grain growth is relatively unimportant.

Conclusions

Preliminary work on the grain growth of titanium carbide in nickel has indicated that the primary mechanism is by dissolution of high energy surfaces and isothermal redeposition to minimize interfacial energies. It has been suggested that although lowering of interfacial energy is the basic driving force for the development of a certain structure, this criterion can be realized in different manners, depending on the particular system involved. In order to understand and control the development of certain structures of theoretical and practical importance better, it would be desirable to investigate a number of cogent factors, such as the role of surface energy and its anisotropy; how this anisotropy is affected by such influences as foreign atoms and lattice strains; the mechanism of diffusion in such systems; and the atomistic picture of the crystal growth process

per se. Such information would be necessary to provide a comprehensive understanding of grain growth of one phase in another.

Acknowledgments

The author wishes to express his gratitude to the Management and Staff of the Sintercast Corp. of America, whose facilities were used for this investigation, and whose help made this work possible. Thanks are due to Claus G. Goetzel for his encouragement and advice; to John P. Nielsen for his help; and to Geraldine Malmborg for assistance in making the grain size counts. This paper is based on a portion of a thesis by Leonard P. Skolnick submitted to the College of Engineering of New York University in partial fulfillment of the requirements for the degree of Master of Science.

References

[1] M. Gensamer, E. B. Pearsall, and G. V. Smith: The Mechanical Properties of the Isothermal Decomposition Products of Austenite. *ASM Trans.*, 1946, vol. 28, p. 389.

[2] E. Orowan: Fracture and Strength of Solids. *Report on Progress in Physics*, 1948-1949, vol. 12, p. 185.

[3] J. Gurland and J. T. Norton: Role of the Binder Phase in Cemented Tungsten Carbide, Cobalt Alloys. *AIME Trans.*, 1952, vol. 194, pp. 1051-1056; JOURNAL OF METALS, October 1952.

[4] J. Gurland and P. Bardzil: Relation of Strength, Composition, and Grain Size of Sintered WC-CO Alloys. *AIME Trans.*, 1955, vol. 203, pp. 311-315; JOURNAL OF METALS, February 1955.

[5] P. Schwarzkopf and W. Leszynski: Note on the Relationship Between Brittleness and Microstructure of Cermets. *Powder Metallurgy Bulletin*, 1954, vol. 7, pp. 19-21.

[6] C. S. Smith: Grains, Phases, and Interfaces: An Interpretation of Microstructure. *AIME Trans.*, 1948, vol. 175, pp. 15-51; METALS TECHNOLOGY, June 1948.

[7] C. G. Goetzel: Treatise on Powder Metallurgy, 1st Ed., vol. 2. Interscience Pub. Co. New York, 1950.

[8] J. Gurland: A Study of the Effect of Carbon Content on the Structure and Properties of Sintered WC-CO Alloys. *AIME Trans.*, 1954, vol. 200, pp. 285-290; JOURNAL OF METALS, February 1954.

[9] E. R. Stover and J. Wulff: Studies in the System Nickel-Titanium-Carbon. WADC Technical Report No. 54-212, January 1954.

[10] J. M. DallaValle: *Micromeritics*, 2nd Ed., chap. 3. Pitman Pub. Co. New York, 1948.

[11] J. M. DallaValle: *Micromeritics*, 2nd. Ed., chap. 4. Pitman Pub. Co. New York, 1948.

[12] R. L. Fullman: Measurement of Particle Sizes in Opaque Bodies. *AIME Trans.*, 1953, vol. 197, pp. 447-452; JOURNAL OF METALS, March 1953.

[13] G. Herdan: *Small Particle Statistics*, chaps. 2, 3, 4, 6, and pp. 256-259. Elsevier Pub Co. Amsterdam, 1953.

[14] C. S. Smith and L. Guttman: One and Two Dimensional Sections of Three Dimensional Structures. *AIME Trans.*, 1952, vol. 194, p. 150; JOURNAL OF METALS, February 1952.

[15] P. Rautala and J. T. Norton: Tungsten-Cobalt-Carbon System. *AIME Trans.*, 1952, vol. 194, pp. 1045-1050; JOURNAL OF METALS, October 1952.

[16] H. S. Cannon: Investigation of the Behavior Observed in Liquid Phase Sintering. Ph. D. Thesis, Rensselaer Polytechnic Institute, 1953.

[17] C. W. Bunn and H. Emmett: Layer Formation on Crystal Faces. *Discussions Faraday Soc.*, 1949, No. 5, p. 119.

[18] R. Silverman: Private communication.

Discussion of this paper sent (2 copies) to AIME by June 1, 1957 will appear in AIME *Transactions* Vol. 209, 1957, and in JOURNAL OF METALS, October 1957.

Strength of Silver Brazed Joints in Mild Steel

An investigation was made of the dependence of the strength of silver brazed, low carbon steel joints on the geometry of the joint. The experimental results indicate that for cylindrical test specimens having transverse brazed joints, the ultimate tensile strength is really a linear function of the thickness to diameter ratio rather than only of the thickness of the filler metal for constant specimen diameter.

by W. G. Moffatt and J. Wulff

BRAZED joints and their strength have for some time been of great practical as well as theoretical interest. A good summary of the previous work in this field may be found in the reports of the Armour Research Foundation.[1] In spite of excessive scatter in test data, the fact that the strength of a brazed joint may exceed the ultimate strength of the brazing material itself by many times continues to be of interest and of value in engineering. That this is qualitatively due to plastic constraint of the brazing material by the faying surfaces of the base metal is not in dispute, yet no complete interpretation of the data exists. The purpose of the present work is not to provide such a new interpretation, but to report new experimental data which we hope may lead to a better understanding of the important variables concerned.

The work of Bredz[2] definitely shows that the thinner a brazed joint is, the greater is its strength. Diameter of a joint has seldom been taken into

W. G. MOFFATT and J. WULFF, Member AIME, are Instructor and Professor, respectively, Metallurgy Dept., Massachusetts Institute of Technology, Cambridge, Mass.

TP 4408E. Manuscript, June 4, 1956. New Orleans Meeting, February 1957.

Table I. Experimental Test Data*

Specimen No.	Silver Thickness, In.	Diameter, In.	Area, Sq In.	t/D	P_{max}	σ	$N = \frac{a-ax}{ab-af}$	Comments
A-1	0.0026	0.5296	0.2203	0.0049	11,550	52,450	0.871	Flaw in center
A-2	0.0026	0.3476	0.0949	0.0075	5,150	54,250	0.921	
A-3	0.0026	0.1578	0.0196	0.0165	510	26,000	0.138	Large flaw edge to center
A-4	0.0026	0.3182	0.0795	0.0082	4,240	53,350	0.896	
A-5	0.0026	0.3550	0.0990	0.0073	5,240	52,950	0.885	
A-6	0.0026		Broke in machining					
A-7	0.0026	0.2678	0.0563	0.0097	3,050	54,150	0.918	
B-1	0.0055	0.3290	0.0850	0.0167	4,300	50,600	0.820	
B-2	0.0055		Broke in machining					
B-3	0.0055	0.5640	0.2498	0.0098	12,800	51,250	0.838	
B-4	0.0055	0.1988	0.0310	0.0276	1,460	47,100	0.723	
B-5	0.0055		Broke in machining					
B-6	0.0055	0.2800	0.0616	0.0196	3,170	51,450	0.843	
B-7	0.0055	0.3429	0.0923	0.0160	4,580	49,400	0.787	
B-8	0.0055	0.1706	0.0229	0.0322	1,090	47,600	0.737	
C-1	0.0007	0.6352	0.3169	0.0011	17,350	54,750	0.935	
C-2	0.0007	0.6797	0.3628	0.0010	19,650	54,150	0.918	
C-3	0.0007	0.4645	0.1694	0.0015	9,150	54,000	0.914	
C-4	0.0007	0.3748	0.1103	0.0019	5,970	54,150	0.918	
C-5	0.0007	0.3447	0.0933	0.0020	4,950	53,050	0.888	
D-1	0.0006	0.6486	0.3304	0.0009	14,400	43,600	0.626	Flaw at edge
D-2	0.0006	0.6000	0.2827	0.0010	15,150	53,600	0.903	Flaw in center
D-3	0.0006	0.4982	0.1949	0.0012	10,550	54,150	0.918	Flaw in center
D-4	0.0006	0.3995	0.1253	0.0015	6,840	54,600	0.931	
D-5	0.0006	0.2975	0.0695	0.0020	3,760	54,100	0.917	
E-1	0.018	0.4620	0.1676	0.0390	8,500	50,700	0.823	
E-2	0.018	0.3594	0.1014	0.0501	5,020	49,500	0.789	
E-3	0.018	0.1278	0.0128	0.1408	500	39,100	0.502	
E-4	0.018	0.2063	0.0334	0.0873	1,480	44,300	0.645	
E-5	0.018	0.1607	0.0203	0.1120	850	41,850	0.577	
E-6	0.018	0.1434	0.0162	0.1255	650	40,100	0.529	
F-1	0.040	0.5190	0.2116	0.0771	9,300	43,950	0.636	
F-2	0.040	0.4000	0.1257	0.1000	5,280	42,100	0.584	
F-3	0.040		Broke in machining					
F-4	0.040	0.3197	0.0803	0.1251	3,050	38,000	0.471	Small gas hole
F-5	0.040	0.1520	0.0181	0.2632	450	24,850	0.107	
F-6	0.040	0.2001	0.0314	0.1999	1,050	33,450	0.345	

* Blank: diameter, 0.5030 in.; area, 0.1987 sq in.; yield load, 6,125 lb; ultimate load, 11,350 lb; yield point, 30,825 psi; and ultimate tensile strength, 57,100 psi.

account save in the work of Meissner and Baldauf.[3] For metal joints made with adhesives they find a strength dependence on the thickness to diameter ratio. For brass soldered with Pb-Sn, the relationship is not as obvious. This may be due in part to the formation of intermetallic compounds at the basis metal interface and in part to gas pockets and inclusions. That it should also obtain with brazed surfaces, provided wetting occurs without the formation of intermetallic compounds, is also suggested by the Prandtl[4,5] analysis for the compression of a cylindrical specimen between the platens of a press. Assuming perfect sticking, this analysis shows that the stress varies and is a function of ratio of thickness to diameter of the slab. The latter work as well as that of Bredz[1] and Meissner and Baldauf[3] led the present authors to believe that in the case of brazed joints new experimental results were needed.

Experimental

The base metal used in this work was hot-rolled SAE 1020 steel. Pure silver was used as a brazing material. Brazing was carried out in a resistance-wound furnace in an atmosphere of purified hydrogen. The specimens in both cases were taken from room temperature to 1100°C and slowly cooled to room temperature.

In order to insure flat and and plane-parallel faying surfaces, the steel was cut into blocks 2½x 2½x2½ in. Before grinding, a ¼ in. diam hole was bored through the center of half of the twelve blocks cut. All blocks were squared by milling and then one surface of each block was ground flat with a Blanchard grinder and in all cases, except those to be used on the 0.018-in. and the 0.040-in. joints, were finish ground to a rms surface finish of 10 μ in. Each pair of blocks, one with a (hole) reservoir and one without, was then degreased and separated at the four corners with molybdenum wire or sheet shims. In the case of the two thick joints, shims were not used, and the two blocks were separated as shown in Fig. 1*b*. All others were separated as shown in Fig. 1*a*. The steel at the periphery of the joint was painted with colloidal graphite to prevent flow-out of the silver. Solid silver was then inserted in the holes in the top blocks, and all blocks were loaded in one furnace for brazing. The heating schedule to 1100°C took 4 hr. The current was shut off after 5 min at temperature, and the blocks were allowed to furnace cool under atmospheric pressure of pure hydrogen for 6 hr.

After removal from the furnace, the top surface and the bottom surface of the blocks were accurately scribed so that center holes could be located for turning bars whose axes were perpendicular to the brazed joint.

Rectangular prisms were next cut and then turned into rounds and finely finished in the region of the joint. The joint thicknesses were then measured with the filar eyepiece of a Bausch & Lomb metallograph. Tensile specimens of various diameters were next turned from the brazed prisms. This gave a range of diameters for each joint thickness. In this manner, it was possible to machine five or six tensile bars from each large brazed block, so that the brazed joint was accurately perpendicular to the axis of the test bar and had plane-parallel faces. The forementioned variation of specimen diameter, D, in any one large block provided, in every case, specimens having a thickness-to-diameter ratio, t/D, which overlapped with the t/D ratios obtained from the block having the next thinner joint.

For the tension test, the specimens were threaded into grips having ball seats which were heavily

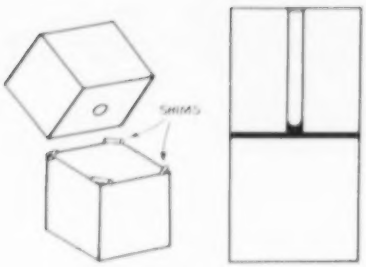

(a)

a) Assembly for thin joints: molybdenum wire or thin sheet molybdenum was used at four corners as shims, silver wire was introduced in vertical reservoir in upper block and both blocks were luted with a colloidal graphite suspension around the periphery of the joint.

Fig. 1—Illustration of manner in which large steel blocks were assembled for brazing.

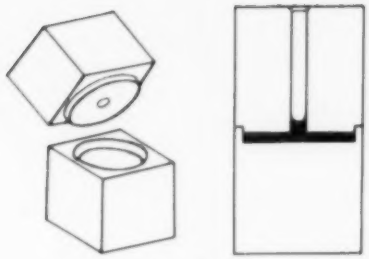

(b)

b) Assembly for thick joints (0.020 and 0.040 in.): no shims used, but cylindrical projection on upper block machined off until proper joint spacing was achieved; silver wire was introduced in vertical reservoir in upper block; and joint periphery was luted with a colloidal graphite suspension.

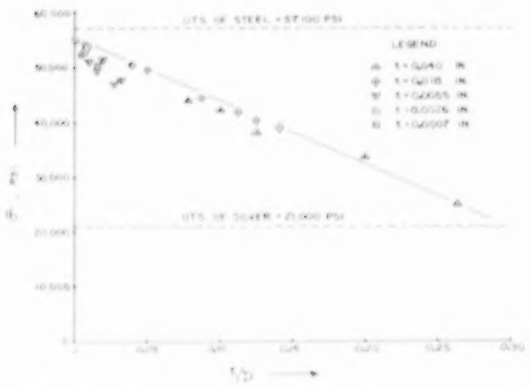

Fig. 2—Plot of $\bar{\sigma}$, ultimate tensile strength of brazed joint, vs t/D, the thickness to diameter ratio of the brazed joint. Only one point is shown on the plot for t = 0.0007 in. and none for t = 0.0006 in. because they are all clustered in the immediate neighborhood of the one point shown and cannot be separated on this graph.

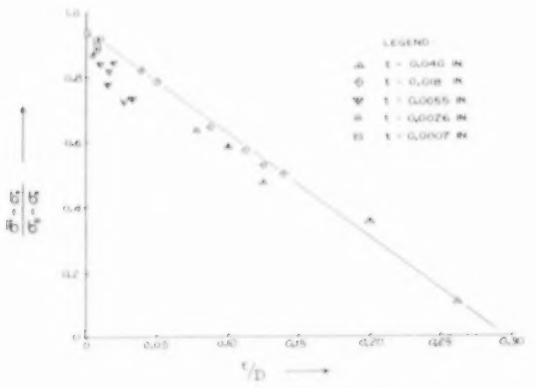

Fig. 3—Plot of the dimensionless quantity $\frac{\bar{\sigma}-\sigma_T}{\sigma_B-\sigma_T}$ vs thickness to diameter ratio, t/D, of the brazed joint.

greased. They were all pulled in tension using the same crosshead speed. In all cases the maximum load was measured. The failure of small diameter specimens with thick joints occurred at low loads. Indeed, after the ultimate load was reached the applied load dropped so rapidly that the load at failure could not be measured with any precision. For larger diameter specimens with thin joints, the fracture load and the ultimate load were practically identical. Data obtained are given in Table I, and plotted in Figs. 2 and 3.

Examination of the fracture joints in the case of thin joints indicated that failure always occurred in the center plane of the silver joint. The appearance of the fracture is shown in Fig. 4. Where the t/D ratio was very small (thin joints) the silver of the joint could be observed to neck before yielding of the steel could be observed. When the steel began to yield, as determined visually by the change in appearance of the highly polished surface of the steel, the load continued to rise and fracture took place at stresses considerably in excess of the yield point of the steel.

Discussion and Conclusions

It is evident from Fig. 2 that a straight line can be drawn through the experimental points using ultimate tensile strength of the joint, $\bar{\sigma}$, as ordinate, and thickness to diameter ratio, t/D, as abscissa. For a series of bars having constant joint thickness, a straight line can also be drawn using ultimate strength of the joint, $\bar{\sigma}$, as ordinate and reciprocal of diameter, $1/D$, as abscissa. The overlap of values of t/D chosen, and the ultimate tensile strength observed at those values, indicate that the same strength may be achieved with different joint thicknesses provided the ratio t/D is the same, i.e., if the joints are geometrically similar. It should be noted that the joints having thicknesses of 0.0006 and 0.0007 in. could not all be plotted because of crowding and that actually a cluster of points exists near the $\bar{\sigma}$ axis on Fig. 2. These are within 5 pct of the ultimate strength of the steel. With a steel or base material of low ductility, if perfect wetting and freedom from gas pockets are achieved, the strength of the joints should be expected to approach the ultimate strength of the base material.

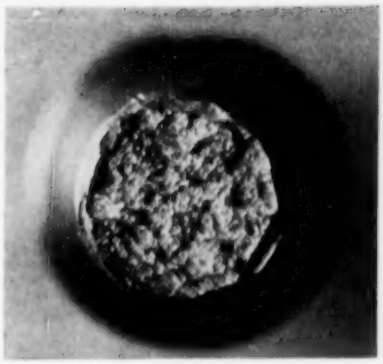

Fig. 4—Two views of fracture surface of test bar E-1, showing the considerable amount of necking of the brazing material encountered in this work. This bar had a joint thickness of 0.018 in. and an original diameter of 0.4620 in., and failed at an ultimate strength of 50,700 psi.

The straight line relationship shown in Fig. 2 may be replotted so that both coordinates are dimensionless as in Fig. 3. There, the ordinate is the quantity $\frac{\sigma-\sigma_f}{\sigma_b-\sigma_f}$, where σ is the observed ultimate stress withstood by the joint, σ_f is the ultimate strength of the filler metal and σ_b is the ultimate strength of the base metal. This dimensionless ratio indicates that fraction of the total difference between the ultimate strengths of the base metal and the filler metal which the joint is supporting in excess of its unconstrained strength.

In conclusion, the experimental work reported indicates that the ultimate tensile strength of low carbon steel joints brazed with pure silver is not merely a linear function of the thickness of the joint, but is also a linear function of the ratio of thickness to diameter.

Acknowledgments

The authors are indebted for financial assistance to Instrumentation Laboratory, Massachusetts Institute of Technology, and to the United States Air Force.

References

[1] N. Bredzs: Investigation of Factors Determining the Tensile Strength of Brazed Joints. *Welding Journal*, Research Supplement, November 1954, p. 545S.

[2] H. P. Meissner and G. H. Baldauf: *ASME Trans.*, 1951, vol. 73, p. 697.

[3] L. Prandtl: *Ztsch. Ang. Math.*, 1923, vol. 3, p. 401.

[4] O. Hoffman and G. Sachs: *Theory of Plasticity*, pp. 240-248. McGraw-Hill Pub. Co. New York, 1953.

Discussion of this paper sent (2 copies) to AIME by June 1, 1957 will appear in AIME *Transactions* Vol. 209, 1957, and in JOURNAL OF METALS, October 1957.

Flaking of Heavy Alloy Steel Sections

In this investigation, potential antiflaking cycles were tested. A 15-ton experimental heat of Cr-Ni-Mo steel was produced in a basic electric furnace with an abnormally high hydrogen content. The proposed cycles were then applied to this steel. As a result, an antiflaking cycle which was primarily an isothermal transformation in the pearlite range produced flake-free steel forgings in spite of extremely high hydrogen content. Proposed cycles in the bainite range were not successful primarily because a 100 pct isothermal transformation in this range was not attained. Sound forgings from this experimental heat of steel that were previously produced flake-free by the use of appropriate antiflaking cycles were severely flaked by subjecting them to a subsequent heat treatment. Evidence is presented which shows the profound effect of transformation stress on the propensity to flaking.

by C. R. Garr and A. R. Troiano

FLAKING or hair-line crack formation has been a major problem confronting the producer of large alloy steel forgings.[1] Today it is generally conceded that hydrogen in one or more forms in alloy steel sections is a requisite for flaking. Hence an obvious remedy is a thermal cycle that reduces the hydrogen content to some low level. In practice, this generally means holding the material at some subcritical temperature for a period of time depending on the size of the ingot or forging. Another method that will suffice in some cases is to cool large forgings slowly, i.e., bury in ashes. In practice, this *hydrogen bake* is sometimes accomplished inadvertently by a series

C. R. GARR, Junior Member AIME, formerly Research Assistant, Dept. of Metallurgical Engineering, Case Institute of Technology, is now Senior Engineer, Bettis Plant, Westinghouse Electric Corp., Pittsburgh. A. R. TROIANO, Member AIME, is Head, Dept. of Metallurgical Engineering, Case Institute of Technology, Cleveland.

TP 4379E. Manuscript, Aug. 6, 1956. New Orleans Meeting, February 1957.

Fig. 1—Transverse slice of block No. 1, surface ground and macroetched. Subjected to treatment *A*.

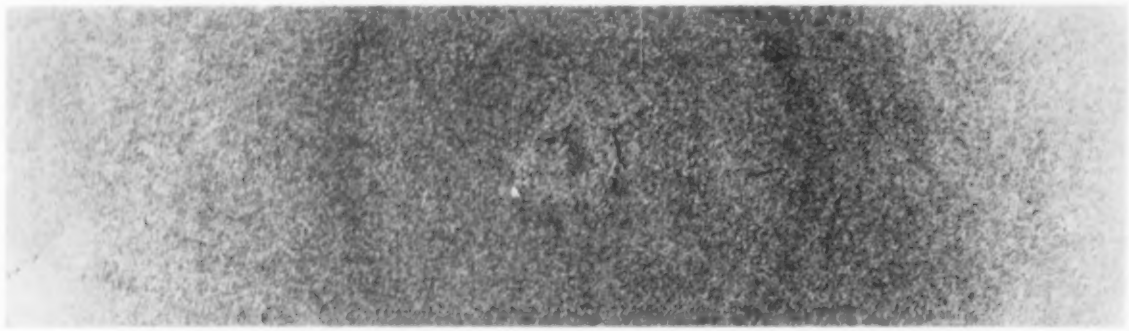

Fig. 2—Transverse slice of block No. 7, surface ground and macroetched. Subjected to treatment *C*.

Fig. 3—Micrograph showing flake in block No. 2. Etched with 3 pct Nital. X200. Reduced approximately 25 pct for reproduction.

Fig. 4—Micrograph showing flake in block No. 7. Etched with 3 pct Nital. X200. Reduced approximately 25 pct for reproduction.

Fig. 5—Transverse slice of block No. 5, originally produced flake free and recycled to produce flakes. Surface ground and macroetched.

of homogenization and tempering treatments. However, it should be noted that these treatments are not always successful in preventing flakes, particularly in the case of large forgings. The time required for the baking period may be prohibitive and there is evidence occasionally to cause doubt about the effectiveness of the baking treatment.

However, a second possible remedy becomes apparent when all the factors required for flaking are considered. In a recent publication by Dana, Shortsleeve and Troiano,[2] it was shown on a laboratory scale that hydrogen alone will not cause the conventional type of flaking but that a combination of transformation stress and hydrogen is required. Therefore, if a steel section can be heat treated so that transformation stresses are eliminated, flaking will be prevented regardless of the hydrogen content of the steel.

The objectives of the investigation presented in this paper are primarily to answer the following two questions: 1) if antiflaking procedures can be developed for commercial practice by extension of these recent laboratory results;[2] and 2) if steel sections that were previously subjected to these treatments and are flake-free can be flaked upon subsequent heat treatment.

Material and Procedure

In order to determine the applicability of antiflaking treatments to commercial practice, it became desirable to produce a heat of flake-susceptible alloy steel following conventional mill practice. The only deviation from mill practice was to devise some method to introduce an unusually high hydrogen content into the steel.

A 15-ton heat of steel was produced by the Midvale Co. of Phila. in a basic electric furnace. The chemical composition of this heat was as follows: 0.45 pct C, 0.74 pct Mn, 0.27 pct Si, 1.83 pct Ni, 0.95 pct Cr, 0.28 pct Mo, 0.010 pct P, and 0.011 pct S.

The steel was produced with a high hydrogen content (10 cu cm per 100 g) by injecting steam into the heat after the oxidizing period was completed and again after the introduction of manganese and chromium. Steam was introduced by means of a 1½ in. diam steel pipe under about 90 lb of steam pressure. The pipe was plunged below the surface of the liquid metal and moved back and forth. A noticeable reaction occurred below the surface of the molten metal with a pronounced boil. This violent action appeared to cause considerable electrode erosion and hence increased the carbon content of the heat.

It was desirable to prevent the flushing action of a boil with the concomitant decrease of hydrogen. To prevent this, the removal of oxygen was accomplished by intermittent additions of ferrosilicon to the bath during the period of steam introduction. The final chemical composition of the heat makes it evident that large amounts of this silicon were oxidized in preference to the carbon. The total time of steam introduction was 70 min. The teeming of the heat occurred without incident, and there was no activity in the ladle.

Three ingots were produced as follows: 1) 26 in. corrugated, 20,000 lb; 2) 19 in. octagon, 7,400 lb; and 3) 13 in. dodecagon, 3,100 lb.

During solidification of the ingots in the mold, a slow gas evolution was apparent. As a result of this slow evolution, the tops of the sink heads or hot tops for the 13 and 19 in. ingots were essentially flat. The 26 in. ingot did show some shrinkage but it was considerably less than is normally encountered. The ingots were stripped and fired for forging as soon as they were completely solidified.

The forging of the three ingots was initiated approximately 12 hr after the stripping operation. The ingots were forged as follows:

1) The 26 in. corrugated ingot was forged in two steps to a 13 in. diam billet and hot cut into 30 in. long blocks.

2) The 19 in. octagonal ingot was forged in two steps to a 9 in. diam billet and hot cut into 25 in. long blocks.

3) The 13 in. dodecagonal ingot was forged in a single step to a 6 in. diam billet and hot cut into 12 in. long blocks.

The forging temperature was 2200°F. A 200°F drop in temperature was allowed during forging. The ingots forged with no indication of tears, cracks, seams, blow holes or other discontinuities. After the forging, the blocks were cut and numbered as follows: 13 in. rounds, 1 through 12, starting at bottom of ingot; 9 in. rounds, 20 through 31, starting at bottom of ingot; and 6 in. rounds, 40 through 61, starting at bottom of ingot. The blocks were then heat treated as described in Table I. The blocks employed for the various heat treatments were in pairs consisting of one block from near the top and one from near the bottom of the original ingot. The blocks were not allowed to cool to room temperature prior to the isothermal treatments indicated in Table I; rather, they were charged directly into heat treating furnaces.

Table I. Heat Treating Cycles

Treatment	13 In. Diam Block No.	9 In. Diam Block No.	6 In. Diam Block No.
A, air cooled after forging	1 10	20 29	40 57
B, equalized 1250°F, cooled 30°F per hr to 1150°F, held 48 hr, cooled 30°F per hr to 600°F, held 24 hr, air cooled	5 9 11 12	24 25 30 31	44 to 53 inclusive 58 to 61 inclusive
C, equalized 1250°F, cooled 30°F per hr to 1150°F, held 48 hr, air cooled	2 7	21 26	41 54
D, air cooled to 700°F, charged into furnace running at 600°F, held 24 hr, air cooled	3 8	22 27	42 55
E, air cooled to 700°F, charged into furnace running at 600°F, held 48 hr, air cooled	4 6	23 28	43 56

Hydrogen analyses employed vacuum fusion techniques on samples taken during teeming and on some blocks after heat treating. The samples taken from the melt were cast as ½ in. rounds in split chill molds. The samples taken from the heat treated blocks were trephined ¾ in. cores about 4 in. in length. The trephine was cooled with ice water during cutting. Immediately after the samples were cast or trephined, they were plunged into liquid nitrogen and held until the analyses were made.*

* Hydrogen analyses were supplied by the Republic Steel Corp. and the Babcock and Wilcox Co.

The heat treated blocks were ultrasonically tested for flakes with both a 1 and 2¼ megacycle crystal by the Midvale Co. All forgings were aged at room temperature for 36 days after the date of forging before ultrasonic tests were made. This aging period was at least 32 days after completion of all heat treatment. The delay is necessary to be assured that the incubation period for flake formation has

Table II. Results of Isothermal Treatments and Hydrogen Analyses

Treatment	13 In. Diam			9 In. Diam			6 In. Diam		
	Block No.	Result	Hydrogen Content, Cu Cm per 100 G	Block No.	Result	Hydrogen Content, Cu Cm per 100 G	Block No.	Result	Hydrogen Content, Cu Cm per 100 G
A	1	Flaked		20	Flaked		40	Flaked	
	10	Flaked		29	Flaked		57	Flaked	
B	5	No flakes		24	No flakes	4.84	44 to 53	No flakes	3.19 ± 45†
	9	No flakes		25	No flakes		58 to 61	No flakes	
	11	Flaked	9.60	30	No flakes				
	12	Flaked		31	No flakes				
C	2	Flaked		21	No flakes		41	No flakes	
	7	Flaked		26	No flakes		54	No flakes	
D	3	Flaked	9.78	22	Flaked		42	No flakes	
	8	Flaked		27	Flaked		55	Flaked	
E	4	Flaked		23	Flaked		43	No flakes	
	6	Flaked	5.39	28	Flaked		56	No flakes	

passed before examination. Further examination for flakes was accomplished by taking transverse slices from the center of the blocks. These slices were surface ground, macroetched and photographed.

Six to nine months after this work was completed, the possibility of flaking sound forgings produced from this heat was investigated by subjecting them to subsequent heat treatment. This material consisted of two 9 in. diam forgings (Nos. 25 and 30) and two halves of the 13 in. diam forgings (Nos. 5 and 9). The sections were austenitized at 1750°F for 1 hr and then air cooled, after which they were allowed to age for one month before examination. They were then examined ultrasonically and by macroetching as previously described.

Results and Discussion

The hydrogen contents, whenever analyzed, were consistently high in terms of normal commercial practice for the various treatments employed, and are indicated in Table II. The results of the ultrasonic inspection of the hydrogen impregnated blocks after the treatments described in Table I are given in Table II. All blocks air cooled from the forging temperature (treatment *A*) were severely flaked, indicating a strong susceptibility for flaking. The photograph of a transverse slice cut from block No. 1, Fig. 1, shows the flakes resulting from a simple air cool (treatment *A*).

The isothermal treatments designed to produce a completely pearlitic microstructure (treatments *B* and *C*) were successful in preventing flaking of all 6 and 9 in. diam blocks and some 13 in. diam blocks. Treatment *B* had an added safety factor, since the treatment designed to obtain a completely pearlitic structure was followed by a bainite transformation cycle. Considering the very high hydrogen content of this heat of steel (four to five or more times greater than normal mill practice), the 6 and 9 in. blocks would probably have flaked without special precautionary heat treating, as evidenced by the blocks given treatment *A* (air cooled).

The results obtained with the large blocks (13 in. diam) require a more detailed consideration, but are amenable to rationalization. Two of the 13 in. diam blocks subjected to treatments *B* and *C* were flake-free and four were flaked. Blocks Nos. 5 and 9 were completely flake-free. The remaining blocks given this treatment (Nos. 2, 7, 11 and 12) were very slightly flaked, as shown in Fig. 2. The microstructure of the slightly flaked blocks is practically complete pearlite with some evidence of low temperature transformation products typified by the structures shown in Figs. 3 and 4. In addition, these figures indicate that the flakes in these blocks were associated with the microconstituents that are low temperature transformation products. It is interesting to note that blocks Nos. 11 and 12, although they were given the additional bainite transformation treatment, were still slightly flaked. On the other hand, these two blocks originated from near the top of the ingot, where *positive segregation* may occur and contribute to flaking susceptibility.[8]

It is entirely possible, considering the extremely high hydrogen content of the steel, that very minute amounts of bainite and/or martensite in these blocks would cause flaking. As previously demonstrated,[7] there is a delicate balance of hydrogen embrittlement and stress required for flaking. Hence, for very high hydrogen content, as in this case, only a low stress would be required.

The isothermal treatments designed to produce a completely bainitic microstructure (treatments *D* and *E*) failed as antiflaking cycles except for three of the 6 in. diam blocks. Examination of the microstructures of some of these blocks revealed a mixed structure of low temperature bainite and martensite. Hence, these blocks would be expected to flake in accordance with the proposed theory.[7] It is obvious that the heat treatment prescribed did not satisfy the conditions for complete transformation to lower bainite. In fact, it is extremely difficult, as shown by the *TTT* diagram, to transform a steel of this composition completely into 100 pct lower bainite. Segregation will contribute to the difficulty of transforming to 100 pct bainite, since the variation in composition would dictate corresponding differences in the time-temperature relationships for complete transformation which cannot be predicted. Indeed, even if the treatment had been successful in producing 100 pct lower bainite, the possibility should not be ruled out that the microstresses associated with the formation of lower bainite might be sufficient to produce flakes in steels with these excessively high hydrogen contents.

If transformation stresses play a major role, then it might be possible to flake a forging by improper cooling (incomplete transformation), which had previously been produced flake-free by the use of an appropriate cycle (complete transformation), despite the fact that the hydrogen level would be lower during the second treatment. The 13 in. blocks (Nos. 5 and 9) that were originally cooled according to antiflaking cycle *B* and were flake free, were halved and recycled. This recycling was comprised of simple air cooling (cycle *A*) and, as anticipated, resulted in severe flaking, see Fig. 5, although the hydrogen content at the initiation of this recycling

was less than half that prior to the original cycle. Precisely the same treatments were applied to the unflaked 9 in. diam forgings (Nos. 25 and 30), but recycling did not produce flakes in this case. In the smaller size forgings, the hydrogen content would be expected to reduce relatively more than in the larger 13 in. diam forgings. In addition, the contributing influence of cooling stresses would be expected to be relatively less than for the larger section.

The results of this investigation indicate that transformation stresses play a major role in the flaking of heavy steel sections and that the influence of hydrogen is primarily through its action as an embrittling agent. However, it should be appreciated that any stress in the presence of hydrogen, regardless of its origin, could be sufficient to cause ruptures which may be considered flakes from a generalized point of view, although it is felt that the conventional flake patterns familiar to the industry are largely the result of transformation stress where other stresses, such as cooling, residual, externally applied, etc., may be contributory.

Acknowledgments

The authors wish to express their appreciation to A. O. Schaefer for his valuable cooperation during this investigation, and to Watertown Arsenal, Department of the Army, for sponsorship of this investigation and permission to publish the results.

References

[1] A. O. Schaefer: Current Studies of Large Forgings. *Metal Progress*, 1956, vol. 69, pp. 62-67.

[2] A. W. Dana, Jr., F. J. Shortsleeve, and A. R. Troiano: Relation of Flake Formation in Steel to Hydrogen, Microstructure, and Stress. *AIME Trans.*, 1955, vol. 203, pp. 895-905; JOURNAL OF METALS, August 1955.

[3] J. B. Gero and A. R. Troiano: Segregation: Major Cause of Flakes in Alloy Gun Steels. *Iron Age*, 1953, vol. 171, pp. 133-137.

Discussion of this paper sent (2 copies) to AIME by June 1, 1957 will appear in AIME *Transactions* Vol. 209, 1957, and in JOURNAL OF METALS, October 1957.

Nucleation of Dislocation Loops by Cracks in Crystals

It is shown by observations of etch-pits that dislocation loops are nucleated ahead of slowly moving cleavage cracks in LiF crystals. The loops are nucleated in dislocation-free regions of crystals. Loops larger than ~5 μ diam are stable at room temperature, but collapse at 400°C. The loops expand and contract under applied stresses.

by J. J. Gilman

IT is well established that dislocations exist in crystals and account for crystal plasticity.[1] However, the origins of the dislocations are not clear. Among the means by which dislocations might originate are: a) through crystal growth accidents, b) by the collapse of condensed sheets of vacancies, or c) by stress-induced nucleation. Theoretical calculations[2] have indicated that the last means should require very high stresses in order to operate. The purpose of this paper is to show that the stresses around the tips of cracks are large enough to nucleate large numbers of dislocation loops. Specifically, it will be shown that (100) cleavage cracks in LiF crystals nucleate dislocations in regions of the crystals where dislocations did not exist previously. It is believed that the use of LiF for this investigation does not restrict the significance of the results. In fact, it is believed that this complements and extends previous papers by the same author which dealt with metal crystals.[3,4]

The dislocations were detected by means of the etching techniques that were described in a previous paper by Gilman and Johnston.[5] In that paper it

J. J. GILMAN, Junior Member AIME, is associated with the Research Laboratory, General Electric Co., Schenectady.

TP 4425E. Manuscript, Aug. 24, 1956. New Orleans Meeting, February 1957.

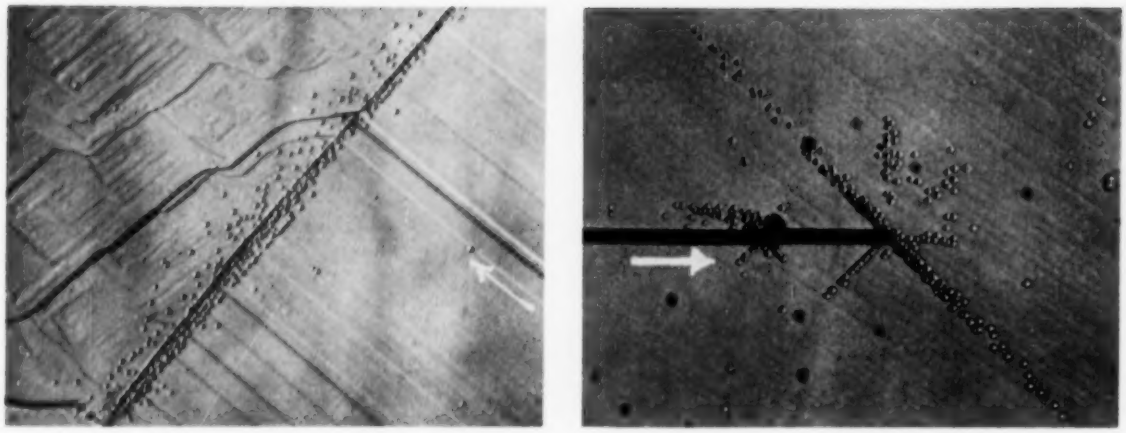

a b

Fig. 1—Etch pits at region of a LiF crystal where a cleavage crack was stopped. Arrows show crack propagation directions. a) A (100) surface of crack after the stopped crack has been moved farther on. X500. b) An (001) surface perpendicular to the plane of the crack. X250. Reduced approximately 20 pct for reproduction.

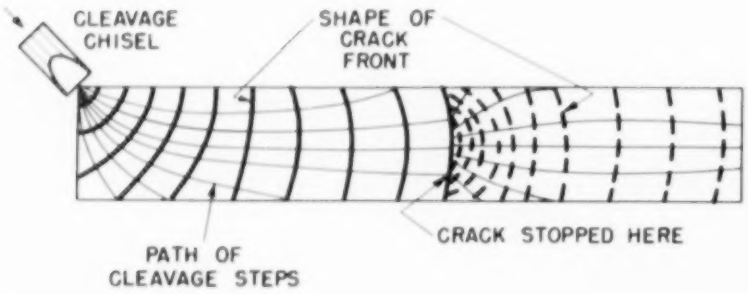

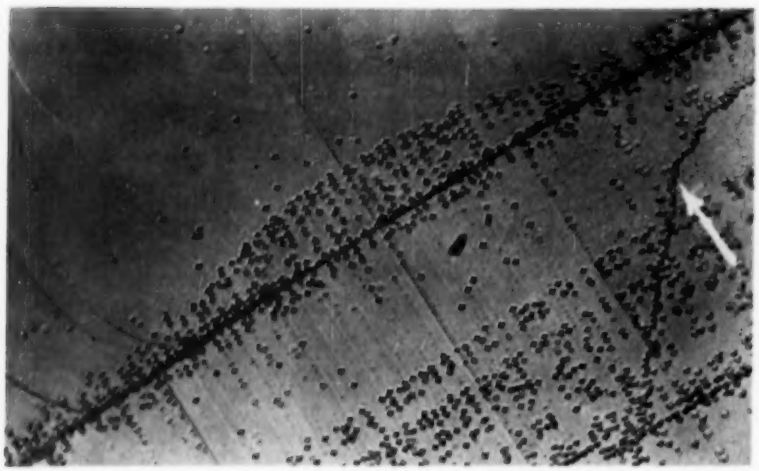

Fig. 2—Successive positions of the front of a cleavage crack as it passes through a LiF crystal. a) UPPER LEFT: Schematic diagram. b) UPPER RIGHT: Crack front positions in an etched and silvered crystal. X1. Enlarged approximately 50 pct for reproduction. c) LEFT: Bulging of crack front as crack starts moving. X250. Reduced approximately 30 pct for reproduction.

was shown that certain chemical reagents produce etch pits at dislocations in LiF in a highly specific way. The pits form only at dislocations and it is believed that all the dislocations (both screw and edge) that are present produce pits. Two reagents were used in the present work: 1) modified CP-4—100 cu cm HF, 160 cu cm HNO_3, 100 cu cm HAc, 1 cu cm Br_2, and at least 15 mg Fe; and 2) etch *A*—1 pt HF and 1 pt HAc, saturated with FeF_3.

Experiments

If a cleavage chisel is placed on a LiF crystal and is struck sharply with a hammer, the high velocity cleavage crack that results will not appreciably

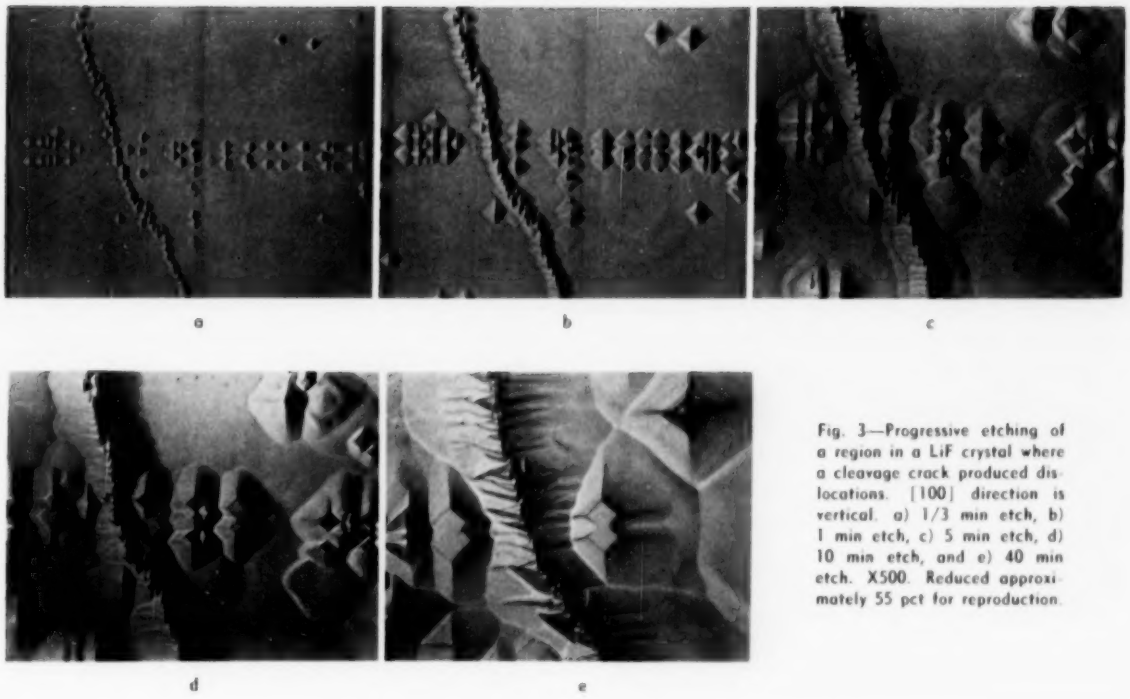

Fig. 3—Progressive etching of a region in a LiF crystal where a cleavage crack produced dislocations. [100] direction is vertical. a) 1/3 min etch, b) 1 min etch, c) 5 min etch, d) 10 min etch, and e) 40 min etch. X500. Reduced approximately 55 pct for reproduction.

change the dislocation content of the crystal (except near corners and edges). This has been shown by etching both halves of cleaved crystals and then matching the etch pit patterns of the two halves.* On the other hand, if the cleavage chisel is tapped lightly, a cleavage crack can be passed relatively slowly into a crystal and stopped somewhere inside. A second tap on the chisel completes the cleavage.

At regions of the cleavage surfaces of crystals where a cleavage crack has moved slowly, and especially where it has stopped, etching produces multitudes of characteristic dislocation etch pits. An example of this phenomenon is illustrated in Fig. 1a. The line of highest etch pit density in Fig. 1a shows where the crack front stopped. Note how the pits increase in density in the region where the crack was slowing down just before it stopped. Note also that the cleavage steps (the continuous dark lines) lie perpendicular to the line of the stopped crack front. Fig. 1b shows an end view of a stopped crack and the deformation at the tip.* When the stopped crack was set in motion again, it began to move at the middle of its front first, and then propagated forward and sidewise. The field of Fig. 1a was near the side of the crystal, so that the new crack front made a large angle with the old one, see Fig. 2a. The cleavage steps, which always lie approximately perpendicular to a moving crack front, indicate the successive positions of the bulging crack front. It may be seen that the number of etch pits caused by the crack decreased as its velocity increased, and approached zero at high velocities. Fig. 2 summarizes the way in which a cleavage crack passes through a crystal.

The significance of the etch pits in regions like the one shown in Fig. 1a was determined by progressively etching several regions of a crystal; Fig. 3 shows one of these regions. Five important factors

* The primary glide plane in LiF is the {110} plane and the glide direction is the <110> direction.

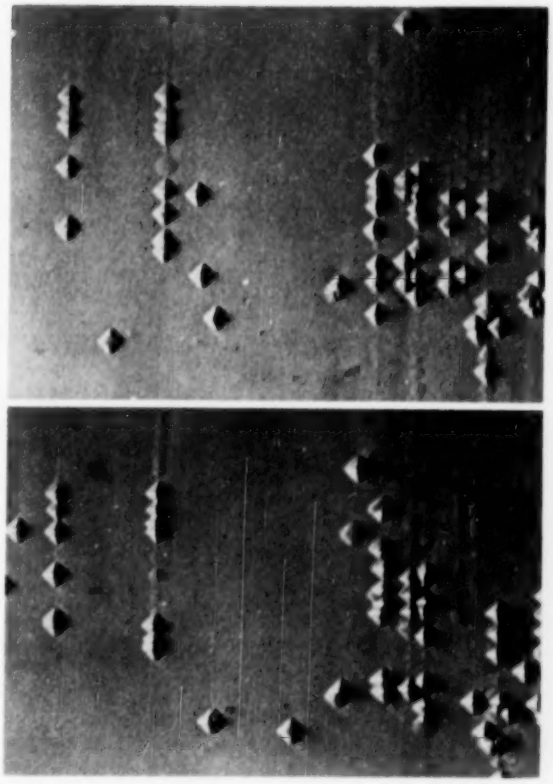

Fig. 4—Matched cleavage surfaces at region in crystal where a cleavage crack stopped momentarily. TOP: piece 1, printed normally; BOTTOM: piece 2, reversed in printing. Note the matched pits at the left. Also, although the pits at the right do not match, they lie along the same lines on both cleavage faces. X1000. Reduced approximately 10 pct for reproduction.

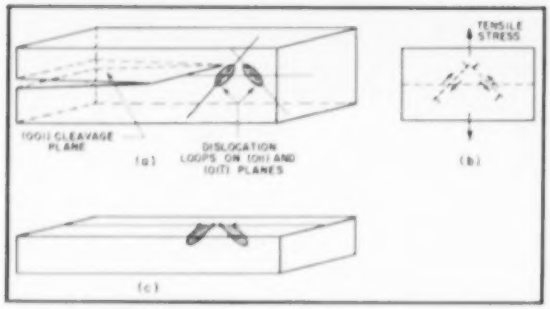

Fig. 5—Schematic drawing of dislocation loops formed by cleavage cracks: a) showing the planes of maximum shear stress (plane strain) on which glide would be expected to occur; b) end view showing the directions of the shear strains for the dislocation loops of Fig. 5a; and c) half-loops with their ends lined up after cleavage. Crystal a etched immediately after cleavage, aged 24 hr at room temperature, then re-etched. Crystal b etched after cleavage 2 hr at 400°C, then re-etched.

were observed. 1) The pits occur in pairs; 2, 4, 6, 8, etc. 2) The pits are asymmetric, see Fig. 3d, indicating that screw dislocations are being etched,[8] and that the dislocations lie on (110) planes which make an angle of 45° with the surface. 3) As etching proceeds the pits suddenly become flat-bottomed in pairs, indicating that the dislocations which produce them suddenly pop out of the crystal surface. In the absence of the dislocations, the pits do not get deeper, but continue to grow sidewise, and so produce flat-bottomed pits. 4) As the depth of etching increases, the distance between two pits of a pair decreases, indicating that one dislocation line connects two pits of each pair. 5) The pit densities in regions like this vary widely, but a typical value is 10^7 dislocations per sq cm. This is 500 to 1000 times higher than the 2 to 5 x 10^4 dislocations per sq cm that are typical after a fast crack has cleaved a crystal.

From these facts it may be deduced that the stress field of a slowly moving crack has sufficient time to form small dislocation loops in a LiF crystal. Some of the loops are created ahead of the tip of the crack, as may be shown by Fig. 4. Here matched cleavage surfaces are shown at a place where a crack stopped momentarily. Note the matching sets of pits on the two crystal faces. Each set of matching pairs of pits indicates the four ends of a dislocation loop that formed ahead of the crack and was severed as the crack passed. The sequence of events is illustrated schematically in Fig. 5. Not all of the pairs of pits on one surface can be matched with pairs on the other surface. In some cases, this may mean that dislocation half-loops were formed after the crack had passed. However, the fact that the unmatched pits usually lie along the same lines on both halves of a crystal suggests that most of the half-loops come from whole loops that formed ahead of the crack front. After these whole loops were severed by the advancing crack, their ends moved so that the two cleavage surfaces no longer matched.

The dislocation half-loops which cracks produce in LiF are not rigidly fixed in the crystal. The loops tend to creep out of a crystal at a rate that depends on the temperature. Also, the action of an applied stress moves them in and out of LiF crystals. The creep of the loops has been demonstrated by etching crystals immediately after loops have been produced in them, waiting 24 hr at room temperature, and then etching again. The second etch reveals that during the period between etches some of the dislocation half-loops move entirely out of the crystal and others shrink in size by various amounts, Fig. 6a. The process can be accelerated by heating a crystal. Fig. 6b shows that virtually all of the dislocation half-loops move out of a crystal if it is heated at 400°C for 2 hr.

A unique opportunity for observing individual dislocations in motion is provided by the half-loops caused by cracks. The dislocation loops are produced by a stress-state in which the principal tensile stress is normal to the plane of the cleavage crack, Fig. 5b.* Therefore, if a tensile stress is applied parallel to the cleavage surface, it will tend to cause shrinkage of the half-loops, whereas a compressive stress parallel to the cleavage surface will tend to cause expansion of the loops. In the present experiments, thin cleaved plates of LiF crystals were etched after they had been slowly cleaved. Then bending stresses were applied to them. Finally, they were re-etched. Where the cleavage surface was stressed in tension, the loops tended to disappear, leaving two or more flat-bottomed etch pits in their wake. On the other hand, where the surface was placed in compression, the loops tended to expand, as shown in Fig. 7.

In Fig. 7, isolated dislocation loops can be seen which were expanded by a stress. They appear as two pyramidal etch pits lying on the same line, but on either side of two flat-bottomed etch pits. One case of the expansion of a double loop may also be seen. This appears as four flat-bottomed pits on the same line as two nearby pyramidal pits and two pyramidal pits that lie some distance away.

* On the interior of the crystal, plane strain prevails, so that the maximum shear stress is on (110) planes containing the crack propagation direction. Near the side external surfaces, plane stress prevails, so the shear stress is higher on the (110) planes that do not contain the propagation direction. Thus, two active glide planes operated in Fig. 1a, whereas four operated in Fig. 1b.

Discussion

Origin of Loops—The evidence of the above experiments indicates quite clearly that the observed dislocation loops are nucleated in dislocation-free regions of the crystals and do not come from existing Frank-Read sources.[2] Three factors are in evidence: a) an incubation time precedes the appearance of the loops,* b) the density of loops is large compared with the initial dislocation density, and c) no pits are found inside the loops; therefore, no dislocations seem to have been present which could have multiplied by the Frank-Read or other self-multiplication mechanisms.

Two observations make it apparent that the dislocation loops are heterogeneously rather than homogeneously nucleated. First, the loops appear at irregularly spaced places along a crack front. Second, more loops than one often appear in sequence at the same place. Both observations indicate that there are special places in the crystals that are preferred for dislocation nucleation and for retention

* Since the loops are about 5μ in diameter, and the maximum crack velocity[4] in LiF is expected to be about 2 x 10^5 cm per sec $= \frac{1}{3}\left(\frac{C_{11}}{\rho}\right)^{1/2}$, where C_{11} is the elastic constant and ρ the density, the incubation time is at least 10^{-3} μ sec and probably is much larger. Also, the time for appearance of the loops does not seem to be limited by the possible dislocation velocity. A crack moving at 1/3 sound velocity would require the loop to expand at about 1/6 sound velocity. This should not restrict the dislocation motion,[1] and therefore is not expected to cause the incubation time.

Fig. 6—Movement of dislocation half-loops in absence of an applied stress. X500. Reduced approximately 10 pct for reproduction.

in the crystal. On the other hand, there are a great many places where dislocations are nucleated, so the difference between a preferred site and any other place in the crystal may not be very great. Even though heterogeneous dislocation nucleation occurs, it will be shown that homogeneous dislocation nucleation is possible near a crack tip.

The energy of a dislocation loop of radius r in a LiF crystal is equal to the loop perimeter, $2\pi r$, times the energy per unit length of dislocation,

$Kb^2 \ln\left(\frac{r}{r_o}\right) + C$.[11] The first term of the expression is the elastic energy around the dislocation line outside a tube of radius r_o. This radius r_o is estimated to be about 5.7A from the latent heat of fusion; $\Delta H_m = 1.1\text{x}10^{10}$ erg per cu cm.[7] K is an elastic constant, and b is the Burger's vector = 2.85Å. According to Eshelby, Read, and Shockley,[5] for (110) [110] dislocations in cubic crystals

$$K = \frac{1}{4\pi}\left[C_{11}(C_{11}-C_{12})\right]^{1/2} \left\{ \frac{\cos^2\alpha}{2} + \frac{(C_{11}C_{12})\sin^2\alpha}{\left[C_{11}(C_{11}C_{12}2C_{44})\right]^{1/2}} \right\}$$

where the C_{ij}'s are the crystal elastic constants and α is the angle between the Burger's vector and the dislocation line. Using $C_{11} = 11.8$, $C_{12} = 4.34$, and $C_{44} = 6.3\text{x}10^{11}$ dyne per sq cm,[6] the average value of K is: $\bar{K} = 4.4\text{x}10^{10}$ dyne per sq cm. C is the inelastic energy inside r_o; estimating from the results of Huntington, Dickey, and Thomson[8] it should average about $1.9\text{x}10^{-7}$ erg per cm for (110) [110] dislocations in LiF.

When a dislocation loop is formed by a stress, τ, the glide inside the loop does work equal to $-\pi\tau b\pi r^2$. Therefore, the energy of formation of a dislocation loop in LiF is

$$U = (Kb^2 \ln\frac{r}{r_o} + C)2\pi r - \tau b\pi r^2.$$

This energy is a maximum at a critical radius

$$r_c = \frac{\bar{K}b}{\tau}(\ln\frac{r_c}{r_o} + 1) + \frac{C}{\tau b}.$$

The graphical solution of this equation is plotted in Fig. 8 together with the energies of dislocation loops of critical size.

The shear stress at a distance (d, θ) from the tip of a crack is given approximately by

$$\tau = \frac{1}{S_{11}}\sqrt{a/d}\sin\theta\cos\theta$$

where a is a dimension of atomic scale ≈ 6Å,[12] and S_{11} is the elastic compliance = $10.6\text{x}10^{-12}$ dyne per sq cm. In the present case the crack is on a (100) plane of LiF and the glide plane is (110), so $\theta = 45°$. If stresses as high as $2.6\text{x}10^{11}$ dyne per sq cm are required to nucleate dislocation loops, Fig. 8, then the stress near a crack tip is high enough to nucleate dislocations at distances not more than about 50Å from the crack tip.

Stability of Loops—Many newly formed dislocation loops probably disappear when the stress that produced them near the crack tip is no longer present. However, some of the loops stick in the crystals and they are the ones that are observed as half-loops. It is believed that the reason for their

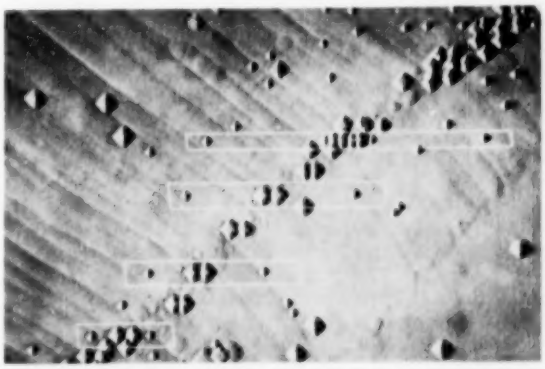

Fig. 7—Expansion of dislocation half-loops under an applied shear stress (approximately 1 kg per sq mm). The screw orientation of the dislocations is seen and the intercept of the glide plane (110) with the cleavage surface (100) is horizontal in the photograph. Several pairs of pyramidal pits may be seen which left a pair of flat-bottomed pits in their wake. Note the two concentric loops indicated by two sets of four pits just above the center of the photograph. X900. Reduced approximately 50 pct for reproduction.

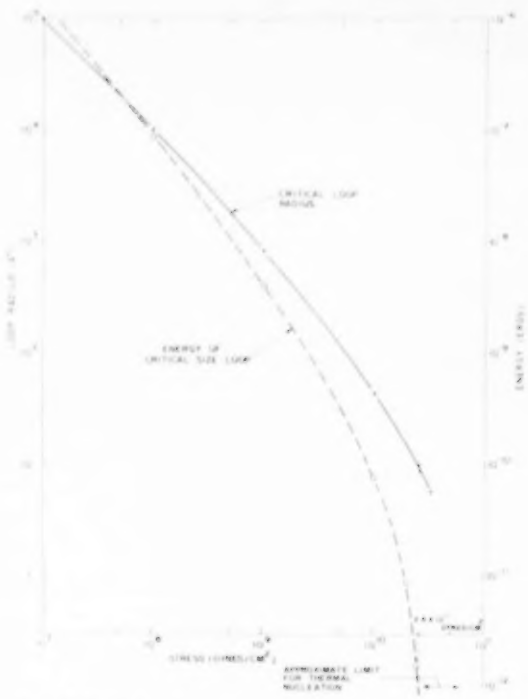

Fig. 8—Critical radius and energy of dislocation loops in LiF crystals.

stability is that the crystal lattice offers a resistance to the motion of a dislocation and the line tension of the loops is not strong enough to overcome the lattice resistance.

The stress required to hold a semicircular loop of diameter, D, inside a crystal is

$$\tau = 2(Kb^2 \ln D/2r_o + C)/bD$$
$$= 4.5 \times 10^7 \text{ dyne per sq cm}$$

when D is large compared with atomic dimensions. This is believed to be approximately equal to the resistance of the LiF lattice to dislocation glide, since it is within a factor of two of the macroscopic yield stress of LiF crystals (unpublished results).

Implications for Fracture and Glide—It is clear from Fig. 7 that the dislocations introduced by cleavage can cause glide during subsequent stressing of a crystal. If the loops glide without multiplication, the amount of glide that they could produce would be relatively small. Actually, they will multiply and hence produce arbitrary amounts of glide. Therefore, the manner in which a crystal is cleaved and treated after cleavage can play an important role in its plastic behavior, as will be discussed in detail in a later paper.

The cleavage process itself is affected by the production of dislocation loops. The work that is done during its production must come from the energy of the moving cleavage crack. For a loop of 5 μ diam, the work done, $\pi\tau bD^2/4$, is about 10^{-4} erg if it forms under a stress of 2×10^{10} dyne per sq cm. Therefore, the energy absorbed by a typical density of loops (10^7 per sq cm) is about 10^3 erg per sq cm, or a few times the surface energy. Clearly, this amount of energy absorption can reduce the velocity of a cleavage crack[10] and thereby raise the stress needed to cause fast cleavage. In addition, since a screw dislocation crosses the cleavage plane at each end of a loop, two small cleavage steps are formed at each loop, and these absorb energy.[10] In previous papers[10, 11] it was postulated that certain cleavage-step patterns in zinc crystals are caused by screw dislocations introduced by local deformation at the tips of cracks; it was also predicted that a strong velocity effect might be expected. Both of these ideas have been confirmed by the present results.

This investigation also has shown that the existing theories of fracture are incomplete. The theories are based on the idea that local stresses as large as the cohesive strength of a solid can be created by *piling-up* a large number of dislocations at an obstacle.[12] Fracture is supposed to be nucleated by the high local stresses. The difficulty is that the local stresses might nucleate dislocations (plastic flow) instead of fracture. The concentrated stresses at a dislocation pile-up are similar to those at a crack tip. Since the latter can nucleate dislocations, it is reasonable to suppose that the former can also. The present results show that this possibility must be taken quite seriously in attempts to construct fracture theories.

Summary

It is shown that slowly moving or stopped cracks in LiF crystals nucleate dislocation loops just ahead of the crack tips. The loops can be nucleated in dislocation-free regions of the crystals. The resistance of the crystals to glide holds the loops in place at room temperature but at 400°C they move out of the surface. The dislocation loops may be expanded or contracted by applied stresses. It is shown that the stresses near a crack tip are sufficiently high to nucleate dislocation loops at distances less than about 50A from the crack tip. It is pointed out that the dislocation nucleation phenomenon has important implications for studies of crystal plasticity and fracture.

Acknowledgments

The author benefited during the course of this work from discussions with N. Thompson, Bristol University, and W. G. Johnston and J. C. Fisher, Research Laboratory, General Electric Co.

References

[1] A. H. Cottrell: *Dislocations and Plastic Flow in Crystals*, pp. 32, 53. Oxford Press, New York, 1953.

[2] F. C. Frank and W. T. Read: *Physical Review*, 1950, vol. 79, p. 722.

[3] J. J. Gilman and W. G. Johnston: Observations of Dislocation Glide and Climb in Lithium Fluoride Crystals. *Journal of Applied Physics*, 1956, vol. 27, p. 1018.

[4] D. K. Roberts and A. A. Wells: The Velocity of Brittle Fracture. *Engineering*, 1954, vol. 178, p. 820.

[5] J. D. Eshelby, W. T. Read, and W. Shockley: Anisotropic Elasticity with Applications to Dislocation Theory. *Acta Metallurgica*, 1953, vol. 1, p. 251.

[6] R. F. S. Hearmon: The Elastic Constants of Anisotropic Materials. *Reviews of Modern Physics*, 1946, vol. 18, p. 409.

[7] L. I. Quill: *The Chemistry and Metallurgy of Miscellaneous Materials*, p. 196. McGraw-Hill Pub. Co. New York, 1950.

[8] H. B. Huntington, J. E. Dickey, and R. Thomson: Dislocation Energies in NaCl. *Physical Review*, 1955, vol. 100, p. 1117.

[9] *Chemistry of the Solid State*, p. 115. Ed. by W. E. Garner. Butterworths, London, 1955.

[10] J. J. Gilman: Propagation of Cleavage Cracks in Crystals. *Journal of Applied Physics*, 1956, vol. 27, p. 1262.

[11] F. C. Frank: The Origin of Dislocations. Pittsburgh Conference, ONR, 1950, p. 89.

[12] E. Orowan: Energy Criteria of Fracture. *Welding Journal*, 1955, vol. 34, p. 157s.

[13] A. N. Stroh: The Formation of Cracks in Plastic Flow II. *Proceedings* Royal Soc., London, 1955, vol. 232, p. 548.

[14] J. J. Gilman: Cleavage Steps on Zinc Monocrystals: Their Origins and Patterns. *AIME Trans.*, 1955, vol. 203, p. 1252; JOURNAL OF METALS, November 1955.

Discussion of this paper sent (2 copies) to AIME by June 1, 1957 will appear in AIME *Transactions* Vol. 209, 1957, and in JOURNAL OF METALS, October 1957.

Strain Induced Transformation in Beta Brass

The β-phase of Cu-Zn and Cu-Zn-Ga alloys partially transforms when cold worked at low temperatures. X-ray data are presented on the new structures formed (which depend upon composition), on densities of stacking faults in them, on M_s temperatures, and on the tendency to revert to body-centered-cubic structure.

by T. B. Massalski and C. S. Barrett

THAT metals and alloys of the body-centered-cubic structure tend to become unstable at low temperatures is so nearly universal that any exceptions are worthy of special attention. Studies of the exceptions may disclose unrecognized examples of metastability or may shed light on the nature of some of the factors that stabilize the body-centered-cubic phase.

Among the structurally analogous body-centered-cubic *3/2 electron compounds*, the β-phase in the Cu-Zn system deserves further attention for, although this phase is known to undergo partial martensitic transformation on cooling below room temperature to the temperature of liquid nitrogen when the composition is less than about 42 wt pct Zn, it does not transform on cooling when there is more than this amount of zinc present.[1-4] The present authors recently found that an alloy containing 48.35 wt pct Zn could be transformed, however, if deformed severely at room temperature or lower temperatures.[5] This discovery led to the suggestion that the jerky flow of β-brass single crystals[6] and some of the unusual temperature variations of the yield strength and hardness are due to strain-induced transformation during the tensile tests. The present investigation is an extension of that work to cover the entire available range of compositions of Cu-Zn β-phase alloys and certain interesting compositions of the β-phase in the Cu-Zn-Ga system. Particular attention is given to the structure of the transformation product resulting from cold work, which is found to vary with alloy composition, and to the temperature range in which transformation can be induced in the various alloys.

The composition limits of the body-centered-cubic phase in the Cu-Zn system, based on a recent review by Raynor[7] and the precision determinations of Beck and Smith,[8] are shown in Fig. 1a; in the β region the alloys are disordered and in the β' region they are ordered. The rate of ordering is so rapid that a high degree of order is found in any of these alloys immediately after quenching.

T. B. MASSALSKI, Junior Member AIME, formerly with the Institute for the Study of Metals, University of Chicago, is now with the University of Birmingham, Birmingham, England. C. S. BARRETT, Member AIME, is with the Institute for the Study of Metals, University of Chicago, Chicago.

TP 4423E. Manuscript, Aug. 3, 1956. New Orleans Meeting, February 1957.

Experimental

The nine binary and four ternary alloys of this investigation were prepared from cathode copper (99.99 pct purity), electrolytic zinc (99.99+ pct), and gallium (99.98+ pct). All alloys were cast in transparent Vycor tubing, homogenized at temperatures between 800° and 890°C, and quenched in water. Ternary alloys were cast in small amounts (~5 g) to predetermined compositions to fall along a line of constant electron concentration in the ternary system. Changes of weight during the casting operation of the ternary alloys were not greater than 1 part in 2500 from the intended nominal weights and therefore their compositions were accepted without chemical analyses. All binary alloys were cast in larger amounts (100 to 150 g), homogenized, and hot rolled after preheating to 800°C. The central portion of the rolled strip of each alloy was annealed for eight days and quenched in brine. All binary alloys were analyzed chemically. The compositions, heat treatments, and metallographic appearances of all alloys are tabulated in Table I.

Various samples were subjected to heat treatment or cold work at several temperatures and were then examined metallographically or by means of X-rays. Specimens about 6x6x3 mm in size were examined metallographically to confirm the presence of the β'-phase after quenching. Cold work was introduced by fastening each sample between two pieces of steel, cooling the assembly to the desired temperature, and transfering it rapidly to a vise where moderate or severe compression was immediately applied. Cold working at liquid helium temperature was done by a chisel-shaped tool mounted on an X-ray spectrometer, described elsewhere.[9] All metal-

Fig. 1—Cu-Zn diagram. A: portion of the equilibrium diagram showing the boundaries of the β phase. B: variation of the M_s temperature with composition after Kurdjumow and Titchener and Bever; and variation of the M_s temperature with composition after present work.

lographic examinations were carried out at room temperature.

For X-ray examination, cold working was introduced by filing the samples at various temperatures; except at liquid helium temperature, in which case cold working was done by severely deforming the surface of a flat specimen mounted inside the X-ray spectrometer. Specimen filings were examined in the powdered form either immediately after filing or after a specified heat treatment.

Initial X-ray work was carried out at low temperatures in the X-ray spectrometer on one alloy (X); the details of these tests have been published earlier.[5] Subsequently the powder X-ray method was employed, using CuKα, FeKα, and CrKα radiations, and for most of the investigation a General Electric X-ray diffractometer was employed with crystal-monochromatized CuKα radiation and a scanning speed of 12° per hr. The recorder charts were calibrated with a copper sample of high purity for which an accurate parameter was obtained by precision powder methods. In later stages of the work additional calibration was introduced by mixing the sample filings with annealed filings of Carbonyl nickel of known parameter ($d = 3.5230 \pm 1$Å). In addition to chart-recording of X-ray intensity the weak lines of the transformation product in alloy X were also investigated by the point counting technique.

Experimental Results

Metallographic—The metallographic appearance at room temperature of alloys cold worked at various temperatures is tabulated in Table II. Alloy X, deformed at liquid helium temperature, showed traces of the transformation product when examined at room temperature. Samples of alloys 6, X, 7, and 8 were cooled to liquid helium temperature without cold working, after prior electropolishing. No scars due to transformation were observed on subsequently examining these alloys at room temperature.

The appearance and the amount detected of the transformation product varied with composition. In alloys where the transformation could be induced relatively easily, i.e., at low zinc contents, the transformation product appeared in the form of large patches or streaks of indefinite shape with slightly pink coloration, as well as in the form of thin platelets lying along certain crystallographic planes of the matrix. In all cases the platelets could be seen to join smoothly into the larger bulk material of the transformation product. A typical microstructure is that of alloy 2 deformed at room temperature, and is shown in Fig. 2.

In samples with high zinc content less transformation product could be produced by cold work and in these it took the form of fine streaks of pink coloration aligned along certain directions of the matrix. Deformation bands could now also be seen within the remaining strained body-centered-cubic (β') matrix. A typical microstructure in this case is that of alloy 6 deformed at liquid nitrogen temperature and examined at room temperature. This is shown in Fig. 3.

With still higher zinc content the amount of observable transformation product decreased further, so that the traces detectable in alloy 7 deformed at liquid nitrogen temperature, see Table II, could well be, at least in part, due to some very fine cracks. However, when the width of the transformation product could be resolved sufficiently to show the typical pink coloration, the identification was unmistakable. The approximate variation of the M_s temperature with composition in zinc-rich alloys is indicated in Fig. 1b.

X-Ray Diffraction Patterns—Details of X-ray work are set out in Table III, and the general appearance of the X-ray spectrograms of several binary and ternary alloys deformed by filing at room temperature are shown in Figs. 4 and 5.

From these two figures it can be seen that both the amount of the transformation product and its general character in the cold worked state changed with composition. In the binary system, alloy 1, when quenched from 891°C into brine, underwent a complete transformation from the β' structure into the face-centered-cubic structure (by means of a mechanism recently referred to as *massive transformation*,[6] in which high speed interphase boundary migration probably plays a prominent role). This alloy was thus face-centered-cubic at room temperature before filing, and no further change of structure occurred with filing. All other alloys possessed the body-centered-cubic structure before filing. In alloys 2 to 7, after filing at room temperature, the amount of the transformation product decreased as the zinc content increased, and in zinc-rich alloys there was observable a gradual reversion to body-centered-cubic at room temperature. (Perhaps this accounts for the failure of previous investigators to notice the transformation.)

Another interesting feature of the X-ray pattern is that as the alloys increase their resistance to transformation the lines from the decreasing amount of transformation product change from the typical face-centered-cubic pattern to a pattern that possesses certain characteristics of the close-packed-hexagonal structure. This is evidenced by the gradual disappearance of the face-centered-cubic 200

Table I. Appearance of Alloys As Quenched

Alloy	Wt Pct Cu	Wt Pct Zn	Wt Pct Ga	Final Time	Annealing Temperature	Metallographic Appearance After Polishing and Etching
1	62.05	37.95	—	8 days	891°C	spontaneously transformed to α* by massive grain boundary growth
2	60.27	39.73	—	8 days	850°C	β'† + traces of α at grain boundary
3	58.25	41.75	—	8 days	800°C	β' + traces of α at grain boundary
4	56.50	43.50	—	8 days	800°C	all β'
5	54.41	45.59	—	8 days	800°C	all β'
6	52.63	47.37	—	8 days	800°C	all β'
X	51.65	48.35	—	4 days	800°C	all β'
7	50.02	49.98	—	8 days	800°C	all β'
8	48.11	51.89	—	8 days	800°C	β' + traces of γ‡ at grain boundaries and inside grains
11-Ga	74.00	1.01	24.99	7 days	750°C	spontaneously transformed to close-packed-hexagonal (martensitic appearance)
D5	63.94	23.90	12.16	7 days	750°C	all β'
1-Ga	53.82	43.35	2.88	5 days	750°C	all β'
2-Ga	56.52	37.97	5.51	5 days	750°C	all β'

* The α represents the face-centered-cubic phase.
† The β' represents the body-centered-cubic phase, presumably ordered.
‡ The γ represents the complex cubic phase.

reflection and the appearance of a broad intensity peak identified as the close-packed-hexagonal 10·0 reflection as the zinc content increases. The nature of the patterns suggests that stacking faults are numerous in the transformation products of all of the alloys, analogous to the faulted products found in lithium and sodium, the patterns of which were recently discussed in detail by Barrett.[9]

Thus, although the transformation product has a close-packed structure at all compositions, the structure has predominantly cubic packing in alloys rich in copper and tends to equal probability of cubic and hexagonal packing at higher zinc contents, with hexagonal predominating in alloys 7 and 8. In terms of atomic configuration this indicates a tendency for the close packed planes gradually to change from the ABCABCABC stacking arrangement into the ABABABABAB stacking arrangement.

Additional evidence for the above general conclusions was provided by the X-ray patterns obtained at liquid nitrogen and liquid helium temperatures from the cold-worked alloys *X*, 7, and 8, see Table III. These alloys showed increasing amounts of transformation with increasing cold work and decreasing temperature. In alloy *X* the indefinite dual character of the transformation product indicated by the presence of both the 200 face-centered-cubic reflection and 10·0 close-packed-hexagonal reflection was maintained, although the relative intensities of these reflections varied somewhat from one experiment to another; some filings yielded only a trace of the 200 face-centered-cubic reflection, while in others the relative intensities were nearly equal. In alloys 7 and 8, however, the transformation structure showed only the close-packed-hexagonal reflections.

The four alloys studied in the ternary system Cu-Zn-Ga were chosen to fall upon a line of constant electron concentration ($e/a = 1.476$) corresponding with alloy *X* of the binary system. Along that line all ternary alloys possess the β-brass structure at high temperatures.[11] On rapid quenching the structure undergoes a martensitic type of transformation in alloys rich in gallium, but can be retained undecomposed in alloys of low gallium content. The retained structure is, however, metastable and can be transformed by cold working, as in the binary Cu-Zn alloys. Of the four ternary alloys studied, the first three (1Ga, 2Ga, and D5) were completely body-centered-cubic (presumably ordered, β') before filing and the last (alloy 11) had transformed on quenching into a structure that was predominantly close-packed-hexagonal. After filing, alloy 11 retained the predominantly close-packed-hexagonal character, alloy D5 transformed completely, and alloys 2Ga and 1Ga transformed partially and showed increasing amounts of retained body-centered-cubic phase. It can be seen from Fig. 5 that the character of the transformation product now changes from almost completely close-packed-hexagonal in the alloy with least zinc to a pattern with nearly equally intense 200 face-centered-cubic and 10·0 close-packed-hexagonal reflections in the alloys with least gallium.

Attempts to repeat the experiments of Greninger,[1] in which additional lines were found after quenched filings of 40 wt pct β'-brass were very lightly deformed, resulted in such irreproducible patterns that structure determination was not possible.

Lattice Parameters—An attempt was made to attain some precision in the measurement of lattice parameters of the phases in the binary Cu-Zn alloys in order to see whether or not the face-centered-cubic product resulting from the strain-induced decomposition of the β' phase has parameters that would be expected from an extrapolation of the α-phase parameters to the higher zinc contents, and to look for line shifts due to stacking faults, of the type predicted by Paterson.[12] In this work two methods were used for calibration of the charts: the body-centered-cubic lines were used as an internal standard, as was recently done in a similar problem,[8] and admixed nickel filings were employed. The lattice constants computed from various individual lines indexed as face-centered-cubic reflections are plotted in Fig. 6. The 311 reflection, which was free from overlapping reflections and should have been shifted least* by the stacking faults, is seen to lie on an extrapolation of the data for the α-phase reported by Beck and Smith.[8]

* Twelve components of this line are sharp and unshifted, six shift outwards, and six shift inwards five times as far.

The superposition of the least broadened close-packed-hexagonal reflections, 00·2, 11·0, 11·2, and 00·4 on the corresponding reflections from the face-centered-cubic component, namely 111, 220, 311, and 222, respectively, prevented an accurate determination of the axial ratio of the hexagonal material. It was obvious, however, that the axial ratio was near the value $c/a = 1.633$ of ideal packing of spheres, as was concluded in the study of alloy *X*.[8]

Stacking Fault Densities—Paterson[12] has shown that an estimate can be made of the frequency of occurrence of stacking faults, from the shifts of

Table II. Metallographic Appearance of Alloys After Cold Work

Alloy	Deformed at Room Temperature; Repolished, Then Examined Metallographically	Deformed at Liquid Nitrogen Temperature; Repolished, Then Examined at Room Temperature	Deformed at Liquid Helium Temperature; Repolished, Then Examined at Room Temperature
1	deformed α;* no other structure		
2	β'† + pink transformation product		
3	β' + pink transformation product, shows deformation bands		
4	β' + pink transformation product, shows deformation bands		
5	β' + pink transformation product, shows deformation bands	β' + pink transformation product	
6	β' + pink transformation product, shows deformation bands	β' + pink transformation product	
X	β' + pink transformation product, shows deformation bands	β' + pink transformation product	β' + pink transformation product
7	β' + traces of pink transformation product, shows deformation bands	β' + pink transformation product	
11-Ga	deformed close-packed-hexagonal		
D5	appears completely transformed		
1-Ga	β' + transformation product		
2-Ga	β' + transformation product		

* The α represents the face-centered-cubic phase.
† The β' represents the body-centered-cubic phase, presumed to be ordered.

powder diffraction lines in face-centered-cubic metals. Warren and Warekois[9] and Greenough and Smith[10] have used Paterson's method and the former have shown that stacking fault densities in cold worked α-brasses increase from about one in every 200 planes to one in every 26 planes as the zinc content increases from 0 to 35 wt pct. The patterns of strain-induced face-centered-cubic material of the present investigation provide an opportunity to extend these determinations of fault densities to higher zinc content.

Referring to Fig. 6, it is seen that the apparent lattice constants computed from the calibrated chart records differ when different reflections are used, and only the 311 reflections, relatively unshifted by faults, lie on the extrapolated α-phase curve. The 200 and 420 reflections are shifted to lower diffraction angles (higher apparent lattice constants), while the 331, 220, and 111 are shifted oppositely. These shifts are of the nature expected from faults, and if stacking fault densities are computed from the shifts of 111 and 200 lines, the results of Fig. 7 are obtained. In this plot the probability that a fault will be induced by deformation at any given close-packed plane, denoted by α, is shown as a function of zinc content for the present alloys and those previously investigated. The probability parameter α can be determined from measurement of the difference in the diffracting angle between two suitable lines, first in the annealed state and then in the cold worked state. In the present work the angular distance 2θ between the 111 and 200 lines, corresponding to the lattice parameter computed from the 311 reflection, was assumed to represent the annealed state separation.

The exact values shown in Fig. 7 are probably not highly significant, for the theory is based on the assumption that the faults are distributed randomly on a single set of parallel planes, and that the effects of the various parallel sets in a crystal are superimposed in the pattern. The assumption is also made that cold-work broadening is symmetrical about the Bragg angle. Also, the precision of the data in the present series was not as high as would be desired. Nevertheless, the general trends seem clear: fault densities increase steadily with zinc concentration through the strain-induced face-centered-cubic phase, in agreement with a similar trend found in the cold-worked equilibrium α-phase.

Reversal of the Transformation Induced by Cold Work—In zinc-rich alloys small amounts of the transformation product produced by severe cold working and filing were unstable and reverted to the β'-phase if the filings were left at room temperature for a period of time. In alloy 8 transformation induced by cold work at temperatures of liquid helium, N_2, and solid CO_2 disappeared on warming to room temperature. (Roughly ½ hr was required for this.) The small amount of the transformation product observed in alloy 7 immediately after filing at room temperature, see Fig. 4, was almost undetectable after about 12 hr. In the case of alloy *X* a trace of the transformation product was still present after three to four months, annealing at room temperature. In all alloys reexamined after such prolonged annealing some evidence of general recovery of the matrix and the transformed phase was observed: the X-ray reflections were less broad.

Alloys *X* and 7 were also subjected to cold work and annealing above room temperature. In alloy *X* decreasing amounts of transformation could be detected after filing at 50° and 100°, and practically none after filing at 115°C. In each of these tests the filings were immediately quenched to room temperature. The M_s temperature for this alloy is therefore in the vicinity of 115°C. If filings obtained at room temperature, which were partially transformed, were annealed for 15 min at 100°C no remaining transformation product lines could be detected. No transformation could be detected in alloy 7 after filing at 75°C and exposing at room temperature.

Similar experiments were also tried with alloys 2 through 6. In these cases, however, the transformation product produced at room temperature was sufficiently stable to resist reversion to body-centered-cubic or to β' up to temperatures at which change of composition by interphase diffusion could no longer be neglected.

Discussion

The copper-rich boundary of the β-phase in the equilibrium diagram, Fig. 1, slopes to higher zinc contents with decreasing temperatures. It is interesting to note that this tendency is continued both in the M_s curve and the M_s curve at lower temperatures. It would not be expected, of course, that either of these curves should be an exact continuation of

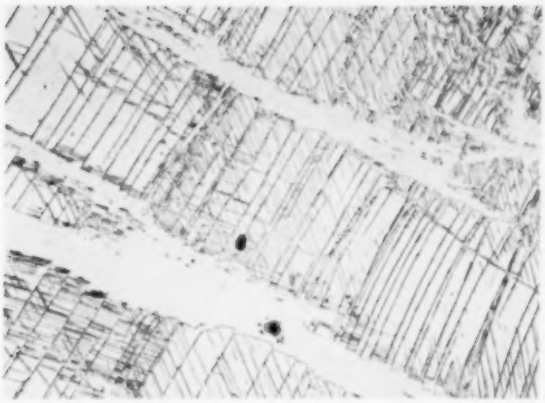

Fig. 2—Microstructure of alloy 2, cold worked at room temperature; showing transformation product within the β matrix. Polished and etched in dichromate. X500. Reduced approximately 40 pct for reproduction.

Fig. 3—Microstructure of alloy 6, cold worked at liquid nitrogen temperature; showing transformation product and β matrix with deformation bands. Polished and etched in dichromate. X150. Reduced approximately 40 pct for reproduction.

the high temperature equilibrium phase boundary, for at low temperatures there is no segregation of zinc to provide different compositions in the two phases.* Nevertheless it is clear that with increasing zinc content the stability of the face-centered-cubic structure decreases and that of the body-centered-cubic increases. M_s drops approximately 47°C per 1.0 wt pct Zn, which, within experimental accuracy, is the same as the rate of drop of the M_s.

* A reader suggests, with reference to Fig. 1, that M_d must lie within the $\alpha + \beta'$ field. This, however, is not a necessity, since the $\alpha + \beta'$ field refers to equilibrium compositions of α and β', whereas the transformation product formed at M_d is of nonequilibrium composition. It was also proposed that the free energies of the structures present are equal at M_d, but this, too, is not necessarily true.

Since β-brasses of any compositions below about 50 wt pct Zn transform if cold worked at room temperature it appears likely that the single crystals tested by Ardley and Cottrell[6] at room temperature were subject to transformation, since their composition was 48.81 wt pct Zn. It therefore remains a possibility, as suggested in an earlier report,[5] that the jerky flow observed by these investigators was due to strain-induced transformation in their crystals. Jerky flow in β-brass of about 49 wt pct Zn has also been observed in polycrystalline samples.[10] This, however, is in the very low temperature region, where a variety of metals of different structure show this type of stress-strain behavior, perhaps for reasons having nothing to do with phase transformations.

It is now apparent that β Cu-Zn is metastable at all compositions at which it can be made homogeneous when quenched to room temperature, and probably at even the highest zinc concentrations. It should be noted that it is perhaps only the disordered phase that is metastable above 43 pct Zn, since plastic deformation is required to initiate the transformation in this composition range, and plastic deformation always causes some disordering of the superlattice. Perhaps also any *reversion* of the transformation product occurs only to β'. Reversion of the strain-induced phase to β or to β' occurs at room temperature in alloys containing more than 48 pct Zn.

If the M_s curve is extrapolated to lower zinc compositions than those for which it can be determined experimentally, a remarkably large temperature interval is found between M_s and M_d, roughly 625°C at 42 pct Zn. Plastic strain is therefore unusually effective in overcoming the barrier to transformation compared with other low temperature body-centered-cubic transformations, such as those in lithium and sodium.[8]

Theoretical attention has been given to the basis for stability of the β Cu-Zn phase by Zener[16] and Jones.[17] Zener has emphasized the importance of a low (110) [110] shear constant, i.e., a low value of

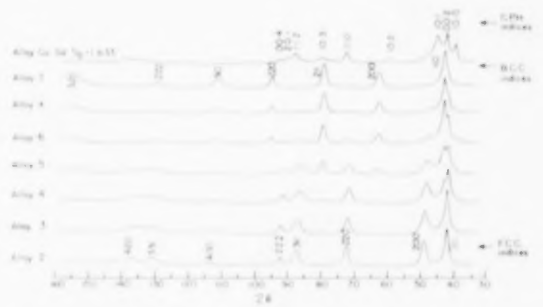

Fig. 4—X-ray diffraction charts of binary Cu-Zn alloys filed at room temperature. One binary Cu-Ga alloy is included as an example of deformed, ideally close-packed hexagonal structure.

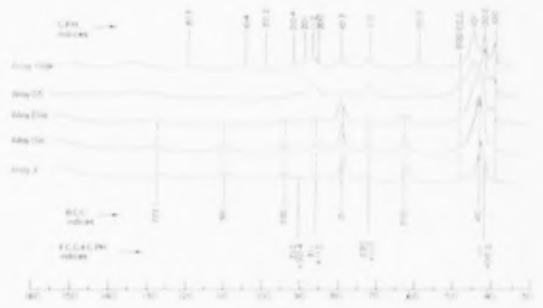

Fig. 5—X-ray diffraction charts of Cu-Zn-Ga alloys lying along a line of constant electron concentration e/a = 1.476.

Table III. Structures as Indicated by X-rays of Cold Worked Alloys After Various Treatments

Alloy	Worked at 5°K, X-rayed at 5°K	Worked at 78°K, X-rayed at 78°K	Worked at 195°K, X-rayed at 195°K	Worked at 25°C, X-rayed at 25°C	Worked at Temperature Below M_d, X-rayed at 25°C after Specified Time
1				α*	
2				α, trace H‡	
3				β',† α, H	
4				β', α, H	
5				β', α, H	
6				β', α, H	
X	β', α, H	β', α, H		β', α, H	after three months, β', trace α, trace H
7	β', H	β', H		β', H	after 14 hr, β'
8	β', H	β', H	β', H	β'	after 30 min, β'
11-Ga				H	
D5				α, H	
1-Ga				β', α, H	
2-Ga				β', α, H	

* The α represents the face-centered-cubic structure identified by the presence of 200 reflection.
† The β' represents the body-centered-cubic structure identified by the presence of 110 reflection, presumably ordered.
‡ The H represents the close-packed-hexagonal structure identified by the presence of 10.0 reflection.

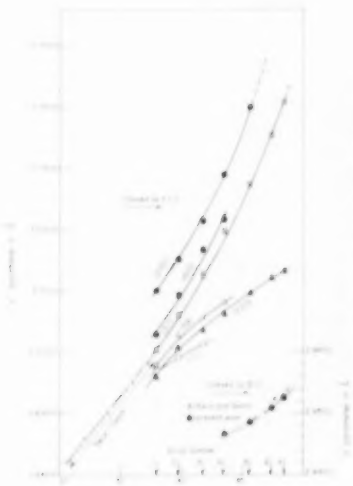

Fig. 6—Variation of lattice parameters with composition of cold worked Cu-Zn alloys. Parameters corresponding with lines indexed as face-centered-cubic are shown individually, and parameters corresponding with the body-centered-cubic structure are shown as one extrapolated value for all lines.

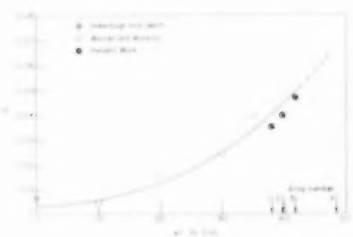

Fig. 7—Variations of the stacking fault probability coefficient α with composition of Cu-Zn alloys.

$\frac{1}{2}$ $(C_{11} - C_{12})$ as a factor decreasing the stability of β-brass; and Jones has proposed that the interaction of nearly free electrons with the {110} faces of the Brillouin zone increases this shear constant and thereby increases the stability of the body-centered-cubic structure. From this latter point of view it is possible that cold work and, connected with it, blurring of the Brillouin zone through stacking fault broadening[9] and perhaps also through stress broadening, reduces the zone stabilization sufficiently to allow transformation. However, the recent work of Zirinsky[9] on transformations of the body-centered-cubic *3/2 electron compound* in Au-Cd alloys shows that the degree of elastic anisotropy (and the tendency toward transformation) in the Au-Cd case is larger than in the Cu-Zn at corresponding temperatures and compositions. The Au-Cd alloys thus transform on simple cooling at all compositions, showing that electron concentration must be of only secondary importance in stabilizing the β structure. Similarly, the ternary alloys of the present series, although lying along a line of constant electron concentration in the phase diagram, were completely unstable when rich in gallium and nearly stable when rich in zinc.

Although these ternary alloys were prepared with identical electron concentration the size factor and the degree of order were not constant throughout the series. The Cu-Ga β-phase is almost certainly disordered, since it is only stable near 25 atomic pct Ga, and it may well be that it is unstable at low temperatures because of the lack of order. On the other hand, the increasing distortion of a lattice due to the relative number and size of the solute atoms present may be an important factor. In the ternary system Cu-Zn-Ga the size factor increases on passing from the gallium-rich to the zinc-rich alloys;[11] previous studies have shown that small or negative size factors favor the equilibrium close-packed-hexagonal structure over the body-centered-cubic structure.[11, 20]

Attention is called to the progressive change in the nature of the transformation product and its amount with composition in the binary alloys, but it is not possible at the present time to state which factor or factors is responsible.

Summary

Binary β'-phase Cu-Zn alloys from 39.73 wt pct Zn through 51.89 pct Zn were found to transform on cold work at low temperatures, according to both metallographic and X-ray diffraction evidence. The amount of the transformation product increased with increasing zinc content, and its structure changed from face-centered-cubic with stacking faults to close-packed-hexagonal with stacking faults. The face-centered-cubic structure has parameters that would be expected from an extrapolation of the α-phase parameters, but with line shifts of the type expected from stacking faults. The close-packed-hexagonal structure has an axial ratio near 1.633.

The β-brasses of any composition below about 50 wt pct Zn transform if cold worked at room temperature; the M_s temperature drops ~47°C per each additional wt pct Zn, similar to the M_s curve. The transformation product is metastable at room tem-

perature and reverts to the body-centered-cubic or β' phase when the zinc content exceeds 45.59 pct.

It is pointed out that possibly disordering by cold work necessarily precedes the transformation (above 43 wt pct Zn), and that reversion may occur only to the ordered (β') phase. The transformation characteristics of body-centered-cubic Cu-Zn-Ga alloys indicate that electron concentration is not the major factor controlling the instability of the β-phase.

Acknowledgments

The authors wish to acknowledge with thanks the assistance of Mrs. L. Castelliz in computing the X-ray data, Mrs. B. Nielsen in the metallographic work, and K. K. Ikeuye for preparation of the samples. This work was supported in part by Contract No. N-6ori-02004 with the Office of Naval Research.

References

[1] A. B. Greninger and V. G. Mooradian: *AIME Trans.*, 1938, vol. 128, p. 337.
[2] E. Kaminsky: *Zh. Tekh. Fiz.* USSR, 1938, vol. 5, p. 953.
[3] G. Kurdjumow: *Zh. Tekh. Fiz.* USSR, 1948, vol. 18, p. 999.
[4] A. L. Titchener and M. B. Bever: *AIME Trans.*, 1954, vol. 200, p. 303; JOURNAL OF METALS, February 1954.
[5] C. S. Barrett and T. B. Massalski: Symposium on Transformations, Institute of Metals, London, November 1955.
[6] G. W. Ardley and A. H. Cottrell: *Proceedings* Royal Soc., London, 1953, vol. A219, p. 328.
[7] G. V. Raynor: Annotated Equilibrium Diagram Series, No. 3, 1944. Institute of Metals, London.
[8] L. H. Beck and C. S. Smith: *AIME Trans.*, 1952, vol. 194, p. 1079; JOURNAL OF METALS, October 1952.
[9] C. S. Barrett: X-ray Study of the Alkali Metals at Low Temperatures. *Acta Crystallographica*, 1956, vol. 9, p. 671.
[10] D. Hull and R. D. Garwood: Symposium on Transformations, Institute of Metals, London, November 1955.
[11] T. B. Massalski and G. V. Raynor: *Journal* Institute of Metals, 1954, vol. 82, p. 539.
[12] M. S. Paterson: *Journal of Applied Physics*, 1952, vol. 23, p. 805.
[13] B. E. Warren and E. P. Warekois: *Journal of Applied Physics*, 1953, vol. 24, p. 951; *Acta Metallurgica*, 1955, vol. 3, p. 473.
[14] G. B. Greenough and E. M. Smith: *Proceedings* Physical Soc., 1955, vol. B68, p. 51.
[15] E. T. Wessel: *Trans.* ASM, 1956, vol. 49, preprint No. 3.
[16] C. Zener: *Physical Review*, 1947, vol. 71, p. 846; *Elasticity and Anelasticity of Metals*. University of Chicago Press, Chicago, 1948.
[17] H. Jones: *Philosophical Magazine*, 1952, vol. 43, p. 105.
[18] S. Zirinsky: *Acta Metallurgica*, 1956, vol. 4, p. 164.
[19] C. S. Barrett: Crystal Structures of Li-Mg Alloys at Low Temperatures. *Acta Metallurgica*, 1956, vol. 4, p. 528.
[20] W. Hume-Rothery, P. W. Reynolds, and G. V. Raynor: *Journal* Institute of Metals, 1940, vol. 66, p. 191.

Discussion of this paper sent (2 copies) to AIME by June 1, 1957 will appear in AIME *Transactions* Vol. 209, 1957, and in JOURNAL OF METALS, October 1957.

High-Strength Zirconium Alloy: Zr-4 Wt Pct Sn-1.6 Wt Pct Mo

A heat-treatable, ternary alloy of zirconium is described. This alloy is readily rolled at 800°C and has more than four times the creep strength of pure zirconium at 500°C. The tensile strength of the alloy in the annealed condition is about 90,000 psi, and it may be heat-treated to a strength of more than 140,000 psi. In the annealed condition, the alloy can be cold reduced more than 20 pct. The alloy is harder in the air-quenched condition than as water quenched. This behavior was found to be associated with a reaction similar to age hardening.

by W. Chubb

FOR the past several years there has been considerable interest in the development of zirconium and zirconium alloys for application in nuclear reactors. In a portion of the development work being conducted, attention has been given to the development of high-strength zirconium alloys. One of the most outstanding alloys developed in the course of this work is Zr-4 wt pct Sn-1.6 wt pct Mo.[1]

W. CHUBB, Member AIME, is Principal Metallurgist, Battelle Memorial Institute, Columbus, Ohio.

TP 4329E. Manuscript, Dec. 20, 1955. Cleveland Meeting, October 1956.

Fabrication and Test Methods

Over 50 ingots of zirconium containing either tin and molybdenum or both have been evaluated in the process of selection of an optimum composition. Most of these were prepared as 20-g arc-melted buttons; a few were prepared by induction melting. All ingots were prepared by the use of Foote Mineral

Fig. 1—Micrograph of Zr-4 wt pct Sn-1.6 wt pct Mo alloy; cold rolled, heated to 900°C for 1 hr, and water quenched; α zirconium in a matrix of retained β, 293 Dph. X500. Reduced approximately 20 pct for reproduction.

Fig. 2—Micrograph of Zr-4 wt pct Sn-1.6 wt pct Mo; heated to 1000°C for 15 min, quenched to 900°C for 10 min, and water quenched; acicular α in β, 274 Dph. X500. Reduced approximately 15 pct for reproduction.

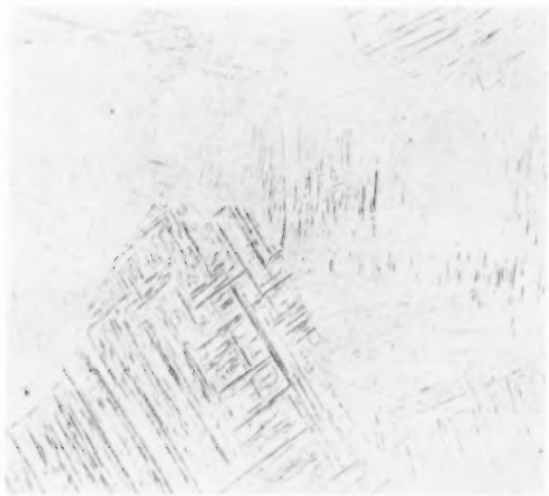

Fig. 3—Micrograph of Zr-4 wt pct Sn-1.6 wt pct Mo; heated to 1000°C for 15 min and water quenched; martensite, 285 Dph. X100. Reduced approximately 15 pct for reproduction.

Co. iodide zirconium. The tin used had a purity of 99.9 wt pct, and the molybdenum was 99 wt pct pure.

Two large ingots have been prepared by double arc melting in a copper crucible, and the properties of these two ingots constitute the basis for most of this report. One ingot weighed 1000 g and had an analysis of 4.0 wt pct Sn and 1.6 wt pct Mo. The other ingot weighed 3800 g and had an analysis of 3.9 wt pct Sn and 1.6 wt pct Mo.

Both ingots were forged at 900°C to 1-in.-thick slabs. Hot rolling to sheet and bar stock was accomplished at 800°C. These operations were performed in air, and no cracking or splitting of any degree was encountered. The hot-rolled products were coated with a powdery white oxide to a depth of 0.001 to 0.002 in. This was removed by sandblasting and by pickling in 50 pct nitric, 2 pct hydrofluoric acid solution.

Quenching rate studies were accomplished by sealing ⅛-in. cubes of metal in evacuated Vycor tubes. The capsules were heated to temperature, held for 1 to 3 hr, depending on the temperature, and cooled at one of three different rates. Water quenching was accomplished by breaking the Vycor capsules directly over a water bath; air quenching was accomplished by pulling the Vycor capsule from the furnace and allowing it to cool on a well-ventilated asbestos sheet; furnace cooling was accomplished by leaving the capsules in a furnace which cooled at a rate of about 100°C per hr.

Isothermal transformation studies were done in much the same manner, except that all samples were heated to 1000°C for 15 min. These samples were quenched by breaking the Vycor capsules under the surface of a lead bath. After a predetermined length of time, the samples were removed from the lead and water quenched.

An end-quench test was performed on a ½-in. sq bar. This bar was 3 in. long and was supported in the end-quench apparatus by means of a carriage bolt screwed into one end of the bar. The bar and attached bolt were sealed in an evacuated Vycor tube. This was heated to 900°C for 1 hr. The Vycor tube was broken on the lip of the furnace, and the bar was end-quenched by a ¼-in. water stream. One side of the bar was ground to a depth of about 0.001 in., and the entire length of the bar was surveyed by Dph measurements at appropriate intervals.

The metallographic technique for this alloy is identical to that for any zirconium alloy containing tin. Zirconium alloys containing tin tend to stain brown or black when etched with dilute HF or NH_4HF_2. This stain can be removed by any strong acid that dissolves tin faster than it does zirconium. The procedure used for this alloy involved grinding to 600 grit, followed by polishing on a cloth lap, and using Linde B alumina. Worked metal was removed by alternate polishing and etching with 10 pct NH_4HF_2 solution. Final etching was accomplished by using a solution containing 10 to 20 pct HNO_3 and ½ to 1 pct NH_4HF_2.

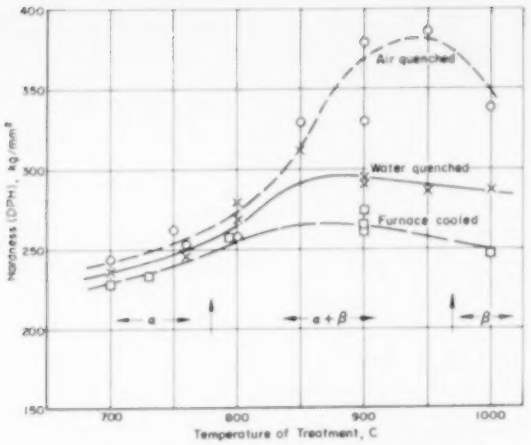

Fig. 4—Effect of cooling rate on the hardness of Zr-4 wt pct Sn-1.6 wt pct Mo alloy taken at room temperature after equilibrating at temperature for 1 to 3 hr.

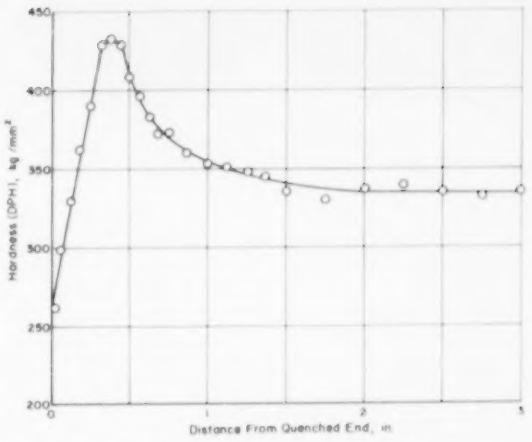

Fig. 5—End-quench test on Zr-4 wt pct Sn-1.6 wt pct Mo alloy; bar quenched from 900°C.

All tensile tests were made in duplicate on a 20,000-lb Baldwin-Southwark universal testing machine. A clip-on extensometer with a 1-in. gage length was used to measure strain. This extensometer utilized SR-4 gages on compression loops and is accurate to ±0.0001 in. per in. The speed of travel of the head of the testing machine was 0.02 in. per min. Tests at room temperature were made in air; tests at 500°C were made in helium. Tensile specimens were made from sheet stock about 0.07 in. thick, and the reduced section of the specimens was ½ in. wide and 2 in. long. Tensile specimens were heat treated in evacuated Vycor tubes or in a stainless steel vacuum furnace. Creep testing at 500°C was performed in vacuum creep units.

Hardness data were obtained at elevated temperatures by means of a hardness-testing device operating in a vacuum chamber. Both the specimen and the indenter are heated to the test temperature. Indentations are made by applying a dead-weight load of 1000 g to a 136° pyramid indenter. By moving the specimen after each indentation, a large number of indentations can be made at any temperature or series of temperatures from room temperature to 1000°C. This equipment has been described in greater detail elsewhere.[3]

Impact tests were run on standard *V*-notch Charpy impact specimens. Specimens were machined from ½-in. sq bar and were heat treated in a stainless steel vacuum furnace.

Olsen ductility tests were performed by using a standard Olsen testing machine (⅞-in.-diam ball) and sheet test specimens about 0.07 in. thick.

The weldability of the alloy was evaluated by seam welding strips together. Tensile specimens were cut from the resultant sheet in such a manner that the weld comprised the longitudinal axis of the test specimen. Welding was accomplished in a vacuum-tight chamber in an atmosphere of argon gas.

Heat-Treatment Response

In their paper on the binary Zr-Mo system, Domagala, McPherson, and Hansen[4] pointed out that the β allotrope of zirconium can be retained on quenching alloys containing more than 5 wt pct Mo. Alloys containing less than 5 wt pct Mo transform on air quenching to acicular α or, on very rapid quenching, to martensite.

By means of suitable heat treatments, it is possible to produce all three forms of zirconium in the Zr-Sn-Mo alloys. The retention of β-zirconium is accomplished by equilibrating the alloy at 800° or 900°C to produce an α phase low in molybdenum and a β phase enriched in molybdenum. When the equilibrated alloy is water quenched, the enriched β phase is retained. Martensite is produced by heating the alloy to 1000°C and water quenching. Acicular α-zirconium is produced by heating the alloy to 1000°C and cooling at any rate slower than about 1000°C per min. Coarse acicular α-zirconium is sometimes called Widmanstatten α-zirconium. Figs. 1 through 3 are examples of these structures. The structure shown in Fig. 2 has slightly lower hardness than the structure shown in Fig. 1. This effect may be a grain-size effect, or it may be that there is more retained β in Fig. 2.

Table I. Effect of Heat Treatment Upon the Tensile Properties of Zr-3.9 Wt Pct Sn-1.6 Wt Pct Mo Alloy

Heat Treatment No.*	0.2 Pct Offset Yield Strength, Psi	Ultimate Strength, Psi	Elongation to Maximum Load, Pct	Total Elongation in 1 In., Pct	Reduction of Area, Pct	Tensile Modulus of Elasticity, 10⁶ Psi
1	86,400	111,700	6	24	41	10
2	71,200	90,600	10	20	24	15
3	86,200	124,000	3	5	9	12
4	89,600	103,300	3	3	2	10
5	123,800	143,300	2	2	1	13
6	74,900	97,600	10	12	3	13
7	62,800	88,600	10	10	10	14

* Treatment 1: Hot rolled at 800°C and air cooled.
Treatment 2: Hot rolled at 800°C, furnace cooled, cold rolled, heated to 730°C for 3 hr, and furnace cooled, see Fig. 13.
Treatment 3: Hot rolled at 800°C, reheated to 800° for 2 hr, and water quenched.
Treatment 4: Heated to 900°C for 1 hr and water quenched, see Fig. 1.
Treatment 5: Heated to 900°C for 1 hr and air cooled in a Vycor capsule, see Fig. 6.
Treatment 6: Heated to 900°C for 1 hr and furnace cooled at a rate of 50°C per hr.
Treatment 7: Heated to 900°C for 1 hr, cooled to 700°C and held for 24 hr, and furnace cooled, see Fig. 7.

Fig. 6—Micrograph of Zr-4 wt pct Sn-1.6 wt pct Mo alloy; cold rolled, heated to 900°C for 1 hr, and air cooled in a Vycor tube; equilibrium α zirconium in a matrix of acicular α zirconium formed from β-zirconium, 380 Dph. X500. Reduced approximately 15 pct for reproduction.

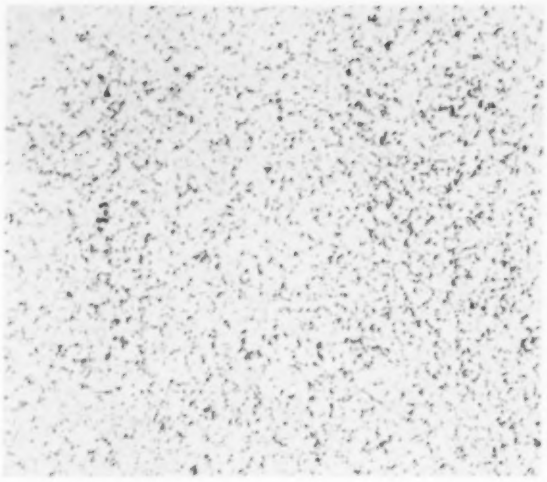

Fig. 7—Micrograph of Zr-4 wt pct Sn-1.6 wt pct Mo; cold rolled, heated to 900°C for 1 hr, cooled to 700°C and held for 24 hr, and furnace cooled. $ZrMo_2$ spheroids formed at α-zirconium grain boundaries, 258 Dph. X500. Reduced approximately 15 pct for reproduction.

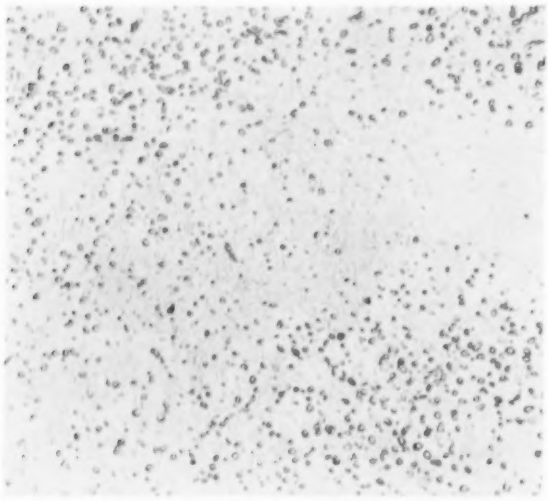

Fig. 8—Micrograph of Zr-4 wt pct Sn-1.6 wt pct Mo; cold rolled, heated to 950°C for 1 hr, and water quenched; equilibrium α zirconium in a matrix of martensite, 287 Dph. X250. Reduced approximately 15 pct for reproduction.

Fig. 9—Micrograph of Zr-4 wt pct Sn-1.6 wt pct Mo; heated to 1000°C for 15 min, quenched in lead at 600°C, held for 2 hr, and water quenched; acicular α-zirconium, 366 Dph. X250. Reduced approximately 15 pct for reproduction.

The effect of quenching rate upon the hardness of the Zr-4 wt pct Sn-1.6 wt pct Mo alloy is shown in Fig. 4. This figure shows that a high quenching rate produces hardnesses intermediate to hardnesses produced in air cooling and in furnace cooling. The low hardness produced by furnace cooling was expected, and the low hardness produced by water quenching could be explained by assuming that β solid solution was retained at room temperature. It has been shown that β-zirconium is much weaker and softer than α-zirconium of the same alloy content.[5] The high hardnesses produced in air quenching were difficult to explain on the basis of any previous work done with zirconium alloys. Further tests showed that variability of the quenching rates was not at fault; the faster the quenching rate (between air-quenching rates and water-quenching rates) the softer the alloy became.

As a final check on the validity of the data shown in Fig. 4, a subsize end-quench test was run. The results of a hardness traverse on this bar are shown in Fig. 5. An X-ray diffraction pattern obtained from the quenched end of the bar disclosed the presence of retained β-zirconium; α-zirconium was also present as an equilibrium structure. The microstructure of the end of the bar was identical to that shown in Fig. 1. Near the end of the bar, small spikes of acicular α-zirconium began to appear in the microstructure of the β phase. At about ¼ in. from the quenched end of the bar, the microstruc-

ture was identical to that shown in Fig. 6. At about $\frac{5}{8}$ in. from the end of the bar, a darker etching behavior suggested that $ZrMo_2$ was beginning to precipitate from the β phase. About 1 in. from the quenched end of the bar, the microstructure was similar to that in Fig. 7. Microscopic particles of acicular α-zirconium appeared long before peak hardness was reached, and microscopic particles of $ZrMo_2$ appeared considerably after peak hardness was reached. Since microscopic α-zirconium is usually relatively soft, and since the quantity of $ZrMo_2$ available for hardening this alloy is extremely small, the microstructural data do not seem adequate to explain the hardness peak shown in Fig. 5.

Possibly the hardness phenomena found in this alloy are related to a very similar type of age-hardening reaction that has been noted in certain titanium alloys.[4] Titanium metallurgists have shown that the hardening reaction is intimately associated with the decomposition of the β-titanium phase. The exact nature of the hardening of β is still a matter of considerable speculation.

The foregoing results on the end-quench bar suggested that useful information might be obtained by studying the time-temperature-transformation characteristics of the Zr-4 wt pct Sn-1.6 wt pct Mo alloy. Generally speaking, the results were disappointing. Apparently the rate of decomposition of β-zirconium containing 1.6 wt pct Mo is many times faster than the rate of decomposition of the enriched β produced by equilibrating the alloy at 900°C. Conversely, the rate of precipitation of $ZrMo_2$ from the enriched β is much faster and more readily detectable than in the case of the homogeneous alloy produced at 1000°C. Figs. 2, 3, 8, 9, and 10 show some of the structures obtained in the course of these studies. Fig. 8 shows that the β to $\alpha+\beta$ transus is near, but above, 950°C. Fig. 10 shows that the $\alpha+\beta$ to $\alpha+ZrMo_2$ transus is above 700°C. The results of the isothermal-transformation studies are summarized in Figs. 11 and 12. These figures show once again that the hardening reaction is associated with the early stages of β decomposition. Within the limits 400° to 700°C, the maximum hardness achieved in isothermal transformation is lower and occurs at shorter times the higher the temperature of transformation.

It is apparent that a wide variety of properties and structures can be produced in the Zr-4 wt pct Sn-1.6 wt pct Mo alloy by controlling fabrication procedures, heat-treatment temperatures, and quenching and aging schedules. Some of the tensile properties that result from typical fabrication and heat-treatment procedures are listed in Table I.

Fig. 10—Micrograph of Zr-4 wt pct Sn-1.6 wt pct Mo; heated to 1000°C for 15 min, quenched in lead at 700°C, held for 2½ hr, and water quenched; acicular α-zirconium and $ZrMo_2$, 302 Dph. X500. Reduced approximately 15 pct for reproduction.

Table II. Creep Properties of Zirconium and Zr-3.9 Wt Pct Sn-1.6 Wt Pct Mo Alloy at 500°C

Property	Arc Melted Iodide Zirconium	Zr-3.9 Wt Pct Sn-1.6 Wt Pct Mo Alloy
Stress to cause 1 pct total deformation in 100 hr, psi	3,700	16,000
Stress to cause 1 pct total deformation in 1000 hr, psi	1,800	11,000
Stress to cause ½ pct total deformation in 1000 hr, psi	1,400	7,500
Estimated stress to cause 1 pct total deformation in 10,000 hr, psi	900	4,000

Treatments 1 and 2 illustrate the high strength and ductility that are achieved in the normal course of fabricating this alloy by standard procedures. Fig. 13 illustrates the disperse structure that results from treatment 2. Treatments 2, 3, and 4 show the effects of heating the alloy to progressively higher temperatures and water quenching; the yield strength of the alloy tends to increase slightly, but the ductility and modulus are drastically reduced. The effect on the modulus is interesting, and can be directly related to the amount of β-zirconium retained in the alloy. It is known that the modulus of β-zirconium is much lower than that of α-zirconium,[5] but a value for retained β at room temperature has never been reported. Assuming that the structure produced by treatment 4, Fig. 1, contains 50 pct retained β and that the moduli of α- and β-zirconium in a mixture of the two are additive, then the modulus of β-zirconium at room temperature must be about 6×10^6 psi. As illustrated in Figs. 4 and 5, retained β-zirconium is a comparatively soft and weak material. This material is probably responsible for the low tensile ductility produced by treatments 3 and 4.

Table III. Deep Drawing Properties of Zirconium Alloys

Alloy Identification	Sheet Thickness, In.	Load at Fracture, Lb	Cup Depth at Fracture, In.
Arc melted, iodide zirconium	0.072	1040	0.24
Arc melted, iodide zirconium	0.071	1950	0.31
Zr-4 wt pct Sn-1.6 wt pct Mo	0.077	1310	0.12
Zr-5.1 wt pct Sn	0.068	860	0.10

Treatments 4 through 7 illustrate the effects of cooling the alloy at progressively slower rates from a temperature at which the alloy contains β-zirconium. Treatment 5 shows that, at first, the tensile strength is greatly increased in accordance with the results shown in Figs. 4 and 5. The ductility is very low, but the modulus has already begun to increase. Treatments 6 and 7 show that considerable ductility can be restored by cooling the alloy at very slow

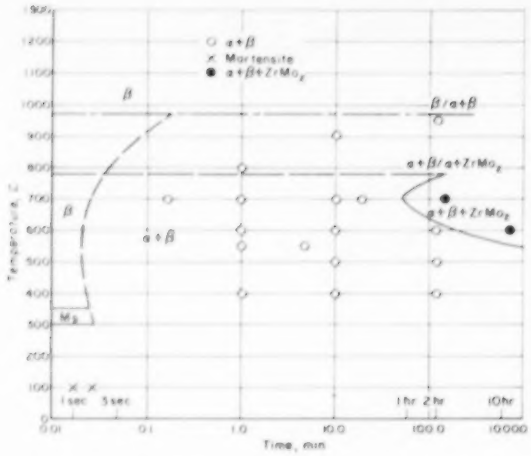

Fig. 11—Transformation characteristics of Zr-4 wt pct Sn-1.6 wt pct Mo alloy.

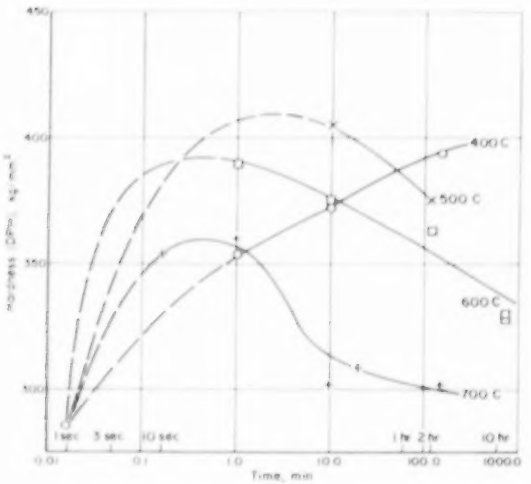

Fig. 12—Transformation hardness characteristics of Zr-4 wt pct Sn-1.6 wt pct Mo alloy. Isothermal transformation at temperatures indicated.

rates. The ultimate difference between treatments 2 and 7 is evidently an effect of grain size and dispersion of the $ZrMo_2$ as illustrated by Figs. 7 and 13. The coarser $ZrMo_2$ and larger grain size produced by treatment 7 result in lower strength and lower ductility.

Variation of Properties with Temperature

The effects of temperature upon the tensile and hardness properties of the Zr-3.9 wt pct Sn-1.6 wt pct Mo alloy are shown in Fig. 14. Compared with the alloy in the α-annealed condition, the hot-rolled alloy is harder at low temperatures and softer at elevated temperatures. This seems to be a characteristic of many zirconium alloys. The effect is probably caused by the presence of unstable β-zirconium and by the unequal distribution of alloying elements between the α and β phases in the hot-rolled alloy. The low hardness of the alloy at 800°C is responsible for the ease with which the alloy can be hot rolled at this temperature.

The tensile properties shown in Fig. 14 are for the alloy as fabricated by hot rolling at 800°C, furnace cooling, cold rolling, and annealing at 730°C for 3 hr and furnace cooling. In this condition, the alloy has also been tested in creep at 500°C. The data contained in Table II show that the Zr-Sn-Mo alloy is much superior to pure zirconium in creep at this temperature. Fig. 15 shows that the alloy is probably superior to pure zirconium in creep at 700°C, but that it is inferior to pure zirconium in creep at 800°C. This reversal is undoubtedly caused by the appearance of β-zirconium in the Zr-Sn-Mo alloy at 800°C.

As hot rolled at 800°C and air cooled, the Zr-3.9 wt pct Sn-1.6 wt pct Mo alloy had an impact strength of 9 ft-lb. It was thought that perhaps this low value was caused by the well-known effect of hydrogen upon zirconium,[6,7] so the alloy was degassed at 840°C and furnace cooled in a vacuum of less than 0.1 mm Hg. The results of impact tests on the material in this condition are shown in Fig. 16. Evidently the embrittlement caused by heating this alloy into a β region is more severe than the effects of hydrogen. No solution to this problem has been found.

Secondary Fabrication Characteristics

As hot rolled at 800°C and furnace cooled, the Zr-4 wt pct Sn-1.6 wt pct Mo alloy can be cold reduced about 20 pct in thickness without cracking. If this worked material is annealed for 3 hr at 730°C and furnace cooled, it can be cold rolled to somewhat greater reductions. A 1-in.-wide strip of this alloy was cold reduced in 42 passes from a 0.076-in. thickness to 0.006-in. thickness. Edge cracking was first noticed at about 40 pct reduction and cracking became appreciable at about 50 pct reduction. Rolling was stopped at 0.006-in. thickness because of mill limitations. At this point, the strip was about 1¼ in. wide and cracks about ⅛ in. long extended into the strip from each edge. The hardness of the alloy increased only 30 Dph in the first 50 pct reduction, and no significant change in hardness occurred in further reductions.

The deep-drawing capacity of high-purity zirconium is very good, but contaminants and alloying

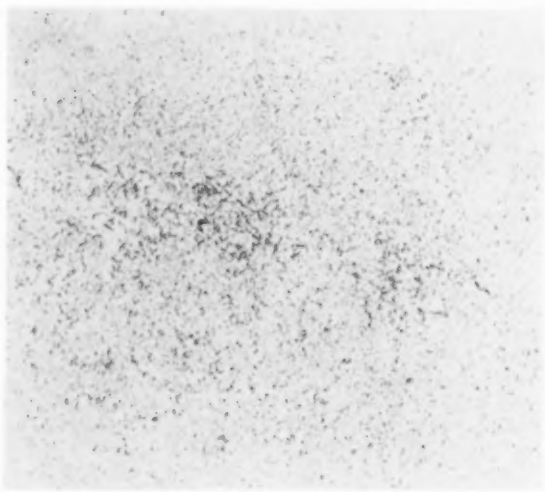

Fig. 13—Micrograph of Zr-4 wt pct Sn-1.6 wt pct Mo; hot rolled at 800°C, furnace cooled, cold rolled, heated to 730°C for 3 hr, and furnace cooled; finely dispersed $ZrMo_2$ in α-zirconium, 235 Dph. X250. Reduced approximately 15 pct for reproduction.

elements tend to reduce this ability greatly. The results of duplicate Olsen ductility tests on a few zirconium alloys are shown in Table III. Obviously, zirconium alloys will not be such desirable materials for deep drawing as high-purity zirconium.

The Zr-4 wt pct Sn-1.6 wt pct Mo alloy can be welded either by butt welding or by seam welding where pure zirconium is used as a filler material. However, the weld and heat-affected zone are extremely brittle in the as-welded condition. This effect could be predicted from the heat-treatment response of the alloy; the weld zone is heated above the β transus and the cooling rate approximates water quenching in some areas and air quenching in others. The structure of the weld zone is martensitic, see Fig. 3, and this structure alone has been known to cause brittleness in zirconium alloys. The average hardness of the weld zone in one sample of the Zr-3.9 wt pct Sn-1.6 wt pct Mo alloy, as welded, was 376 Dph. This hardness can be greatly reduced and the ductility of the weld can be partially restored by proper heat treatment. Table IV shows the effect of heat treatment on tensile specimens having a seam weld down their axis.

Table IV. Effect of Heat Treatment on the Tensile Properties of Welds in Zr-4 Wt Pct Sn-1.6 Wt Pct Mo Alloy

Heat Treatment No.*	0.2 Pct Offset Yield Strength, Psi	Ultimate Strength, Psi	Total Elongation in 1 In., Pct	Reduction of Area, Pct
1	—	106,600	0	0
2	80,000	88,300	3	3
3	70,800	75,000	2	6

* Heat treatment 1: As butt welded (no filler material).
Heat treatment 2: Butt welded, heated to 730°C for 3 hr, and furnace cooled.
Heat treatment 3: Seam welded using pure zirconium as a filler material, heated to 900°C for 1 hr, cooled to 700°C for 15 hr, and furnace cooled.

Variation of Properties with Composition

Molybdenum is responsible for the heat-treatment character of the Zr-4 wt pct Sn-1.6 wt pct Mo alloy. Increasing amounts of molybdenum increase the stability of the β phase. This effect delays the onset of the age-hardening reaction, but does not eliminate it. Alloys containing metastable β are not desirable as creep-resistant alloys at 500°C. Decreasing amounts of molybdenum cause a decrease in the stability of the β phase. As the stability of the β phase decreases, the age-hardening reaction is accelerated until it is effectively eliminated by overaging at even the fastest cooling rates.

One of the major advantages of the ternary Zn-Sn-Mo alloys over binary Zr-Sn alloys is the comparative ease with which the ternary alloys can be hot rolled at 800°C. The 800°C hardness of Zr-4 wt pct Sn alloys decreases with increasing molybdenum content up to about 2 wt pct Mo.[1] The β-zirconium phase is responsible for this unusual effect.

Over a wide range of compositions, the room-temperature strength and ductility of the Zr-Sn-Mo alloys are not affected as much by minor changes in composition as they are by changes in heat treatment. A comparison of Table V with Table I shows this to be true. In general, of course, the strength

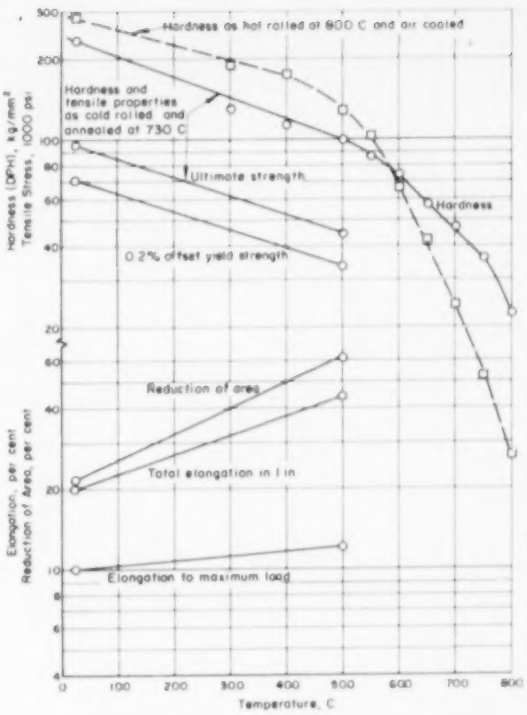
Hardness as hot rolled at 800 C and air cooled
Hardness and tensile properties as cold rolled and annealed at 730 C
Ultimate strength
Hardness
0.2% offset yield strength
Reduction of area
Total elongation in 1 in.
Elongation to maximum load
Hardness (DPH), kg/mm²
Tensile Stress, 1000 psi
Elongation, per cent
Reduction of Area, per cent
Temperature, C

Fig. 14—Effect of temperature on the hardness and tensile properties of Zr-3.9 wt pct Sn-1.6 wt pct Mo alloy.

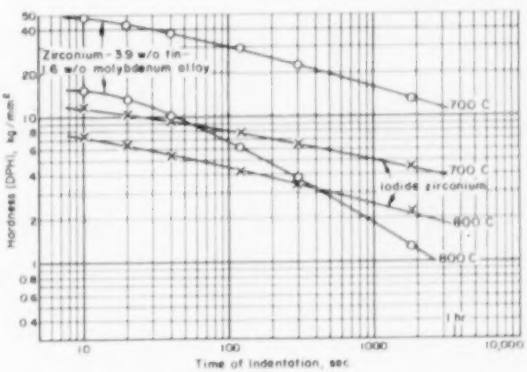

Fig. 15—Hot hardness vs time of indentation for zirconium and Zr-3.9 wt pct Sn-1.6 wt pct Mo alloy.

of alloys increases and ductility decreases with increases in total alloy content.

Conclusions

The Zr-4 wt pct Sn-1.6 wt pct Mo alloy can be heat treated to yield a variety of properties. In its most ductile condition, it has a tensile strength of 90,000 psi; in its strongest state, it has a tensile strength in excess of 140,000 psi. Its hot-rolling character at 800°C is nearly ideal and, after proper heat treatment, it can be cold reduced more than 20 pct without cracking. It has relatively good creep strength at 500°C, and its properties are not drastically changed by minor variations in composition.

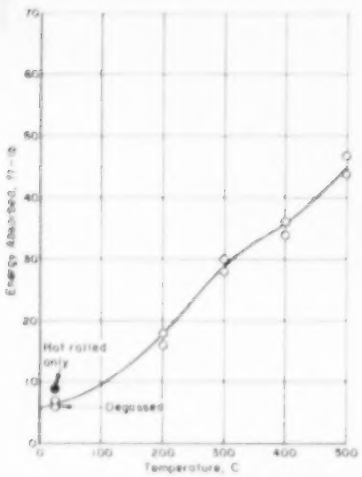

Fig. 16—Impact strength of Zr-3.9 wt pct Sn-1.6 wt pct Mo alloy.

Acknowledgment

This work was performed under AEC Contract No. W-7405-eng-92.

References

[1] W. Chubb: Progress in the Development of Creep-Resistant Zirconium Alloys. *ASM Trans.*, 1956, vol. 48, p. 804.

[2] W. Chubb: The Contribution of Crystal Structure to the Hardness of Metals. *AIME Trans.*, 1955, vol. 203, p. 189; JOURNAL OF METALS, January 1955.

Table V. Effect of Composition on the Tensile Properties of Zr-Sn-Mo Alloys at Room Temperature. All Alloys Cold Rolled and Annealed Below 780°C

Alloy Analysis (Balance Zirconium), Wt Pct	0.2 Pct Offset Yield Strength, Psi	Ultimate Strength, Psi	Elongation to Maximum Load, Pct	Total Elongation in 1 In., Pct	Reduction of Area, Pct
3.9 Sn-0.8 Mo	56,200	76,400	13	29	40
4.0 Sn-1.6 Mo	59,000	86,700	13	25	43
3.9 Sn-1.6 Mo	71,200	90,600	10	20	24
5.0 Sn-1.4 Mo	65,800	77,600	9	25	24
4.5 Sn-2.2 Mo	70,800	95,000	10	18	21
5.0 Sn-1.3 Mo	82,200	101,000	8	10	14
7.0 Sn-0.6 Mo	83,300	90,300	2	3	4
7.0 Sn-1.5 Mo	99,800	103,200	1	1	1

[4] R. F. Domagala, D. J. McPherson, and M. Hansen: Systems Zirconium-Molybdenum and Zirconium-Wolfram. *AIME Trans.*, 1953, vol. 197, p. 73; JOURNAL OF METALS, January 1953.

[5] L. D. Jaffe: Heat Treatment of Titanium Generalized in Terms of Beta Prime. *AIME Trans.*, 1954, vol. 200, p. 210; JOURNAL OF METALS, February 1954.

[6] W. Koster: The Temperature Dependence of the Elastic Modulus of Pure Metals. *Ztsch. für Metallkunde*, 1948, vol. 39, p. 1.

[7] W. L. Mudge: Effect of Hydrogen on the Embrittlement of Zirconium and Zirconium-Tin Alloys. *Zirconium and Zirconium Alloys*, p. 146. ASM, Cleveland, 1953.

[8] A. D. Schwope and G. T. Muehlenkamp: Effect of Hydrogen on Mechanical Properties of Zirconium and Its Tin Alloys. Battelle Memorial Institute Report No. BMI-845, June 30, 1953.

Discussion of this paper sent (2 copies) to AIME by June 1, 1957 will appear in AIME *Transactions* Vol. 209, 1957, and in JOURNAL OF METALS, October 1957.

Effect of Small Amounts of Alloying Elements on the Ductility of Cast Molybdenum

by L. E. Olds and G. W. P. Rengstorff

PREVIOUS research has shown that cast molybdenum has good ductility at room temperature if the metal is sufficiently pure.[1] In practice, however, it is very difficult to reduce the impurity content of molybdenum to a few parts per million—the maximum content of impurities allowable to obtain reasonable ductility in coarse-grained molybdenum.[2] Also, subsequent fabrication may reintroduce enough impurity to damage ductility greatly, unless extreme precautions are taken to protect the metal during working.

The major impurities which embrittle molybdenum are oxygen, nitrogen and, to a lesser degree, carbon. It is reasonable to assume that the harmful effects of such impurities might be neutralized by small amounts of alloying additions. The desired alloying elements would be those which might form stable metal oxides or nitrides that would not be harmful to ductility, or those which might increase the tolerance of molybdenum for oxygen and nitro-

L. E. OLDS, formerly with Battelle Memorial Institute, is with the Denver Research Institute, Denver. G. W. P. RENGSTORFF, Member AIME, is associated with Battelle Memorial Institute, Columbus, Ohio.

TP 4372E. Manuscript, Apr. 13, 1956. Cleveland Meeting, October 1956.

Fig. 1—Micrograph of Mo-0.7 pct Ti alloy, as cast; etched with $K_3Fe(CN)_6$-KOH. X500. Reduced approximately 30 pct for reproduction.

Fig. 2—Micrograph of Mo-10 pct Th alloy, as cast; etched with $K_3Fe(CN)_6$-KOH. X500. Reduced approximately 25 pct for reproduction.

gen by some mechanism such as an increase in the solubility of these impurities in the matrix phase.

Preliminary Investigation

A number of strong oxide, nitride, and carbide formers were investigated in a preliminary survey to determine which, if any, held promise as additions for neutralizing contaminants in molybdenum. The addition elements studied in this survey were chosen from the various groups in the Periodic Table, as follows: group 2, beryllium; group 3, boron, aluminum, and cerium; group 4, silicon, titanium, zirconium, and thorium; group 5, vanadium, columbium, and tantalum; and group 6, chromium.

Table I. Raw Materials Used to Prepare Alloys

Element	Grade
Molybdenum	Purified by vacuum fusion*
Titanium	Iodide
Thorium	Iodide
Aluminum	99.9 pct pure
Cerium	98.6 pct pure
Vanadium	Union Carbide & Carbon Corp., ductile grade
Boron	Halide purified
Zirconium	Iodide

Helium atmosphere: Grade A—Bureau of Mines

* Purified by melting sinter bar stock once in high vacuum. This procedure lowers the oxygen content to about 5 ppm and leaves about 10 to 20 ppm N and 10 to 30 ppm C.

To determine possible neutralizing effects, alloys of these elements with molybdenum were prepared by arc melting once in a vacuum. This type of melting normally produces unalloyed molybdenum ingots of little or no ductility, since an insufficient quantity of impurities is volatilized while the metal is molten. Thus, the presence of ductility in any of the once-melted alloys would indicate that the additive was causing a desirable reaction.

The alloys were tested for ductility at room temperature by bending small specimens cut from the ingots. From these tests it was observed that, of the alloying elements studied, boron, aluminum, cerium, titanium, zirconium, and vanadium improved the cold ductility of cast molybdenum when added in amounts less than about 0.5 pct. Thorium also improved ductility, although additions in the range of 5 to 10 pct were required. On the other hand, additions of 0.5 pct and less of beryllium, silicon, columbium, tantalum, and chromium gave little improvement. On the basis of this preliminary investigation, a more extensive study was made of the promising alloy systems.

Preparation of Alloys

The alloys for more detailed studies were prepared as 2½ in. diam, 2 in. high ingots by arc melting high-purity raw materials in an atmosphere of high-purity helium gas maintained at a slight positive pressure. This type of melting has been found to result in a residual impurity content in molybdenum of from 5 to 10 ppm O, with a similar range for the nitrogen content. In contrast, the minimum impurity content necessary for good low-temperature ductility of unalloyed cast molybdenum is about 1 to 2 ppm O and 10 to 20 ppm N.

The raw materials from which the experimental alloys were prepared are listed in Table I. The amounts of the alloy additions which were made, along with the percentage retention of the addition during melting, and the method of making the alloying addition, are given in Table II. The master alloys were prepared by arc melting in helium, using a tungsten electrode and direct current. The small (50 to 100 g) buttons were made from high-purity materials as noted in Table I. The retention of the alloying elements during the vacuum-melting operation was very good in the case of titanium and thorium. However, the aluminum volatilized readily. The retention of vanadium, boron, cerium, or zirconium was not determined, but since only minor

Table II. Alloys Prepared for Investigation

Alloying Element	Range of Alloying Addition, Pct	Retention of Addition after Melting, Pct	Method of Making Alloyed Additions
Titanium	0.1 to 4	99 to 100	Master alloy (10 or 20 pct Ti)
Thorium	0.1 to 10	99 to 100	Machined chips or sheared sheet for additions above 1 pct Th. Master alloy (20 pct Th) for additions of 1 pct Th and less
Aluminum	0.5 to 20	5 to 50	Master alloy (9 pct Al)
Cerium	0.1 to 0.5	Not determined	Master alloy (5 pct Ce)
Vanadium	0.25 to 5	Not determined	Master alloy (20 pct V)
Boron	0.0002 to 0.5	Not determined	Master alloy (0.5 pct B)
Zirconium	0.25 to 5	Not determined	Master alloy (15 pct Zr)

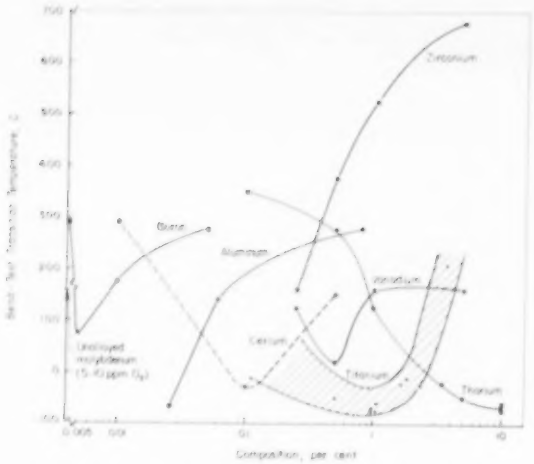

Fig. 3—Effect of various elements on bend-test transition temperature of cast molybdenum. Aluminum and titanium compositions are actual values. Boron, cerium, zirconium, vanadium, and thorium compositions are the amounts which were added. Bend tests were made at a strain rate of 0.038 in. per in. per sec.

amounts of these elements would volatilize during melting, it is likely that most of the addition was retained.

Microstructure of Alloys

In general, the microstructures of all but the Mo-Th alloys were single phased except for small amounts of nonmetallic inclusions. A typical microstructure for these alloys is shown in Fig. 1. All of the Mo-Th alloys, however, contained a major second phase which increased in amount as the thorium content of the alloys increased. This phase was identified by X-ray diffraction as thorium. A typical microstructure of the Mo-Th alloys is shown in Fig. 2.

Ductility Tests

The ductility of the alloys was measured by a simple bend test, using specimens taken from slabs which were cut from the ingots so that the columnar grain structure of the ingots was transverse to the length of the specimen axis. Specifications for this test are given in Table III.

Table III. Bend-Test Specifications

Size of specimens:*	0.150 x 0.250 x 1 in.
Length between center of supports:	$\frac{5}{8}$ in.
Diameter of loading pin:	$\frac{1}{8}$ in.
Deflection rate:	1 in. per min
Elastic strain rate in outer fibers during initial deformation:	0.038 in. per in. per sec

* Surface of specimens was ground parallel to longitudinal axis.

Multiple tests were made at a series of temperatures to determine the temperature at which the specimens changed from ductile to brittle behavior. Previous research has shown that, if sufficient specimens are tested at various temperatures, there is a sharp inflection of the curve relating the limits of the maximum bend angles to testing temperature.[4] This inflection occurs on the curve at approximately the 4° bend angle value. For the present study, the temperatures at which this inflection occurred were taken as the transition temperatures of the experimental alloys.

Typical test data obtained for the Mo-Ti alloys are given in Table IV. The transition temperatures which were selected on the basis of the test data are summarized in Table V.

Discussion

The results of this study are summarized in Fig. 3, wherein the transition temperatures of the ingots are plotted with respect to composition. If the curves shown in this figure are limited to the alloys tested, the seven alloying elements fall into three general classes:

1) Those elements which have an optimum value in the curve of transition temperature vs composition. Included in this class are titanium, cerium, vanadium, and boron.

2) Those elements which have no optimum value in the curve of transition temperature vs composition, but which cause an increase in brittleness as the alloy content increases. Zirconium and aluminum were of this class.

3) Those elements which have no optimum value in the curve of transition temperature vs composition, but which cause a decrease in brittleness with increasing alloy content. Of the seven elements studied, only thorium fell in this class.

Of the elements in Class 1, titanium not only imparted the greatest degree of ductility to the ingots, but also extended this improvement over the broadest range of composition. This is fortunate, since ductility may then be obtained over a range of titanium contents. Therefore, compositional control is not so critical for the titanium alloys as it is for some of the other alloy systems.

Table IV. Typical Bend-Test Data

	Bend Angle, Degrees				
Testing Temperature, °C	Ingot Ti-1 (0.11 Pct Ti)	Ingot Ti-4 (0.70 Pct Ti)	Ingot Ti-6 (0.98 Pct Ti)	Ingot Ti-10 (1.63 Pct Ti)	Ingot Ti-13 (3.66 Pct Ti)
220					5, 2
180					2
150					2
100					1, 0, 0, 0
60	40				
40	16, 5				
20	12, 1, 0	8, 5	14, 8	4	
	0				
0	10, 2			13, 8	
−20	2, 2, 0	5, 1	6, 3	2, 0, 0	
−40				0, 0	
−50		6, 6, 2, 1	14, 10, 2		
−75		5, 4, 4, 1	2, 2, 2		

The optimum values in the curves for boron, cerium, vanadium, and titanium are belived to be associated with the effects of the elements on neutralizing the harmful effects of impurity elements. The exact mechanism is not known. However, since all of the alloying elements are strong oxide or nitride formers, it is likely that at least part of the improvement in ductility is the result of the formation of oxides or nitrides of the added elements and that these oxides or nitrides are less harmful to the ductility of the cast molybdenum than is molybdenum oxide or nitride. The quantity of an element which is needed to form such compounds is not expected to be large because only small amounts of gaseous impurities are normally present in molybdenum. Thus, it is not surprising that the great improvement in the ductility of cast molybdenum by the elements in Class 1 occurred at or below the

Table V. Transition Temperatures of Binary Molybdenum-Base Alloys Melted in a Helium Atmosphere

Mo-Ti Alloys			Mo-Th Alloys			Mo-Al Alloys			Mo-V Alloys		
	Pct Ti	Transition Temperature, °C		Pct Th*	Transition Temperature, °C		Pct Al	Transition Temperature, °C		Pct V*	Transition Temperature, °C
Ti-1	0.11	−10	Th-1	0.1	350	Al-1	0.026	−70	V-1	0.25	125
Ti-2	0.28	60	Th-2	0.5	275	Al-2	0.06	140	V-2	0.5	20
Ti-3	0.50	−50	Th-3	1.0	125	Al-3	0.70	275	V-3	1.0	160
Ti-4	0.70	−80	Th-4	2.5	−20				V-4	5.0	160
Ti-5	0.92	−30	Th-5	5.0	−50						
Ti-6	0.96	−75	Th-6	10.0	−60						
Ti-7	0.97	−70	Th-7	10.0	−75						
Ti-8	1.02	−75									
Ti-9	1.05	−60									
Ti-10	1.63	−20									
Ti-11	1.84	−10									
Ti-12	2.34	−30									
Ti-13	3.66	210									

Mo-B Alloys			Mo-Ce Alloys			Mo-Zr Alloys		
	Pct B*	Transition Temperature, °C		Pct Ce*	Transition Temperature, °C		Pct Zr*	Transition Temperature, °C
B-1	0.002	290	Ce-1	0.01	290	Zr-1	0.25	160
B-2	0.005	80	Ce-2	0.10	−30	Zr-2	0.5	375
B-3	0.01	175	Ce-3	0.50	150	Zr-3	1.0	525
B-4	0.05	275				Zr-4	5.0	675

* Nominal compositions.

level of 1 pct of alloy. Of course, the alloy addition may have other effects on the impurities, such as that of increasing the solubility of the impurity element in either the matrix or in some second phase. Such a reaction would also be expected to result in improved ductility.

When the content of an element in Class 1 (titanium, cerium, vanadium, and boron) was increased beyond that for maximum ductility, neutralization appeared to be offset by the normal solid solution hardening effect of the addition. Thus, the ingots became progressively more brittle until the transition temperature reached or exceeded that of unalloyed molybdenum.

The Class 2 elements (aluminum and zirconium) showed no optimum value in the curve of transition temperature vs composition over the composition range studied. However, it is possible that an optimum value may occur at lower percentages. In that case, the same mechanism to explain neutralization as postulated for elements in Class 1 would probably apply. Any improvement in ductility expected from aluminum and zirconium would occur, therefore, at lower percentages than for either titanium or vanadium.

Thorium was the only element which fell in the third class. In the case of thorium, the alloys become more ductile as the alloy content was increased. For this reason, the improvement in ductility at the higher levels of thorium is believed to occur by a different mechanism than for the other systems studied. Rather than a deoxidation type of action, the improvement in ductility probably resulted from an alloying effect in which a soft envelope of substantially pure thorium was formed at the grain boundaries. Ductility of the alloy would then occur when this ductile envelope was of sufficient thickness to offset the usual intergranular brittleness of molybdenum.

Because of the excellent ductility at low temperatures of alloys containing thorium, a number of samples were stressed in tension at 1500° to 1800°F. All failed rapidly at low loads without apparent elongation. This weakness at elevated temperatures is probably due to the thorium which surrounds the grains of molybdenum. Thus, the structure which gives good ductility at low temperatures appears to cause weakness at high temperatures.

Table VI. Optimum Alloy Contents for Maximum Ductility

Alloying Element	Lowest Bend-Test Transition Temperature in System, °C	Percentage of Alloying Element Needed for Maximum Ductility
Titanium	−80	0.5 to 1.0
Thorium	−75*	10*
Aluminum	−70	0.026
Cerium	−30	0.1
Vanadium	20	0.5
Boron	80	0.005
Zirconium	0 to −50 (extrapolated)	0.05 to 0.1

* A maximum of 10 pct Th was investigated, and the transition temperature was still dropping with increasing thorium content.

A listing of optimum alloy contents for maximum ductility for each of the seven elements studied is shown in Table VI.

Conclusions

1) Of the elements studied, the most effective addition for lowering the bend angle transition temperature of cast molybdenum containing limited amounts of oxygen and nitrogen was titanium in amounts of 0.5 to 1 pct.

2) Other additions in the order of their decreasing effectiveness were 10 pct Th, 0.026 pct Al, 0.1 pct Ce, 0.5 pct V, and less than 0.25 pct Zr.

3) The high-thorium addition improved the ductility of cast molybdenum at temperatures near and below room temperature, but impaired the ductility at temperatures above 1500°F, actually rendering the metal *hot short*.

Acknowledgments

The support of this work by the ONR is gratefully acknowledged, The generous assistance given by H. B. Goodwin; C. H. Lorig; R. B. Fischer; H. W. Lownie, Jr.; F. L. Wilkinson; and other staff members of Battelle Memorial Institute is appreciated by the authors.

References

1 G. W. P. Rengstorff and R. B. Fischer: Cast Molybdenum of High Purity, *AIME Trans.*, 1952, vol. 194, pp. 157-160; JOURNAL OF METALS, February 1952.

2 L. E. Olds and G. W. P. Rengstorff: Effects of Oxygen, Nitrogen, and Carbon on the Ductility of Cast Molybdenum, *AIME Trans.*, 1956, vol. 206, pp. 156-155; JOURNAL OF METALS, February 1956.

Discussion of this paper sent (2 copies) to AIME by June 1, 1957 will appear in AIME *Transactions* Vol. 209, 1957, and in JOURNAL OF METALS, October 1957.

Structural Changes Associated with Strain-Induced Grain Boundary Migration in Si-Fe

Strain-induced grain boundary migration was observed in several bicrystal sheet specimens of Si-Fe (3¼ pct Si) which were cold rolled 2 to 12 pct and then annealed at temperatures up to 1200°C. A chrome-acetic acid electroetching method was used to reveal the dislocation sites before and after grain boundary migration. Recovery effects were noted in the microstructure prior to boundary motion. Consequently, the residual strain energy in neighboring grains may determine if boundary migration with resulting increase of area occurs, and its direction of movement. Microstructural data indicate that the region initially traversed by the moving grain boundary has many structural defects in the form of low-angle boundaries and random dislocations of relatively high density. With increased distance of grain boundary migration, the density of these imperfections was found to decrease. Continued annealing at 1200°C, after boundary migration, lowered the density of random dislocations in the *swept* region to a limiting value of about 2×10^6 lines per sq cm.

by K. T. Aust and C. G. Dunn

SEVERAL studies[1-6] have reported a type of grain boundary migration which occurs when a strained grain grows into an adjacent deformed grain during annealing. Beck and Sperry[1] called this phenomenon *strain-induced* grain boundary migration, since the observed boundary movement, which takes place in a direction away from the center of curvature, is apparently motivated by the excess free energy of strain hardening. However, little information has been obtained on the detailed structural changes accompanying such grain boundary motion.

The problem of driving force for strain-induced boundary migration was considered by Dunn and Daniels,[5] who used bent bicrystals of Si-Fe. They demonstrated that two grains of differing energy, in the form of subboundaries, behaved according to the concept that the low-energy grain would grow at the expense of the high-energy grain. Beck[6] reported experiments of Sperry for high-purity aluminum, which indicated that generally the particular grain of a pair which work-hardened more was invaded. The measure of work hardening here was

K. T. AUST, Junior Member AIME, and C. G. DUNN, Member AIME, are associated with the Research Laboratory, General Electric Co., Schenectady.

TP 4426E. Manuscript, Sept. 10, 1956. New Orleans Meeting, February 1957.

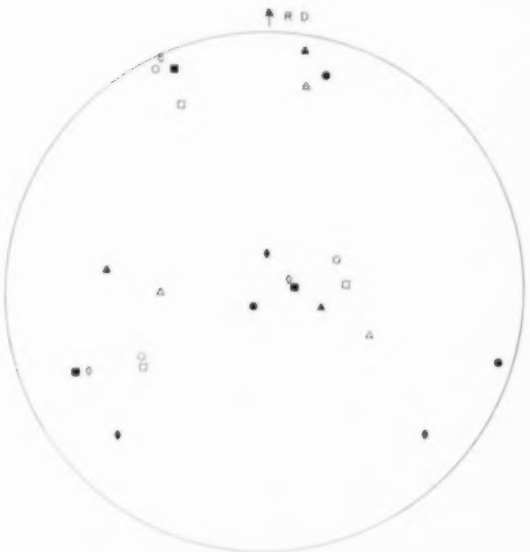

Fig. 1—Stereogram gives {100} poles of grains in four bicrystal specimens. Circles refer to specimen S1; squares, S2; triangles, S3; and diamonds, S4. Open symbols refer to grain *A* and closed symbols to grain *B* in each specimen.

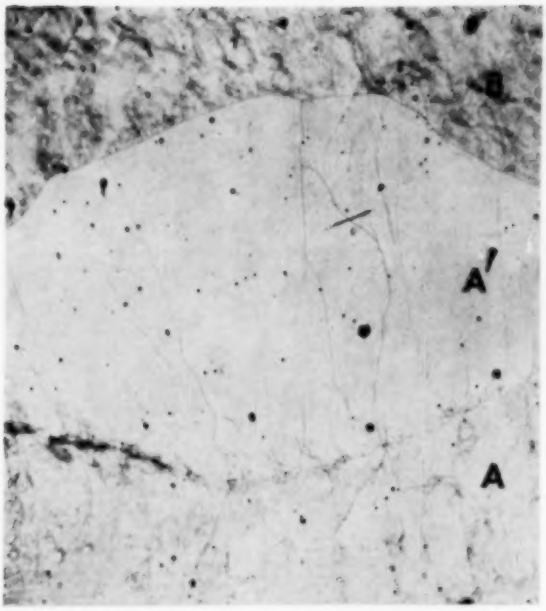

Fig. 2—Micrograph of specimen S1 shows the region *A'* swept by boundary migration during growth of grain *A* into grain *B*, after ½ hr anneal at 1200°C. Electropolish and chrome-acetic acid electroetch. X55. Reduced approximately 15 pct for reproduction.

Fig. 3—Enlarged Laue X-ray reflections, top to bottom, are for the regions *B*, *A'*, and *A*, respectively, shown in Fig. 2.

based on Knoop hardness tests conducted before and after cold rolling. However, there were a few instances noted where the grain being invaded was less work-hardened than the adjacent grain. Bron and Machlin[15] reported boundary mobilities for high purity silver, where the driving force was the decrease in strain energy associated with the difference in dislocation density across the grain boundary.

Several investigators[2,4,6,7] have suggested that the area swept by strain-induced boundary migration is essentially strain-free. Beck[16] also reported that low-angle boundaries were found in the swept-out region and accounted for their presence in terms of growth of parts of the adjacent strain-hardened grain.

In the present study, suitable orientation relationships, amount of cold-rolling deformation, and annealing treatments were employed to obtain strain-induced grain boundary migration in bicrystals of Si-Fe. A chrome-acetic acid electroetching method[9,13] was used to reveal dislocation sites, since Hibbard and Dunn[12] have demonstrated that this technique is reliable for determining edge dislocation densities in Si-Fe. It was believed that the application of the electroetch method to the problem of strain-induced grain boundary migration might clarify the structural features involved, such as dislocation configurations and densities in adjacent grains before and after boundary movement, and the extent of crystal perfection in the swept-out region.

Experimental Procedure

Bicrystal specimens of 3¼ pct Si-Fe were prepared by annealing critically strained polycrystalline sheet material of 1 mm thickness. The specimens were then annealed at 1200°C in H_2 atm for 30 to 60 hr, to obtain relatively stable grain boundaries. The orientations of adjacent grains (grains *A* and *B*) in each bicrystal are given in Fig. 1, as determined from X-ray Laue transmission patterns.

The specimens were cold rolled 2 to 12 pct, etched lightly in a 30 pct nitric acid solution, and then given the various annealing treatments listed in Table I.

After each anneal, the specimens were lightly etched in a solution consisting of 2 cu cm HNO_3, 2 cu cm HF, and 100 cu cm H_2O, to reveal both the initial and final positions of the grain boundary. X-ray Laue transmission patterns were also obtained from adjacent grains and the area swept-out by the advancing boundary.

It was noted in preliminary tests that the prolonged anneals at 1200°C in H_2 atm, employed in the specimen preparation, lowered the carbon content to such an extent that subsequent electroetching in chrome-acetic acid failed to reveal the dislocation sites. The importance of carbon in revealing dislocation etch pits in Si-Fe was demonstrated by Suits and Low.[13] Consequently, a small amount of carbon (approximately 0.005 pct) was added to each specimen by means of an anneal in low-pressure acetylene at 775°C for ½ to 1 hr, except in one case, when a 575°C anneal was used. The

Table I. Annealing Treatments

Specimen No.	Cold Rolling Reduction, Pct	Treatment
S1	2.5	1½ hr at 1100°C, plus ½ hr at 1200°C
S2	12	¼ to 1¼ hr at 1000°C, plus ¼ hr at 1200°C
S3	2.5	Intermittent annealing at 1200°C, total time 88 hr
S4	3.5	½ hr at 1200°C

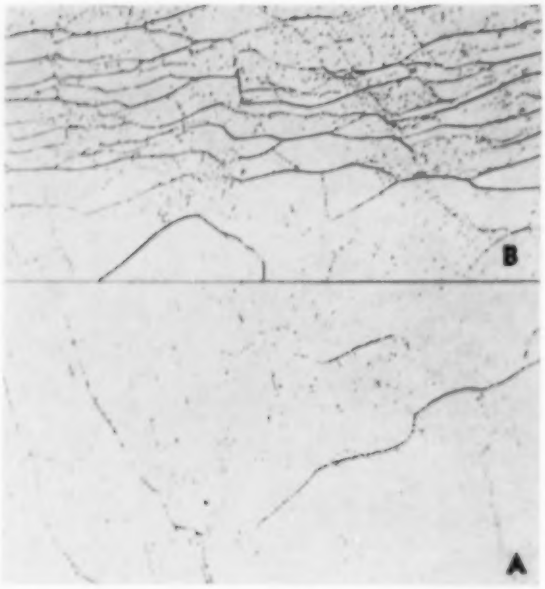

Fig. 4—Micrograph of specimen S1 depicts an area where no grain boundary migration occurred, after ½ hr at 1200°C. X1000. Reduced approximately 5 pct for reproduction.

specimens were then electropolished by a Diesa-Electropol in an electrolyte consisting of 15 cu cm perchloric acid (60 pct), 60 g sodium thiocyanate, 75 g citric acid, 800 cu cm ethanol, and 100 cu cm propanol, and finally were electroetched in the chrome-acetic acid bath. Micrographs were obtained at magnifications from X50 to X1250.

Results

Structural Observations—An example of strain-induced grain boundary migration is shown in Fig. 2 for S1 (specimen No. 1). Grain A has grown at the expense of grain B, thereby producing region A', which has the same average orientation as grain A. The positions of the grain boundary, which have advanced further into grain B, have moved away from their centers of curvature. If the darkness of the areas shown in Fig. 2 is taken as a qualitative indication of the relative strain energies remaining after annealing, then $\epsilon_{A'} < \epsilon_A < \epsilon_B$, where $\epsilon_{A'}$, ϵ_A, and ϵ_B are the residual strain energy densities in A', A, and B, respectively. Since the energy density varies with dislocation arrangement at constant dislocation density, the term strain energy density here is taken to mean the net effect of arrangement and density of dislocations. The energy density in the region A' adjacent to the initial position of the grain boundary appears to be higher than in regions of A' further away from this boundary position.

Fig. 3 shows enlarged Laue X-ray reflections obtained from regions B, A', and A of S1. The inequality of residual strain energy between grains A and B, observed in the microstructure, is confirmed by the spread in the individual Laue reflections, Figs. 3a and 3c. The break up of the Laue reflection, Fig. 3b, for region A' indicates the presence of several disoriented regions; such regions may correspond to the relatively large subgrains revealed in the microstructure.

Microscopic examination generally revealed an apparent equality of residual energy between grain

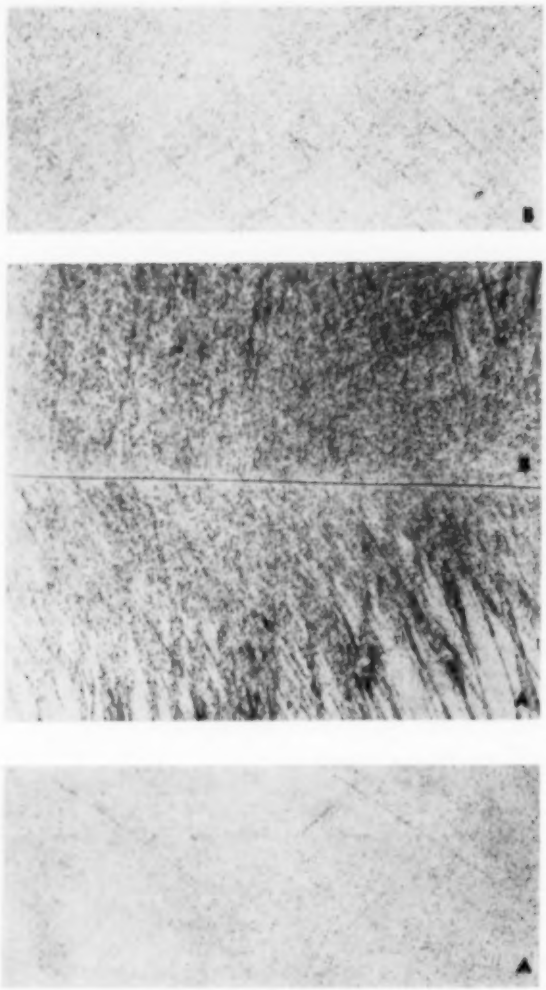

Fig. 5—Microstructure is shown for sample 1 of specimen S2 after 12 pct cold rolling reduction and 4 hr anneal at 575°C. X500. Reduced approximately 30 pct for reproduction.

A and B in regions of S1 where no boundary migration had occurred. Fig. 4 depicts an area where grain A did not advance into grain B (after the 1200°C anneal), although the overall energy remaining in grain B seems to be higher than that in grain A. However, recovery has apparently occurred to a greater extent in the region of grain B adjacent to the grain boundary than elsewhere in grain B. The absence of boundary movement for the area shown in Fig. 4, therefore, may be due to a low or zero driving force on the grain boundary as a result of recovery.

S2 was divided into three samples, which were subjected to various anneals at increasing temperatures and times in order to follow the structural changes prior to and after boundary migration. Fig. 5 shows the microstructure revealed in the first sample, which was cold rolled 12 pct and then given a carbon-addition treatment for 4 hr at 575°C. Although the *carbon* anneal may have modified the initially *as cold-rolled* structure to some extent, it did not change the structure sufficiently to erase the appearance of slip bands. The slip band structure

is evident for both grains *A* and *B* in areas remote from the grain boundary (upper and lower micrographs) after a light electroetching treatment (2 min at 4 volts). It is apparent from Fig. 5 that grain *B* has a higher strain energy than grain *A*. X-ray Lauegrams also revealed more orientation spread in grain *B* than in grain *A*. However, the center micrograph of Fig. 5 indicates that the strain configuration associated with grain *B* is fairly continuous across the grain boundary into grain *A*, suggesting little difference in strain energy between grains *A* and *B* in areas adjacent to the grain boundary. Nevertheless, grain *A* later grew into grain *B* in the second and third samples from S2 when annealed at higher temperatures.

The microstructure of the second sample after an anneal of 15 min at 1000°C is illustrated in Fig. 6, in a boundary region where no boundary migration occurred. Carbon was added after the anneal in order to reveal the dislocation configurations. It is evident that the *worked* structure, Fig. 5, has been replaced by a partially polygonized structure, Fig. 6. A difference in energy between grains *A* and *B* at the boundary is now observed in Fig. 6, which may be explained in terms of a greater degree of recovery in grain *A* near the boundary. Fig. 7a shows a region where boundary migration did occur in this same sample, in which grain *A* grew into grain *B* for a maximum distance of 0.09 mm. An enlarged micrograph of part of the area shown in Fig. 7a is given in Fig. 7b. The area swept out by the grain boundary is far from perfect, as indicated by the presence of numerous subboundaries and random dislocations of relatively high density (about 10^9 lines per sq cm) within each subgrain.

The third sample from S2 was annealed for 75 min at 1000°C, and then for 15 min at 1200°C, since no migration was observed after the 1000°C anneal. During the 15-min anneal at 1200°C, grain *A* advanced into grain *B* for a distance of 0.55 cm, corresponding to an average rate of migration of 2.2 cm per hr. The top micrograph of Fig. 8 depicts the final growth front separating grain *B* and the *swept-out* region *A'*. A typical recovered area in grain *A* is shown in the lower picture. The occurrence of increased amount of recovery in both grain *A* and grain *B* is evident when the microstructures of Figs. 6 and 8 are compared. Generally the area traversed by the growth of grain *A* into *B*, i.e., region *A'*, has many subboundaries, although that shown in Fig. 8 is free of subboundaries and corresponds to a dislocation density of about 1.5×10^8 lines per sq cm. However, subboundaries were found to increase in number as the position of the grain boundary prior to migration is approached.

It is evident from Fig. 8 that grain *B* consists essentially of a system of subgrains, which in turn have smaller subdivisions according to the various arrangements of dislocation sites seen in the microstructure. The small subgrains have less misorientation than the larger subgrains, as indicated by the spacing of etch pits in the subboundaries. These two kinds of subboundaries may be similar to the primary and secondary subboundaries observed by Jacquet[14] in the microstructure of slightly deformed and annealed α-brass. Weissmann,[15] using combined X-ray microscopy and diffraction analysis, has also reported similar observations for nickel and several nickel alloys which were annealed ½ hr at 1150°C, prestrained 0 to 4 pct and recovered for 1 hr at 800°C.

An example of mutual invasion by two adjoining grains is of interest since this behavior would suggest a variable strain energy density along the grain boundary. Beck[16] has reported one instance in high-purity aluminum where two grains mutually invaded each other, although one of these invasions was indirect, by way of a third grain. An example of direct mutual invasion was found in the present work for S4, after a ½ hr anneal at 1200°C, and is shown in Fig. 9. Growth of grain *B* into grain *A* is evident in the macrograph, but the growth of *A* into *B* producing the region *A'* is predominant. This observation indicates that the local strain energy density near the grain boundary is an important factor in determining the direction of strain-induced boundary motion.

Variation of Dislocation Density in the Region *Swept-Out* by Boundary Migration—Strain-induced boundary migration was found in S3 after 6½ hr anneal at 1200°C, but very little additional migration occurred on further annealing at this temperature. The density variation of random dislocations in various areas of the swept region (*A'*) in S3 was determined by etch-pit counts from micrographs (X500), as a function of annealing time at 1200°C. The number of etch-pits varied between 850 and 4600 in individual areas, each 4×10^{-4} sq cm. The data are shown in Fig. 10; the numbers 1, 2 and 3 refer to the individual areas in *A'*. The results indicate a variation in dislocation density in the region swept out by boundary migration, at least in the early stage of annealing at 1200°C. Further annealing at 1200°C lowered the dislocation density in the higher density areas until all the areas had a common value of about 2×10^8 lines per sq cm. The observed decrease in dislocation density with annealing time is a recovery process which occurred after grain boundary movement, resulting in a more stable *swept-out* region having lower energy.

Variation of dislocation density with distance from the initial grain boundary position was found

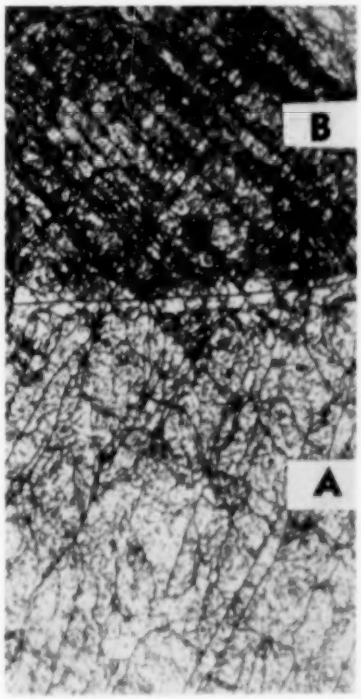

Fig. 6—Micrograph of sample 2, specimen S2, after 15 min at 1000°C shows the structure near the grain boundary where no migration occurred. X500. Enlarged approximately 20 pct for reproduction.

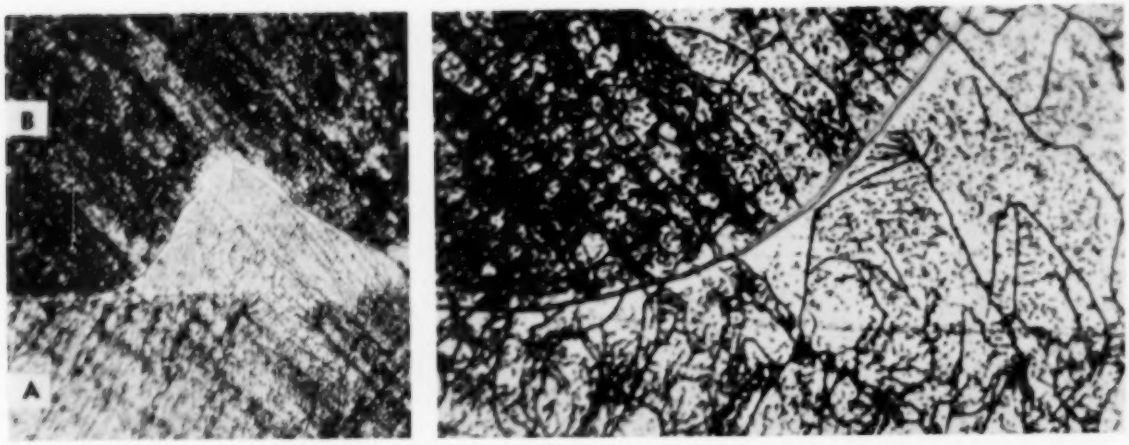

a b

Fig. 7—Micrographs of sample 2, specimen S2, after 15 min at 1000°C illustrate an area where grain boundary migration was found. LEFT: X250; RIGHT: part of area shown at left at X1250. Reduced approximately 10 pct for reproduction.

in S4 in the region A' produced by the growth of grain A into grain B, Fig. 9. The microstructure of Fig. 11 shows the initial grain boundary position after the ½ hr anneal at 1200°C in which a low-angle boundary separates the regions A and A'. This low-angle boundary (running horizontally in Fig. 11) is in the growth direction, based on an interpretation of Fig. 9. The dislocations in A', immediately adjacent to the initial grain boundary position, are randomly distributed within a single subgrain and correspond to a density of 4.3×10^8 lines per sq cm. At distances of 0.13 and 0.25 cm from this position, and still within the same subgrain in A' but not shown in Fig. 11, the density decreased to 3.4×10^8 and 2.2×10^8 lines per sq cm, respectively. Also, recovery has occurred in grain A (lower part of Fig. 11) in which the dislocations have aligned into partial arrays corresponding to a density of about 8×10^8 lines per sq cm.

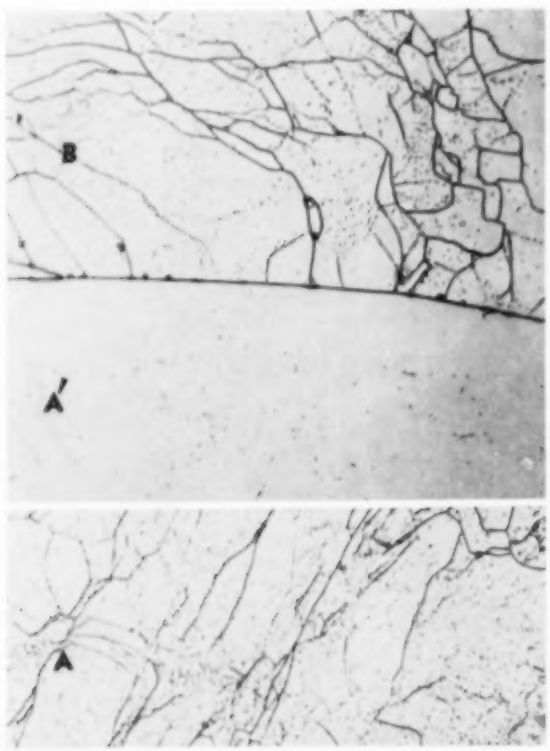

Fig. 8—Micrographs of sample 3, specimen S2, depict the structure obtained after 15 min at 1200°C. TOP: area showing grain boundary between B and A'. BOTTOM: area within grain A. X500. Reduced approximately 15 pct for reproduction.

Discussion

The observations made in the present study concerning recovery prior to grain boundary migration are in agreement with the results for aluminum obtained by Crussard,[9] who found that *recrystallization-in-situ* or polygonization occurred in two adjacent grains during a time delay of 50 min at 495°C prior to boundary movement. Although Beck[10] reported no apparent induction period at 350°C for strain-induced boundary migration in high-purity aluminum, some recovery may have occurred at room temperature and undoubtedly should have been very rapid at high temperatures in this material.

The present results indicate that the swept-out area becomes more perfect, in terms of fewer subboundaries and decreased density of random dislocations, with increased distance of grain boundary migration. The propagation of a polygonized structure was demonstrated by Dunn and Daniels,[7] and the formation of low-angle boundaries as a result of growth from points along the grain boundary was indicated by Beck and Sperry.[7] There is no suggestion, however, in these earlier studies of any overall decrease in dislocation density with distance of migration. If the boundary region in the growing grain is considered as a system of subgrains with more or less random dislocations within the subgrains, then as atoms are transferred across a boundary it is evident that dislocations which are parallel to the boundary will remain behind.[10] Also, certain subboundaries may be lost due to termination in the surface, and direct observation in swept areas confirms this in the present work.

Since the area being swept becomes more perfect with increased distance of boundary migration, an increase in the difference in strain energy density, i.e., the driving force for boundary migration, might be expected. The results also indicate that recovery

occurs in the grain being consumed, which decreases the strain energy driving force. These two variations tend to cancel and, therefore, the exact change in driving force with time at temperature is not clear. However, a partial treatment of this problem is discussed elsewhere.[17]

No evidence was obtained that a grain of higher strain energy grows at the expense of a grain with lower strain energy, although a few cases reported by Beck[16] indicate that this may be possible. In this connection, a more rapid recovery of the higher energy grain in the vicinity of the grain boundary might reverse the energy difference across the boundary, and thus induce the growth of the original higher energy grain. The importance of recovery in regions adjacent to the boundary on strain-induced boundary movement has already been emphasized in discussions of Figs. 4 through 6.

The dislocation density of 2 x 10^6 lines per sq cm which was found in the *swept-out region* after prolonged annealing at 1200°C, Fig. 10, corresponds to the same density reported for undeformed Si-Fe crystals.[12] The undeformed Si-Fe crystals were grown by a strain-anneal method and were at temperatures near 1200°C during their formation. It appears, therefore, that annealing (at least as high as 1200°C) may not decrease the dislocation density below a value of about 10^6 lines per sq cm. At this density, the interaction forces between dislocations may be too low to overcome the pinning by impurities and by intersections.

Summary

Microscopic observations are presented on the dislocation configurations existing in bicrystals of Si-Fe before and after strain-induced grain boundary migration. Recovery effects were noted prior to boundary motion; consequently, the residual strain energy in neighboring grains may determine if boundary migration with resulting increase of boundary area occurs, and its direction of movement. Evidence was obtained in contradiction to the concept that the area swept by the moving grain boundary is essentially strain-free. Such a region has many structural defects in the form of low-angle boundaries and random dislocations of relatively high density, at least in the regions initially traversed by the boundary. However, with increased distance of grain boundary migration, the density of imperfections in these regions decreases. Recovery after boundary motion was found in a *swept* region, in which the density of random dislocations reached a limiting value of about 2 x10^6 lines per sq cm after continued annealing (1200°C).

Acknowledgments

The authors wish to thank W. R. Hibbard, Jr. for helpful criticism of the manuscript, B. Chalmers for several useful discussions of the data, and E. Koch for assistance throughout the experimental phase of the investigation, particularly the metallographic work.

References

[1] H. C. H. Carpenter and C. F. Elam: Crystal Growth and Recrystallization in Metals. *Journal* Institute of Metals, 1920, vol. 24, p. 83.

[2] S. E. Maddigan and A. I. Blank: Recovery and Recrystallization in Long-Time Annealing of 70-30 Brass. *AIME Trans.*, 1940, vol. 137, p. 170; METALS TECHNOLOGY, February 1940.

[3] C. Cussard: Etude du Recuit de l'Aluminium. *Revue de Metallurgie*, 1944, vol. 41, p. 193.

[4] C. G. Dunn: Some Aspects of Crystal Recovery in Silicon Ferrite Following Plastic Strains. *AIME Trans.*, 1946, vol. 167, p. 373.

[5] W. Boas and R. W. K. Honeycombe: The Plastic Deformation of Non-Cubic Metals by Heating and Cooling. *Proceedings* Royal Soc., London, 1946, vol. A186, p. 57.

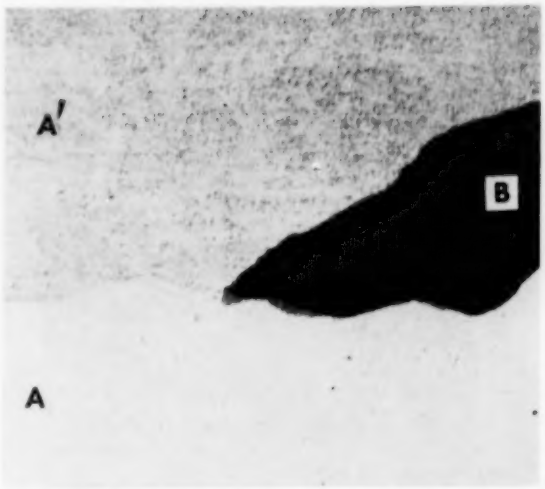

Fig. 9—Macrograph of specimen S4, after ½ hr anneal at 1200°C, illustrates the advance of grain *A* into grain *B*, and grain *B* into grain *A*. X2.4. Reduced approximately 25 pct for reproduction.

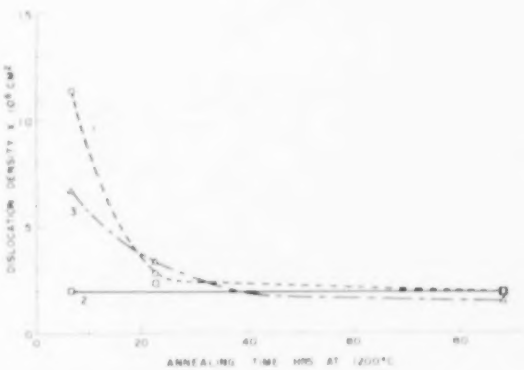

Fig. 10—Plot shows variation in dislocation density for various areas in *A'* of specimen S3 as a function of annealing time at 1200°C.

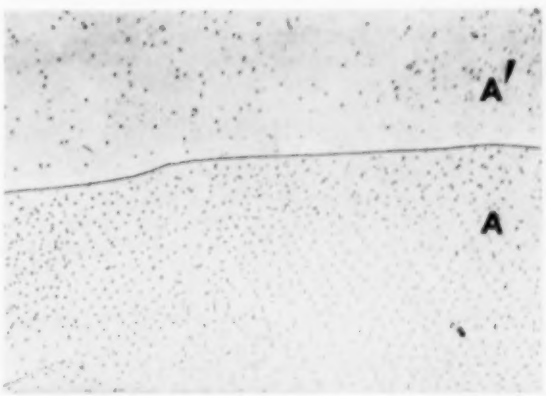

Fig. 11—Microstructure of specimen S4 shows the dislocation configurations in grains *A* and *A'* after ½ hr anneal at 1200°C. X500. Reduced approximately 15 pct for reproduction.

[6] J. E. Burke and Y. G. Shiau: The Effect of Mechanical Deformation on Grain Growth in Alpha Brass. *AIME Trans.*, 1948, vol. 175, p. 141; METALS TECHNOLOGY, September 1947.
[7] P. A. Beck and P. R. Sperry: Strain-Induced Grain Boundary Migration in High Purity Aluminum. *Journal of Applied Physics*, 1950, vol. 21, p. 150.
[8] P. R. Sperry: Two Types of Grain Boundary Migration in High-Purity Aluminum. *AIME Trans.*, 1950, vol. 188, p. 468A; JOURNAL OF METALS, March 1950.
[9] C. G. Dunn and F. W. Daniels: Formation and Behavior of Subboundaries in Silicon-Iron Crystals. *AIME Trans.*, 1951, vol. 191, p. 147; JOURNAL OF METALS, February 1951.
[10] P. A. Beck: Interface Migration in Recrystallization. *Metal Interfaces*, p. 223. ASM, Cleveland, 1952.
[11] C. E. Morris: Electropolishing of Steel in Chrome-Acetic Acid Electrolyte. *Metal Progress*, 1949, vol. 56, No. 5, p. 696.
[12] W. R. Hibbard, Jr. and C. G. Dunn: A Study of <112> Edge Dislocations in Bent Silicon-Iron Single Crystals. *Acta Metallurgica*, 1956, vol. 4, p. 306.
[13] J. C. Suits and J. R. Low, Jr.: Dislocation Etch Pits in Silicon Iron. Acta Metallurgica. To be published.
[14] P. A. Jacquet: Recherches Expérimentales sur La Microstructure De La Solution Solide Cuivre-Zinc 65/35 Polycrystalline Très Faiblement Déformée Par Traction et Sur Son Evolution Au Recuit Entre 200 et 600°C. *Acta Metallurgica*, 1954, vol. 2, p. 770.
[15] S. Weissmann: Method for the Study of Lattice Inhomogeneities Combining X-ray Microscopy and Diffraction Analysis. *Journal of Applied Physics*, 1956, vol. 27, p. 389.
[16] B. Chalmers: Private communication.
[17] C. G. Dunn and K. T. Aust: Dislocation Energy as a Driving Force for Boundary Migration. Acta Metallurgica. To be published.
[18] W. E. Bron and E. S. Machlin: Grain Boundary Mobilities in High Purity Silver. *AIME Trans.*, 1956, vol. 206, p. 513; JOURNAL OF METALS, May 1956.

Discussion of this paper sent (2 copies) to AIME by June 1, 1957 will appear in AIME *Transactions* Vol. 209, 1957, and in JOURNAL OF METALS, October 1957.

Zone Purification of Reactive Metals

A description is given for an apparatus and technique used to zone melt reactive, high-melting-point metals by the floating zone method. The use of radioactive tracers to determine the redistribution of solute during zone melting is discussed and results are shown for P^{32} in iron, Au^{198} in titanium and zirconium, and Zn^{65} in titanium. Some tensile results on iron at liquid nitrogen and liquid helium temperatures are given which indicate that the removal of trace impurities markedly increase the low temperature ductility of iron.

by R. L. Smith and J. L. Rutherford

ZONE refining, as developed by W. G. Pfann,[1] has been used extensively for the purification of semiconductors. This method has made it possible to obtain the extremely high purity material necessary for the transistor industry. It has also been utilized to some extent for the purification of relatively low-melting-point metals. However, very little attention has been given to reactive, high-melting-point materials, with the exception of silicon.[2-5] For this element, it has been necessary to use the floating zone technique in order to avoid contamination from the crucible containing the melt.

The method is one in which a narrow molten zone is formed in a vertical rod by induction heating. The molten zone is supported between the two solid sections of the rod by surface tension. It is then moved longitudinally along the rod in order to effect a redistribution of solute. This technique has an advantage over the horizontal boat method, since crucible contamination is avoided. It has the disadvantage of being a much more difficult technique than zone refining in a crucible. Furthermore, it is necessarily a slow process, since only one zone at a time can be formed. However, the floating zone process offers a means of obtaining high-purity metals that are either not available, or can only be obtained in powder or pellet form as the result of complex chemical or electrochemical methods. It should be emphasized that the process is not effective in removing all impurity elements. Those that cannot be redistributed in an ingot during zone melting must be removed by some other means.

Very little is known of the properties of very high purity reactive metals such as iron, titanium, zirconium, beryllium, etc. It is quite likely that trace elements in such metals can affect their properties drastically. Therefore, one of the primary objectives of this work is to study the properties of metals which have been obtained in the purest form available and then zone refined.

Trace elements can be introduced in a variety of ways, such as by inserting wafers between solid portions of the ingot to be melted, by placing the

R. L. SMITH, Member AIME, and J. L. RUTHERFORD, Junior Member AIME, are associated with Solid State Physics Division, Franklin Institute Laboratories for Research and Development, Philadelphia.

TP 4424E. Manuscript, Apr. 13, 1956. Buffalo Regional Reactive Metals Conference, March 1956.

impurity elements in holes drilled in the ingot, etc. They may then be homogeneously distributed by zone leveling,[1] that is, by passing the zone back and forth in the bar. This allows experiments to be conducted for the determination of the effect of such elements on the properties of metals. It is known that the presence of another element in a base metal will affect its properties in a certain way. However, it often cannot be determined whether this is because of its interaction with the base metal or with other elements present in the base metal. For example, the removal of elements such as oxygen, nitrogen, and sulfur raises the ductile-to-brittle transition temperature in steel and the addition of other elements, such as manganese, lowers it. It is not clear, however, whether the addition of the manganese improves the low temperature behavior solely by its solid solution alloying effects with iron, or because of its tendency to form sulfides, oxides, etc., with other impurities. The controlled addition of trace impurities to ultra-pure metals is an ideal experiment to evaluate such effects.

An additional use of the floating zone technique is to solidify powder compacts. In some cases, the highest purity metal obtainable may be in powder form as a result of some chemical process. This powder can be pressed into a porous ingot and sintered, but it will always retain some porosity. To avoid this, the green pressed compact can be brought to a solid ingot by passing a floating molten zone through it, thus avoiding contamination by a crucible.

Equipment for Floating Zone Method

An apparatus for the floating zone method of zone melting silicon is described in detail by Keck et al.[2] In their apparatus, an induction coil encircles a necked-down portion of a Vycor furnace tube containing the vertically supported ingot. The silicon ingot is moved through the field of the induction coil while the coil and the furnace tube remain stationary.

Ordinarily, the high melting point metals have a higher specific gravity and thermal conductivity than silicon. This makes the floating zone technique somewhat more difficult to control because of the tendency for the zone to lengthen and therefore to collapse. The primary problem is to maintain a sufficiently short zone to prevent this collapse.

A schematic diagram of the apparatus used for the present work is shown in Fig. 1. The whole furnace assembly, including the ingot, moves through the induction coil, thus providing a clean Vycor surface which permits the operator to see the molten zone.

The present apparatus utilizes a 450 kc Ecco high-frequency oscillator. Fig. 1 is a schematic diagram of the melting assembly. This consists of a Vycor tube, *L*, containing the specimen to be purified, *N*, which is mounted between two movable carriages, *C* and *E*. The carriages move vertically along tracks, *D*, powered by a hydraulic piston mounted at the top of the tracks and connected to the carriages by the concentric shafts, *A*. The rate of travel of the carriage assembly is controlled by needle valves in the hydraulic lines. A specimen mounting shaft, which rotates in ball bearings, *G*, is attached to each carriage. The specimen is attached to the top mounting shaft, *F*, by set screws, *M*. At the bottom mounting shaft, *S*, the specimen is fastened to a chuck, *P*, by set screws; this chuck is a sliding fit over the top of the bottom mounting shaft. The Vycor tube,

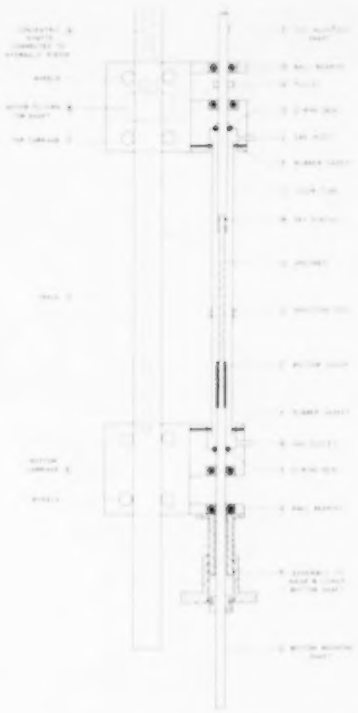

Fig. 1—Schematic diagram of zone melting apparatus.

L, is placed between the two carriages and the pressure seals are formed by the rubber gaskets, *K*. An assembly, *R*, to raise and lower the bottom shaft, *S*, is attached to the bottom carriage. This assembly allows vertical motion of the bottom shaft independent of the motion of the carriages. O-ring seals, *I*, on the shafts, make the system gas tight. The top shaft, *F*, can be rotated by a motor, *B*, mounted in the top carriage. The induction coil, *O*, remains stationary while the furnace moves through it.

In operation, a molten zone is established in the specimen. To ascertain that the molten zone extends completely through the rod, the bottom mounting shaft is lowered independently of the bottom carriage. If the bottom chuck follows the shaft down, then the molten zone is complete. If the specimen is not melted completely, the bottom chuck will not ride down with the bottom shaft. The rotation of the top shaft also serves to determine whether the molten zone is complete. If there is any solid material between the upper and lower portions of the specimen, the loose fitting belt-drive will slip or the bottom part of the specimen will rotate along with the top part.

An inert gas is passed through the furnace for two purposes. First, it supplies a pure atmosphere for the melting to take place. Second, it carries any vaporized material away from the portion of the Vycor tube inside the induction coil and deposits the vaporized material along that part of the tube that has already gone through the induction coil. Thus, the Vycor tube inside the induction coil remains clear. In addition, any of the vaporized material which deposits on the specimen is readily removed and is not melted into the specimen as would be the case if the flow of gas were in the same direction as the zone travel. For the studies of titanium, zirconium, molybdenum, and nickel, the atmosphere used was spectroscopically pure argon. For the present experiments helium, which has previously

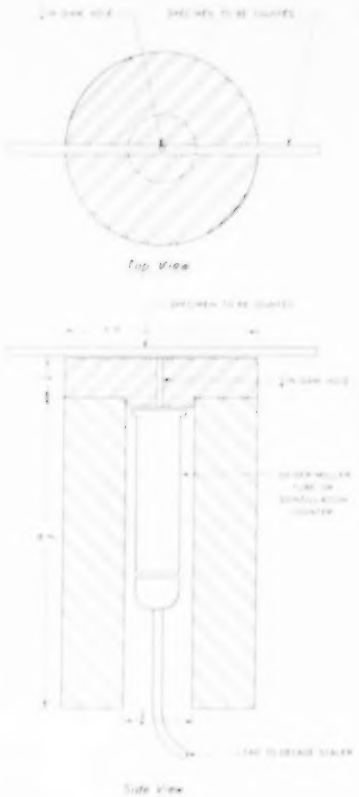

Fig. 2—Schematic diagram of counting arrangement.

been liquified in an A. D. Little Inc. Collins Cryostat, is being used. Iron was purified in a dry hydrogen atmosphere. The hydrogen was removed later by high temperature vacuum annealing.

Analysis by Radioactive Tracers

In order to establish the effectiveness of a given set of conditions for zone refining, it is necessary to analyze a specimen periodically during the purification process. This is expensive, time consuming, and wasteful of specimens if chemical, colorimetric, spectrographic or activation analyses are used. Radioactive tracers provide an easy means of analysis. Albert et al.[5] have recently used Zn^{65} in aluminum to study the redistribution during horizontal zone melting.

In the present study a tracer is chosen with the desired distribution coefficient. It is added to the ingot to be zone melted and then evenly distributed by zone leveling. The distribution of the radioactive tracer along the length of the specimen is measured with the apparatus shown in Fig. 2. The Geiger-Muller tube is encased in a cylindrical lead safe with walls 1½ in. thick. A collimating hole ¼ in. in diameter is directly above the center of the tube. The specimen to be counted is placed directly above this hole and is measured at regular intervals. Background is measured at these same points by replacing the top of the safe with a top that has no collimating hole. To measure γ radiation when the isotope has a complex spectrum, the tube is replaced by a scintillation detector and the β radiation is filtered out with an aluminum sheet. In calculating the distribution of radioactive tracer, the natural decay is taken into account and a correction applied. The advantages of this method can be readily seen. It does not destroy or consume a sample and it is accurate and rapid.

Results

Rods of iron, titanium, zirconium, nickel and molybdenum have been zone melted. Initial experiments on nickel and molybdenum were made to ascertain the feasibility of the method. In general, preliminary experiments are utilized to determine the conditions necessary for supporting a molten zone and moving it at a proper rate to effect a redistribution of solute. It is important to maintain a reasonably uniform cross section during a pass. Otherwise, the succeeding passes will become increasingly difficult to control. In addition, the ratio of zone length to ingot length will vary continuously and thus affect the redistribution of solute. Samples of satisfactorily zone melted ingots are shown in Fig. 3. If the bars become too nonuniform, it is necessary to swage them, which increases the danger of contamination. It is very difficult to eliminate nonuniformities in brittle materials once they are formed.

When the proper conditions of melting are established, the refining process is started. Usually, the preliminary experiments are carried out on commercially pure material, since it is necessary to establish quite accurate control procedures. For iron, a vacuum melted Fe-C alloy (about 0.3 pct C) was zone melted. After eight zone passes at a rate of 2 in. per hr a clean microstructure was obtained. Fig. 4 shows the microstructure of this material before and after zone melting. The zone purified material is remarkably free from carbides and inclusions.

Radioactive phosphorus, P^{32}, was deposited in a series of transverse holes ¼ in. apart along a 4 in. length of 3/16 in. diam Swedish iron rod (99.7 pct Fe). The holes were eliminated by successively melting a short volume of the rod at each hole, and then pushing the ends of the rod together to restore the 3/16 in. diam. Only the first 2¾ in. of the radioactive part of the rod were zone melted; the remaining 1¼ in. served as a monitor. Hence, the natural decay could be measured and the activity for the zone-melted section corrected. Because of the slow rate of molten zone travel (1.5 in. per hr) and the need for analysis after each pass, only one pass per day could be obtained. The zone-melted rod, while it was of nearly constant cross section, showed a slightly wrinkled surface. Since the activity measured is surface radiation, a wrinkled surface would result in a higher count. Hence, the specimen was swaged to eliminate the wrinkles.

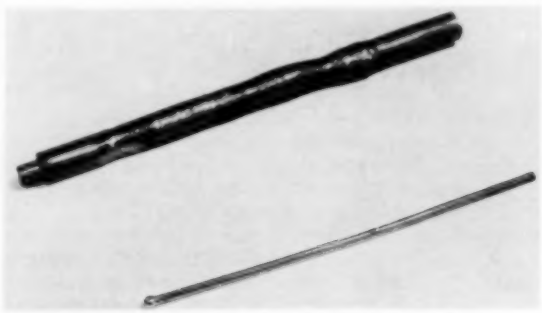

Fig. 3—Zone melted iron bars, 3/8 and 3/32 in. diam.

Fig. 4—Fe-C alloy. LEFT: before; and RIGHT: after zone melting. X500. Reduced approximately 20 pct for reproduction.

Fig. 5 shows the changes in distribution of phosphorus radioactive tracer for six zone passes. It can be seen that the concentration of phosphorus in the starting end is only 2.2 pct of its original concentration. The concentration of solute does not exceed the initial concentration for the first 90 pct of the bar. This is because of the relatively short zone length used. The zone length was about 7 pct of the bar length and, although the shorter zone does not redistribute the solute as fast, it becomes more effective after a number of passes have been made. The effect of the last zone to freeze is not reflected back toward the starting end as badly when short zone lengths are used. The final concentrations, as shown in Fig. 5, cannot be considered as very accurate, since the final zone could not be deposited in exactly the same place.

Fig. 6 shows the microstructure of the Swedish iron before zone purification. The black globules on the grain boundaries are probably iron carbide. Fig. 7 shows the end at which the impurities were deposited. A second phase, presumably a phosphorus-rich phase, is apparent in the microstructure. Fig. 8 shows the purified end, which is relatively free from visible inclusions and second phase material.

Burris et al.[5] have taken into account the effect of normal freezing in the last zone length, and have calculated the concentration profiles of solutes having various distribution coefficients and zone lengths for successive passes.

Fig. 9 shows the theoretical concentration profiles from their calculations for the fifth pass and for distribution coefficients of 0.2 and 0.5. The zone length for this plot is 10 pct of the bar length. The value for the fifth pass on the iron bar containing radioactive phosphorus with a zone length 7 pct of the bar length is also shown. It can be seen that it lies between the theoretical curves. This means that the true distribution coefficient lies between 0.2 and 0.5. In this case, it cannot be accurately determined, since the initial concentration, C_o, was not the same throughout the bar. The value of k obtained from the phase diagram is 0.27.

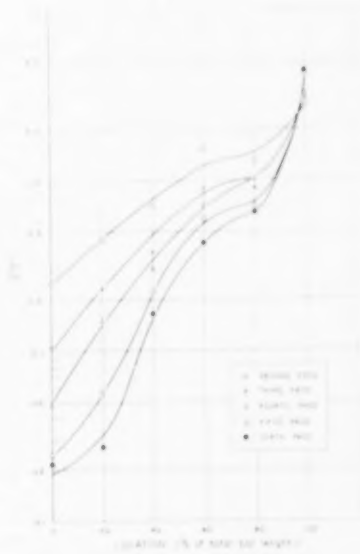

Fig. 5—Distribution of phosphorus in iron.

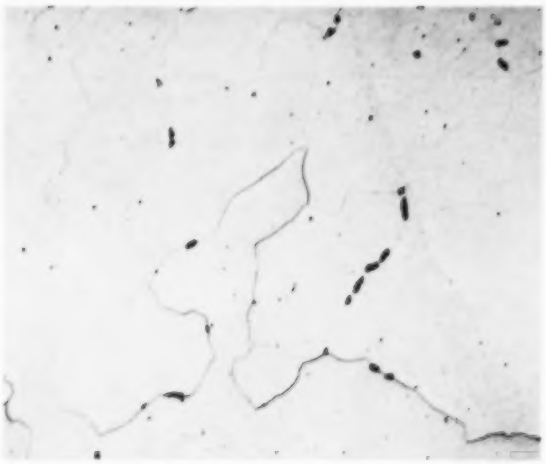

Fig. 6—Micrograph of Swedish iron which was not zone melted; 2 pct Nital etch. X200. Reduced approximately 15 pct for reproduction.

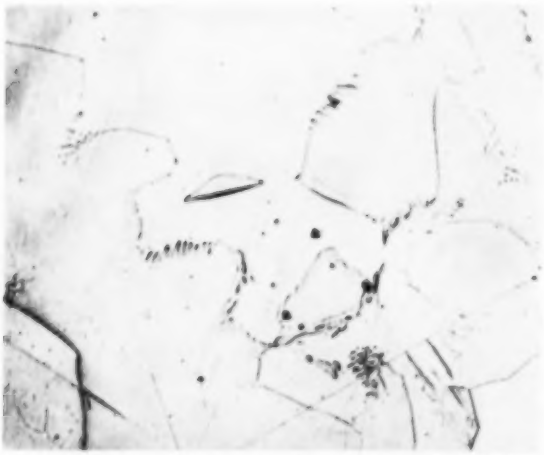

Fig. 7—Micrograph of impure section of zone melted Swedish iron; 2 pct Nital etch. X200. Reduced approximately 15 pct for reproduction.

Fig. 8—Micrograph of pure section of zone melted Swedish iron; 2 pct Nital etch. X200. Reduced approximately 15 pct for reproduction.

Radioactive tracer (Au^{198}) was added to an iodide zirconium bar. A zone pass was made through the bar in each direction over a length of 5 in. at a rate of 1.4 in. per hr. Activity determinations were made at ¼ in. intervals after each pass. No zone leveling was observed. Due to the presence of a high peak in the center, a pass was then taken from the center, first toward the top end and then toward the bottom end. Again, no change in distribution was observed. Because of the short half life of Au^{198} (2.69 days) the activity became too low to be determined with any accuracy. However, there was no detectable redistribution of Au^{198} at this rate of zone movement. This could mean either that the distribution coefficient was near 1 or that the rate of zone travel was too fast.

Au^{198} was then added to a commercially pure grade of titanium (Rem Cru-A-55). Since it was expected that gold in titanium would behave similarly to gold in zirconium, a slower rate of travel was used and the top portion of the bar rotated. The first pass was put through the bar at ½ in. per hr with the upper section rotating at 4 rpm. A noticeable redistribution of Au^{198} was observed. The second pass was slowed to ¼ in. per hr with the upper section rotating at 20 rpm. The distribution of the Au^{198} after the second pass is shown in Fig. 10. This is an autoradiograph taken in a special camera with the film directly in contact with the sample, and demonstrates another technique to determine solute distribution. The exposure was 2½ hr on Kodak No-Screen X-Ray film. The bar was ground to a flat surface. There are no pressure artifacts on the autoradiograph. The blackened area on the right is the point at which the zones were solidified. The vertical line on the left end of the autoradiograph represents the start of the purification.

Fig. 11 shows the activity curve for the distribution of Zn^{65} in titanium (Rem Cru-A-55) after one zone pass at 1½ in. per hr, with the upper section rotating at 4 rpm. This curve shows a marked redistribution of tracer, but cannot be considered in a quantitative way since the original distribution was not zone leveled. However, the distribution should have been very uniform, since the Zn^{65} was electroplated evenly on a 3 in. section of a 3/32 in. titanium rod. This rod was then inserted in a hole drilled longitudinally in the center of a 3/16 in. titanium bar. The open end was plugged and a section of solid rod added for holding purposes. Because of the difference in melting points and the high volatization of the zinc, it was not possible to obtain the effect of multiple passes.

Tensile Test Results and Discussion

A hydraulic tensile-testing apparatus was constructed for use over a range of temperatures to include testing in liquid helium. This apparatus utilizes a proving ring to measure the load. The extension is determined by means of a dial indicator.

High purity iron prepared at the University of Pennsylvania for an earlier study[7] was zone melted in dry hydrogen. This iron was swaged to 0.055 in. diam and annealed 48 hr in a dynamic vacuum at 900°C. The rod was wire drawn to a 0.031 in. diam, hand polished to a four zero paper finish for tensile testing and heat treated 20 min at 650°C.

Fig. 12 shows engineering stress-strain diagrams for four specimens tested in tension at −196°C. The material not zone melted shows some ductility. This amount of ductility is not unusual for iron with low

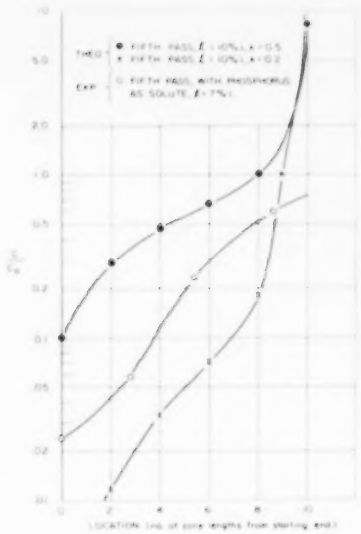

Fig. 9—Distribution of solute as a function of k.

Fig. 10—Autoradiograph of zone melted titanium bar, doped with Au^{198}. Vertical mark on left indicates start of zone; dark area on right indicates section in which zones were solidified.

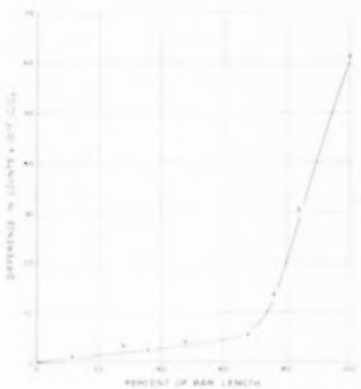

Fig. 11—Redistribution of Zn^{65} in titanium after one zone pass.

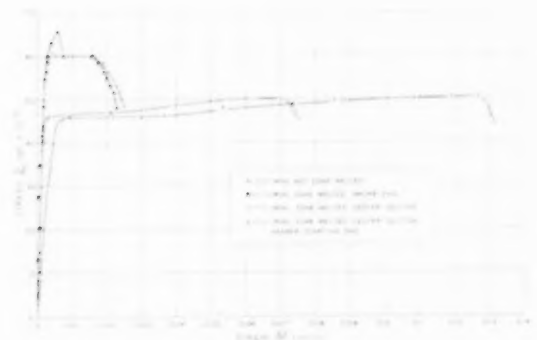

Fig. 12—Tensile tests of iron at —196°C.

gas content and small grain size (ASTM No. 8). The other curves are for specimens taken from the zone melted stock. The greatest ductility was exhibited in the specimen at 0.15 of the distance from the starting end. The specimen with the second greatest ductility was 0.42 of the distance from the starting end; the least ductility was shown by the specimen taken from the part of the rod where the impurities were deposited. The specimens from the center section had badly duplexed grain structures ranging from ASTM No. 4 to ASTM No. 7. There were only a few grains across the section in some areas. The impure material showed an equiaxed fine grain structure (ASTM No. 7). The specimen not zone melted shows a sharp yield point because of the presence of carbon. The absence of an inhomogeneous yield for the zone purified material indicates that the carbon was effectively removed.

Tensile tests have been made on the same iron at 4.2°K and are reported separately.[8] Fig. 13 shows the fractured end of a specimen of the zone purified iron (0.15 of the distance from the starting end) tested at this temperature. The fracture is ductile and shows an 80 pct reduction of area with twins or *Neumann bands* all along the gage section. The extent of the twinning is shown in the micrograph of Fig. 14, which was taken near the end of the gage section. In contrast, the impure material fractured in tension at 4.2°K showed only a few twins at the point of fracture and exhibited no ductility.

The 80 pct reduction of area for the zone purified specimens tested in tension at 4.2°K is highly significant. The ductility of hexagonal and body-centered-cubic metals decreases with decreasing temperatures so that usually such materials are completely brittle long before liquid helium temperatures are reached. On the other hand, face-centered-cubic metals retain their ductility at low temperatures. Such information indicates that the body-centered lattice is brittle at low temperatures. Although an 80 pct reduction of area, as obtained in this investigation, is somewhat less than that which can be obtained at room temperature, it is certainly high enough so that the metal can be considered ductile. Thus, it can be concluded that the body-centered-cubic lattice in itself is not a brittle structure in simple tension, but that it is much more strongly affected by impurity atoms than is the face-centered-cubic lattice. An excellent review on the ductility of metals at low temperatures has been published by Seigle and Brick.[9]

It should be kept in mind that brittle behavior can best be evaluated by impact tests such as the Charpy V-notch test. A material may show considerable ductility in tension and yet be completely brittle in impact tests. Thus, the present results do not show that all types of brittle behavior can be removed from iron. However, they do show that considerable ductility in tension can be retained. This is an important step, since it indicates that it may be possible to develop room temperature ductility at very low temperature as higher purity material is obtained. As was pointed out previously, certain elements with unfavorable distribution coefficients cannot be removed by the zone melting process, so that the success of the process in yielding ultra-pure material depends on the starting stock.

There is no reason to assume that the improvement in low temperature ductility with removal of trace impurities will be restricted to iron. Other

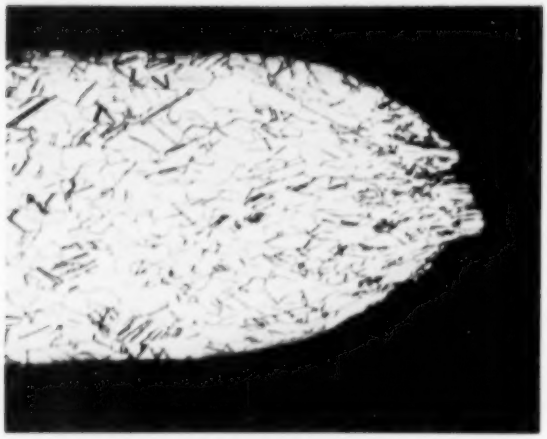

Fig. 13—Micrograph of fractured end of pure zone melted iron tested at 4.2°K; shows ductile fracture with an 80 pct reduction of area. X100. Reduced approximately 20 pct for reproduction.

Fig. 14—Micrograph of electrolytic iron, oxidized heavily by air-melting, then deoxidized in vacuum with carbon. Zone melted pure end was reduced to 0.031 in. diam with intermediate anneals. Final heat treatment: 650°C for 20 min. Tensile tested at 4.2°K. Shows twins 0.5 in. from fracture. X500. Reduced approximately 20 pct for reproduction.

body-centered-cubic and hexagonal metals might be even more strongly affected. Furthermore, other parameters such as residual resistivity, thermoelectric power at low temperatures, certain magnetic properties, etc., will probably undergo unusually large changes as metals are obtained in states of higher purity.

Summary

The floating zone technique of zone purification can be successfully applied to reactive high-melting-point metals. The experimental conditions necessary for effective redistribution of solute atoms may be established by the use of radioactive tracers. This method provides a fast economical way to determine the optimum combination of such factors as coil design, ingot size, speed of zone travel, number of passes needed, etc.

Phosphorus and carbon in iron, and gold and zinc in titanium have been shown to segregate to the end of the ingot to solidify last during zone melting.

At liquid nitrogen temperature, tensile tests on iron show that there is a progressive increase in ductility as higher purity specimens are used. Tensile tests at 4.2°K show that a large reduction in area can be obtained in highly purified iron.

Acknowledgments

This research was supported by the United States Air Force through the Air Force Office of Scientific Research under Contract No. AF 18 (600)-1581. The authors are indebted to I. G. Greenfield and J. B. Drew for their assistance in preparing the micrographs and autoradiographs.

References

[1] W. G. Pfann: *AIME Trans.*, 1952, vol. 194, p. 747; JOURNAL OF METALS, July 1952.
[2] H. Theurer: Unpublished research.
[3] P. H. Keck and M. J. E. Golay: *Physical Review*, 1953, vol. 89, p. 1297.
[4] P. H. Keck, W. Van Horn, J. Solad, and A. MacDonald: *Review of Scientific Instruments*, 1954, vol. 23, p. 331.
[5] P. A. Albert, F. Montariol, R. Reich, and G. Chaudron: *Radioisotope Conference*, 1954, vol. 2, p. 75.
[6] L. Burris, Jr., C. Stockman, and I. Villon: *AIME Trans.*, 1955, vol. 203, p. 1017; JOURNAL OF METALS, September 1955.
[7] R. L. Smith, G. Spangler, and R. M. Brick: *ASM Trans.*, 1954, vol. 46, p. 973.
[8] R. L. Smith and J. L. Rutherford: To be published.
[9] L. Seigle and R. M. Brick: *ASM Trans.*, 1948, vol. 40, p. 813.

Discussion of this paper sent (2 copies) to AIME by June 1, 1957 will appear in AIME *Transactions* Vol. 209, 1957, and in JOURNAL OF METALS, October 1957.

Technical Note

Compounds in the Titanium-Rich Region of the Ti-Al System

by Elmars Ence and Harold Margolin

E. ENCE and H. MARGOLIN, Members AIME, are Associate Engineering Scientist and Engineering Scientist, respectively, Research Division, College of Engineering, New York University, New York.

TN 387E. Manuscript, May 10, 1956.

BUMPS, Kessler, and Hansen[1] have reported that the solubility of aluminum in α titanium is about 31 pct at 1240°C. Despite this large solubility, and no evidence of other phenomena, alloys containing 12 pct Al or more were found to be brittle. The

Table I. X-Ray Diffraction Data of Ti_3Al*

hkl	Observed, d, A	Estimated Relative Intensity	Calculated, d, A
100	5.012	0.1	5.001
101	3.396	0.2	3.399
110	2.880	0.05	2.887
200	2.502	0.5	2.500
002	2.320	0.7	2.319
201	2.205	1.0	2.201
210	1.886	0.06	1.890
112	1.810	0.08	1.809
211	1.751	0.06	1.751
202	1.700	0.6	1.700
103	1.474	0.04	1.477
220	1.443	0.5	1.444
302	1.351	0.02	1.353
203	1.315	0.6	1.315
400	1.251	0.1	1.251
222	1.227	0.4	1.226
401	1.208	0.3	1.208
004	1.160	0.2	1.160
402	1.102	0.2	1.101
204	1.050	0.2	1.052
403	0.973	0.3	0.973
420	0.945	0.1	0.945
421	0.927	0.4	0.926
224	0.905	0.4	0.905
422	0.876	0.1	0.875
205	0.870	0.4	0.870
404	0.850	0.1	0.850
215	0.834	0.2	0.833
423	0.806	0.5	0.806
602	0.784	0.4	0.784

* As obtained from a Ti-25 pct Al alloy annealed at 1000°C and water quenched. $CuK\alpha_1$—radiation.

Table II. X-Ray Diffraction Data for a Ti-14 Pct Al Alloy Annealed at 1000°C*

d, A	Estimated Relative Intensity
5.00	0.08
3.40	0.2
2.90	0.05
2.50	0.6
2.46†	0.08
2.38†	0.2
2.32	0.6
2.26†	0.02
2.20	1.0
2.14†	0.2
2.07†	0.3
1.89	0.08
1.81	0.08
1.75	0.08
1.71	0.7
1.51†	0.1
1.46†	0.1
1.45	0.7
1.32	0.7
1.26	0.1
1.25	0.1
1.23	0.6
1.21	0.4
1.16	0.1
1.10	0.1
1.06	0.1

* Pattern contains Ti_3Al and an unidentified compound.
† These are d-values of the unidentified compound.

investigation also reported that the c/a ratio of aluminum alloyed α increased because as aluminum content increased the c parameter decreased less than the a parameter. Similar observations have been made by others.[5, 6]

Van Thyne and Kessler[4] reported the results of the effects of oxygen, nitrogen, and carbon on the constitution of Ti-Al alloys. They found no new phases, but reported anomalous hardness behavior which would appear to be a precipitation hardening phenomenon.

It has also been observed that oxygen raises the c/a ratio of α-titanium, but this is achieved primarily by increasing the c parameter.[5] Since aluminum decreases a lattice parameters it appeared worthwhile to investigate the joint effects of aluminum and oxygen on the lattice parameters. This was undertaken as a senior thesis by Pon,[6] who was unable to carry his investigation to extensive aluminum and oxygen compositions because of the appearance of unexpected extra lines in X-ray diffraction patterns. Pon used sponge titanium as his base material.

As a result of Pon's findings a reinvestigation of the Ti-Al-O and, subsequently, the Ti-Al system was undertaken by the authors. A preliminary report of these findings has been given at Watertown Arsenal.[7]

Reinvestigation of the Ti-Al-O system with iodide titanium and high purity aluminum has shown that the extra lines found by Pon were due to the existence of a compound which appeared to exist in the Ti-Al system itself. A check of the binary system with alloys containing 20 to 30 pct Al confirmed this conclusion.

Between 1000° and 1200°C, the compound has a range of solubility about the composition Ti_3Al. The compound could be indexed as hexagonal with lattice parameters $a = 5.775$A, $c = 4.638$A, and $c/a = 0.803$, a value approximately half that of α-titanium. The diffraction pattern of a Ti-25 pct Al alloy, together with calculated d-values, is given in Table I. The structure of Ti_3Al is isomorphous with Ti_3Sn,[8] as pointed out by Pietrokowsky.[9]

Further investigation of the binary Ti-Al system has revealed additional complexities in the region of the Ti-Al system below Ti_3Al. It has been shown that, at 1000°C, adjacent to the Ti_3Al field there is a two phase region which does not include α. The pattern of a Ti-14 pct Al alloy is given in Table II. The same two-phase structure of this alloy has also been observed to occur in a Ti-20 pct Al alloy.

The existence of the compounds reported here would account for the brittleness observed in Ti-Al alloys containing 12 pct Al or more and indicate that the Ti-Al diagram of Bumps et al.[1] must be revised.

Acknowledgment

The authors wish to thank the U. S. Army Ordnance Corps, Watertown Arsenal, for financial support and the permission to publish this work. The investigation was carried out under Contract No. DA-30-069-ORD-1481 and is being continued under Contract No. DA-30-069-505-ORD-1781.

References

[1] E. S. Bumps, H. D. Kessler, and M. Hansen: Titanium-Aluminum System. *AIME Trans.*, 1952, vol. 194, p. 609; JOURNAL OF METALS, June 1952.

[2] H. R. Ogden, D. J. Maykuth, W. L. Finlay, and R. I. Jaffee: Constitution of Titanium-Aluminum Alloys. *AIME Trans.*, 1951, vol. 191, p. 1150.

[3] C. I. McHargue, S. A. Adair, Jr., and J. P. Hammond: Effects of Solid Solution Alloying on the Cold-Rolled Texture of Titanium. *AIME Trans.*, 1953, vol. 197, p. 1199; JOURNAL OF METALS, September 1953.

[4] R. J. Van Thyne and H. D. Kessler: Influence of Oxygen, Nitrogen and Carbon on the Phase Relationships of the Ti-Al System. *AIME Trans.*, 1954, vol. 200, p. 193; JOURNAL OF METALS, February 1954.

[5] H. T. Clark, Jr.: The Lattice Parameters of High Purity Alpha Titanium, and the Effects of Oxygen and Nitrogen on Them. *AIME Trans.*, 1949, vol. 185, p. 588; JOURNAL OF METALS, September 1949.

[6] K. J. Pon: Lattice Parameters of Ti-Al-O Alloys. New York University Senior Thesis, May 1954.

[7] E. Ence and H. Margolin: Preliminary Report on Ti-Al-O and Ti-Al Phase Diagrams. Physical Metallurgy Symposium, Watertown Arsenal, Sept. 21-22, 1955.

[8] P. Pietrokowsky: Crystal Structure of Ti_3Sn. *AIME Trans.* 1952, vol. 194, p. 211; JOURNAL OF METALS, February 1952.

[9] P. Pietrokowsky: Private communication.

Crack Propagation in the Hydrogen-Induced Brittle Fracture of Steel

The macroscopic features of hydrogen-induced static fatigue have been identified. The process is one of crack initiation and slow crack growth, followed by cataclysmic crack propagation (fracture). An electrical resistance method was developed to permit analysis of the crack growth kinetics. Specimens containing a high hydrogen concentration in the surface layers were examined. Three distinct stages of crack growth were identified. The first stage was characteristic of crack growth through a pre-existent hydrogen-rich region (surface layer), while the second stage was associated with the gross inward diffusion of hydrogen. The third stage was associated with imminent fracture.

by W. J. Barnett and A. R. Troiano

IN recent years the demands of space limitations and increased loads, particularly in the aircraft industry, have accelerated the trend toward utilization of ultra-high strength steels. The increased application of such steels has focused attention on the phenomenon of delayed failure or static fatigue. Parts subjected to a *static* load, after successfully sustaining the load for an extended period of time, may fail in a brittle manner. Subsequent examination of such failed parts by conventional laboratory tests in many cases reveals no apparent signs of embrittlement. That is, the material exhibits good ductility and impact resistance. Furthermore, consideration of the service conditions (environment and temperature) under which this brittle failure occurred eliminates its classification as a stress-corrosion or creep type of failure. Recently this unique time dependent fracture process has been the subject of numerous investigations. The most significant result of these studies was the recognition of hydrogen as the source of embrittlement. While the effect of numerous variables on the occurrence of static fatigue failure has been defined, an adequate explanation of these behaviors is lacking.

W. J. BARNETT, formerly Research Associate, Dept. of Metallurgical Engineering, Case Institute of Technology, is now associated with the Aircraft Gas Turbine Div., General Electric Co., Cincinnati. A. R. TROIANO, Member AIME, is Professor and Head, Dept. of Metallurgical Engineering, Case Institute of Technology, Cleveland.

TP 4285E. Manuscript, Sept. 15, 1955. New York Meeting, February 1956.

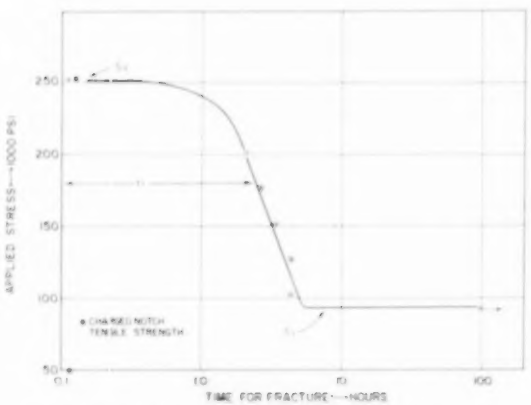

Fig. 1—Static fatigue characteristics of 4340 steel at the 230,000 psi strength level; charging condition A, aged 5 min, sharp notch specimens.

The occurrence of this phenomenon in steels generally has been limited to strength levels in excess of 180,000 lb per sq in. Although steels at high hardness levels have exhibited delayed failure in the absence of hydrogen introduction after heat treatment,[1,2] this behavior was most prevalent when the material in processing had been subjected to an environment conducive to the absorption of hydrogen. Delayed failures have been produced in high strength steels by the introduction of hydrogen

either by cathodic charging[1,2] or other means.[4] These results amply demonstrated the significant role of hydrogen. Thus, static fatigue failure in high strength steels is but another facet of the problem of hydrogen embrittlement. However, it manifests itself in a more cataclysmic fashion than the usual loss of ductility which has been recognized as the trademark of hydrogen embrittlement, and indeed may occur when the conventional tensile ductility criterion reveals no apparent embrittlement.

Frohmberg, Barnett, and Troiano[5] provided a comprehensive study of hydrogen-induced static fatigue and embrittlement behavior of 4340 steel quenched and tempered to strength levels of 200,000, 230,000, and 270,000 psi. Delayed failure was observed over a wide range of relatively low applied stresses. This stress range was dependent on strength level, notch acuity, and the aging time after the introduction of hydrogen. As schematically illustrated in Fig. 1, the delayed failure behavior of cathodically charged sharp notch specimens, see Fig. 2, exhibited three distinguishing features which characterized the phenomenon of delayed failure:

1) An upper critical stress, S_u, above which instantaneous fracture occurred; the charged notch tensile strength.

2) A lower critical stress, S_l, below which fracture did not occur; the static fatigue limit.

3) A stress range between S_l and S_u, in which time dependent fracture was observed. Within this stress range the static fatigue life, t_f, exhibited a slight stress dependence.

Regardless of the strength level, the fracture time was of the same order of magnitude—from approximately 1 to 8 hr. Decreasing the notch acuity resulted in an increase in S_l and a decrease in S_u, thereby reducing the stress range within which delayed failure was observed.

Table I. Composition of SAE 4340 Steel, Wt Pct

C	Mn	Si	Ni	Cr	Mo	H_2
0.39	0.76	0.28	1.80	0.75	0.24	0.000143

Observations by these investigators[5] on the effect of aging under load gave an indication of the nature of the delayed failure fracture process. The room temperature charged notch tensile strength recovery pattern was unaltered by aging under an applied load, unless the static fatigue limit, S_l, was exceeded. In this case, permanent damage of an unspecified nature was evidenced by an abnormal decrease in the notch tensile strength. It was suggested that, in view of the insensitivity of fracture time to strength level, the failure time may be associated with the diffusion of hydrogen—the time to accomplish a critical redistribution of hydrogen.

The present investigation was initiated for the purpose of analyzing the nature of the static fatigue fracture process. The fracture process was analyzed with respect to its two basic components, crack initiation and crack propagation.

Materials and Procedure

Material—The material was taken from the same commercial heat of SAE AISI 4340 steel used in a previous investigation.[3] The chemical analysis is given in Table I.

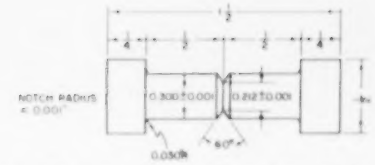

Fig. 2—Static fatigue and notch tensile specimen.

Heat Treatment—Test specimens taken from ⅝ in. round hot rolled bars were prepared according to the following schedule:

1) Normalized at 1650°F (899°C) for 1 hr and air cooled.

2) Stress relieved at 1200°F (650°C) for 4 hr and furnace cooled.

3) Rough machined 1/16 in. oversize (notches were not rough machined).

4) Austenitized at 1550°F (843°C) for 1 hr and oil quenched.

5) Tempered for 1 hr at 450°F (232°C), 700°F (371°C), or 750°F (399°C) to obtain respective nominal strength levels of 270,000; 240,000; or 230,000 lb per sq in., and water quenched.

6) Finish machined.

All specimens at a given strength level were heat treated as a group.

Specimen Types—The notch specimen, shown in Fig. 2, was employed in the static fatigue and notch tensile tests. A 0.212 in. diam, 2 in. radius test section specimen was used for conventional tensile tests.

Testing Methods—Static fatigue tests were conducted on a dead weight (constant load), lever arm type stress-rupture machine. A concentric test fixture was used for both static fatigue and tensile tests in order to give uniaxial loading with a maximum eccentricity of 0.001 in. Except where strain rate is noted as a variable, tensile tests were performed at a constant cross-head speed of 0.05 in. per min.

Hydrogen was introduced by cathodic charging for 5 min at a current density of 0.02 amp per sq in. in a 4 pct sulfuric acid electrolyte at 80°F. This procedure, subsequently referred to as charging condition *A*, has been described in a previous publication.[4] The button-head fillet of the notch specimens employed in the precrack static fatigue study was masked with collodion or glyptal prior to cathodic charging. Aging time was considered as the interval between the termination of charging and the commencement of a test. Except where aging time is specified as a variable it was 5 min. All tests were performed at room temperature.

Table II. Effect of Cathodic Charging on the Mechanical Properties of 4340 Steel Heat Treated to Several Strength Levels

Nominal Strength Level, Psi	230,000	240,000	270,000
Uncharged			
Tensile Strength, Psi	227,000	236,000	279,000
Yield Strength, Psi	—	220,000	235,000
Reduction in Area, Pct	45.5	46	44
Fracture Strength, Psi	318,000	345,000	388,000
Notch Tensile Strength, Psi	306,000	315,000	330,000
Cathodically Charged, Condition *A*, 5 Min Age			
Tensile Strength, Psi	227,000	236,000	255,000
Reduction in Area, Pct	16	11	3
Fracture Strength, Psi	265,000	261,000	265,000
Notch Tensile Strength, Psi	251,000	250,000	207,000

The hydrogen distribution resulting from this procedure is extremely heterogeneous;[3] a high hydrogen concentration exists in the surface layer, whereas the specimen core is hydrogen free.

Notch Section Resistance Measurement—Resistance measurements were made with a precision Kel-

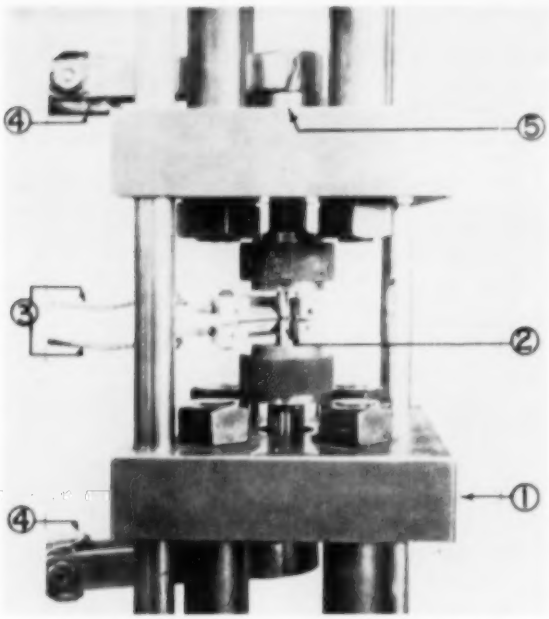

Fig. 3—Experimental arrangement for measurement of the notch section electrical resistance under an applied tensile load: 1) concentric loading fixture, 2) notch specimen, 3) potential leads (note knife edges), 4) current leads, and 5) insulated split collar.

vin double-bridge. A bridge current of 17.5 ± 0.5 amp gave adequate sensitivity. Fig. 3 illustrates the manner in which the notch static fatigue specimen was incorporated in the bridge circuit. The concentric loading members serve as current leads. The two knife edge potential leads attached to the specimen on opposite sides of the notch and approximately 0.10 in. apart define the resistance gage length. Each is free to move relative to the other but is fixed with respect to the specimen.

Crack Detection and Size Measurement—Either of two methods was employed for measurement of crack size, the metallographic-sectioning method or heat tinting method. In the former method, the static fatigue specimen was longitudinally sectioned and polished and the *effective radial crack depth* (the component normal to the applied stress) was measured at the extremities of the notch diameter. In the alternative method, heat tinting, the cracked static fatigue specimen was heated in air at 650°F for 1 hr, air cooled, and fractured in tension. The extent of the static fatigue crack was clearly delineated by the slightly oxidized concentric rim on the fracture surfaces. A tracing of the crack area was made at a magnification of X20. The crack area expressed as a percentage of the notch area was obtained from planimeter measurements. Crack size was expressed by either of two geometrically related parameters, percentage of the notch cross sectional area or radial crack depth.

Results and Discussion

Mechanical Properties—The conventional tensile and notch tensile properties of 4340 steel, heat treated to the indicated strength levels, and the manner in which they are altered by cathodic charging are summarized in Table II. The room temperature recovery characteristics of this steel at the 240,000 and 270,000 psi strength level have been reported.[7]

Static Fatigue Fracture Process—The most striking phenomenological characteristic of this time dependent fracture process, *slow crack growth*, was revealed by the examination of specimens stressed within their static fatigue stress range for various times short of fracture. Results obtained for the 240,000 psi strength level are representative of many experimental observations. The static fatigue characteristics of this material, aged 5 min at room temperature, are summarized in Fig. 4.

Examples of the appearance and growth of static fatigue cracks formed at respective applied stresses of 80,000 psi (slightly above the static fatigue limit) and 175,000 psi (the midpoint of the static fatigue stress range) are illustrated in Fig. 5. At the lower applied stress the path of crack propagation remained in the notch plane, while at the higher applied stress the advancing crack exhibited a tendency to branch and deviate from the notch plane; i.e., the plane normal to the applied tensile stress, and passing through the notch diameter. This point

Table III. Effect of Applied Stress on the Static Fatigue Fracture Properties: 4340 Steel; 230,000 Psi Strength Level; Aged 5 Min at Room Temperature

Static Applied Stress, Psi	Fracture Time, Min	Crack Area, Pct of Notch Area	Radial Crack Depth, 1×10^{-3} In.	Static Fatigue Fracture Stress, Psi
100,000	253	70.5	48.0	339,000
125,000	256	63.5	41.5	343,000
150,000	207	52.5	32.5	316,000
175,000	160	45.5	27.5	321,000
200,000	127	39.0	23.0	328,000

of branching occurred at varied positions, usually somewhat below the root of the notch. The plastic (permanent) opening of the crack, as evidenced by the crack width, was somewhat greater at the higher applied stress, but in both cases it remained quite small even after considerable crack growth. In general, observations at high magnifications revealed the cracks to be continuous. However, occasional instances of apparent discontinuous growth or advance nucleation[8] were noted. Attempts to ascertain the relation of the crack path to the prior austenitic grain boundaries were inconclusive.

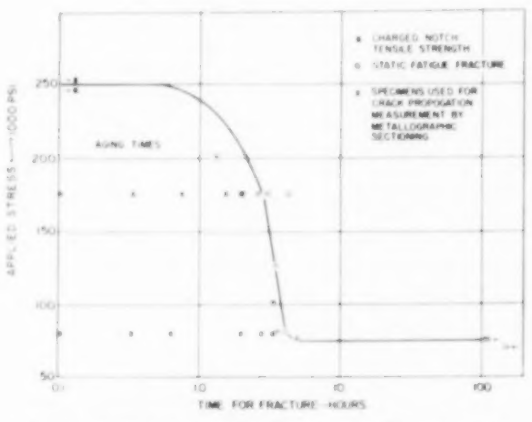

Fig. 4—Static fatigue characteristics of 4340 steel at the 240,000 psi strength level; charging condition A, aged 5 min, sharp notch specimens.

The crack propagation occurs primarily in the radial direction. This geometrical feature is demonstrated in Fig. 6, which depicts the static fatigue crack growth at an applied stress of 90,000 psi.

There appears to be a relation between the static fatigue limit and crack initiation. This was vividly demonstrated by a simple experiment in which a specimen, charged and aged in a like manner, was strained in tension. During the test the root of the notch was observed at X130 magnifications. A crack was first observed to form at the notch root at an applied tensile stress of 73,000 psi. This value is in good agreement with the observed static fatigue limit of 75,000 psi, see Fig. 4.

Thus, the fracture delay time observed on static loading within the static fatigue stress range (between S_c and S_i) is primarily a function of crack propagation. The crack originates at, or probably slightly below, the root of the circumferential notch and grows radially inward. The static fatigue limit appears to be related to the minimum stress necessary to initiate the crack.

Electrical Resistance Method for Measurement of Crack Propagation—This method is based on an empirically established relation between crack area and the change in resistance of the notch section of the static fatigue specimen. On application of a static tensile stress the resistance of the notch section gage length increased. This resistance increase may be attributed to the attendant geometrical alteration of the gage section resulting from one or more of the following factors: elastic deformation, plastic deformation,* and crack formation.

* In addition to the geometrical effect, plastic deformation increases the resistivity of the material. The effect of occluded hydrogen on resistivity is believed to be negligible.

In the absence of premature crack formation (hydrogen-induced static fatigue) the relation between resistance increase and applied stress was quite similar to a conventional stress-strain curve. The magnitude of the resistance increase at fracture was only 150 to 250 x 10^{-6} ohms as compared with an original unstressed gage length resistance of approximately 3000 x 10^{-6} ohms. Superimposing a circumferential crack at the root of the notch augmented the measured increment of resistance change by several orders of magnitude.

A correlation between the resistance change, measured at a fixed applied tensile stress, and the crack area was obtained in the following manner. The resistance increase was determined for a series of specimens stressed for various times within the static fatigue life. On release of the applied stress the area of the ensuing crack was measured by the heat tinting method. This relationship, established at several levels of applied stress, is shown in Fig. 7. It is evident that interpolation within the applied stress range of 90,000 psi to 175,000 psi is permissible. Frequent checks of the calibration revealed no drift, or anomalous behavior. The measurements of crack area (percentage of notch area) are estimated to be within ±1.5 pct of the stated values. It should

Fig. 5—Cracks observed in notch specimens sectioned after loading at 80,000 psi and 175,000 psi for the indicated times within the static fatigue life shown in Fig. 4; 4340 steel at the 240,000 psi strength level, longitudinal axial section. LEFT: 80,000 psi for 165 min; RIGHT: 175,000 psi for 120 min. Unetched. X75. Reduced approximately 35 pct for reproduction.

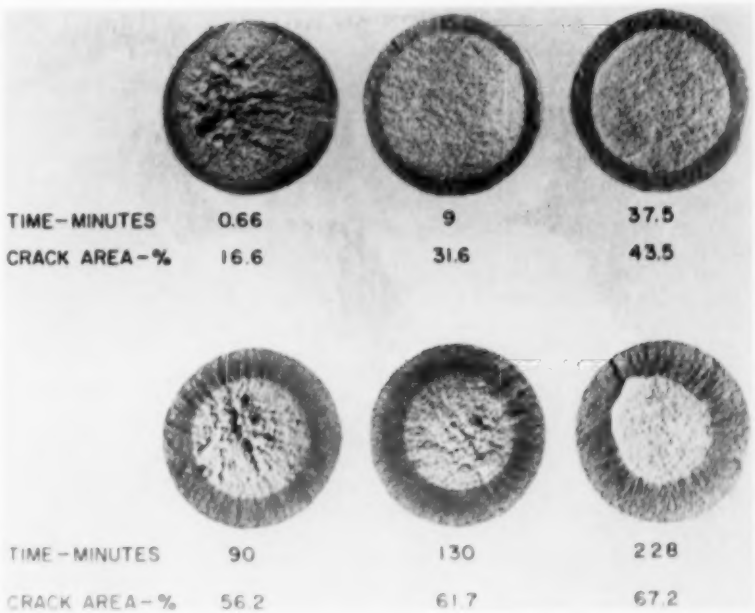

Fig. 6—Fracture surface of notch specimens heat tinted and fractured after static loading at 90,000 psi for the indicated times within the static fatigue life, see Fig. 4; 4340 steel at the 240,000 psi strength level. The area of the cracked zone is delineated by the concentric heat tinted region on the fracture surface and is expressed as a percentage of the notch area. X7. Reduced approximately 30 pct for reproduction.

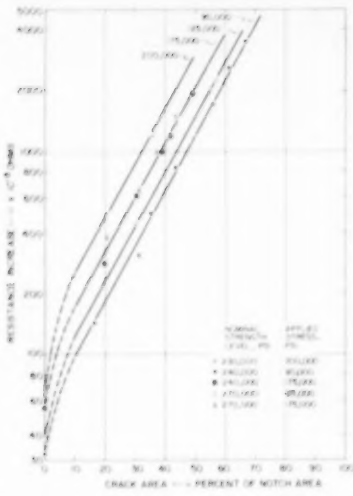

Fig. 7—Calibration curves for the determination of crack area from notch section resistance measurements. Relationship between notch section resistance increase and crack area (percentage of notch area) as observed at several values of applied stress within the static fatigue range: 4340 steel at the indicated strength levels; charge condition *A*, aged 5 min at room temperature, sharp notch specimens.

be emphasized that this calibration of the resistance measurements is empirical and as such is limited to the specific specimen geometry and loading conditions for which it was determined.

The relatively high current required for the resistance measurement did not influence the static fatigue behavior. In addition, identical results were observed with reversal of polarity between each resistance measurement. The momentary current flow during the intermittent measurements limited measurable heating of the specimen to less than 4°F.

Crack Initiation, Crack Propagation, and Fracture—The resistance method of crack propagation measurement was employed in evaluating the effect of applied stress, prior room temperature aging, and stepped static loading on the static fatigue fracture process. The three stages of the fracture process—crack initiation, crack propagation, and conditions at fracture—were studied as a function of these variables for 4340 steel at the 230,000 psi strength level.

Table IV. Effect of Static Fatigue Crack Size on the Fracture Stress in the Absence of Hydrogen

Static Fatigue Crack Area, Pct of Notch Area	Static Fatigue Radial Crack Depth, 1×10^{-3} In.	Fracture Stress, Psi
16.6	9.0	300,000
30.6	17.5	327,000
38.4	22.5	312,000
42.0	25.0	328,000
56.2	35.5	307,000
61.7	40.0	300,000

Effect of Applied Stress After 5 Min Aging Time: The static fatigue characteristics of 4340 steel at the 230,000 psi strength level, cathodically charged and aged 5 min at room temperature, are illustrated in Fig. 1. The measured resistance increments observed as a function of time at several stresses within the range of 100,000 psi to 200,000 psi are shown in Fig. 8. Combining the data of Fig. 8 and the resistance calibration curves in Fig. 7 yielded the curves in Fig. 9; that is, the (average) radial crack depth as a function of time. Examination of Fig. 9 indicates that there is little* or no incubation time for crack initiation. Immediately on loading above the static fatigue limit the material is permanently damaged; that is, a crack has been initiated. Three distinct stages of growth are evident in each of the crack propagation curves. The primary stage initiated on application of the static load is short lived (1 min or less) and is characterized by a high rate of crack propagation. In the second stage, which extends over the major portion of the static fatigue life, the rate of crack growth diminished with time. A brief interval of accelerated growth rate immediately preceding cataclysmic crack propagation (fracture) features the third stage.

The distinguishing feature of the second stage, the diminution of the crack growth rate as cracking progressed, occurred in spite of the concurrent increase in stress acting on the uncracked core. A comparison of the crack propagation rate at several applied stress levels reveals a maximum divergence in growth rate in the initial portion of the second stage. In addition, the growth rate, for example after 10 min, is a minimum for the highest applied load and increases to a maximum at the lowest applied load.

Although a minimum stress is required for crack initiation, it appears that additional increments of applied stress tend to retard crack growth. This unusual behavior shall be considered in a later section.

Table V. Effect of a Static Fatigue Crack on the Tensile Fracture Properties: 4340 Steel; 230,000 Psi Strength Level

Static Fatigue Test			Tensile Test	
Applied Stress, Psi	Static Loading Time, Min	Crack Area, Pct of Notch Area	Notch Tensile Strength, Psi	Fracture Stress, Psi
175,000	10	36	211,000	330,000
175,000	90	42	195,000	326,000

The general shape of the major portion of the crack propagation curves (second stage), Fig. 9, suggests the following parabolic relation:

$$C.D. = (Kt)^{1/2} + C \qquad [1]$$

where $C.D.$ is the radial crack depth; t, the time of growth (static loading time); K, the crack growth constant; and C, the constant. Fig. 10 reveals that over most of the range of applied load and for times in excess of 10 min there is good agreement with this parabolic relation. Near the static fatigue limit the relation degenerated into two parabolic components. The crack growth constant, K, decreased as the applied load was increased. The variation in the crack growth constant with applied load reflects the previously noted influence of applied load on the instantaneous radial crack growth rate.

A comparison of the first and second stages of crack growth with the unnotched tensile ductility distribution study of Frohmberg, Barnett, and Troiano[5] suggests a correlation between crack growth and hydrogen distribution. It was shown that cathodic charging for a short time interval produced a shallow embrittled surface layer, evidently of high hydrogen concentration. Subsequent room temperature aging increased the depth of the embrittled zone. More specifically, cathodically charging according to condition *A* and aging 5 min at room temperature produced an embrittled surface rim approximately 0.012 in. in depth.* Thus, the extent of rapid crack growth observed during the first stage is comparable with the size of the coexisting brittle, high hydrogen case. The slow crack growth observed

* The minimum time required for a reliable resistance measurement was 30 sec after application of the load.

* A 0.212 in. diam unnotched tensile specimen (4340 steel) was employed by these investigators.

in the second stage may be attributed to the inward movement of the embrittled case. In other words, at the start of the test the high hydrogen concentration in the case fulfilled the conditions for crack propagation, while growth beyond this region was dependent on a buildup of the hydrogen concentration at the advancing crack front by the inward diffusion of hydrogen.

As a first approximation a diffusion (macroscopic) controlled crack propagation would predict a second stage growth behavior identical with that expressed in Eq. 1. In this case the constant K would assume the value for the room temperature diffusion coefficient of hydrogen in steel. An evaluation of the crack growth constant (K in Eq. 1) from the slope of the crack depth vs $\sqrt{\text{time}}$ curves, Fig. 10, yielded values in the range 1×10^{-4} to 6×10^{-4} sq cm per sec, which are of the same order of magnitude as the available values for the room temperature diffusion coefficient for hydrogen in steel.[7]

The conditions existing at the end of the third stage, that is, at fracture, are summarized in Table III. The static fatigue fracture stress (instantaneous value of stress at fracture) in every case is slightly higher than the uncharged notch tensile strength of the base material. Two factors are involved: crack (or notch) geometry and the potential embrittling influence of hydrogen.

The influence of crack geometry on the fracture stress is revealed by a review of the tensile fracture properties of notch specimens which were partially cracked in static fatigue and tested after aging at 650°F for 1 hr (i.e., the heat tinting cycle). The aging treament, in addition to delineating the size of the static fatigue crack, effected a removal of the hydrogen. These data, in Table IV, clearly show that in the absence of hydrogen the fracture stress is independent of the crack size and is approximately equal to the notch tensile strength of the base material. Thus, the constancy of the static fatigue fracture stress and its approximate equality with the uncharged notch tensile strength of the base material clearly reveal the absence of a significant embrittling effect of hydrogen. In other words, the *core* ahead of the advancing crack front shows no apparent embrittlement.

Several tests were conducted in which a specimen was tested in tension immediately after forming a static fatigue crack of known size. The data of Table V indicate that the fracture stress of the uncracked *core* is independent of the crack size and the time, and is identical with the static fatigue fracture stress, see Table III. Again, the uncracked *core* showed no signs of embrittlement.

The fracture data in Table III present an opportunity for testing the Griffith-Orowan relationship for the brittle fracture of metals[8]

$$\sigma = \sqrt{\frac{E\,S}{C}} \qquad [2]$$

where σ is the brittle fracture stress (stress normal to crack); E, Young's Modulus; C, the crack length; and S, the surface energy per unit area of the fracture surface, i.e., surface tension, w, plus the energy of plastic deformation per unit area of the fracture surface, p.

This relation is based on an energy criterion. Fracture occurs only if the decrease in strain energy (elastic strain energy release) accompanying growth of the crack is greater than the increase in surface

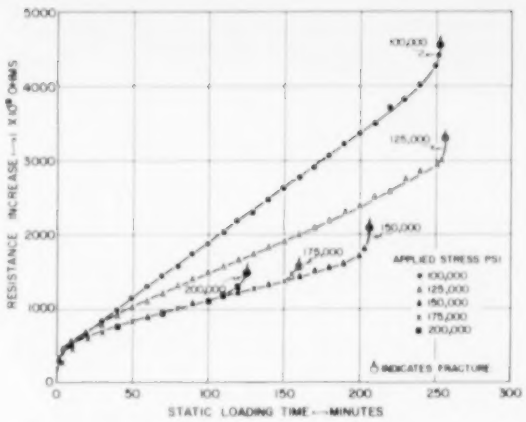

Fig. 8—Effect of static loading time on the electrical resistance of the notch section of specimens stressed within the static fatigue range of 4340 steel at the 230,000 psi strength level; charging condition *A*, aged 5 min, sharp notch specimens.

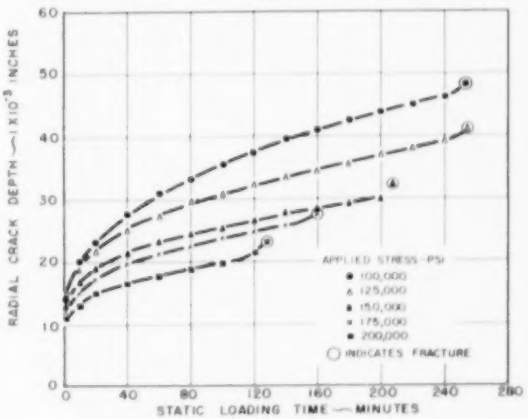

Fig. 9—Effect of applied stress on the radial crack propagation characteristics; derived from Fig. 8: 4340 steel at the 230,000 psi strength level; charge condition *A*, aged 5 min, sharp notch specimens.

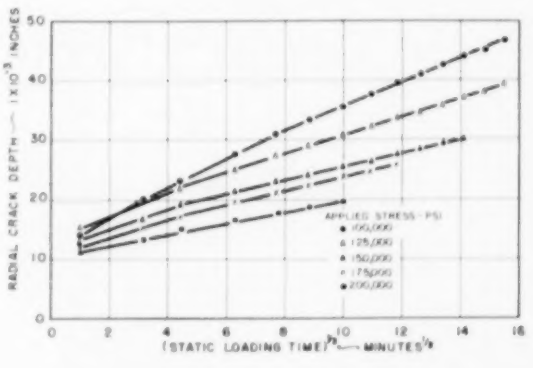

Fig. 10—Parabolic relation for the second stage of static fatigue crack growth, derived from Fig. 9; 4340 steel at the 230,000 psi strength level.

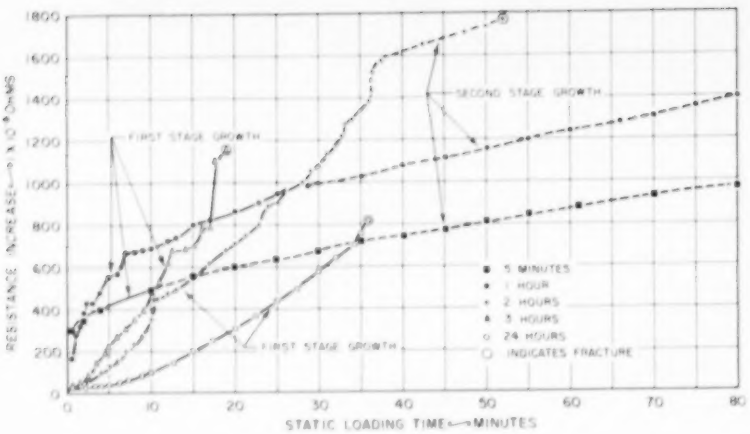

Fig. 11—Effect of prior room temperature aging on crack propagation at an applied stress of 175,000 psi; 4340 steel at the 230,000 psi strength level; charging condition *A*, sharp notch.

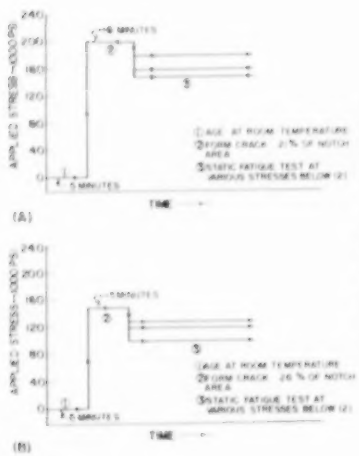

Fig. 12—Schematic representation of the loading cycles used in the determination of the effect of precracking at applied stresses of A) 200,000 psi, and B) 150,000 psi on static fatigue behavior at sub-precrack applied stresses; 230,000 psi strength level.

energy of the new surface. The Orowan modification[8] of the Griffith relation[1, 2] consisted of the inclusion of the energy of plastic deformation, p, in the surface energy term. This was deemed necessary since brittle fracture in ordinarily ductile metals is always accompanied by a slight plastic deformation in a thin layer at the fracture surface. Eq. 2 was derived for a thin infinite plate containing an elliptical crack. However, equations of the same form have been derived for other specimen geometries.

The Griffith-Orowan relationship predicts a decreasing fracture stress with increasing crack size. However, experimentally the fracture stress was constant and independent of crack size, see Table IV. This constancy of the static fatigue fracture stress, regardless of crack size, indicates that the Griffith-Orowan relation does not hold.

Prior Room Temperature Aging: The crack growth characteristics determined at an applied stress of 175,000 psi for room temperature aging times in the range of 5 min to 24 hr are indicated in Fig. 11. The analysis is presented in terms of the resistance vs loading time curves obtained for the various aging times. Crack areas were not computed from the resistance data, since it is felt that the resistance vs crack area calibration curve is dependent upon the hydrogen distribution (aging time). Although this variation is probably small, it precludes a precise calculation of crack areas and fracture stresses for different aging times.

The marked alteration in the crack growth kinetics introduced by room temperature aging is consistent with the three-stage crack propagation process. However, the effect of hydrogen redistribution which accompanies aging must be considered.

Inspection of Fig. 11 reveals several significant features. The period of second stage growth was reduced as the aging time was extended and was eliminated for times in excess of 2 hr. The crack size at which the second stage growth characteristics became apparent increased as the aging time was extended, indicating that the depth of hydrogen penetration was greater for longer aging times. Hence the crack size and the corresponding instantaneous stress at the instant when the advancing crack reached the hydrogen diffusion front increased with prior aging time. For aging times in excess of 2 hr the hydrogen diffusion front was in advance of the growing crack during the entire static fatigue life. Thus, second stage crack growth was eliminated and only first stage crack propagation was observed.

In addition, the crack propagation rate during the first stage of growth decreased as the aging time was extended. The hydrogen concentration in the region through which the crack propagated also may be expected to decrease with extended aging. These data suggest that the first stage growth is controlled by localized microscopic hydrogen diffusion.

Of particular interest is the apparent incubation time (4 to 6 min) for crack initiation which was observed after relatively long aging times. It is not certain whether this is a true incubation period or an interval of extremely slow crack growth. Attempts to resolve this question by metallographic techniques have, thus far, been inconclusive. This behavior was also reflected in the notch tensile properties of specimens aged 24 hr at room temperature and tested at several strain rates. The embrittlement, see Table VI, as revealed by the notch tensile strength was quite sensitive to small variations in strain rate. It appears that the incubation period persists at all levels of applied stress up to the notch tensile strength of the uncharged material. Thus, it is not surprising that delayed failure has been observed under conditions for which full recovery was indicated by conventional notch tensile tests.[9]

Precracking: The delayed fracture process has been viewed under conditions of sustained static loading. A somewhat different behavior pattern might be anticipated for a more complex loading cycle such as is often encountered in actual service.

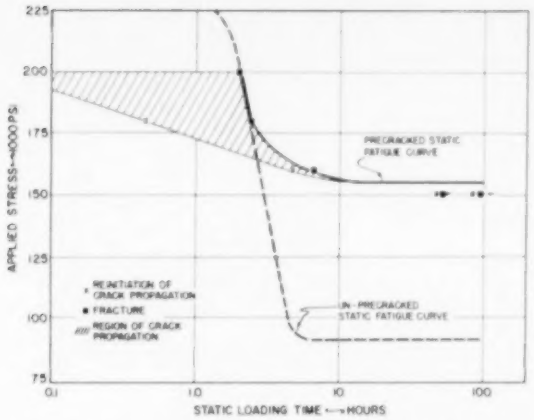

Fig. 13—Effect of precracking (21 pct of notch area) at an applied stress of 200,000 psi on static fatigue behavior at lower applied stresses, see Fig. 12 for loading cycle; 4340 steel at the 230,000 psi strength level; charge condition *A*, sharp notch specimen.

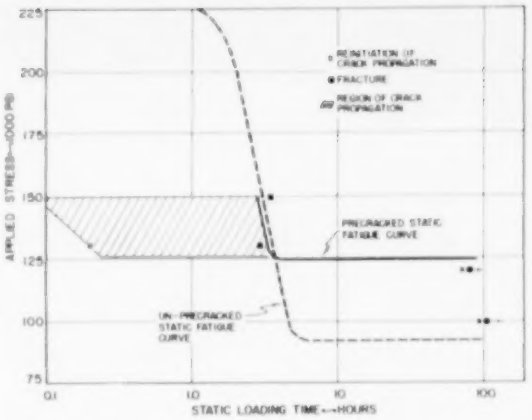

Fig. 14—Effect of precracking (26 pct of notch area) at an applied stress of 150,000 psi on static fatigue behavior at lower applied stresses, see Fig. 12 for loading cycle; 4340 steel at the 230,000 psi strength level; charge condition *A*, sharp notch specimen.

A stepped loading cycle was selected as the most appropriate for a simplified analysis.

This loading cycle may be described as a two-stage or a stepped static fatigue test. A static fatigue crack of predetermined size was formed at a fixed applied stress (first step) and the static fatigue behavior of this precracked specimen observed at a lower applied stress* (second step). The extent of precracking in the initial step was observed by resistance measurements. It was established that a resistance increase during the second step was indicative of crack growth, while a constant resistance denoted a cessation of crack growth.

* Nominal stress based on the original notch area.

The precracked static fatigue behavior was evaluated for two precracked conditions. The corresponding schematic loading cycles are illustrated in Fig. 12. The resultant precracked static fatigue curves, Figs. 13 and 14, depict the crack initiation and fracture characteristics observed during the second step. The shaded region represents the time and stress interval over which growth of the preformed crack occurred.

A comparison of the precracked and unprecracked static fatigue behavior, Figs. 13 and 14, reveals two pronounced effects introduced by precracking. Strangely enough, permanent damage to the material (precracking) enhanced its resistance to static fatigue, i.e., the static fatigue limit was raised. At stress levels above the static fatigue limit (after precracking) but below the precracking stress, the preformed crack remained dormant for a period of time before resuming growth. This incubation period tended to decrease and eventually disappear as the stress level approached the precracking stress. The magnitude of these effects was greater at the higher precracking stress. With the exception of applied stress, the two conditions of precracking are in essence identical. Thus, it appears that the applied stress and the attendant strains are the controlling external factors in this behavior.

The following is offered as a tentative mechanism. If crack growth is considered as a succession of tensile (or shear) failures occurring within a small volume of metal at the leading edge of the crack, growth would occur when the fracture strain of this element is exceeded. Since hydrogen is known to reduce the fracture strain, the conditions for fracture are dependent on a critical combination of both stress (and attendant strain) and hydrogen concentration. Thus, when the applied load was lowered subsequent to precracking, the conditions for growth (fracture) were not satisfied or, in other words, the hydrogen concentration was below the critical value required by the new stress state. The time for reinitiation of crack growth was related to the time required for the inward movement of the hydrogen diffusion front such that the critical hydrogen concentration was attained.

The increase in the static fatigue limit induced by precracking indicates that the critical hydrogen concentration associated with this stress value was not attainable. Thus, this distinction between the two test conditions appears related to some effect on the availability of hydrogen induced by the precracking operation. While aging at room temperature is known to increase the static fatigue limit,[7] the variance of this limit with precracking stress and the brevity of the precracking cycle indicate that aging is not the controlling factor.

Table VI. Effect of Strain Rate on Notch Tensile Strength, Charge Condition *A*, Aged at Room Temperature 24 Hr; 4340 Steel; 230,000 Psi Strength Level

Nominal Strain Rate, Cross-Head Speed, In. per Min	Total Time of Test, Min	Time from 80,000 Psi Stress to Maximum Load, Min	Notch Tensile Strength, Psi
0.07	1.75	0.75	301,000
0.05	2.5	1.75	262,000
0.002	47.0	20.0	200,000

A consideration of the plastic strain introduced during precracking offers a possible explanation. Darken and Smith[10] and others[11-13] have shown that plastic deformation produces *traps* for atomic hydrogen, and the number of *traps* increases with deformation. Thus, in the present case, the strain introduced in precracking produces *traps* for the hydrogen and reduces the amount available for diffusion. The deformation which occurs on application

of the initial load is most effective in influencing the subsequent hydrogen diffusion controlled crack growth since it is concentrated in the zone of highest hydrogen concentration (the hydrogen-rich *case*). Thus, the increase in the precracked static fatigue limit is attributed to a reduction in the concentration of the active or diffusible hydrogen because of strain induced *trapping*. The previously noted influence of stress (or, more correctly, strain) on the crack propagation rate in the second stage of growth, see Fig. 9, may be rationalized in an identical manner.

Summary and Conclusions

The mechanism of static fatigue fracture of high strength steels has been identified as a process of hydrogen-induced crack initiation and propagation, climaxed by catastrophic fracture. On application of a load in excess of the static fatigue limit a crack formed at the root of the circumferential notch and propagated radially inward. The initiation process in general was independent of time, although the possibility of an induction period does exist under certain conditions which may involve a relatively homogeneous hydrogen distribution. The static fatigue life at a given applied stress was determined by the crack propagation and fracture behavior.

The development of an electrical resistance method for the measurement of crack propagation permitted an analysis of the kinetic features of crack propagation. The state of hydrogen distribution produced by cathodic charging and the subsequent redistribution on aging determined the crack propagation and fracture characteristics.

For the charging conditions employed, a relatively thin case of high hydrogen content resulted. On subsequent aging, inward diffusion increased the depth of hydrogen penetration. The depth of the hydrogen-containing *case* and the hydrogen concentration gradient existent at the initiation of crack growth determined the kinetics of crack propagation. Propagation through the hydrogen-rich *case* was relatively fast and appeared to be controlled by a local microscopic diffusion process. This has been termed the first stage of crack growth. The kinetics of the second stage of crack propagation, growth beyond the pre-existent *case*, were controlled by the macroscopic diffusion of hydrogen. If fracture followed second stage crack growth, the *core* ahead of the advancing crack was essentially free of hydrogen and exhibited a fracture strength which was characteristic of the hydrogen-free material.

Crack propagation appeared to be dependent on some critical combination of stress and hydrogen concentration. A mechanism based on the strain induced *trapping* of hydrogen was proposed as a tentative explanation of the observed effect of precracking on subsequent static fatigue behavior and the effect of stress on the second stage crack growth rate.

Acknowledgments

The authors wish to express their appreciation to the Aeronautical Research Laboratory, Wright Air Development Center, for sponsorship of this investigation under Contract No. AF 33(038)-22371 and for permission to publish these data. The cooperation of Republic Steel Corp., which provided the steel employed in this study, is gratefully acknowledged.

References

[1] E. H. Bucknall, W. Nicholls, and L. H. Toft: Delayed Cracking in Alloy Steel Plates. Symposium on Internal Stresses in Metals and Alloys. Monograph and Report Series No. 5, Institute of Metals, 1948.

[2] W. A. Bell and A. H. Sully: Some Effects of Hydrogen on the Delayed Fracture of High-Tensile Steel. *Journal* Iron and Steel Institute, 1954, vol. 178, pp. 15-18.

[3] R. P. Frohmberg, W. J. Barnett, and A. R. Troiano: Delayed Failure and Hydrogen Embrittlement in Steel. *ASM Trans.*, 1955, vol. 47, pp. 892-925.

[4] C. L. M. Cottrell: Delayed Brittle Fracture of Alloy Steel at Low Stress Levels. *Nature*, 1952, vol. 170, pp. 1079-1080.

[5] G. Sachs, J. D. Lubahn, and L. J. Ebert: Notch Bar Tensile Test Characteristics of Heat Treated Low Alloy Steels. *ASM Trans.*, 1944, vol. 33, p. 340.

[6] D. Post: Photoelastic Stress Analysis for an Edge Crack in a Tensile Field. *Proceedings* Soc. for Experimental Stress Analysis, 1954, vol. 3, No. 1, p. 99.

[7] W. Geller and T. Sun: Influence of Alloying Additions Upon Diffusion of Hydrogen in Iron and Contribution to the Iron-Hydrogen System. *Archiv für das Eisenhuttenwesen*, 1950, vol. 21, p. 423.

[8] E. Orowan: Fundamentals of Brittle Behavior in Metals. *Fatigue and Fracture of Metals*, p. 139. J. Wiley & Sons. New York, 1952.

[9] A. A. Griffith: The Phenomenon of Rupture and Flow in Solids. *Philosophical Trans.* Royal Soc., 1920, vol. A221, p. 163.

[10] A. A. Griffith: The Theory of Rupture. *Proceedings* First International Congress of Applied Mechanics, Delft, 1924, p. 55.

[11] A. A. Wells: The Mechanics of Notch Brittle Fracture. *Welding Research*, London, 1953, vol. 7, No. 2, p. 34r.

[12] L. S. Darken and R. P. Smith: Behavior of Hydrogen in Steel During and After Immersion in Acid. *Corrosion*, 1948, vol. 5, p. 1.

[13] J. H. Andrews and H. Lee: Internal Stresses and Formation of Hair-Line Cracks in Steel. Institute of Metals Symposium on Internal Stresses in Metals and Alloys, 1948, pp. 265-273.

[14] J. H. Keeler and H. M. Davis: The Density and Hydrogen Occlusion of Some Ferrous Metals. *AIME Trans.*, 1953, vol. 197, p. 44; Journal of Metals, January 1953.

[15] W. R. Heller: Hydrogen in Iron and Its Alloys. *Stress Corrosion Phenomena*, 1956, pp. 163-175. Ed. by W. D. Robertson. New York. John Wiley & Sons.

Discussion of this paper sent (2 copies) to AIME by June 1, 1957 will appear in AIME *Transactions* Vol. 209, 1957, and in Journal of Metals, October 1957.

Technical Note

Cleavage Steps and the Cleavage Plane in Chemically Embrittled Cu_3Au Single Crystals

by Robert Bakish

VARIOUS aspects of structure-sensitive corrosion of single crystals and polycrystalline aggregates of Cu_3Au have been presented in papers by the author[1-3] in association with W. D. Robertson. Prompted by some observations in the course of these studies, a new approach to the problem was undertaken. Results of these new experiments are reported here.

Thin slices, less than 2 mm thick, were prepared from single crystals 3.5 mm in diam grown by the Bridgman technique. The crystals were homogenized for 300 hr at 850°C. Crystals with no deformation, crystals deformed in tension to the yield point, and crystals deformed 20 pct in excess of the yield point were used. Crystals of several different orientations were studied.

Slices were immersed for one month in 2 pct aqueous solution of FeCl, and, subsequent to this immersion, were subjected to bending. Immersion and bending were carried out at room temperature. The size and geometry of the crystals did not permit accurate data on the loads involved.

A most unexpected result was obtained in the process of bending these slices of Cu_3Au crystals normal to the (110) plane. Completely brittle be-

R. BAKISH, Junior Member AIME, is associated with the Sprague Electric Co., North Adams, Mass.

TN 361E. Manuscript, Apr. 27, 1956.

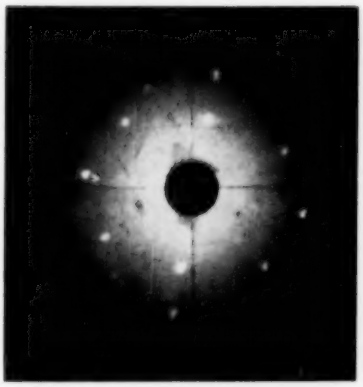

Fig. 1—Laue back-reflection from cleavage plane.

havior and *cleavage* along this plane was observed to take place; *cleavage* occurred whether or not the slice in question had been deformed prior to the slicing operation. Laue back-reflection photographs of these cleavage faces show very little asterism or evidence of plastic deformation associated with the cleavage face. Fig. 1 shows a typical Laue photograph taken with the X-ray beam normal to the cleavage face.

The cleavage faces themselves are most interesting. Cleavage steps are visible on all faces, and two types of cleavage steps are observed. The first kind is irregular in form with a fairly coarse dimension of the step. These coarse steps radiate from the region where the cleaving action is apparently initiated and may be seen as diagonal lines in Fig. 2. Subgrain boundaries and fine cleavage steps also may be seen in this figure. These fine cleavage steps are crystallographic and coincide with the (111) slip plane. In crystals having no deformation prior to the slicing process, the crystallographic character of these fine steps is very pronounced, and their height seems to be very small. The appearance of these steps is shown in Fig. 3. Sloping surfaces bonded by straight (111) segments are evident on close examination.

Introduction of plastic flow prior to the slicing operation alters the appearance of the cleavage steps. Fig. 4 shows this roughening in the cleavage face in the vicinity of a slip band. This photograph was taken in a crystal which deformed by unevenly distributed slip clusters. More extensive deformation produces a general roughening of the cleavage surface.

It is proposed that the *cleavage* on bending is due to the presence of a very thin layer of brittle gold-rich sponge along the (110) planes. This sponge is formed as a result of preferential leaching of copper from the alloy along highly active (110) planes.

The reasons for this high activity are not known. The chemical composition of the (110), a possible segregation of some impurities along these planes, or the energetics of the plane itself could be responsible for the high chemical activity of the (110). Similar cleavage phenomena have been reported[4] in Mg Sn.

The (111) slip plane plays an important role in this cleavage process. Interaction of dislocations at the lines where the cleavage plane meets with stationary dislocation loops, which are introduced in the material in the process of its prior deformation, could well account for the roughening of the cleavage surface as deformation is introduced and increased.

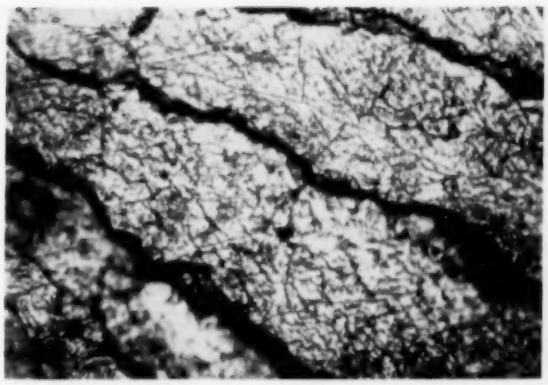

Fig. 2—Coarse cleavage steps, fine cleavage steps, and subgrain boundaries on a cleavage face. X500. Reduced approximately 25 pct for reproduction.

Fig. 3—Fine steps on a cleavage face. X2000. Reduced approximately 25 pct for reproduction.

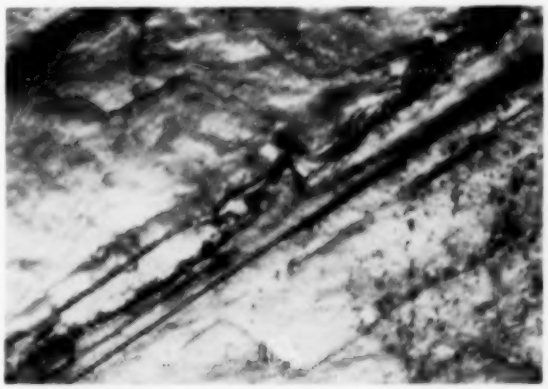

Fig. 4—Roughening of cleavage surface in the vicinity of the slip band. X2000. Reduced approximately 25 pct for reproduction.

Acknowledgments

The author wishes to acknowledge his indebtedness to F. Behnke, who carried out the X-ray work; and to W. D. Robertson for discussion of this work.

References

[1] R. Bakish and W. D. Robertson: *Acta Metallurgica*, 1955, vol. 3, p. 513.

[2] R. Bakish and W. D. Robertson: *Acta Metallurgica*, 1956, vol. 4, p. 342.

[3] R. Bakish and W. D. Robertson: *AIME Trans.*, 1956, vol. 206, p. 1277; JOURNAL OF METALS, October 1956.

[4] H. H. Uhlig and W. D. Robertson: *Journal of Applied Physics*, 1948, vol. 19, p. 864.

Deformation of Magnesium Single Crystals By Nonbasal Slip

Magnesium single crystals, oriented to suppress (0002) basal slip and {10$\bar{1}$2} twinning, were strained in tension parallel to the basal plane, in a <1010> direction, at four temperatures (—190°, 25°, 150°, and 286°C) and at two strain rates. Microscopic and X-ray evidence shows that at —190° and 25°C slip occurred primarily on {1010} prism planes. At 150° and 286°C, X-ray asterism shows rotations indicating {1011} pyramidal slip as the major slip process. The critical resolved shear stresses have been evaluated at each temperature.

by Robert E. Reed-Hill and William D. Robertson

DEFORMATION of magnesium crystals in a direction parallel to the basal plane has a special significance as a result of the preferred orientation characteristic of cold worked and recrystallized polycrystalline magnesium sheet and extruded rod in which the basal plane tends to lie in or near the plane of the sheet or the axis of a rod. The principal objective of the present study is a determination of the modes of plastic deformation in magnesium single crystals in this orientation.

Evidence for nonbasal slip in magnesium has been presented by a number of authors. Schmid and Wasserman[1] indicated that pyramidal slip on {1011} <1120> or {1012} <1120> could occur above 225°C. Bakarian and Mathewson[2] established that the slip system {1011} <1120> operates at high temperatures and that 225°C was a lower limit for pyramidal slip. The latter authors also showed that the critical resolved shear stress for {1011} slip was 400 g per sq mm at 330°C, while that for basal slip was 66 g per sq mm at the same temperature. Thus, at 330°C basal slip should be expected for all orientations except those in which the stress axis lies almost in the basal plane. More recently Burke and Hibbard[3] observed pyramidal slip at 25°C, when the stress axis was 6° to the basal plane and 14° to a <1120> slip direction. The critical resolved shear stress for pyramidal slip was 52 g per sq mm, which is only slightly greater than their value for basal slip (46 g per sq mm).

Chadhuri, Chang, and Grant[4] have observed nonbasal slip in creep tests with polycrystalline specimens in the temperature range 250° to 350°C. The observed slip bands, which were extremely irregular in appearance, can be explained in terms of cooperative slip on {1011} and {1010} planes which have a common slip direction.

Prismatic {1010} slip in polycrystalline magnesium was observed by Hauser, Landon, and Dorn.[5] It was found to occur at low temperatures (78° and 195°K) and it was accompanied by cross slip in which the cooperating plane was the basal plane. Since prismatic slip occurred only at regions of high stress concentrations, the critical resolved shear stress could not be determined.

Experimental Procedure

The present work was performed on crystal specimens which were all cut from the same large single crystal. The original cylindrical crystal, 0.5 x 7 in., was grown in a Bridgman type furnace in which the temperature gradient was moved past the stationary crystal in the manner described by Jillson[6] and Burke.[7] High purity magnesium was furnished by the Dow Chemical Co. with the following spectrographic analysis in weight percent: 0.003 pct Al, <0.01 pct Ca, 0.002 pct Cu, <0.001 pct Fe, 0.008 pct Mn, <0.001 pct Ni, <0.002 pct Pb, <0.01 pct Si, <0.001 pct Sn, and <0.01 pct Zn.

The large crystal was cut into four cylindrical pieces about 1.5 in. long. A flat surface parallel to the basal plane was made by hand grinding with lubricated metallographic paper on one side of each cylinder. In order to prevent bending in subsequent cutting operations, the crystals were supported by

R. E. REED-HILL, Member AIME, Commander U. S. Coast Guard, is Associate Professor, U. S. Coast Guard Academy, New London, Conn. W. D. ROBERTSON, Member AIME, is Associate Professor, Hammond Metallurgical Laboratory, Yale University, New Haven, Conn.

TP 4469E. Manuscript, Sept. 10, 1956. New Orleans Meeting, February 1957.

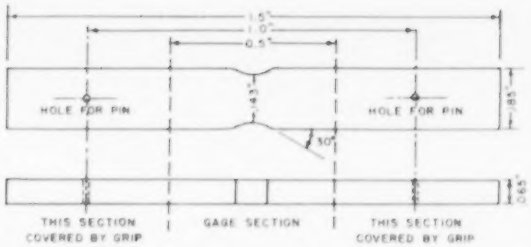

Fig. 1—Shape of single crystal tension specimen with the basal plane parallel to the wide face surface.

wax in suitable aluminum fixtures, which also served as guides for aligning a jeweler's saw. After completion of the cutting and grinding operations, the specimens were etched in 20 pct HCl, removing about 0.045 in. and producing specimens which were free of surface deformation and approximately 0.205 in. wide, 0.085 in. thick, and 1.5 in. long. Rounded notches were formed with an acid thread saw similar to that described by Maddin and Asher,[7] using concentrated HCl and a single Dacron thread; these notches were made in order to define the location of fracture. Final dimensions of a typical specimen are shown in Fig. 1. For purposes of identifying areas of interest clearly on the specimens, the following terminology will be used: the wider longitudinal surfaces are faces of the specimens, while the thinner surfaces are designated as edges.

Orientations were checked at the center of the gage section of each specimen by the Laue back-reflection technique. It was found that the basal plane coincided with the face surface to within less than 2° in the direction parallel to the stress axis, and to within less than 3° in the direction at 90° to the stress axis. The crystal orientation was such that for perfect coincidence of basal plane and face surface, the stress axis made an angle of 2°±1° with a <1010> direction.

Measurement of Stress and Strain

Seven of the tensile specimens were strained at the slow rate of 0.005 lb per sec, by a simple lever device similar to that used by Miller.[8] Thus, at the minimum cross section of the specimens (0.01 sq in.), the rate of application of stress was about 5 psi per sec.

Two specimens were extended at a faster stress rate of 500 psi per sec, by sliding a dead weight along the beam of the testing machine.

The method of gripping specimens, shown in Fig. 2, was designed to permit accurate alignment of specimens and, as a precaution against slipping in serrated grips, steel pins were inserted through the grips and the specimens.

Room temperature tests were performed in air. Elevated temperature tests were carried out with the specimens and grips immersed in heated and stirred paraffin oil. For tests at −190°C, the specimens and grips were immersed in liquid air.

The extensometer used for strain measurements at high temperatures consisted of a small aluminum cantilever beam. The moving end of the beam rested on a ferrule mounted on the loading rod, outside the oil bath, and 10 in. from the crystal. An A-7, SR4, resistance strain gage was cemented to each side of the beam. The extensometer was calibrated with a micrometer reading to 0.001 in. and the calibration factor was 65 micro-in. per in. (strain indicator reading) per 0.001 in. (micrometer reading). The error introduced by the elastic strain in loading rods and related equipment was corrected by deformation measurements on a polycrystalline aluminum bar.

A similar extensometer was used for measuring the deformation of the specimens at the two lower temperatures. In this case, however, it was mounted on the moving grip so that it read directly the relative movement of the two grips at room temperature and at −190°C.

All extensometer readings at the slow rate of loading were recorded with a Baldwin-Southwark Portable Strain Indicator. In the two tests which were carried out at a more rapid rate, the extensometer readings were recorded by a high speed Brush Strain Analyzer. Pen movements of this instrument may be estimated to about 0.2 mm and the sensitivity employed varied from 46 micro-in. per in. per mm to 61 micro-in. per in. per mm.

Experimental Results

Two tests were performed at each temperature, −190°, 25°, and 150°C, at 5.0 to 6.0 psi per sec. The reproducibility of the stress-deformation curves at each temperature was found to be remarkably good and consequently only one specimen was tested at 286°C. Representative stress-deformation curves are shown in Fig. 3 at each temperature. The plots contain all of the data that it was possible to record before fracture occurred, except for the curve of specimen No. 147 (286°C), which was extended to 0.106 in.

The yield stress for nonbasal slip is shown in Fig. 4 as a function of absolute temperature. The yield stress is taken as the intercept of the dashed lines in Fig. 3 (the start of plastic deformation), and it is expressed in terms of the normal stress at the reduced section. This stress falls to a very low value at 286°C, where it is about 500 psi (0.350 kg per sq mm).

Deformation was symmetrical about the stress axis, as shown in Fig. 5, which is in accord with the

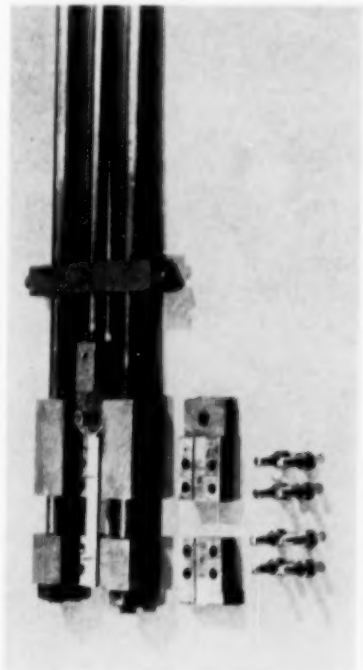

Fig. 2—Apparatus used to hold flat single crystal specimens when determining their stress-strain characteristics.

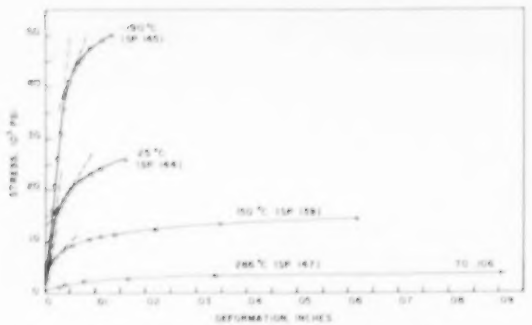

Fig. 3—Stress deformation curves for single crystals of magnesium oriented with the axis of tension in the basal plane.

fact that two slip directions, $<11\bar{2}0>$, were symmetrically placed with respect to this axis. Furthermore, deformation was primarily two-dimensional; no significant difference in the thickness of the specimens could be detected in regions where the deformation had occurred by slip.

The reduction in area at fracture is plotted as a function of absolute temperature in Fig. 6. The data clearly shows the large plasticity of magnesium crystals at high temperatures, a negligible ductility at room temperature, and a surprising amount of ductility at −190°C.

The effect of increasing the rate of loading by a factor of about 100, at 25° and 150°C, is shown in Fig. 7. A faster rate of loading considerably reduces the amount of plastic deformation preceding fracture and increases the yield stress by a factor of approximately two, as shown by the comparative curves in Fig. 7.

Table I. Critical Resolved Shear Stress for Prism and Pyramidal Planes

Test Temperature, °C	Yield Stress on Normal Cross Section (At Position of Notches), Kg per Sq Mm	Critical Resolved Shear Stress Prism Plane {1010}, Kg per Sq Mm	Critical Resolved Shear Stress Pyramidal Plane {1011}, Kg per Sq Mm
190	27	10	—
25	11	4	
150	4.2	1.6	1.4
298	0.35	0.13	0.1

Observations Regarding the Primary Mechanisms of Deformation

Specimens deformed at −190°C exhibit the most detail as regards slip lines visible with a light microscope. All specimens, regardless of the temperature of testing, show nonbasal slip bands on the surface containing the basal plane. However, only at −190°C could any significant amount of detail be found on the edge surfaces of the specimens, initially {1120} planes.

Mechanical twinning on planes other than the usual $\{10\bar{1}2\}$ was also observed. The crystallographic identification of these twins, which are associated with fracture, will be considered in a subsequent paper.

$\{10\bar{1}0\}$ Prism Slip at −190°C—In both specimens, fine {1010} prismatic slip lines were found, primarily on the edge surfaces. However, they could be followed over the rounded corner onto the face surfaces far enough to use the two-surface method of stereographic analysis to define their prismatic character. The disappearance of slip lines on the face surface is in accord with the fact that the slip direction lies in the basal plane.

Prismatic slip lines may occasionally be resolved at X500, but a magnification of X900 or higher is usually necessary. Fig. 8 shows a region in which the $\{10\bar{1}0\}$ slip lines are well-defined. They are also found in clusters of more or less continuous straight lines with spacing measured to values as low as 5×10^{-5} cm.

Slip bands containing groups of fine slip lines whose traces are parallel to a $<11\bar{2}0>$ direction may be found on the basal plane face, Fig. 9a. The main bands are generally long and nearly straight; within bands the fine lines are quite wavy. As the bands are followed across the specimen face, away from the edges, they tend to fade out as the surface approaches the basal plane. On the other hand, if the bands are pursued around the corner and onto the edge surfaces, most of them disappear again. Some, however, may be clearly traced around the corner and are found to connect with well-defined cross-slip bands visible on the edge surfaces. These latter run parallel to $\{10\bar{1}0\}$ prism planes with a cross-slip component on the basal plane.

In Fig. 9a, the primary and secondary $\{10\bar{1}0\}$ $<11\bar{2}0>$ slip systems are clearly indicated by the displacements of the primary bands by the secondary bands. The large, well-defined bands on the edge side, in Fig. 9b, correspond to the secondary bands and not to the primary. Although it is not apparent in these photographs, the two large bands at the top of Fig. 9b are connected to the secondary bands shown at the bottom of Fig. 9a. The connecting basal cross-slip, which ties together the components of the left-hand band, occurs in the rounded corner area not covered by either of the photographs.

The operating slip direction is clearly indicated in Fig. 9a. The large displacement of the primary lines, where they have been intersected by secondary lines, is in accord with shear along $<11\bar{2}0>$. Corresponding to this movement is the large width and shallow depth of the bands on the edge surfaces. In this regard, note how, in Fig. 9b, the surface is still clearly in focus on both sides of the bands. Furthermore, a study of a number of these bands has given no visible evidence for shear parallel to the prism components of the bands on the edge surfaces. It is quite

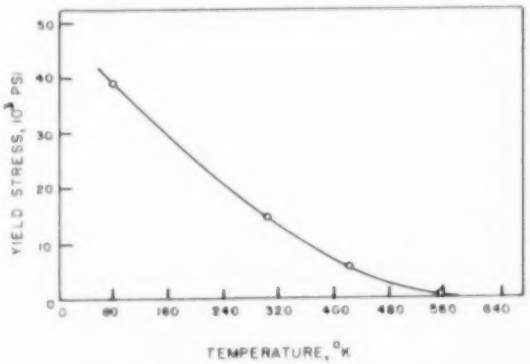

Fig. 4—Yield stress for nonbasal slip in magnesium as a function of temperature.

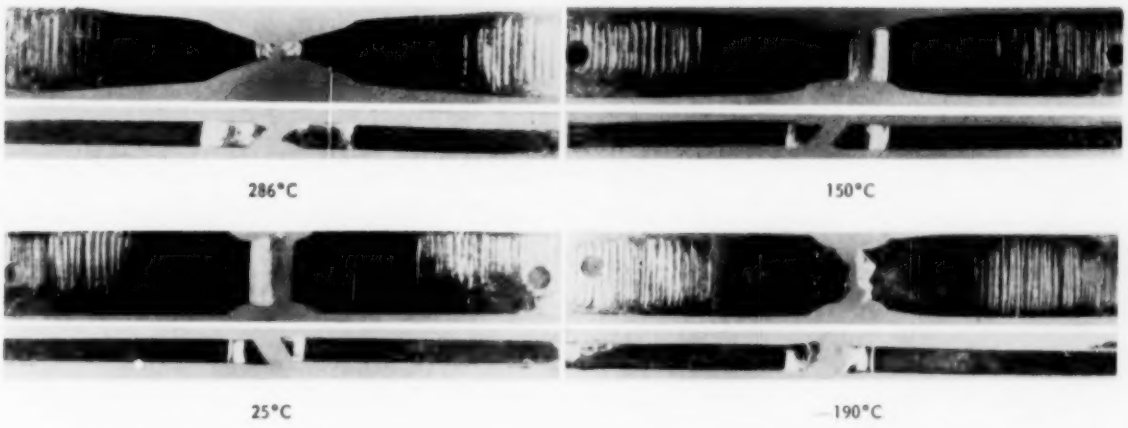

Fig. 5—Face and edge views of single crystal specimens of magnesium fractured in tension parallel to the basal plane; slow rate of loading.

clear, therefore, that the shear is along a $<11\bar{2}0>$ direction.

Slip at Temperatures Above —190°C—Typical slip bands obtained at 25°, 150°, and 286°C are shown in Fig. 10. These bands have many similar characteristics which may be summarized as follows. Their average direction is $<11\bar{2}0>$; the bands tend to align themselves in groups which are interconnected by cross-slip on the basal plane. The close spacing of slip lines, visible on the face surface as a slip band, widens as a result of cross-slip on the basal plane until the band is no longer definable after the band has passed over the corner joining the face surface with the edge.

Prism and basal cross-slip bands are observed on the edge surface of specimens fractured at room temperature, but only in the highly strained regions adjacent to fractures. Fig. 11 shows such an area.

The phenomenon of sublimation pits that form along slip planes at high temperatures, first observed by Bakarian and Mathewson,[2] is shown in Fig. 10c.

X-Ray Asterism—Confirmation of the preceding microscopic observations was obtained from a study of X-ray asterism observed on specimens subsequent to fracture. The X-ray beam, 1 mm diam, covered an area roughly equivalent to the field of view in the microscope at X125.

Even in areas of little apparent deformation, and in the absence of mechanical twins, the asterism is complicated, and it also changes as the point of investigation is changed, indicating shifts in the operating slip systems. Because of the complexity of the observed asterism, an indirect method of analysis was used for the face surface exposures in an attempt to determine the axis of rotation of the lattice. In this method, a series of drawings, with asterated spots corresponding to the most probable lattice rotations, were prepared on tracing paper. A stereographic projection of the distortion of the planes was made and then this projection was redrawn, with the aid of a Greninger net, to correspond with the X-ray pattern. Fig. 12a shows the pattern for a 4° rotation about an axis perpendicular to the slip direction and lying in a $\{10\bar{1}1\}$ pyramidal plane; Fig. 12b is a pattern assuming double bending about two axes, each lying in a different $\{10\bar{1}1\}$ plane, and perpendicular to

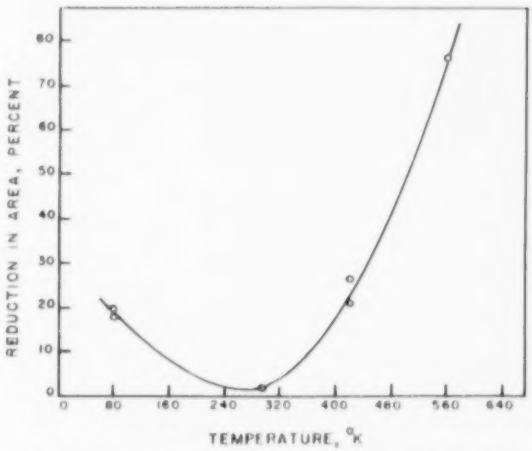

Fig. 6—Reduction in area at fracture in magnesium single crystals, oriented with the axis of tension in the basal plane, as a function of temperature.

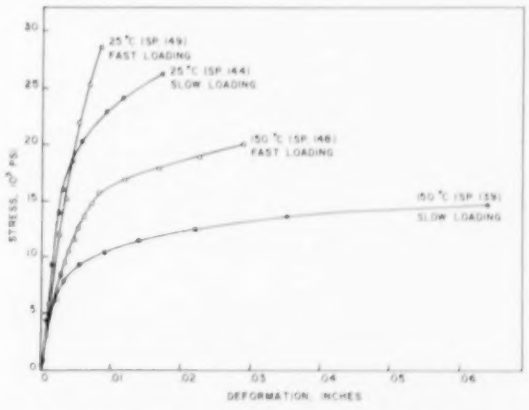

Fig. 7—Stress-deformation curves for magnesium single crystals at two rates of loading differing by a factor of 100.

two different slip directions. With the aid of these and similar patterns for other probable slip planes,

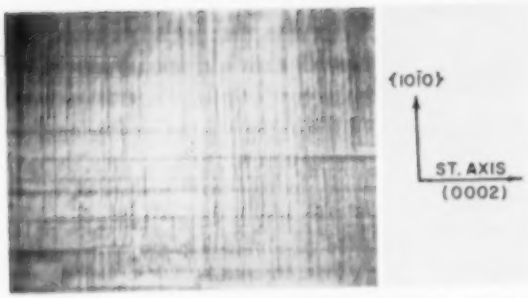

Fig. 8—Well separated {1010} prism slip lines on an edge surface — {1120} of a magnesium crystal specimen tested at —190°C. X450. Reduced approximately 45 pct for reproduction.

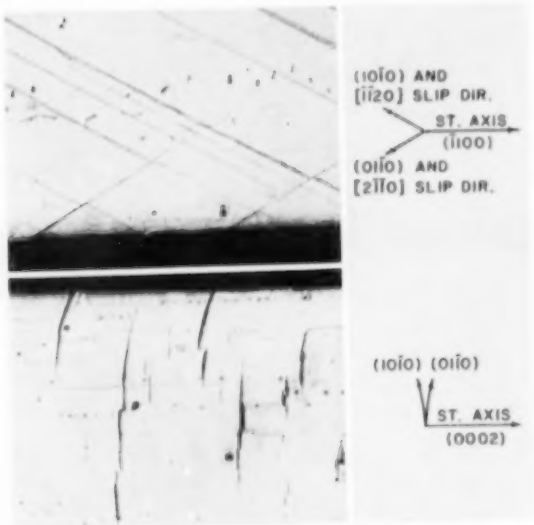

Fig. 9—{1011} prism (0002) basal cross slip bands on two mutually perpendicular surfaces of a magnesium crystal specimen extended at —190°C. a) TOP: Face surface — (0002). b) BOTTOM: Edge surface — {1120}. X290. Reduced approximately 50 pct for reproduction.

possible lattice rotations may be deduced by matching the X-ray photographs.

The least complex Laue patterns were obtained at 150°C. Figs. 13, 14, and 15 show the face surface patterns of a series of three exposures, taken in pairs along the length of the boundary of a face and an edge surface, starting close to the grips and moving toward the reduced section. The edge exposures showed lattice rotations and asterisms which were in agreement with those shown in face exposures. Beside each Laue pattern a sketch is drawn corresponding to the axes of rotation which most closely fit the observed asterisms.

Fig. 13 corresponds to an area adjacent to the grips. The asterism is symmetrical and may be explained in terms of a uniform double rotation about axes in two {1011} planes.

The asterism changes as the point of observation moves away from the grips. Fig. 14 was taken at a point midway along the corner between the notch and the edge of the gripped area. The latter photograph shows a general lattice rotation about the normal to the basal plane, and the asterism of the spots about an axis lying approximately in a {1011} pyramidal plane and perpendicular to a slip direction. The asterism in this photograph is close to that predicted in Fig. 12a.

Fig. 15 corresponds to an area close to the notch. In this case, the general lattice rotation is greater but in the same sense as before. The asterism is, however, more complicated. The principal rotations are about two axes lying in {1011} pyramidal planes, but the planes in this case are different.

If it is assumed that the observed asterism is due to lattice rotations, i.e., the axis of asterism lies in the slip plane and perpendicular to the slip direction, then it may be concluded that slip occurs primarily upon {1011} planes, at 150°C.

The asterism observed at —190° and 286°C is more complicated. At —190°C the angular spread is about the same order of magnitude as that observed at 150°C, but the patterns are neither as regular nor as symmetrical. This is in agreement with the fact that at least one additional secondary plane of slip has been observed at —190°C, namely, {1122}. It is also in accord with the findings of Lange and Lücke[9] and Honeycombe[10] that asterism develops primarily from inhomogeneous glide. At 286°C the very large plastic deformation has a pronounced effect on the observed asterism. The spreading of the spots is much greater than at —190° and 150°C and, in general, the patterns indicate multiple gliding whose interpretation is subject to ambiguity.

Because of the symmetrical shape of the fractured specimens, it might be assumed that the lattice at the center of the section between the notches deformed by a process of duplex slip, which is borne out by Laue back-reflection patterns of —190° and 150°C specimens, see Fig. 16.

Discussion

The observations of {1010} prismatic slip and {1010} prismatic-basal cross-slip in polycrystalline specimens tested at —195°C by Hauser, Landon, and Dorn[7] have been fully confirmed on single crystals tested at —190°C. In addition, the slip direction for prismatic slip has been identified as <1120>, in terms of the direction of the shears resulting from this glide. The authors mentioned above also observed prism-basal pencil glide on specimens tested at —78°C, but found no evidence for it on specimens tested at room temperature. In the present work at 25°C, this slip phenomenum was observed in the neighborhood of fractures. This apparent discrepancy may be explained in terms of the different types of specimens and the stress required for prismatic slip.

A reproducible yield point has been found for single crystal specimens tested at both —190° and 25°C. Since prismatic slip, in conjunction with cross-slip on the basal plane, is the *predominating* mode of nonbasal slip at —190°C, the observed yield stress may be expressed in terms of a critical resolved shear stress for duplex prismatic glide which is 10 kg per sq mm. The fact that prism-basal cross-slip bands are the most frequently observed phenomena at 25°C is evidence that prism glide may also be the predominant mode at 25°C. On this assumption, the critical resolved shear stress for duplex prism slip at 25°C is 4 kg per sq mm.

It has not been possible to designate accurately the predominating nonbasal mode of slip at 150° and 286°C because of lack of resolved slip lines or bands on two surfaces which would identify the operating

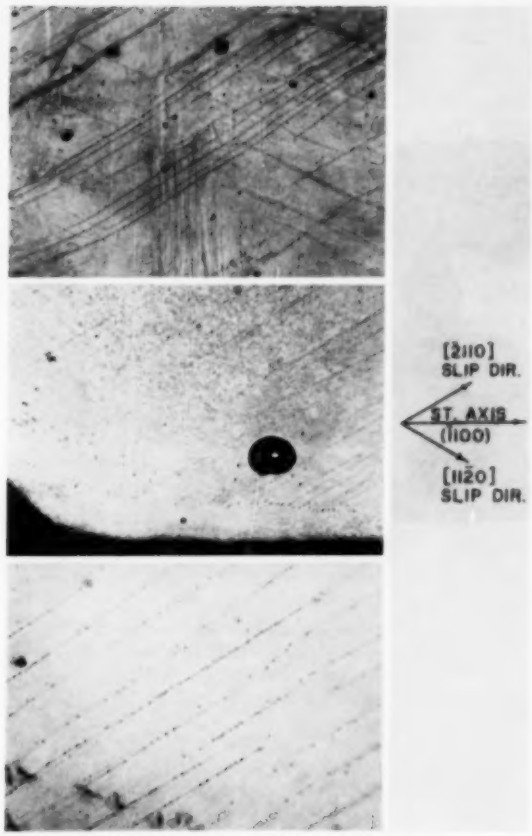

Fig. 10—Slip bands visible on the face surfaces of magnesium crystal specimens strained in tension parallel to the basal plane at temperatures above —190°C. a) TOP: Test temperature, 25°C. X150. b) CENTER: Test temperature, 150°C. X150. c) BOTTOM: Test temperature, 286°C. Pits visible on slip traces are the result of sublimation. X500. Reduced approximately 45 pct for reproduction.

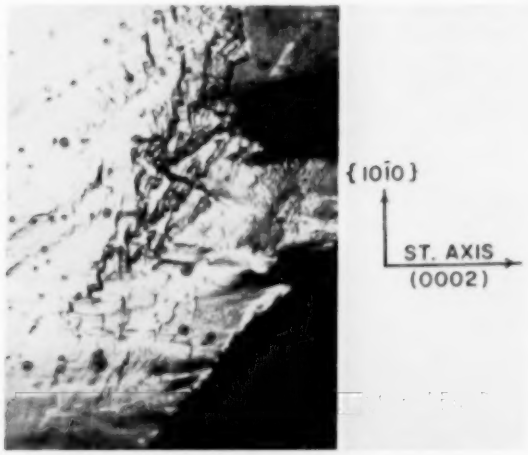

Fig. 11—Basal and {1010} prism cross-slip in region adjacent to fracture on a magnesium crystal specimen extended at 25°C. Edge surface = {1120}. X190. Reduced approximately 30 pct for reproduction.

Fig. 12—The predicted asterism in Laue back-reflection X-ray patterns corresponding to two possible lattice rotations in magnesium crystals. X-ray beam assumed normal to (0002). a) Axis of rotation in {1011}, ⊥ ⟨1120⟩. b) Conjugate rotation, two axes in {1011}, ⊥ ⟨1120⟩.

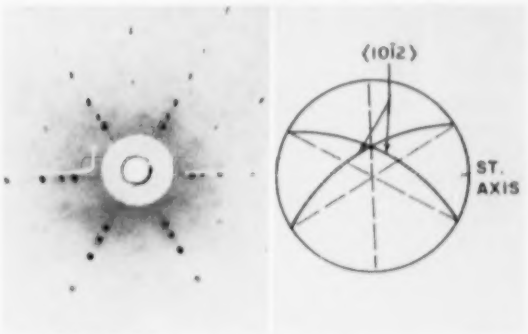

Fig. 13—Face surface Laue photograph of a 150°C test specimen at a position close to the grips and an edge surface.

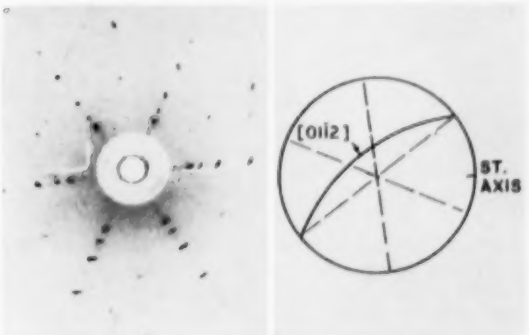

Fig. 14—Face surface Laue photograph of a 150°C test specimen at a position halfway between the grips and the reduced section and close to an edge surface.

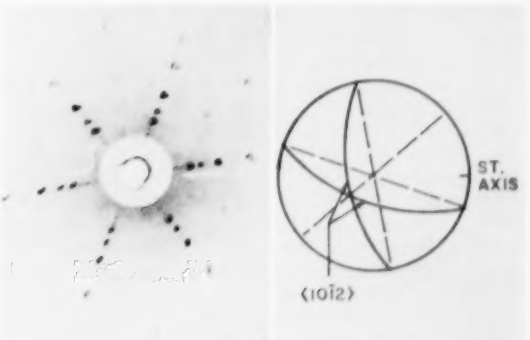

Fig. 15—Face surface Laue photograph of a 150°C test specimen at a position close to the reduced section at the notches and an edge surface.

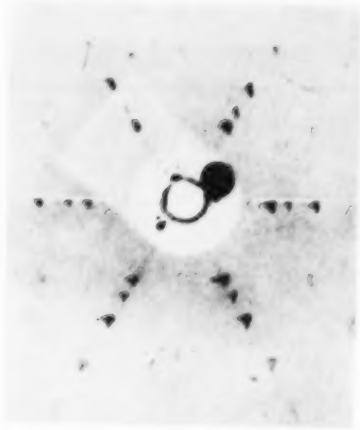

Fig. 16—Face surface Laue photograph of an area at the center of the reduced section of a 150°C test specimen. Note the absence of a general lattice rotation signifying symmetrical conjugate slip. Stress axis is horizontal.

slip planes. While the observed bands indicate the active slip directions as $<11\bar{2}0>$, they cannot be used to determine the active slip planes unambiguously. However, X-ray asterism in specimens tested at 150°C indicates that the predominant mode of deformation may be pyramidal slip, which is in general agreement with the results of other investigators.[1, 2] Since the experimental evidence does not rule out the possibility that slip on both pyramidal and prism planes[2] may have occurred, the yield point is expressed, in Table I, as a critical resolved shear stress for both $\{10\bar{1}0\}$ $<11\bar{2}0>$ duplex prism slip and $\{10\bar{1}1\}$ $<11\bar{2}0>$ duplex pyramidal slip.

When the curve of yield stress as a function of temperature for nonbasal slip is compared with that for basal slip,[3] an important difference may be noted. The yield stress for nonbasal glide falls continuously from 38,000 psi (27 kg per sq mm) at −190°C to about 500 psi (0.35 kg per sq mm) at 286°C, while the critical resolved shear stress for basal slip is essentially constant from 300°C to room temperature. Below room temperature it rises steadily in a manner similar to nonbasal slip, and the ratio of the yield stress for nonbasal slip (expressed in terms of resolved shear stress on $\{10\bar{1}0\}$ to that for basal slip appears to have an almost constant value of 85. Above room temperature the same ratio is not constant and falls rapidly with rising temperature to a value of approximately 3 to 1 at 286°C.

At 25°C, the yield stress for nonbasal slip is high and is approximately the same as the stress for the start of failure. On the other hand, at 286°C, there is a large difference (a ratio of about 20) between the fracture and yield stresses. The large ductility of magnesium, in tension parallel to the basal plane at 286°C, is, therefore, easily explained. Until strain hardening or reduction in cross sectional area has permitted the stress to rise to the value of the fracture stress, flow will occur by nonbasal slip.

An examination of the two curves for slow and fast-loading rates at 150°C shows that the yield stress is increased by a factor of about 2 (i.e., from 6000 psi to 12,000 psi). An increase is also indicated for 25°C but, in this case, fracture occurred in the rapidly loaded specimen before any appreciable yielding could occur.

According to the present data, the experimental values for rapid loading at 150°C are very close to those found by interpolation of the curves for slowly loaded specimens at a temperature of 90°C (363°K). Thus, an increase in the speed of testing by a factor of 100 has an effect on mechanical properties roughly equivalent to a 60°C decrease in temperature.

Conclusions

Magnesium single crystals, oriented to suppress (0002) basal slip and $\{10\bar{1}2\}$ twinning, were strained in tension parallel to the basal plane and in a $<10\bar{1}0>$ direction at four temperatures (−190°, 25°, 150°, and 286°C) and at two strain rates.

1) Under the conditions of loading, the ductility of magnesium is a minimum and very small at 25°C. At 286°C, the ductility is extremely high (reduction of area = 77 pct) and at −190°C it is again high (reduction of area = 20 pct).

2) The yield stresses, expressed in terms of critical resolved shear stresses for duplex prismatic slip at −190° and 25°C, and in terms of both duplex prismatic and pyramidal slip at 150° and 286°C, were determined, Table I.

3) Increasing the rate of loading by a factor of 100, at 25° and 150°C, reduced the ductility of the specimens and approximately doubled the yield stress for nonbasal slip. An increase in the speed of testing by a factor of 100 at 150°C was approximately equivalent to decreasing the temperature by 60°C.

4) Prism slip lines $\{10\bar{1}0\}$ $<11\bar{2}0>$, with a minimum spacing of less than 5 x 10^{-5} cm, have been found on specimens tested at −190°C. Cross-slip bands consisting of groups of fine prism slip lines with cross-slip components on the basal plane were identified on specimens tested at −190° and 25°C.

5) The lattice rotations, observed by X-ray analysis, the two-dimensional nature of the plastic strain, and the slip bands which are visible on surfaces nearly parallel to the basal plane all indicate that plastic deformation at all temperatures was accomplished primarily by conjugate slip along $<11\bar{2}0>$ slip directions. Microscopic evidence shows that at −190°C, and probably at 25°C, slip was primarily on $\{10\bar{1}0\}$ prism planes. At 150° and 286°C the asterism in Laue back-reflection photographs shows rotations which may be interpreted as favoring $\{10\bar{1}1\}$ pyramidal slip as the predominant form.

Acknowledgments

The authors would like to thank Rear Admiral K. K. Cowart, U. S. Coast Guard, for his aid and continuing interest in this work. This paper is based on a portion of a thesis by R. E. Reed-Hill submitted to the School of Engineering, Yale University, in partial fulfillment of the requirements for the degree of Doctor of Engineering.

References

[1] E. Schmid and G. Wasserman: *Handbuch der physikalische, und technische Mechanik*, 1931, vol. 4, Part 2, p. 319.
[2] P. W. Bakarian and C. H. Mathewson: *AIME Trans.*, 1943, vol. 152, p. 226; METALS TECHNOLOGY, April 1943.
[3] E. C. Burke and W. R. Hibbard, Jr.: *AIME Trans.*, 1952, vol. 194, p. 295; JOURNAL OF METALS, March 1952.
[4] A. R. Chaudhuri, H. C. Chang, and N. J. Grant: *AIME Trans.*, 1955, vol. 203, p. 682; JOURNAL OF METALS, May 1955.
[5] F. E. Hauser, P. R. Landon, and J. E. Dorn: *ASM Trans.*, 1956, vol. 48, p. 986.
[6] D. C. Jillson: *AIME Trans.*, 1950, vol. 188, p. 1005; JOURNAL OF METALS, August 1950.
[7] E. C. Burke: Doctoral Thesis, Yale University, May 1951.
[8] R. Maddin and W. R. Asher: *Review of Scientific Instruments*, 1950, vol. 21, p. 881.
[9] R. F. Miller: *AIME Trans.*, 1936, vol. 122, p. 176.
[10] H. Lange and K. Lucke: *Ztsch. für Metallkunde*, 1953, vol. 44, pp. 183 and 514.
[11] R. W. Honeycombe: *Journal* Institute of Metals, 1951-1952, vol. 80, p. 49.
[12] E. Schmid and W. Boas: *Plasticity of Crystals*, p. 149. F. A. Hughes and Co. Ltd. London, 1950.

Discussion of this paper sent (2 copies) to AIME by June 1, 1957 will appear in AIME *Transactions* Vol. 209, 1957, and in JOURNAL OF METALS, October 1957.

Effect of Temperature on the Flow Stress And Strain-Hardening Coefficient Of Magnesium Single Crystals

The initial yield stress and plastic flow characteristics of magnesium single crystals have been investigated by means of incremental creep experiments in tension and direct shear, in the temperature range of 78° to 364°K. It was found that the strain rate, $\dot{\gamma}$, could be related to the applied stress, τ, and the temperature, T, by the expression $\dot{\gamma} = C \exp\left(-\frac{\Delta H}{kT}\right) \exp B(\tau - h\gamma)$, where B and C are constants, h is the strain-hardening coefficient, γ is the strain, and ΔH is an activation energy equal to 10.3 kcal per g atom. The strain-hardening coefficient was constant in the temperature range of 78° to 203°K, but decreased at higher temperatures; the decrease is attributable to recovery. The constant coefficient, in the absence of recovery, is consistent with the idea that strain hardening in hexagonal crystals is associated with the elastic interaction of accumulated dislocations.

by Hans Conrad and W. D. Robertson

FORMAL theories of yielding and flow have been developed to describe thermally activated plastic flow in metal crystals.[1-5] They are all based on Becker's[1] original idea that thermal fluctuations aid the applied stress in overcoming internal barriers to flow and lead to the following relation.

$$\dot{\gamma} = C \exp - \left\{ \frac{E(\tau)}{kT} \right\} \qquad [1]$$

where $\dot{\gamma}$ is the strain rate; C is a constant which includes a frequency factor, the entropy, the number of flow units, and the amount of strain associated with each successful fluctuation; $E(\tau)$ is the activation energy associated with flow, and is a decreasing function of the applied stress, τ; k is Boltzmann's constant; and T is the temperature in °K.

The various theories differ mainly in the model chosen and in the nature of the relationship between the applied stress and the activation energy. Becker[1] and Orowan[2] suggest a relationship of the form $E \alpha (\tau_i - \tau)^2$, where τ_i represents the stress required for flow without the aid of thermal fluctuations; Kauzmann,[3] Cottrell,[4] and Seeger[5,6] suggest $E \alpha (\tau_i - \tau)$; Fisher[7] suggests $E \alpha 1/\tau$; while Cottrell and Bilby[8] suggest a more complex relationship between E and τ. Additional data are needed to test these various theories, especially in view of Dorn's[9] work, which indicates that the activation energy for creep is independent of the stress and strain.

The present paper presents the stress-strain data derived from incremental loading of magnesium single crystals in tension and direct shear, in the temperature range of 78° to 364°K. Incremental loading was employed in order that the creep component of the strain could be determined. Stress-strain curves of aluminum[10-12] and copper[13] single crystals, derived from incremental loading tests, have been found to be in agreement with those obtained by the more conventional constant strain rate or loading rate tests.

Two types of tests were conducted in the present investigation: 1) tests in which the temperature was maintained constant throughout the entire

H. CONRAD, Associate Member AIME, is associated with Research Laboratories, Westinghouse Electric Corp., Pittsburgh. W. D. ROBERTSON, Member AIME, is with the Hammond Metallurgical Laboratory, Yale University, New Haven, Conn.

TP 4422E. Manuscript, Sept. 14, 1956. New Orleans Meeting, February 1957.

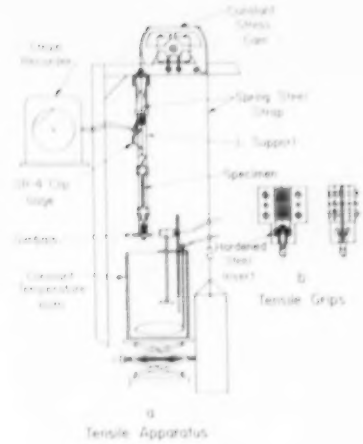

Fig. 1—Apparatus and grips used for tensile creep tests.

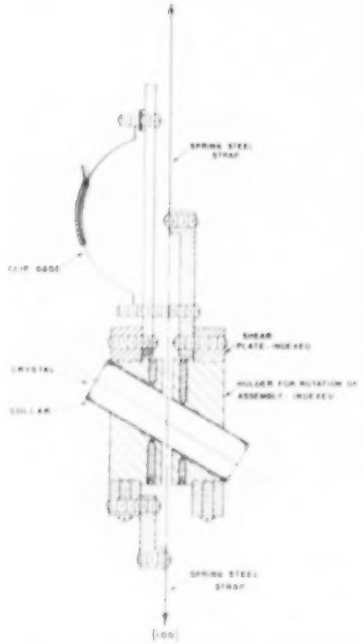

Fig. 2—Cross section of apparatus used to strain crystals in shear.

series of stress increments; and 2) tests in which the specimens were loaded at one temperature, the load removed, the temperature changed, and the load reapplied. These tests are similar to those employed by Cottrell and Stokes[15] and Adams and Cottrell[16] to determine the effect of temperature on the flow stress of aluminum and copper crystals.

Experimental Procedure

Preparation of Magnesium Single Crystals—The crystals* used in the present investigation (½ in. in diam and 6 to 7 in. long) were grown in a temperature gradient furnace from the liquid in a graphite crucible under an argon atmosphere. The purity of the magnesium is indicated by the following spectrographic analysis: 0.003 pct Al; < 0.01 pct Ca; 0.002 pct Cu; < 0.001 pct Fe; 0.008 pct Mn; < 0.001 pct Ni; < 0.002 pct Pb; < 0.01 pct Si; < 0.001 pct Sn; and < 0.01 pct Zn.

The crystals, described in Table I, were oriented by the back-reflection Laue technique.[17] Four photograms were taken (using Cu or Mo radiation with a 0.5 mm pin hole) at 90° intervals in a helical pattern along the length of each specimen. Split Laue spots were generally obtained on at least one of the photograms, indicating a lineage structure which varied from ¼° to 1° (most crystals showing a maximum of ½°).

Before testing, the crystals were chemically polished to the required diameter by gently rolling in a tray containing 25 pct hydrochloric acid in water. Following polishing they were successively rinsed in tap water, distilled water, and acetone, after which they were allowed to dry in air. Tension tests were generally run within 24 hr after chemical polishing and drying; the shear tests were conducted within two days.

Tension Tests—Tension tests were made on crystals with X_o and λ_o° <35°. A cam, similar to that used by Cottrell and Aytekin,[18] was constructed to maintain a constant resolved shear stress (within 1 pct) during the elongation of crystals with λ_o <27°. This cam was also used for the crystals with λ_o >27°. However, the strain for a given stress increment was small enough so that the shear stress could be considered to be constant within 1 pct during each creep test. Even for larger strains (numerous increments), the results from crystals with λ_o >27° agreed with those in which λ_o <27°.

Fig. 1a shows the equipment used for the tension tests. The cam was supported on a 1 in. steel shaft rotating in ball bearings. The specimen grips, Fig. 1b, were made of an aluminum alloy to minimize weight. Axiality of loading was attained by applying the load from the cam through a flexible spring steel strap, a hook, and the action of hardened steel balls against hardened steel inserts in the grips. The bottom grip was aligned through the action of a hardened steel ball against a universal joint attached to the frame.

The specimen length between grips, the gage length, was fixed at 10 cm for tests at 78° and 203°K, and at 12.5 cm for tests at 298° and 364°K.

Shear Tests—A modified Bausch type of shear apparatus[19] was employed in the shear tests, Fig. 2. Shear tests were run on specimens with two orientations, X_o = 85° and X_o = 60°, and at two temperatures, 298° and 364°K.

The shear specimens were prepared by acid cutting 1 in. long sections from the cylindrical crystals. Clamping collars for the shear specimens were of hard copper tubing, cut to the proper angle to out-

* X_o is the initial angle between the specimen axis and the basal plane, and λ_o is the initial angle between the specimen axis and the slip direction.

Table I. Orientation of Magnesium Single Crystals

Crystal No.	X_o°	λ_o°	Test Method
7	19°	35°	Tension
11	85°	85°	Shear
22	24°	24°	Tension
23	18°	29°	Tension
29	23°	31°	Tension
32	14°	15°	Tension
34	34°	34°	Tension
35	13°	21°	Tension
36	10°	20°	Tension
40	60°	62°	Shear
52	23°	27°	Tension

* Angle between specimen axis and the basal plane.
† Angle between specimen axis and the slip direction.

* The authors are indebted to Dr. E. C. Burke, who supplied the crystals, and to the Dow Chemical Co. for the high purity magnesium.

line the trace of the slip plane, and they were separated by ⅛ in. The collars were cemented to the crystals with Dupont cement No. 5458 or Sauereisen cement. Orientation of the crystals was rechecked after mounting in the collars and it was always found to agree within 5° of the desired orientation.

The shear apparatus, Fig. 2, was loaded in the equipment used for the tension tests. Although the cam relaxed the load with increasing strain, the elongation during a shear test was so small that the shear stress was essentially constant throughout the test.

Measurement of Dimensions and Temperature Control—Dimensional measurements on the tension and shear specimens were made with a travelling microscope which could be read to 0.0001 in. The tension specimens, measured at two circumferential positions at ½ in. intervals, were 0.4 ±0.005 in. in diam. Diameter and length measurements were made on the shear specimens at the minor axis of the glide ellipse.

Temperatures of 298° and 364°K were obtained with a silicone oil bath controlled by a mercury thermoregulator. At 298°K, the temperature was controlled to within ±0.01°C, as determined by a Beckman thermometer, and at 364°K to within ±0.2°C. A temperature of 203°K was obtained with a mixture of dry ice and acetone in a dewar flask and 78°K with liquid nitrogen. The latter two temperatures were measured by means of a low temperature thermometer placed near the specimen. Dry ice and liquid nitrogen were continually added during the tests.

Method of Loading—Incremental loading was employed; i.e., the stress was increased, starting from zero stress, in increments which varied from 1 to 10 g per sq mm. After an initial elastic strain, creep was observed for each stress increment; no significant instantaneous plastic flow was observed following any of the loading increments. The stress increments were added by manually pouring steel shot into the loading container. Generally, the load increments were applied in 3 to 5 sec.

With the exception of one test designed to determine if a limiting stress for creep existed, constant stress increments were added every minute until creep was observed. After creep was first observed, equal stress increments were added after equal time intervals for a number of increments; following this, stress increments and time intervals were varied. Numerous tests were also conducted in which the stress increment and time interval were varied immediately following the first occurrence of creep. The time interval between increments was varied from 0.6 min to 15,000 min. However, 10 to 30 min intervals were most common.

Strain Measurement—Strain in both tension and shear tests was measured by a clip gage employing two A-7, SR-4 resistance strain gages connected to a Baldwin indicating recorder operating at 1/12 rpm. This combination gave a tensile strain sensitivity of 3×10^{-5} for the tension tests and a sensitivity of 1×10^{-4} for the shear tests. The position of the clip gage is shown in Figs. 1a and 2.

Since the clip gage was not mounted directly on the specimen, the elastic strain from the supporting apparatus was included in all strain measurements. The possibility that strain in the apparatus contributed to the creep strain was investigated on two crystals at 298°K by simultaneous strain measurements with the clip gage and a cathetometer

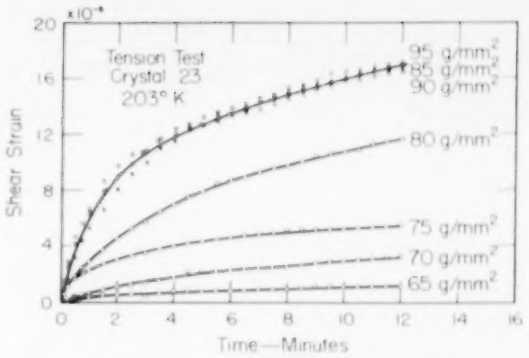

Fig. 3—Typical creep curves in tension at 203°K.

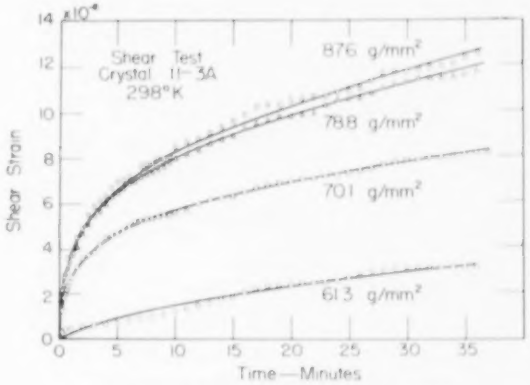

Fig. 4—Typical creep curves in shear at 298°K.

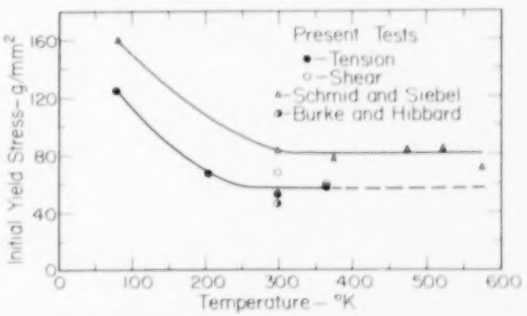

Fig. 5—Initial yield stress as a function of temperature.

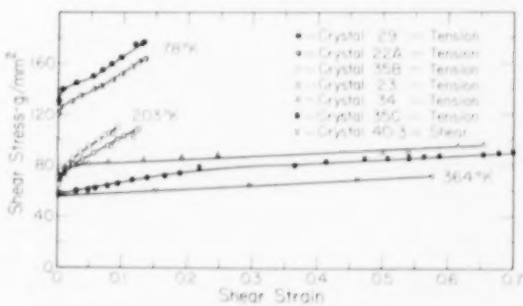

Fig. 6—Stress-strain curves at 78°, 203°, and 364°K.

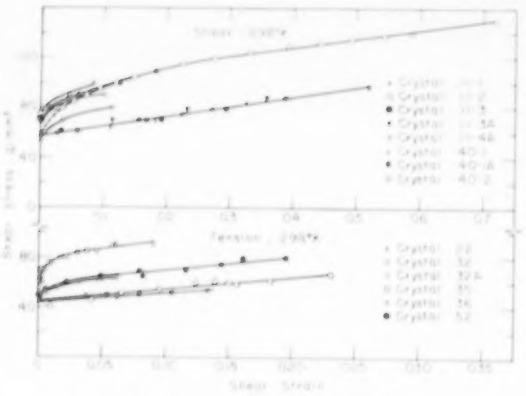

Fig. 7—Stress-strain curves at 298°K.

sighting on the crystals. Good agreement was obtained between the clip gage and the cathetometer creep strain measurements. It was concluded that the apparatus was sufficiently rigid so that the observed creep strain (total strain minus total elastic strain) could be associated with the crystal only.

In order to compare the results of one crystal with another, and the results of the tension tests with the shear tests, all stresses and strains were converted to resolved shear stress, τ, and shear strains, γ, in the slip plane and slip direction by means of formulae given by Schmid and Boas.[20]

Recovery of Magnesium Crystals—Since magnesium crystals deform by glide on one plane in the temperature and orientation range of the present investigation,[21, 22] it was expected that after homogenous deformation the crystals could be completely recovered by heating at a sufficiently high temperature.[20] Complete recovery was experimentally demonstrated by heating strained crystals for 1 to 2 hr at 450°C. For example, compare stress-strain curves for crystals 11-3 and 11-3A, 40-1 and 40-1A, 32 and 32A of Fig. 7. Tests on the recovered crystals are indicated by the original number of the crystal followed by the letter *A*.

In view of this recovery, successive experiments could be conducted on the same crystal. The letter *B* indicates that the crystal was recovered a second time, etc.

Experimental Results

Limiting Stress for Creep and Initial Yield Stress—A limiting stress for macrocreep, as distinguished from microcreep,[24] has been found for most metal single crystals, including magnesium.[25] This stress is generally the same as the critical resolved shear stress, determined in tension tests at a constant loading rate or a constant strain rate. To determine the limiting stress for creep of magnesium crystals at 298°K, 5 g per sq mm stress increments were added to one crystal (crystal 52) at intervals of two days, after a small initial load. No creep was detected until a resolved stress of 54 g per sq mm was reached, after which measurable creep occurred. Similarly, when the time interval between stress increments in the elastic range was 1 min, a limiting stress for creep was found for all crystals tested in tension or shear, at all temperatures. Typical creep curves in tension and shear at stresses in excess of the limiting stress are shown in Figs. 3 and 4.

The values of the limiting stress (designated as the initial yield stress, τ_i) at the various temperatures are given in Table II. The following should be noted particularly.

1) The average value of the limiting stress in tension at 298°K, for virgin and recovered crystals, is 53 g per sq mm ±25 pct maximum deviation from the average. The higher initial yield stresses exhibited by the recovered tension specimens 32A and 35A at 298°K, as compared to their virgin counterparts, may be associated with non-axiality during initial loading of the virgin crystals or perhaps with a yield point phenomenon appearing after the initial strain.

2) The average initial yield stress obtained in shear at 298°K, 68 g per sq mm, is 15 g per sq mm higher than the average obtained in tension. Other than differences associated with the individual crystals, the higher values obtained with the shear test may be due to a) the lower sensitivity of strain measurement in the shear test, b) the addition of larger stress increments in some of the shear tests. No systematic difference in initial yield stress was observed between virgin and recovered crystals strained in shear.

3) The initial yield stress values obtained in shear for specimens from the same crystal are reproducible within the size of the loading increment with one exception, specimen 11-2. There is some reason to believe that this discrepancy is associated with experimental technique rather than variation in the crystal.*

* Some Duco cement had flowed onto the shear section of this crystal during the mounting of the collars. Although this area was cleaned with acetone, a film may have remained and caused the irregular behavior of this specimen.

For comparison, the critical resolved shear stress values obtained for magnesium single crystals at room temperature by other investigators using different methods are given in Table III.

The average initial yield stress values obtained in the present tests and those given by Schmid[20, 21] are plotted as a function of temperature in Fig. 5. The curve joining the values of the present investigation is approximately parallel to that of Schmid and Siebel, but displaced 25 to 35 g per sq mm below it. Although the initial yield stress can be assumed to be essentially constant above 250°K, the tension data can also be interpreted to indicate a slight hump at higher temperatures, characteristic of a yield point behavior.[26]

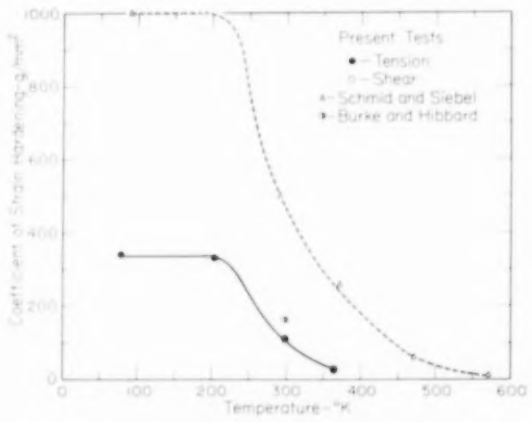

Fig. 8—Coefficient of strain hardening, $h = d\tau/d\gamma$, as a function of temperature.

Strain-Hardening Coefficient—Stress-strain curves for each temperature, derived from the creep tests by plotting the accumulated sum of the stress increments against the accumulated sum of the strain increments, are given in Figs. 6 and 7. Most curves are characterized by an initial curvature followed by a linear region, although some at 298° and 364°K are linear from zero strain. The extent of the curved region generally increased with increase in loading rate.

Two unusual effects are noted in the stress-strain curves: 1) at 78°K some of the early stress increments gave more strain for a given time interval than was indicated by the later linear region, resulting in a reversal of curvature of the stress-strain curve; and 2) at 364°K the early stress increments in the tension tests (but not in the one shear test) gave less strain for a given time interval than was indicated by the subsequent linear region, resulting in an extended region of curvature. Both of these observations have the characteristics of yield point phenomena.

The linear region of the stress-strain curve is characteristic of easy-glide; i.e., glide on one plane in one direction. Its slope, $\frac{d\tau}{d\gamma}$, is termed the strain-hardening coefficient, h. The values of h derived from the stress-strain curves are given in Table II, and the average values are shown as a function of temperature in Fig. 8, together with values derived by Cottrell[20] from the curves of Schmid and Siebel[20, 21] at much larger strains. Also included is the value obtained from the data of Burke and Hibbard.[22]

It is evident in Fig. 8 that the values of h, obtained from the present tests, remain essentially constant between 78° and 203°K, then decrease between 203° and 298°K, and continue to decrease, though at a less rapid rate, from 298° to 364°K. The data of Schmid and Siebel can be interpreted to follow the same trend. A similar variation of h with temperature; i.e., a constant value at low temperatures followed by a decrease at higher temperatures, has been reported for cadmium[23] and zinc.[24-26]

Effect of Stress, Strain, and Temperature on Flow Rate—A plot of the initial creep rate following the addition of a stress increment vs the quantity $(\tau - h\gamma)$, where τ is the applied stress, h is the strain-hardening coefficient, and γ is the total strain up to the time of the addition, is given in Fig. 9. The initial creep rate was taken as twice the amount of strain which occurred during the first ½ min after the addition of a stress increment. Similar straight lines were obtained when the initial rate was taken as the limit of the ratio $\frac{\Delta\gamma}{\Delta t}$ as Δt goes to zero. The points for each curve are not in order of increasing applied stress, for the stress increments and time intervals were varied for the later increments.

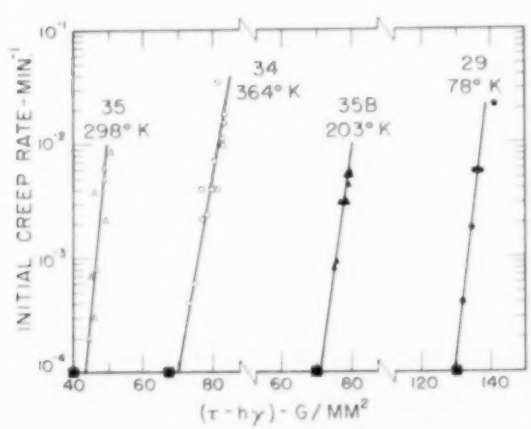

Fig. 9—Variation of the initial creep rate with the function $(\tau - h\gamma)$. Solid squares are initial yield stress values.

Table II. Initial Yield Stress, τ_o, and Coefficient of Strain-Hardening, h, of Magnesium Single Crystals

Crystal		Incremental Loading Rate in Elastic Range, G per Sq Mm per Min	Resolved Yield Stress τ_o, G per Sq Mm	Average Loading Rate in Plastic Range, G per Sq Mm per Min	Strain-Hardening Coefficient h, G per Sq Mm
			78°K		
22A	T*	10	120	0.50	325
29	T	10	130	0.35	350
			125 Avg		338 Avg
			203°K		
23	T	5	65	0.17	300
35B	T	5	70	0.31	355
			68 Avg		328 Avg
			298°K		
22	T	2.2	50	0.014	80
32	T	5	55	5.0	130
32A	T	5	65	0.55	130
35	T	5	40	0.053	98
35A	T	5	55	0.27	100
36	T	4	48	0.0007	137
52	T	0.002	54	0.0005	100
			53 Avg		110 Avg
11-1†	S	5	55	0.15	80
11-2†	S	5	80	0.33	70
11-3†	S	8.7	61	0.12	80
11-3A†	S	8.7	61	0.12	80
11-3B†	S	5	60		
11-4A†	S	5	60		
			63 Avg		78 Avg
40-2‡	S	10	80	5.0	160
40-1A‡	S	10	70	5.0	150
40-1‡	S	10	70	5.0	125
			73 Avg		143 Avg
Average for the two crystals tested in shear			68		110
			364°K		
7	T	2	48		
34	T	2	67	0.11	27
35C	T	2	60	0.004	27
			58 Avg		27 Avg
40-3‡	S	5	60	0.17	30

* T = tension; S = shear.
† Shear specimens from crystal 11.
‡ Shear specimens from crystal 40.

The straight lines of Fig. 9 indicate that the strain rate, $\dot{\gamma}$, is given by

$$\dot{\gamma} = A \exp B\,(\tau - h\gamma) \qquad [2]$$

where A and B are constants given by the intercept and slope, respectively. An exponential effect of stress on the rate of plastic flow of metals was first reported by Ludwik[27] and has been observed more recently by other investigators.[5, 9, 10]

Comparing the slopes of the plots of Fig. 9, it is noted that B is relatively independent of temperature. Cottrell and Aytekin[10] and Dorn[9] similarly found B to be independent of temperature for the creep of zinc single crystals and aluminum polycrystals, respectively. On the other hand, the constant A is strongly dependent on the temperature, Fig. 9, suggesting a thermally activated process. The nature of the variation of A with temperature will be discussed below.

Since the initial creep rate, $\dot{\gamma}_o$, associated with the initial yield stress, τ_o, in the tensile tests was ap-

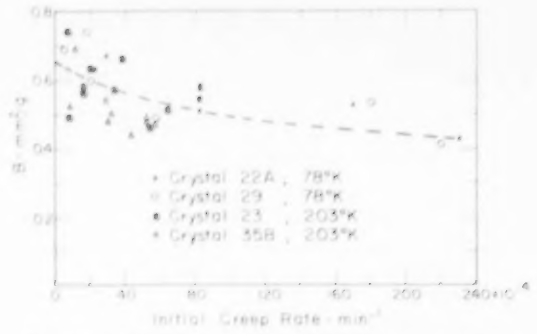

Fig. 10—Variation of B, in the expression $\dot{\gamma} = A \exp B (\tau - h\gamma)$, with the initial creep rate for stress increments at 78° and 203°K.

proximately 10^{-4} min^{-1} (the stress increments were added every minute in the elastic range and the resolved shear strain sensitivity for the tensile tests was approximately 10^{-4}), it is of interest to compare τ_0 with the value of $(\tau - h\gamma)$ associated with a creep rate of 10^{-4} min^{-1}. Fig. 9 and Table IV show that the extrapolated value of $(\tau - h\gamma)$ associated with an initial creep rate of 10^{-4} min^{-1} is approximately equal to τ_0 obtained in the tension tests, Table II.

Since the value of $(\tau - h\gamma)$ associated with a strain rate of 10^{-4} min^{-1} can be taken as equal to the initial yield stress, τ_0, it is seen from Fig. 9 that

$$A = \dot{\gamma}_0 \exp - B\tau_0 \qquad [3]$$

Eq. 2 can then be written

$$\dot{\gamma} = \dot{\gamma}_0 \exp B(\tau - \tau_0 - h\gamma). \qquad [4]$$

From Eq. 2 the value of B for a constant temperature is also given by

$$B = \ln \frac{\dot{\gamma}_{n+1}}{\dot{\gamma}_n} \cdot \frac{1}{\Delta\tau} \qquad [5]$$

where $\dot{\gamma}_n$ is the creep rate just previous to the addition of a stress increment, $\Delta\tau$, and $\dot{\gamma}_{n+1}$ is the creep rate immediately after the addition. The values of B obtained by means of Eq. 5 for a series of tests on one crystal were independent of the total stress and strain. Although equal stress increments gave good reproducibility in the value of B, there was an increment size effect whereby the larger stress increments generally gave smaller values of B and vice versa. This effect can probably be attributed to the method used to determine the creep rate immediately following the addition of a stress increment, rather than due to the size of the increment per se. The larger stress increments generally produced greater amounts of strain during the first 0.5 min and, consequently, the average rate based on this period was farther removed from the instantaneous rate than was the case for the smaller increments. Fig. 10 shows how B varied with the initial creep rate for tests at 78° and 203°K. An extrapolation to zero initial creep rate gives a value of $B = 0.65 \pm 0.15$ sq mm per g, independent of temperature.

Table III. Critical Resolved Shear Stress of Magnesium Crystals at Room Temperature

Investigator	Impurity Content	Approximate Strain Sensitivity	Method of Test	Stress Range, G per Sq Mm	Stress Average G per Sq Mm
Schmid[6]	—	—	Tension	57 to 127	83
Bakarian and Mathewson[8]	0.02	—	Tension	71 to 84	78
Burke and Hibbard[10]	<0.05	10^{-6}	Tension	40 to 50	46
Krashes and Burr[9]	<0.05	10^{-7}	Tension	18 to 50	32
Nash and Sheely[7]	<0.05	10^{-6}	Tension	30 to 50	38
Hsu and Cullity[3]	0.02	—	Tension	—	66
Hsu and Cullity[3]	0.02	—	Torsion	—	38
This investigation	<0.05	10^{-6}	Tension	40 to 65	53
This investigation	<0.05	10^{-6}	Shear	55 to 80	68

Effect of Temperature Changes—Several tension tests were run in which the temperature was changed between tests. The procedure was to load a crystal incrementally at one temperature, record the creep curves, unload, change the temperature of the specimen, and then incrementally reload, again recording the creep curves. From these tests a comparison was made between the stress which produced the final creep rate at the previous temperature, and the stress required to produce the same initial creep rate at the new temperature. The final creep rate was taken from the slope of the previous creep curve, while the initial rate was determined by the amount of strain occurring during the first ½ min after the addition of a stress increment at

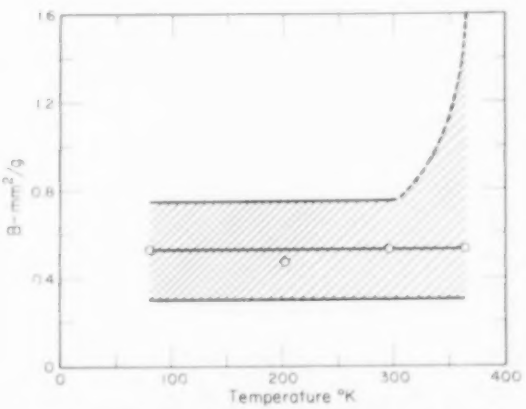

Fig. 11—Variation of B, in the expression $\dot{\gamma} = A \exp B (\tau - h\gamma)$, with temperature. Band represents 95 pct of values from 228 creep tests. Open circles are average values for 5 g per sq mm increments and less than 15 min intervals.

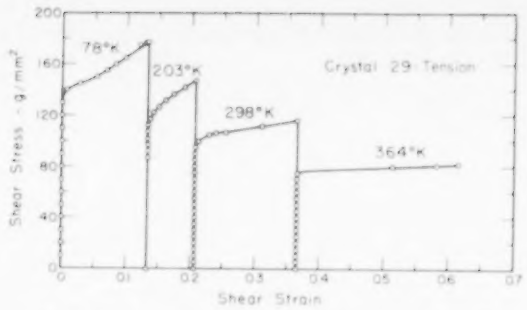

Fig. 12—Effect of increasing the temperature from 78° to 364°K on the stress-strain curve.

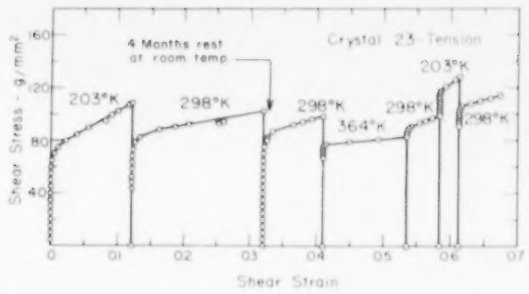

Fig. 13—Effect of temperature changes on the stress-strain curves at 203°, 298°, and 364°K.

the new temperature. Generally 2 g per sq mm increments were added every minute initially, and the stress at the new temperature which produced the same creep rate as the final rate at the previous temperature was estimated to the nearest 1 g per sq mm by interpolation of the linear plot of the logarithm of the initial creep rate vs $(\tau - h\gamma)$, where γ was the total strain at the new temperature. Both increases and decreases of temperature were investigated. The range covered was the same as that of the constant temperature tests, namely, 78° to 364°K.

The results from these tests are given in Table V. Typical stress-strain curves are shown in Figs. 12 and 13 for a variety of temperature combinations. The following observations were made from these tests:

1) When the temperature was *decreased* from 298° to 203°K or *increased* from 78° to 203°K the change in stress required to maintain a constant strain rate (stress equivalence of the temperature change) was approximately equal to the difference in the average initial yield stress for the two temperatures. This change represents a reversible change in the flow stress, since recovery does not occur for these temperature changes. In comparison, the reversible change in flow stress of aluminum and copper crystals for a given temperature change increased with strain to 10 to 15 pct elongation and thereafter settled down to a constant ratio of flow stresses.[15,16]

2) When the temperature was *decreased* from 364° to 298°K, an increase in stress of 6 to 7 g per sq mm was required to produce the same strain rate, in spite of the fact that the average initial yield stress at 364°K, Fig. 5, is approximately equal to or slightly higher than that at 298°K.

3) When the temperature was *increased* from 203° to 298°K, or from 298° to 364°K, a greater decrease in stress was required to give the same strain rate than that associated with the effect of temperature on the initial yield stress. This larger difference is associated with recovery and contributes an irreversible change in the flow stress, in addition to the reversible change.

4) The strain-hardening coefficient for a given temperature was independent of the previous strain history. For example, see Fig. 13 and compare h at 298°K for crystal 35B in Table V with 35 and 35A in Table II. Rosi and Mathewson[17] likewise indicated that the strain-hardening coefficient for easy glide in aluminum crystals was unaffected by previous straining at another temperature. On the other hand, Cottrell and Stokes[15] and Adams and Cottrell[16] found *work-softening* to occur when aluminum and copper crystals were strained at higher temperatures after previous straining at lower temperatures, beyond the region of easy glide.

5) The data of Table V are not too clear on the effect of strain history on the value of B, due in part to the scatter in the data. In general, B is relatively independent of strain history. However, the values of B at 203° and 298°K after previous straining at 78°K are slightly lower than expected. Also, the values of B (determined from a comparison of strain rates before and after a stress increment) at 298° after previous straining at 364°K are slightly higher than expected. No explanation can be offered for these effects.

Table IV. Value of $(\tau - h\gamma)$ for an Initial Creep Rate of 10^{-4} Min^{-1}

Crystal	Type of Test	$(\tau - h\gamma)$, G per Sq Mm
	78°K	
22A	Tension	117
29	Tension	130
		Avg 124
	203°K	
23	Tension	69
35B	Tension	71
		Avg 70
	298°K	
22	Tension	42
32	Tension	53
32A	Tension	60
35	Tension	43
35A	Tension	52
36	Tension	48
52	Tension	54
11-1	Shear	48
11-3	Shear	52
11-3A	Shear	52
		Avg 50
	361°K	
34	Tension	70*
35C	Tension	60*
40-3	Shear	47
		Avg 61

* Extrapolation of data for stress >78 g per sq mm.

Discussion

An attempt was made to interpret the plastic flow of magnesium single crystals in terms of the formal theories.[1-5] None of the theories was found to be in accord with all of the observed facts. The major disagreement was with regard to the observed effect of stress on the strain rate, i.e., that it was of the form $\gamma \alpha e^{B\tau}$, where B is independent of temperature. In view of the lack of agreement with the formal theories it was decided to describe the flow of magnesium single crystals by means of an empirical equation based on the experimental data.

A plot of the initial yield stress obtained in the present tension tests vs the reciprocal of the abso-

Table V. Effect of Change of Temperature on Stress, Coefficient of Strain-Hardening, and the Constant, *B*

Crystal	Temperature Change, °K	$\dot{\gamma}$, † 10^{-4} per Min	t, ‡ Min	$\Delta\tau$, § G per Sq Mm	h, ¶ G per Sq Mm	B, ‖ Sq Mm per G	
						Method 1	Method 2
29 T*	78		15		350	0.61	0.41 to 0.74
	78 to 203	1.2	15	−65	335	0.19	0.26 to 0.43
	203 to 298	6.1	600	−48	75	0.33	0.41 to 0.58
	298 to 364	20.1	60**	−41	24	0.66	0.58 to 0.75
21 T	203		15		390	0.56	0.46 to 0.66
	203 to 298	2.4	600	−29	92	0.49	0.49 to 0.76
	298		4 months		140	0.49	0.48 to 0.84
	298 to 364	6.0	60**	−24	38	0.56	0.89 to 0.95
	364 to 298	22.0	60	6	188	0.54	0.66 to 1.07
	298 to 203	3.5	15	15	400	0.46	0.50 to 0.64
	203 to 298	3.5	60	−25	140	0.44	0.55 to 0.95
158 T	203		15		355	0.42	0.44 to 0.54
	203 to 298	7.2	600	−25	100	0.57	0.57 to 0.73
156 T	364		60**		27	0.65	0.36 to 1.55
	364		60††		80	0.58	0.73 to 1.34
	364 to 298	15.0	60	7	260	0.40	0.81 to 1.15
	298 to 364	5.0	60**	−20	77	0.46	0.55 to 1.23
	364 to 298	9.3	60	6	280	0.46	0.69 to 0.97
	298 to 364	3.9	60**	18	80	0.40	0.55 to 1.13
49-1 S	364		60**		30	0.38	0.37 to 0.43
	364 to 298	39.0	60	6	150		0.51

* T = tension; S = shear.

† $\dot{\gamma}$ = creep rate just previous to temperature change.

‡ t = time at new temperature previous to reloading.

§ $\Delta\tau = \tau_2 - \tau_1$, where τ_2 = shear stress at new temperature which produced the same value of $\dot{\gamma}$ as that just previous to the temperature change and τ_1 = shear stress acting previous to temperature change.

¶ h = strain-hardening coefficient; i.e., slope of stress-strain curve derived from creep tests.

‖ B = constant given in the equation $\dot{\gamma} = A \exp B(\tau - h\gamma)$; method 1, from slope of plot of log initial creep rate vs $(\tau - h\gamma)$; method 2, from comparison of creep rates previous to and subsequent to the addition of a stress increment.

** Specimen heated in silicone oil bath as temperature of bath was changed from 298° to 364°K.

†† Specimen rested at room temperature for three months previous to running this series of tests.

lute temperature gives a straight line, Fig. 14. Similarly, the data of Schmid and Siebel[6, 7] yield a straight line parallel to that of the present tests. This procedure leads to the following expression for the variation of the initial yield stress, τ_o, with temperature in the temperature range of the data

$$\tau_o = a + \frac{b}{T} \qquad [6]$$

where a is 26 g per sq mm, from the present data, and b is 8.0×10^{-3} °K g per sq mm.

Substituting $a + \frac{b}{T}$ for τ_o in Eq. 4 gives the following expression for the flow rate of magnesium crystals

$$\dot{\gamma} = \dot{\gamma}_o \exp(-Ba) \exp\left(\frac{-Bb}{T}\right) \exp B(\tau - h\gamma). \qquad [7]$$

Letting

$$\dot{\gamma}_o \exp(-Ba) = C \qquad [8]$$

and assuming a thermally activated process with an activation energy

$$\Delta H = Bb\,k \qquad [9]$$

Eq. 7 can be rewritten to give

$$\dot{\gamma} = C \exp\left(\frac{-\Delta H}{kT}\right) \exp B(\tau - h\gamma) \qquad [10]$$

where C is a constant having the dimensions of time^{-1}. The effect of stress and temperature given by Eq. 10 is in agreement with that observed by Dorn and his co-workers[8] for the creep of polycrystalline aluminum at high temperatures, i.e., greater than half of the melting temperature.

Taking $B = 0.65$ sq mm per g and $\dot{\gamma}_o = 10^4$ min^{-1}, Eqs. 8 and 9 give $C = 4.5 \times 10^{17}$ min^{-1} and $\Delta H = 10{,}300$ cal per g atom, which is approximately one third the value of the activation energy for self-diffusion in magnesium crystals.[9] A physical interpretation of this activation energy cannot be offered at this time.

Strain-hardening in hexagonal metals may be due to the elastic interaction of dislocations accumulated in the crystal during slip, in which case the change in strain-hardening coefficient with temperature should be no greater than the change of shear modulus with temperature and hence relatively independent of temperature.[5, 7] The fact that h for magnesium crystals was found to be constant in the temperature range of 78° to 203°K where no recovery occurs is consistent with this idea. In view of this, the total elastic interaction, τ_a, can be represented by

$$\tau_a = \tau^o_a + \tau_a(\gamma) \qquad [11]$$

where τ^o_a represents the stress field associated with the original dislocation network in the crystal, i.e., before straining, and $\tau_a(\gamma)$ is equal to $h\gamma$. The h can vary with temperature (and strain-rate) in the temperature range in which recovery occurs.

Combining Eqs. 10 and 11 gives

$$\dot{\gamma} = C^* \exp\left(\frac{-\Delta H}{kT}\right) \exp B(\tau - \tau_a) \qquad [12]$$

where

$$C = C^* \exp(-B\tau^o_a). \qquad [13]$$

From Eq. 12 the flow stress is given as

$$\tau = \tau_a - 1/B \ln\frac{C^*}{\dot{\gamma}} + \frac{\Delta H}{BkT}. \qquad [14]$$

Eqs. 12 and 14 differ from those given by Seeger[5, 7] in that the *activation volume*, v, equals BkT rather than being independent of temperature.

Eq. 14 indicates that the *reversible* change in flow stress with temperature is independent of prior strain history. This is supported by the data in Table VI where, for a given temperature change,

the change in flow stress for zero strain (change in initial yield stress as predicted by Fig. 14) is approximately equal to the reversible change in flow stress after appreciable amounts of strain (10 to 100 pct). The *irreversible* change in flow stress which occurred for an increase in temperature above 203°K can then be attributed to a decrease in τ_0 resulting from recovery during heating to the higher temperature.

Seeger[6,7] suggests that τ''_0 is given by the relatively flat portion at higher temperatures of the initial yield stress vs temperature curve. The data in Fig. 5 for the present tests can be interpreted to indicate a constant value of approximately 60 g per sq mm for the initial yield stress above 250°K. However, since the higher initial yield stress in tension at 364°K as compared to 298°K may be associated with yield phenomenon, there is some question as to whether the average value of the initial yield stress in this temperature range is actually τ''_0. Furthermore, as indicated above, it was found that the flow stress increased by 6 to 7 g per sq mm when the temperature was decreased from 364° to 298°K. This increase is somewhat larger than anticipated from the change of elastic constants of magnesium with temperature.[29] It might, however, be explained in terms of recovery, in which case the reversible change in flow stress between 364° and 298°K would be rate sensitive. The data of the present tests do not permit an evaluation of this.

Table VI. Stress Equivalence of a Temperature Change

	$\Delta\tau$ — G per Sq Mm	
Temperature Change, °K	Initial Yield Stresses*	Flow Stresses†
78 to 203	62	65
298 to 203	14	15
364 to 298	5	6

* Taken from Fig. 14.
† Average values from Table V.

Summary

Stress-strain curves for magnesium single crystals were determined by incremental tensile creep tests in the temperature range of 78° to 364°K. Similar tests were made in direct shear at 298° and 364°K. The results from these tests can be summarized as follows:

1) The limiting stress for macrocreep of magnesium single crystals (the initial yield stress) was found to increase linearly with the reciprocal of the absolute temperature, in the temperature range of the data. The value of this limiting stress at room temperature, 53 g per sq mm, is essentially the same as the critical resolved shear stress obtained in constant loading-rate tensile tests by other investigators.

2) The strain-hardening coefficient was constant in the temperature range of 78° to 203°K, but decreased at higher temperatures; the decrease is attributable to recovery. The constant coefficient, in the absence of recovery, is consistent with the idea that strain-hardening in hexagonal metals is associated with the elastic interaction of accumulated dislocations.

3) The strain-hardening coefficient of magnesium crystals over the entire temperature range of 78° to 364°K was found to be independent of prior strain history.

4) From the present results, the strain rate, $\dot{\gamma}$, of magnesium single crystals could be related to the applied stress, τ, and temperature, T, by the expression

$$\dot{\gamma} = C \exp\left(\frac{-\Delta H}{kT}\right) \exp B\,(\tau - h\,\gamma)$$

where B and C are constants, γ is the strain, and h is the strain-hardening coefficient. The activation energy ΔH derived from this expression is 10.3 kcal per g atom.

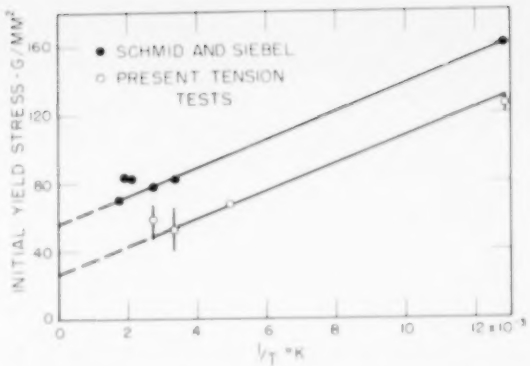

Fig. 14—Initial yield stress as a function of 1/T°K.

Acknowledgments

One of the authors, H. Conrad, wishes to thank D. K. Crampton for sponsoring part of this work during his stay at the Chase Brass and Copper Co. He also wishes to thank G. Schoeck, H. Wiedersich, and P. Shewmon of the Westinghouse Research Laboratories for reading and discussing the manuscript. This paper is based on a portion of a thesis by H. Conrad submitted to the Faculty of the School of Engineering, Yale University, in partial fulfillment of the requirements for the degree of Doctor of Engineering.

References

[1] R. Becker: *Physikalische Ztsch.*, 1925, vol. 26, p. 919.
[2] E. Orowan: *Ztsch. für Physik*, 1934, vol. 89, pp. 605, 614, 634.
[3] W. Kauzmann: *AIME Trans.*, 1941, vol. 143, p. 57; METALS TECHNOLOGY, June 1941.
[4] A. H. Cottrell and B. A. Bilby: *Proceedings* Physical Soc., 1949, vol. 62A, p. 49.
[5] A. H. Cottrell: *Journal of Mechanics and Physics of Solids*, 1952, vol. 1, p. 53.
[6] A. Seeger: *Philosophical Magazine*, 1954, vol. 45, p. 771.
[7] A. Seeger: *Ztsch. für Naturforschung*, 1954, vol. 9a, pp. 758, 810, 856.
[8] J. C. Fisher: *ASM Trans.*, 1955, vol. 47, p. 451.
[9] J. E. Dorn: *Journal of Mechanics and Physics of Solids*, 1954-1955, vol. 3, p. 85.
[10] G. Masing and J. Raffelsieper: *Ztsch. für Metallkunde*, 1950, vol. 41, p. 65.
[11] P. Haasen and G. Leibfried: *Ztsch. für Metallkunde*, 1952, vol. 43, p. 317.
[12] G. Masing and H. Weik: *Ztsch. für Metallkunde*, 1954, vol. 45, p. 417.
[13] M. Bauser and U. Dehlinger: *Ztsch. für Metallkunde*, 1954, vol. 45, p. 618.
[14] P. W. Neurath and J. S. Koehler: *Journal of Applied Physics*, 1951, vol. 22, p. 621.
[15] A. H. Cottrell and R. T. Stokes: *Proceedings* Royal Soc., London, 1955, vol. 233, p. 17.
[16] M. A. Adams and A. H. Cottrell: *Philosophical Magazine*, 1955, vol. 46, p. 1187.
[17] A. B. Greninger: *AIME Trans.*, 1936, vol. 122, p. 74.
[18] A. H. Cottrell and V. Aytekin: *Journal* Institute of Metals, 1950, vol. 77, p. 389.
[19] K. Bausch: *Ztsch. für Physik*, 1935, vol. 93, p. 479.
[20] E. Schmid and W. Boas: *Plasticity of Crystals*. Translated by F. A. Hughes and Co., London, 1950.
[21] E. Schmid: *Ztsch. für Elektrochemie*, 1931, vol. 37, p. 447.
[22] E. C. Burke and W. R. Hibbard: *AIME Trans.*, 1952, vol. 194, p. 295; JOURNAL OF METALS, March 1952.
[23] A. S. Nowick: *Acta Metallurgica*, 1955, vol. 3, p. 312.
[24] B. Chalmers: *Proceedings* Royal Soc., London, 1936, vol. 156A, p. 427.
[25] D. Krashes and A. A. Burr: The Creep Behavior of Magnesium Single Crystals at Room and Elevated Temperatures. Ordnance Project No. TB4-15 D11. Rensselaer Polytechnic Inst., Troy, N. Y., 1954.
[26] P. W. Bakarian and C. H. Mathewson: *AIME Trans.*, 1943, vol. 152, p. 226; METALS TECHNOLOGY, April 1943.
[27] R. R. Nash and W. F. Sheely: Properties of Magnesium and Magnesium Alloy Crystals at Room Temperature. Ordance Project No. TB 4-15 D-9. Rensselaer Polytechnic Inst., Troy, N. Y., 1954.

[5] S. S. Hsu and B. D. Cullity: *AIME Trans.*, 1954, vol. 200, p. 595; JOURNAL OF METALS, February 1954.
[6] J. H. Bechtold: *AIME Trans.*, 1953, vol. 197, p. 1469; JOURNAL OF METALS, November 1953.
[7] A. H. Cottrell: *Dislocations and Plastic Flow in Crystals*, p. 157. Clarendon Press, Oxford, 1953.
[8] W. Boas and E. Schmid: *Ztsch. für Physik*, 1930, vol. 61, p. 767.
[9] W. Fahrenhorst and E. Schmid: *Ztsch. für Physik*, 1930, vol. 64, p. 845.
[10] E. H. Edwards, J. Washburn, and E. R. Parker: *AIME Trans.*, 1953, vol. 197, p. 1525; JOURNAL OF METALS, November 1953.
[11] R. Dennard, J. Washburn, and E. R. Parker: *AIME Trans.*, 1953, vol. 197, p. 1226; JOURNAL OF METALS, September 1953.
[12] C. H. Li, J. Washburn, and E. R. Parker: *AIME Trans.*, 1953, vol. 197, p. 1223; JOURNAL OF METALS, September 1953.
[13] P. Ludwick: *Physikalische Ztsch.*, 1909, vol. 10, p. 411.
[14] F. Rost and C. H. Mathewson: *AIME Trans.*, 1950, vol. 188, p. 1163; JOURNAL OF METALS, September 1950.
[15] P. G. Shewmon: *AIME Trans.*, 1956, vol. 206, p. 918; JOURNAL OF METALS, August 1956.
[16] W. Köster: *Ztsch. für Metallkunde*, 1948, vol. 39, p. 1.

Discussion of this paper sent (2 copies) to AIME by June 1, 1957 will appear in AIME *Transactions* Vol. 209, 1957, and in JOURNAL OF METALS, October 1957.

Technical Note

Comparison of the Strength of Sintered Carbides

by Joseph Gurland

SEVERAL carbide-cobalt compositions were prepared for the purpose of determining the transverse rupture strength of various carbide-binder systems. The binder content was held at 10 and 37 volume pct Co, so as to be representative of low and high binder compositions. The carbides used, WC, TiC, TaC, CbC, VC and ZrC, were selected on the basis of availability, knowledge of their properties, and small solid solubilities in the binder metal at room temperature.

The methods of preparation and carbon analysis of the carbides are summarized in Table I.

The carbides with cobalt added were ball milled, pressed, and sintered. Vacuum sintering was used throughout, except for the WC-Co alloys, which were sintered in hydrogen. The sintering temperatures ranged from 2500° to 2750°F for the low binder alloys and from 2300° to 2550°F for the high binder alloys.

Compositions and properties of the sintered compacts are presented in Table II. For the transverse rupture strength, the average and range of the five best samples of each alloy are listed. Discrepancies between the actual and theoretical densities are attributed to carbon deficiencies in some samples. The theoretical densities were calculated by assuming mixtures of carbides of stoichiometric compositions and cobalt.

Representative microstructures are shown in Figs. 1 to 6. The porosity was A-2 or better[3] in all alloys except those with ZrC. A grain size of about 3 μ was

J. GURLAND, Member AIME, is associated with Brown University, Providence.

TN 388E. Manuscript, Aug. 13, 1956.

Table I. Preparation and Carbon Contents of Carbides

Carbide	Raw Materials	Carburization Temperature, °F	Analyses: Total Carbon, Pct	Analyses: Graphitic Carbon, Pct	Analyses: Theoretical Carbon, Pct
WC	W, C	2650	6.14	0.05	6.13
TiC	TiO_2, C	3800	19.2	0.3	20.0
TaC	Ta_2O_5, C	4000	6.20	0.05	6.23
CbC	Cb_2O_5, C	3800	11.76	0.32	11.45
VC	V_2O_5, C	3275	18.97	0.19	19.08
ZrC	ZrO_2, C	4000	11.58	0.31	11.64

Table II. Composition and Properties of Carbide-Cobalt Compacts

Volume Pct Co	Carbide	Wt Pct Co	Density, G per Cu Cm: Actual	Density, G per Cu Cm: Theoretical	Hardness, R_A	Transverse Rupture Strength, x10³ Psi: Average	Transverse Rupture Strength, x10³ Psi: Range
37	WC	25.0	13.04	13.05	83	346	305 to 381
	TaC	26.5	12.41	12.44	82¾	269	230 to 295
	TiC	51.6	6.44	6.38	85	254	243 to 273
	CbC	40.3	8.19	8.18	83	205	194 to 220
	VC	49.3	7.00	6.75	83½	183	175 to 194
	ZrC	43.8	7.25	7.51	83	113	90 to 125
10	WC	6.0	14.89	14.90	91⅛	241	221 to 266
	TaC	6.37	13.74	13.96	88¾	163	150 to 182
	TiC	16.8	5.55	5.30	91¾	162	126 to 178
	CbC	11.3	7.90	7.87	88¾	132	125 to 146
	VC	15.6	6.18	5.71	87	83	76 to 89
	ZrC	12.9	6.70	6.92	—	37	31 to 42

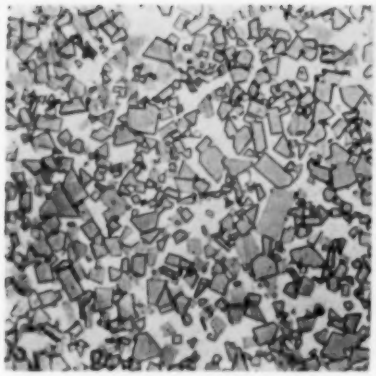

Fig. 1—Micrograph of 75 pct WC-25 pct Co alloy. X1500. Reduced approximately 30 pct for reproduction.

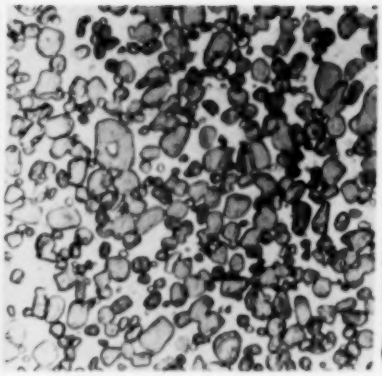

Fig. 2—Micrograph of 48.4 pct TiC-51.6 pct Co alloy. X1500. Reduced approximately 30 pct for reproduction.

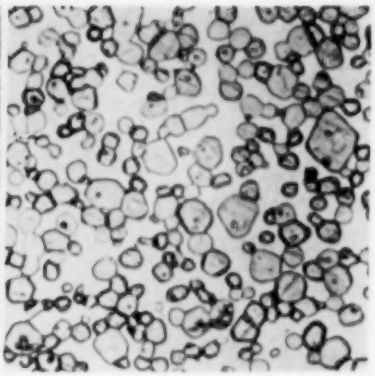

Fig. 3—Micrograph of 73.5 pct TaC-26.5 pct Co alloy. X1500. Reduced approximately 30 pct for reproduction.

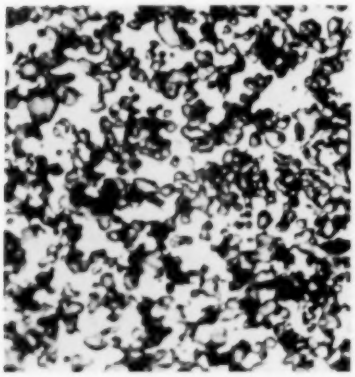

Fig. 4—Micrograph of 59.7 pct CbC-40.3 pct Co alloy. X1500. Reduced approximately 30 pct for reproduction.

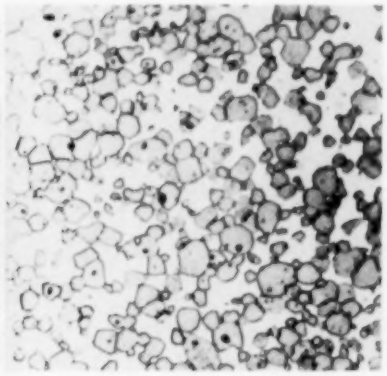

Fig. 5—Micrograph of 50.7 pct VC-49.3 pct Co alloy. X1500. Reduced approximately 30 pct for reproduction.

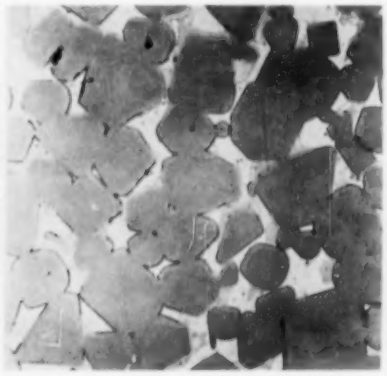

Fig. 6—Micrograph of 56.2 pct ZrC-43.8 pct Co alloy. X1500. Reduced approximately 30 pct for reproduction.

attained in all cases, except with ZrC. The latter carbide showed appreciable porosity, and it is not believed that the greatest strength was reached in the low binder alloy. The microstructure of ZrC and cobalt reveals an unidentified light gray constituent around the carbide grains. Similar observations on the difficulty of obtaining good properties and on the presence of another phase were made by Kieffer.[2]

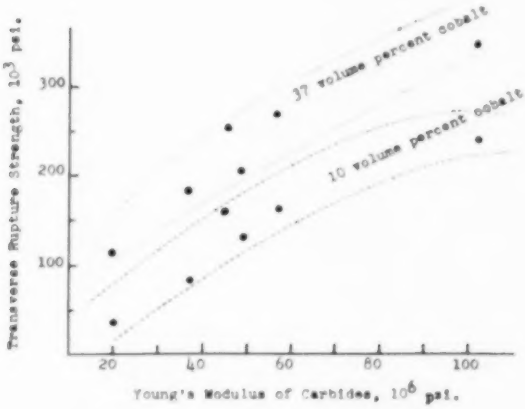

Fig. 7—Relation of strength and elastic modulus.

In an effort to relate the different strengths of the carbide-binder systems to a fundamental property of the carbides, the transverse rupture strengths were plotted against the elastic moduli of the carbides used, Fig. 7. The elastic moduli are literature values,[3] Table III. There seems to be a fair relation since, for systems with different carbides but similar grain sizes and binder contents, the strength increases with the elastic modulus of the carbides.

Table III. Young's Modulus of Elasticity of Carbides[3]

Carbide	Young's Modulus, Psi
WC	102 x10⁶
TaC	56.8x10⁶
TiC	45.8x10⁶
CbC	49.3x10⁶
VC	37.0x10⁶
ZrC	19.9x10⁶

Acknowledgments

This work was carried out at the Research Laboratory of Firth-Sterling, Inc., with the invaluable assistance of P. Bardzil. Permission to publish these results is gratefully acknowledged.

References

[1] Recommended Practice for Evaluating Cemented Carbides for Apparent Porosity. ASTM Standards ASTM-B276-54, 1955, Part 2, Non-Ferrous Metals, p. 771.

[2] R. Kieffer: Suitability of Zirconium Carbide and Thorium Carbide Additives to Cemented Carbides. *Metall*, 1950, vol. 4, p. 132.

Action of Vibration on Solidifying Aluminum Alloys

Acoustic energy is introduced into small melts of solidifying aluminum alloys using a metal probe vibrating at 8 kc per sec. Several changes caused by this treatment are observed in the solidified ingots. These include size reduction of intermetallic crystals, a decreased gravity segregation of these crystals, grain refinement, and porosity reduction. No large increases of tensile strength are observed. The power radiated into the melt is estimated by a calorimetric method. It is shown that a cavitation mechanism is in qualitative agreement with the observations.

by P. D. Southgate

VIBRATION, both ultrasonic and sonic, can affect the course of a variety of metallurgical processes. Reports of work on this subject have appeared at intervals over the last twenty years and a thorough review has been made by Hiedemann,[1] who gives a full list of references. It has been established that both refinement of structure and outgassing of the melt can be produced in most metals with sufficiently intense vibration. Many of the experiments in this field have been carried out using alloys of direct commercial interest in production type casting equipment. Here a different approach is adopted, and simple binary alloys which exhibit different types of structure are used to facilitate examination of the effects produced under well-controlled conditions. Results from this kind of experiment should enable the basis of larger scale experiments with similar types of materials to be better substantiated. The alloys selected for this work are: 1) aluminum of 99.2 pct purity, the principal impurity being iron, near 0.4 pct; 2) Al-1.8 pct Fe, which is near eutectic composition; 3) Al-4 pct Fe—the second phase, of composition $FeAl_3$, forms distinct acicular crystals; and 4) Al-12 pct Si—although this is of eutectic composition, the silicon normally appears in the form of large plates.

Experimental Method

There are three practicable methods by which acoustic vibration can be transferred to liquid metals: *a)* vibration of the whole of the container; *b)* electromagnetic induction; and *c)* insertion of a vibrating probe into the liquid. Method c is chosen here, and a frequency of 8 kc per sec is used. The end of the probe is electrically heated so that the metal near it will be the last to solidify. This ensures that vibration is transmitted directly to the liquid metal without passing through any solidifying and pasty intermediate region, which would attenuate acoustic waves severely. In addition, the heating prevents solid metal adhering to the probe, with consequent detuning.

The transducer assembly is shown in Fig. 1. A stack of Permendur laminations 30 cm long acts as a half-wave vibrator and a winding along its length carries polarizing and energizing currents. It is joined by a half-wave coupling bar to a mild steel exponential horn, which tapers from 3.8 to 1.1 cm diam. A stainless steel stub 3 cm in length is welded on the free end. The assembly is supported by a plate located at the node of the coupling bar. Acoustic radiation losses are minimized by allowing the free end of the transducer to protrude above the surface of the cooling water. The exponential horn serves the function of matching the acoustic output impedance of the transducer to the radiation resistance of the probe into the melt. Electrical drive is provided by a 1 kw generator.

Measurements of probe vibration amplitude during melt treatment are obtained from a gramophone pick-up with the needle attached to the wide end of the horn. This device is calibrated with a microscope before use.

Liquid aluminum is very actively erosive and solution of materials with which the molten metal comes into contact causes difficulties. Erosion of the probes in particular can be severe since it is greatly accelerated by the vibration. Tests of various acous-

P. D. SOUTHGATE is associated with Mullard Research Laboratories, Surrey, England.

TP 4435E. Manuscript, Apr. 2, 1956. New Orleans Meeting, February 1957.

tically suitable materials show that stainless steel is only slightly attacked, however.

After preliminary experiments, in which the liquid aluminum was cast into plumbago crucibles, an insulated mold apparatus was constructed. The metal is poured in this from the bottom of a gas fired furnace through a stream divider into two horizontal molds 30 cm long and approximately 6 cm sq. These are constructed of alumina-coated insulating brick, and each has a probe inserted at one end, one *live*, the other a dummy. The opposite end of each mold is water-cooled. The metal thus solidifies from this end, solidification times varying from 2 min (at a distance of 3 cm) to 20 min (at the probe). Short metal pegs on the cooling plate prevent separation of the solidifying aluminum and consequent change in the rate of heat abstraction. A thermocouple is located 13 cm from the cooling end.

The advantage of this form of apparatus is that the effects of gravity segregation can be clearly separated from those of varying cooling rate, since the two effects occur in perpendicular directions. A large variation of solidification time can be observed in a single ingot, and the close similarity of treatment of the pair of ingots ensures a good control sample. The insulating properties of the mold walls result in the solidification face being almost plane, thus eliminating shrinkage stresses or piping.

The Al-Fe alloys are preheated to 850°C and stirred to prevent the intermetallic crystals sinking and failing to dissolve. The temperature is allowed to fall to 750°C before pouring. Preheating of the Al-Si is around 850°C, but is varied from sample to sample. No protective flux is used, so in the Al-Si alloys gas solution is marked. The molds are preheated to redness before pouring, and the probes are maintained above the melting point of the metal by their heating coils until they are removed. Cooling curves are recorded with galvanometer-amplifier instruments which give a continuous record, enabling relatively rapid fluctuations of temperature to be followed, such as supercooling of the melt.

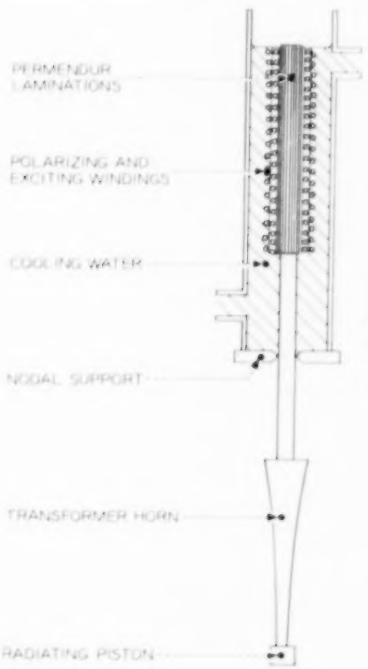

Fig. 1—Diagram of transducer assembly. When operating, the radiating piston dips below the melt surface.

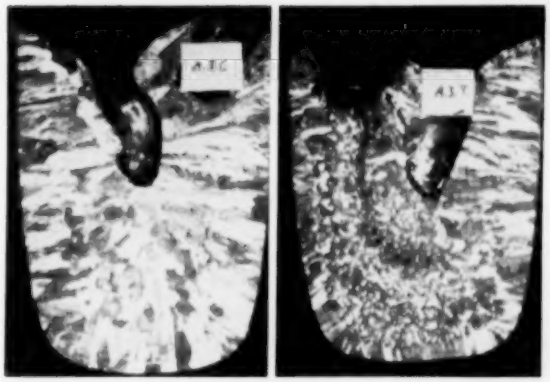

Fig. 2—Sections of crucible cast commercial aluminum ingots with etched surfaces. The probe position is in a top corner of each ingot. LEFT: control. RIGHT: Treated. Probe vibration amplitude, 25μ. The vibration has produced considerable grain refinement over half the ingot. X1/2. Reduced approximately 30 pct for reproduction.

During the commercial aluminum and Al-Fe runs, the transducer vibrates continuously during the entire solidification time. With the Al-Si the period of treatment is varied.

After casting, the ingots are sectioned longitudinally. One face is machined and etched for macroscopic examination. Five tensile test pieces 4 cm in length are taken from fixed horizontal positions along the center section, and tested in a Hounsfield tensometer. Spectrographic analysis is carried out on one of the broken halves, and the other half is mounted and polished for microexamination.

Results

Commercial Aluminum and Al-1.8 Pct Fe—Experiments with commercial aluminum have been carried out both in plumbago crucibles and in the horizontal mold. In the crucible experiments grain refinement is observed over most of the casting, see Fig. 2; whereas in the horizontal molds refinement is produced only near the probe. Columnar growth from the chilled face is unaffected by the vibration. It is evident that in the horizontal mold the small grain size is not due to impurities dissolved from the probe, for the small amount of metal which solidifies after probe removal has the coarse-grained structure of the control.

Similar results to the above are obtained with Al-1.8 pct Fe. A supercooling of about 1.5°C is recorded for both treated and untreated samples. The probe amplitude is about 25 μ in all these experiments.

Al-4 Pct Fe Alloy—Five runs were carried out with the Al-4 pct Fe alloy. During normal solidification gravity segregation of intermetallic crystals occurs. Vibration can eliminate this completely, with an accompanying reduction in crystal length of about five times. Table I lists the treatments of the different ingots. Comparison of the figures in columns 6 and 9 shows a fairly close association between crystal size reduction and gravity segregation reduction. It seems a reasonable hypothesis that the smaller segregation is a consequence of the reduced size crystals in the treated ingot.

Sections from the ingots of run No. 19 are shown in Fig. 3. Crystal size reduction is most marked in

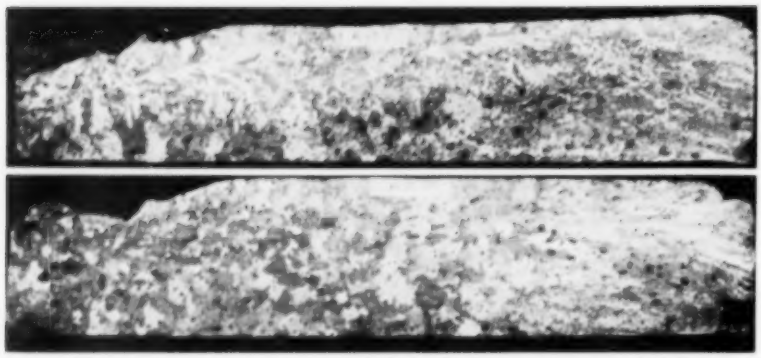

Fig. 3—Sections of ingots of Al-4 pct Fe alloy cast in a horizontal insulated mold, with etched surfaces. The right-hand end of each ingot is chilled, and the probe position is at the left-hand end. TOP: Control, showing gravity segregation of intermetallic needles. BOTTOM: Treated. Probe vibration amplitude, 16μ. Intermetallic crystal size and gravity segregation have been greatly reduced. X½. Reduced approximately 25 pct for reproduction.

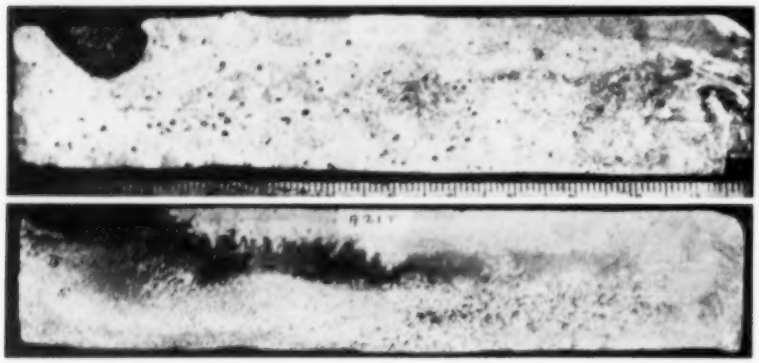

Fig. 4—Sections of ingots of Al-12 pct Si alloy cast in a horizontal insulated mold, with etched surfaces. The right-hand end of each ingot is chilled, and the probe position is at the left-hand end. TOP: Control, showing high porosity. BOTTOM: Treated. Probe vibration amplitude, 30μ. The pores have been greatly reduced in size. X½. Reduced approximately 25 pct for reproduction.

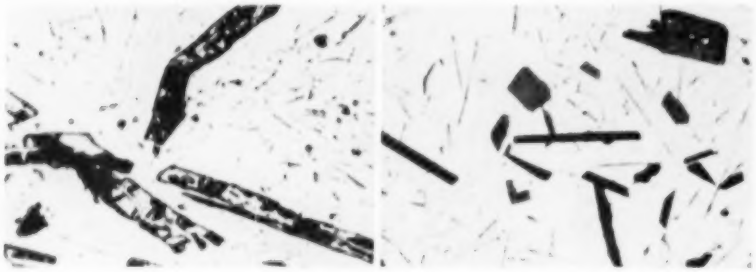

Fig. 5—Micrographs from the probe end of the Al-4 pct Fe ingots of Fig. 3. The iron content of both these samples is near 4 pct. LEFT: Control. RIGHT: Treated. X75. Reduced approximately 25 pct for reproduction.

this run. In the control ingot the gravity segregation of the crystals increases with distance from the chilled end and length of solidification time. There is no such effect in the treated ingot, showing that continuous vibration at the power level used here is effective over the whole range of solidification rates. Vibration does not seem to alter the grain size of the matrix of aluminum. Two typical micro-sections, taken from immediately below the probes of run No. 19, are shown in Fig. 5. The iron content of these particular samples is almost identical.

In many regions of the treated sample the intermetallic crystals have a fractured polygonal appearance. Adjacent crystals throughout the control specimens tend to form star-shaped patterns, but in the treated specimens these patterns are never seen in regions where size reduction has occurred.

The tensile strength of Al-Fe alloys is dependent on composition. This dependence causes the major difference in strength between similarly located samples in the treated and control ingots. Taking this factor into account, there is no systematic difference in strength between treated and control samples having the same composition, despite the difference in crystal size.

Al-12 Pct Si Alloy—Four successful runs have been carried out using the Al-12 pct Si alloy, with a probe amplitude of 30 μ. In each case a reduction of porosity is observed, but with considerable variation between similarly treated samples. In the castings shown in Fig. 4 the relative pore volume is reduced by more than 20 times, while in a similar run the reduction factor is only about 1.5. The cause of this variation cannot be determined from the small number of runs carried out. In one run the transducer was not switched on until after solidification had commenced, and the treated ingot still shows reduction in porosity.

Fig. 4 also shows that treatment accentuates a dark band lying along the length of the ingot near the center. Microscopic examination reveals a much finer structure in the dark band than in the light portion. It is suggested that eutectic formation has been promoted, but more work is needed to elucidate this effect.

The average tensile strength of the treated Al-Si alloys is about 10 pct greater than the control.

Acoustic Power Level

A measure of the vibration power transferred to the melt would be very valuable, but unfortunately is difficult to obtain. Technical difficulties preclude

the use of refractory pressure-sensitive devices in the melt. Changes of transducer electrical input impedance when the probe is dipped in the melt are small, and are influenced by other factors, such as probe heating, so these cannot be used to measure power transfer.

Temperature rise measurements on the metal in an electrically heated and insulated crucible of approximately the same volume as the treatment mold show that a probe vibrating with an amplitude of 34 μ radiates 20 w into the melt. This power measurement gives a guide to the vibrating pressure amplitude during treatment. Calculations on the basis of the radiation resistance into an infinite medium give a theoretical dissipation of the order of 18 w.

Discussion

Four definite effects have been demonstrated in these experiments: *a)* the reduction of the grain size in commercial aluminum cast into cold crucibles, *b)* the reduction of intermetallic crystal size in hypereutectic Al-Fe alloys, *c)* decrease of gravity segregation in these alloys, and *d)* degassing of Al-12 pct Si alloys. It also seems likely that vibration alters the structure of Al-Si alloys in some regions. These results agree in most respects with those obtained by other workers using frequencies of the order of 10 kc per sec. At widely differing frequencies, different effects might be expected. This is indeed indicated by the results of Rostoker and Berger.[2]

In Al-Fe alloys the effects seem to occur at relatively small levels of acoustic power, being considerable even in run No. 18, where the acoustic input was calculated to be only of the order of 1 w. The distribution and size of intermetallic crystals do not change throughout the length of the treated ingot, indicating that these parameters are not very dependent on the duration of treatment over the range used.

Grain refinement appears to require a higher power density than that needed for intermetallic crystal size reduction. In the longitudinal mold apparatus, grain refinement only occurs near the probe, where the acoustic power is high. In the crucible castings more metal is refined but the total volume is less, and hence the power density is greater. There is no definite indication of the threshold of power for outgassing the Al-Si alloys.

Size reduction of both grains and intermetallic crystals can occur in two ways: *a)* by the breakup of crystals or dendrites which have already formed, or *b)* by an increase in the rate of nucleation. These two mechanisms are related, since small fragments of a large crystal form nuclei for new crystals. It seems that both these processes have taken place in these experiments. The reduction of supercooling in the Al-12 pct Si shows that nucleation can be affected by vibration. In the Al-4 pct Fe, on the other hand, the fractured appearance of the crystals would not be expected to be a consequence of increased nucleation rate.

It has been suggested[4, 5] that cavitation is responsible for outgassing of melts by vibration, and also[6] for grain refinement. Cavitation voids form on the negative pressure part of the vibration cycle, and can grow into gas bubbles. If this does not occur, they usually collapse on the positive pressure part of the cycle, generating large local pressures.[7] It is reasonable to suppose that these forces will fracture solid particles in the immediate vicinity of the void. Nucleation of cavitation voids will occur on particles suspended in the melt if the negative pressure is sufficient to overcome both the atmospheric pressure and the adhesive force between the liquid and the nucleus.

A different mechanism of crystal breakup was proposed by Schmid and Roll,[8] which involves the viscous force acting on the crystals. These authors found good numerical agreement when their theory was applied to Wood's metal. It is doubtful whether the mechanism applies here, though, since it predicts as marked a breakup of hypoeutectic alloy dendrites as of hypereutectic intermetallic crystals.

Table I. Effect of Vibration on Al-4 Pct Fe Alloys

Run No.	Probe Amplitude, μ	Casting Temperature, °C	Crystal Lengths in Section, Mm			Gravity Segregation†		
			Control	Treated	Size Reduction*	Control	Treated	Dispersion*
13	30	765	3.2	0.8	4	0.8	0.2	4
14	38	770	3.0	0.6	5	—	—	—
18	7	780	0.8	0.3	2.7	0.9	0.3	3
19	16	775	5	0.5	10	1.5	0.2	7.5
20	16	763	2.4	0.4	6	1.1	0.4	2.8

* Ratio of previous two columns.

† Spectrographic analyses are made at upper, center, and lower parts of a vertical line through the ingot center. This column gives the rms deviation from the mean of the percentage of iron content of these three samples.

It seems that in the Al-4 pct Fe alloy the intermetallic crystals do not nucleate solidification of the remaining melt, judging by its independently coarse-grained structure. Adhesion between the melt and the crystals must therefore be low. Hence, they should form nuclei for cavitation bubbles. Dendrites of hypoeutectic alloys, on the other hand, adhere well to the melt, since solidification is a continuous process. Here, then, the acoustic power for breakup would be expected to be larger, which is in fact observed. Calculated pressure amplitudes support this argument, since a radiated power of the order of 1 w (run No. 18) corresponds to a pressure amplitude of about 1 atm. This is sufficient to produce cavitation on nuclei with low adhesion to the melt, but not on those having high adhesion.

Thus, these observations of crystal breakup are consistent with the cavitation hypothesis. Further experiments are needed, however, to substantiate this hypothesis and to determine the thresholds of power and time of treatment.

Acknowledgments

This study was suggested and supervised by K. Hoselitz, to whom the author is grateful for considerable help in the preparation of this paper. Many of the metallurgical examinations were carried out by E. J. Williams and A. F. Smith, who assisted with the performance of the experiments.

References

[1] E. A. Hiedemann: *Journal* Acoustical Soc. of America, 1954, vol. 26, p. 831.

[2] W. Rostoker and M. J. Berger: *Foundry*, 1953, vol. 81, p. 100.

[3] K. F. Alder: *The Australasian Engineer*, Dec. 8, 1952, p. 53.

[4] H. J. Seemann and H. Staats: *Metall*, 1955, vol. 9, p. 868.

[5] M. Kornfeld and L. Suvorov: *Journal of Applied Physics*, 1944, vol. 15, p. 495.

[6] G. Schmid and A. Roll: *Ztsch. für Electrochemie*, 1939, vol. 45, p. 769.

Discussion of this paper sent (2 copies) to AIME by June 1, 1957 will appear in AIME *Transactions* Vol. 209, 1957, and in JOURNAL OF METALS, October 1957.

Discussion — Institute of Metals Division*

Chemical Activity of Polycrystalline Cu-Au—Experiments Relating to the Mechanism of Stress-Corrosion Cracking of Homogeneous Solid Solutions 518
Robert Bakish and William D. Robertson

Deformation and Recrystallization of Silicon Iron 519
George Wiener and Robert Corcoran

Effect of the Annealing Temperature on the Formation of the Cube Texture 519
Alfonso Merlini

Intermediate Phase in the Uranium-Zirconium System 521
A. N. Holden and W. E. Seymour

Internal Friction in Zirconium 521
W. J. Bratina and W. C. Winegard

Phase Transformations in Titanium-Rich Alloys of Nickel and Titanium 524
D. H. Polonis and J. Gordon Parr

Primary Recrystallization Textures in Cold Rolled Si-Fe Crystals 526
C. G. Dunn and P. K. Koh

Recovery of Cold Worked High Purity Al-Mg Alloys 527
E. C. W. Perryman

Recrystallization and Grain Growth in Iodide Zirconium 528
R. M. Treco

Relative Interfacial Energies of Symmetrical Tilt Grain Boundaries in Silver 528
K. T. Aust

Study of the Fe-Si Order-Disorder Transformation 529
Frank W. Glaser and W. Ivanick

Temperature Dependence of Recovery Phenomena in a Cold Rolled Aluminum Single Crystal 530
A. H. Lutts and Paul A. Beck

X-Ray Diffraction Determination of the Coefficients of Expansion of Alpha Uranium 532
J. R. Bridge, C. M. Schwartz, and D. A. Vaughan

*TP 4334E

Chemical Activity of Polycrystalline Cu-Au—Experiments Relating to the Mechanism of Stress-Corrosion Cracking of Homogeneous Solid Solutions

by Robert Bakish and William D. Robertson

JOURNAL OF METALS, October 1956; *AIME Trans.*, 1956, vol. 206, pp. 1277-1282.

David J. Mack (*University of Wisconsin, Madison, Wisc.*)—Have the authors considered that the effects reported in their paper are readily explainable on the basis of equilibrium grain boundary segregation rather than ordering? It seems to the writer that all of their experiments and observations correlate well with known behavior associated with equilibrium grain boundary segregation.

Although at first glance one would tend to dismiss such a possibility because of the similarity of the gold and copper atoms, their sizes differ by 12.8 pct which is in the range where segregation at grain boundaries would be expected. Then, too, the electrochemical differences between the copper, the Cu_3Au, and the gold strongly suggest that a segregation mechanism is involved in the corrosion of the Cu-Au alloys.

R. Bakish and **W. D. Robertson** (*authors' reply*)—The authors would like to thank Dr. Mack for his consideration of the problem of grain boundary segregation as an explanation of the observed phenomena. We had considered the problem in the following terms:

Assuming a pure binary Cu-Au alloy and an ideal solid solution, the surface excess, $\Gamma_2 = N_2^s - N_2$, of the second component (gold) may be expressed in the following way[20]

$$\Gamma_2 = N_2 \cdot \frac{1 - \exp(-\delta a/kT)}{N_1 \exp(-\delta a/kT) + N_2}$$

where δ is the difference in surface tension of copper and gold, $\gamma_1 - \gamma_2$, and a is the surface area per atom. In the present case, δ is positive which implies that the component in excess at the boundary is gold. Since the only chemically active component in ferric chloride is copper, it does not appear that the segregation of gold is likely to increase the boundary activity.

A small concentration of a third component could profoundly affect the situation. Analysis indicated only spectrographic traces of impurities, all of which are soluble in both copper and gold. Quenching experiments, reported in the paper, also tended to eliminate significant effects attributable to a third component.

[20] R. Speiser and J. W. Spretnak: *Stress Corrosion Cracking and Embrittlement*, 1956, p. 97. New York, John Wiley & Sons Inc.

Deformation and Recrystallization of Silicon Iron

by George Wiener and Robert Corcoran

JOURNAL OF METALS, August 1956, *AIME Trans.*, 1956, vol. 206, pp. 901-906.

C. G. Dunn *(General Electric Co., Schenectady)*—The authors have presented an interesting paper covering such points as hardness, microstructure, composition, and textures. For the most part, the discusser agrees with their interpretations of the data including the circumstance for the retention of portions of the cold rolled texture. However, my preference in terminology for the *low angle recrystallization* of grains of the (001)[110] orientation would be their alternate term *polygonization* or *unrecrystallized areas*. Also I would like to draw attention to the recrystallization behavior of the (001)[110] orientation in a bicrystal having, after 70 pct cold rolling, this orientation and the (111)[112] orientation which was reported two years ago.[10] The two crystals were in the form of two layers, one above the other. On annealing at 980°C for various periods of time, the crystal in the (111)[112] orientation recrystallized rapidly to a fine grained structure while the crystal in the (001)[110] orientation recrystallized slowly to a coarse grained structure. Annealing at lower temperatures would, I feel certain, lead to the retention of the (001)[110] orientation and recrystallization with reorientation away from the (111)[112] orientation, which is what the authors found in their polycrystalline samples.

In the discussion of Table I the authors pointed out that *unrecrystallized* areas had softened by about 90 pct. This is the same phenomenon reported by Dunn and Daniels,[8] who obtained essentially 100 pct softening in 1 min at 800°C and considerable softening near 600°C. The discusser's sample was a single crystal in the (112)[$1\bar{1}0$] orientation, which had been cold rolled 20 pct. It was thought that polygonization or subgrain growth may have been involved. More recently Hibbard and Dunn[9] obtained evidence of polygonization near 700°C in weakly bent single crystals, but no attempt has been made to correlate such microstructure data with hardness.

The authors refer to work[11] on recrystallization involving single crystals in the (111)[112] cold rolled orientation by saying that the textures after recrystallization were best described as (110)[001]. I wish to emphasize that the texture did have (110)[001] as a strong component, but that there were also a number of specific weak components for primary recrystallization at 980°C. If primary recrystallization occurred at about 550°C, however, the (110)[001] component was considerably weaker, and there also were two rather strong (120)[001] type components. Thus there was a pronounced effect of temperature on recrystallization.

I should like to amplify the authors' reference to grain growth in my samples playing a role after primary recrystallization by summarizing some of the results obtained. Magnetic torque measurements on disk specimens provided part of the important data. Annealing at 980°C after recrystallizing at 550°C lead to normal grain growth and some increase in the (110)[001] component. Direct recrystallization at 980°C, however, produced a stronger (110)[001] component. Further annealing at 980°C, according to torque data, produced about a 5 pct increase in the (110)[001] component after which it completely vanished due to secondary recrystallization. The increase, which occurred prior to secondary recrystallization, could only be explained in terms of small grains in deviating orientation being removed by growth of (110)[001] grains. However, such growth could not remove grains in deviating orientation when they were above a critical size. The larger grains of this kind grew and finally produced secondary recrystallization.

[8] C. G. Dunn and F. W. Daniels: *AIME Trans.*, 1954, vol. 200, p. 1313; JOURNAL OF METALS, November 1954.
[9] W. R. Hibbard, Jr. and C. G. Dunn: *Acta Metallurgica*, 1956, vol. 4, p. 306.
[10] C. G. Dunn: *AIME Trans.*, 1954, vol. 200, p. 549; JOURNAL OF METALS, May 1954.

Effect of the Annealing Temperature on the Formation of the Cube Texture

by Alfonso Merlini

JOURNAL OF METALS, August, 1956; *AIME Trans.*, 1956, vol. 206, pp. 967-972.

C. G. Dunn *(General Electric Company, Schenectady)*—The author has obtained important results concerning texture changes that occur following primary recrystallization; more data of this kind are needed, I believe, to clarify the mechanisms involved. My own work along these lines has been with Si-Fe. However, some time ago I pointed out the importance of growth processes in a paper partly concerned with the subject of the cube texture in copper.[20]

If we consider the effect of temperature on the primary recrystallization texture—and this is important in the two theories discussed by the author—it seems to me that the present results provide little information on this point. The data needed are the textures obtained after completion of primary recrystallization and not after subsequent grain growth. Two recent papers on Si-Fe treat this problem and also the problem of grain growth under rather ideal conditions.[8,21] The effect of annealing on textures could be followed with considerable accuracy. Since the results lead to different conclusions from those of the author, I would like to summarize some of this work on Si-Fe.

Two groups of samples from a single cold rolled crystal provided material for 1) quantitative pole figures, 2) transmission Laue patterns, 3) microstructures, and 4) texture data from magnetic torque tests. Annealing involved primary recrystallization either at 550° or at 980°C with annealing changes after primary recrystallization at the same temperature of 980°C. A comparison between the two groups showed the following: Primary recrystallization was nearly 100 pct complete after 64 hr at 550°C with a slightly larger grain size than the other which was complete in 1 min at 980°C. Noticeable growth in the former occurred upon annealing 1 min at the higher temperature of 980°C. At this point, pole figure data and magnetic torque data disclosed that direct 980°C annealing produced a much stronger (110)[001] component in the texture than did 550° + 980°C annealing. In fact, the latter had relatively strong (120)[001] components in addition to the (110)[001] component. Clearly, these data showed that the primary recrystallization textures were different and that temperature of annealing had a marked effect.

The effect of growth following primary recrystallization also disclosed the marked differences in structures and textures of the two groups. For example, continued annealing of the 550° + 980°C group produced only normal grain growth with increase in the (110)[001] component. However, the level of the (110)[001] com-

ponent remained far below the level of this component obtained during primary recrystallization at 980°C. On the other hand, continued annealing of the 980°C group produced secondary recrystallization and complete loss of the (110)[001] component. During the induction period of secondary recrystallization, the (110)[001] component increased by 5 pct (an increase that could be measured by the nondestructive and very sensitive magnetic torque method), proving that grains in deviating orientation had been present but were removed. Occurrence of secondary recrystallization proved, of course, that not all such grains were removed; the larger ones that belonged to specific weak components of the primary recrystallization texture produced similarly oriented components in the secondary recrystallization texture. Among them were the (120)[001] type components. These were also the orientations of the relatively strong (120)[001] components in the primary recrystallization texture of the low temperature group. Qualitatively, low and high temperature annealing produced very similar results for primary recrystallization; quantitatively, however, they were very different. Just as different, of course, was their behavior during grain growth after primary recrystallization. The results show that such factors as relative grain sizes and oriented nuclei have to be considered and that oriented growth alone cannot account for the results.

I should now like to compare these results on Si-Fe and the data of the author on copper, since the latter bear on the question of nuclei for secondary recrystallization. It will be noted that his choice of penultimate anneal and final percentage of reduction gave him, in addition to the cube texture component, large amounts of other components; he identifies the latter as four components similar to those of the deformation texture. These the author calls *A* components. With lower penultimate anneal and high reductions, the cube component would be expected to increase and the four *A* components therefore to decrease but without entirely disappearing. If this is so, then the author's data provide evidence in support of my earlier assumption that there are four components in the primary recrystallization texture providing nuclei for secondary recrystallization.[6] These four components, in other words, supply oriented nuclei for secondary recrystallization. Thus, contrary to Beck,[12] oriented nucleation in this case should provide four components and not 28 or more as he suggests.

In the author's experiment the four *A* components as well as the cube component are relatively strong. These may be compared with the mixture of (110)[001] and (120)[001] components for the case of Si-Fe annealed at low temperatures. Such mixtures undoubtedly favor normal grain growth on annealing. Whether the *A* components increase or decrease, I think, depends more on relative grain size than on mobility because the kinds of boundaries involved are the same for absorption as for growth. Thus, if most of the cube grains are small, annealing will enhance the *A* components. The author found the opposite, so it can be concluded that more of the *A* component grains were smaller. However, it is unlikely that all *A* component grains would be too small to survive. If large *A*-type grains survived, it is possible they could grow and remove the cube component, producing secondary recrystallization with *A*-type components. On the other hand, if normal grain growth should go quite far, it is unlikely that secondary recrystallization would occur. The Si-Fe sample recrystallized at low temperature and annealed for long periods of time at 980°C is, I think, an example of this kind.

Y. C. Liu *(New York University, New York)*—Kronbery and Wilson[14] observed that a 1 hr anneal at 400°C of a 98.5 pct reduced OFHC copper strip produced a heavily twinned cubically aligned structure and that no apparent change in orientation took place when it was annealed 1 hr at 850°C. This result is similar to that observed in a 96 pct reduced electrolytic tough-pitch copper strip annealed 5 min at 200°C.[11] Because of the apparent difference in recrystallization textures, the cube texture on one hand and the one observed by Dr. Merlini in his investigation on the other, I would like to ask, what are the factors which cause this difference and how should these factors be taken into consideration in the *oriented growth* hypothesis?

Dr. Merlini asserted that "on the basis of the oriented growth hypothesis the high temperature annealing texture is determined by the preferential grain growth at the expense of the fully annealed matrix." Am I right to deduce that if the second anneal on specimen 2 were made longer than 20 min at 825°C, the *A* component in Fig. 5 could disappear and would eventually exhibit a pole figure of *C* component entirely, the cube texture?

Alfonso Merlini *(author's reply)*—In answer to Dr. Liu, it should be pointed out that the relative amount of cube texture present is known to be affected by such variables as the penultimate grain size and the final rolling reduction. The explanation of these effects in terms of the theory of oriented growth has been given many years ago by Beck.[12] As stated in the paper, conditions in the present work were deliberately chosen to insure that the annealing texture retained components other than the cube texture. One of the pertinent variables is the thickness of the sheet during annealing. It is difficult to state with assurance whether, under the particular conditions selected, additional annealing at 825°C would or would not have sufficed to practically complete the transformation to the cube texture.

It is only fair that Dr. Dunn should be given credit for his early support of the view that the orientation dependence of boundary mobility is an important factor in the formation of recrystallization textures and, more specifically, for having expressed the view that the increase of the intensity and of the sharpness of the cube component in face-centered-cubic metals with increasing annealing temperature is a result of continued grain growth.

Unquestionably, Dr. Dunn's work[1,4] clearly established the great importance of various annealing treatments on the recrystallization texture and also on the coarsening behavior of Si-Fe. However, particularly in view of the variations in coarsening behavior, an alternative explanation of his results might be based on the effect of varying annealing treatments on the state of distribution of the dispersed second phase impurity particles always present in commercial Si-Fe. It is well known[20] that variations in heat treatment may have a great effect on the state of distribution of dispersed second-phase particles and thereby on the coarsening behavior. Consequently, in materials containing substantial amounts of impurity phases, these variations in the distribution of the dispersed particles also have an important effect on the annealing texture. Whether these variations can be adequately described in terms of oriented growth, or whether they actually do require in addition *oriented nuclei*, is difficult to decide at the present state of knowledge of these phenomena.

It has been known for a long time that the rolling texture of copper and of aluminum includes very considerable orientation spreads. The results of the present paper indicate that the *A* components of the recrystallization texture of copper, which are similar to the four deformation texture components but somewhat sharper, also include a rather considerable spread of orientations. If the grains corresponding to the orientations present in the recrystallization texture act as

oriented nuclei for coarsening, as Dunn suggests, it is difficult to see why the whole orientation spread of the recrystallization texture is not represented in the coarsening texture, unless there is in addition a selective principle due to oriented growth. The relatively narrow orientation range of the coarse grains found by Kronberg and Wilson[19] suggests that such a selective principle is actually effective. It is, furthermore, significant that Bowles and Boas[20] found eight groups of coarse grains growing in cube texture copper, including orientations quite different from those of the four *A* components of the low temperature recrystallization texture. In this case, the oriented nuclei proposed by Dunn apparently did not play a significant role. On the other hand, all the eight coarsening texture components did have the correct orientation relationship with regard to the cube texture for maximum boundary mobility. Thus, it seems that, in accordance with the results of the present paper with regard to the formation of the cube texture, oriented growth is by far the most universally effective factor in governing the formation of annealing textures.

[17] C. G. Dunn: *Cold Working of Metals*, 1949, p. 113. Cleveland, ASM.
[18] C. G. Dunn: *Acta Metallurgica*, 1953, vol. 1, p. 163.
[19] C. G. Dunn: *Acta Metallurgica*, 1954, vol. 2, p. 386.
[20] P. A. Beck, M. L. Holzworth, and P. R. Sperry: Effect of a Dispersed Phase on the Grain Growth in Al-Mn Alloys. *AIME Trans.*, 1949, vol. 185, p. 163; JOURNAL OF METALS, February 1949.
[21] J. S. Bowles and W. Boas: The Effect of Crystal Arrangement on "Secondary Recrystallization." *Journal*, Inst. of Metals, 1948, vol. 24, p. 501.

Intermediate Phase in the Uranium-Zirconium System

by A. N. Holden and W. E. Seymour

JOURNAL OF METALS, October 1956; *AIME Trans.*, 1956, vol. 206, pp. 1312-1316.

J. M. Silcock *(Fulmer Research Institute, Stoke Poges, England)*—The authors have shown the existence of an intermediate phase of approximate composition UZr_2 in the UZr system. It has also been shown that this phase δ forms with a large body-centered-cubic cell of side three times that of the simple body-centered-cubic high temperature phase, the sides of the cubic cells being parallel.[1] The similarity with ω phase formation[2] in titanium alloys is immediately apparent and it is suggested that the large cubic cell is more probably a result of four hexagonal cells oriented with [0001] δ || [111] γ and (1120) δ || (110) γ. A hexagonal cell would explain the domain formation and the optical activity.

The indices for a hexagonal cell of parameters $a = 5.03$A and $c = 3.08$A are given in Table II. A similar phase forms in the U-Ti system.[3] This is definitely a stable phase and its composition is U.Ti. The intensities for the UZr_2 compound do not agree with the supposition that uranium atoms are in the position (000) occupied by titanium in U_2Ti and zirconium in (1/3 2/3 1/2) (2/3 1/3 1/2). However, fairly promising results (especially if a little γ remains) are obtained by supposing zirconium in (000) sites and that the (1/3 2/3 1/2) and (2/3 1/3 1/2) sites are shared between uranium and zirconium. This is however an unusual structure and requires further investigation, but it is interesting to note that U_2Ti, $Ti_{1-n}X_n$ (where X_n is a very small quantity of a transition element), and now UZr_2 all probably form a hexagonal cell of similar type. It appears that all simple body-centered-cubic solid solutions containing large quantities of titanium or zirconium tend to form this structure, but it is only rarely stable.

Table II. Intensities of Reflections Compared with Values Calculated for a Hexagonal Structure*

d, A†	Observed Intensity†	F^2_{hkl} for Zr.U	Indices for Hexagonal δ,* *hkl*
4.28	W	3	100
3.05	M	12	001
2.49	½VS	384	101 + 110
2.16	W	3	200
1.94	M	72	111
1.77	½S	120	201
1.64	W+	6	120
1.54	M	44	002
1.45	½S+	378	102 + 121 + 300
1.31	S	270	112 + 301
1.25	½M	138	202 + 220
1.20	VW	6	130
1.16	M	72	221
1.12	½M+	252	122 + 131
1.06	M	264	302
1.02	½M	132	003 + 401
1.00	W+	126	103 + 230
0.973	M	264	222
0.949	½S	788	113 + 132 + 231 + 410
0.929	W	120	203
0.907	M+	144	141
		8	402
? 0.881	½W+	3	500
0.838	½S	346	232 + 501 + 303 + 330
0.809	S+	600	331 + 142
0.795	½M	240	241
0.783	W	240	133

* $a = 5.03$A; $c = 3.08$A; zirconium in 000; zirconium and uranium randomly in (1/3 2/3 1/2), (2/3 1/3 1/2).
† *d* spacings and intensities observed by Holden and Seymour.

[1] M. H. Mueller: *Acta Crystallographica*, 1955, vol. 8, p. 849.
[2] J. M. Silcock, M. H. Davies, and H. K. Hardy: *Symposium on the Mechanism of Transformations in Metals*, 1955, p. 93. London, Inst. of Metals.
[3] A. G. Knapton: *Acta Crystallographica*, 1954, vol. 7, p. 457.

Internal Friction in Zirconium

by W. J. Bratina and W. C. Winegard

JOURNAL OF METALS, February 1956; *AIME Trans.*, 1956, vol. 206, pp. 186-189.

F. Forscher *(Westinghouse Electric Corp., Pittsburgh)*—The interesting results reported in the paper by Bratina and Winegard are in good agreement with some experiments performed by H. W. Cooper and W. J. Babyak in the Westinghouse laboratories during the summer of 1954. It is particularly gratifying to note the agreement between specimen II-6 (Fig. 6) and curve *a* in Fig. 4 of this paper. Both series of experiments are based on the amplitude independent free decay of a torsional pendulum with a frequency of about 1 cycle per sec; the quantity Q^{-1} is identical in definition to tan δ, i.e., the logarithmic decrement divided by π.

The main difference between these two investigations appears to be the effect of oxygen and its interpretation. It is known that oxygen, picked up from the

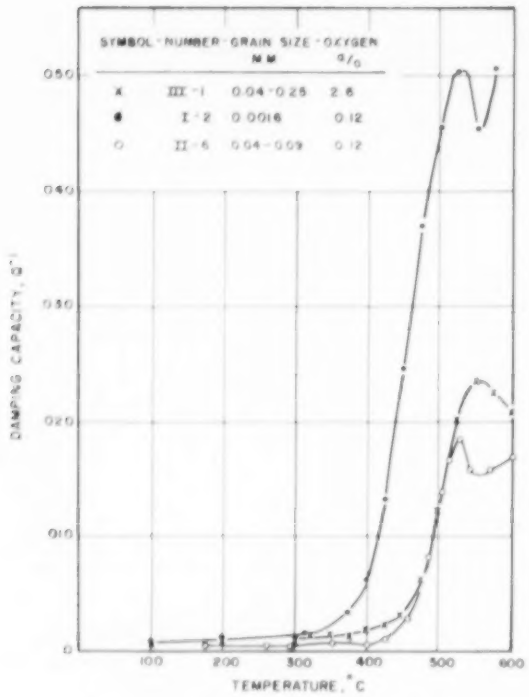

Fig. 6—Oxygenation of Forscher's specimen III-1.

environment, remains at or near the surface of α zirconium so that in the case of torsion a considerable strengthening effect must be expected.

It is not clear from the description in the paper whether the *oxygenation in situ* took place before, during, or after curve *a* (Fig. 4) was produced. Assuming that oxygen contamination took place after curve *a* but before curve *b* was produced, the lower values of the latter curve may be explained on the basis of a harder oxygen-rich surface layer which is the main contributor to tan δ in torsional damping.

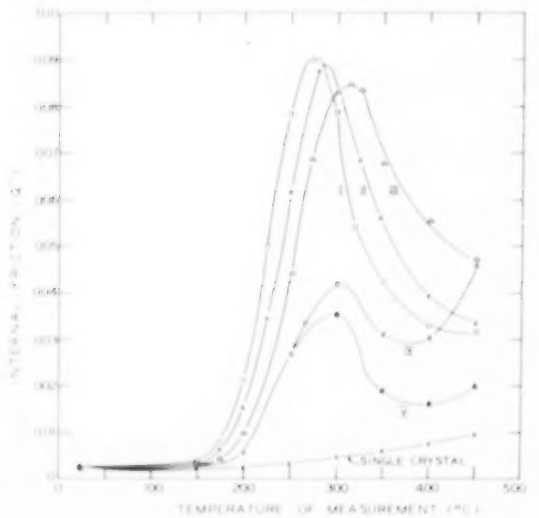

Fig. 7—Curves reproduced from Ke.[11] I, average grain diameter 0.02 cm; II, average grain diameter 0.04 cm; III, average grain diameter 0.07 cm, IV and V, average grain diameter larger than the diameter of the wire, 0.084 cm.

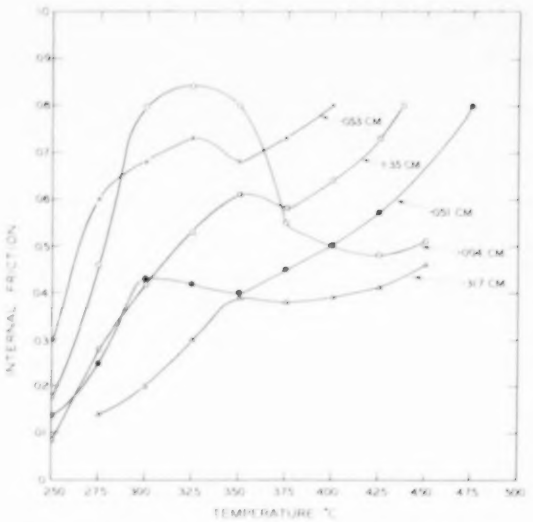

Fig. 8—Absence of correlation between grain size and internal friction.

The oxygenation of the discusser's specimen III-1 (Fig. 6) was performed in a heat treatment apparatus by the introduction of a known amount of oxygen. The oxygen content was verified by weighing the specimens, by chemical analysis, and resistivity and hardness measurements.

Homogenization with respect to oxygen in specimen III-1 was not achieved even after 7 hr at 800°C. Microhardness readings across the 0.060 in. diam specimen showed pronounced case hardening. Furthermore, resistivity readings differed greatly from the value of 57.5$_{\mu}$ ohm-cm (ref. 3) predicted on the basis of the oxygen content (2.6 atomic pct).

In summary, it appears to be difficult to achieve homogeneity of oxygen in α zirconium either by the method of the author or by the method of the writer of this discussion. Consequently any evaluation of the effect of oxygen on the damping capacity must be postponed until homogeneity can be achieved.

Table I. Description of Damping Specimens*

Designation	Heat Treatment	Oxygen Content, Atomic Pct	Oxygen Content, Ppm	Resistivity at 0°C, μ Ohm-Cm	Grain Size, Mm
II-6	800°C, 7 hr, in vacuum, furnace cooled	0.12	200	40.5	0.04 to 0.09
I-2	600°C, ¼ hr, in vacuum, furnace cooled	0.12	200	39.8	0.0016
III-1	Oxygenated and annealed at 800°C, 7 hr, furnace cooled	0.6	4670	44.0	0.04 to 0.25

* 99 pct reduced by swaging to 0.060 in. diam.

H. H. Bleakney *(Dept. of Mines and Technical Surveys, Ottawa, Ont., Canada)*—The experimental evidence of the viscous behavior of grain boundaries in metals, presented by Kê,[11] included internal friction and torsion modulus experiments as part of the argument. Since then, similar phenomena in other metals have been reported by other authors, and in nearly every case the results obtained have been attributed to viscous flow of atoms at the grain boundaries.

The writer of this discussion has consistently opposed the concept of stress-relaxation across grain

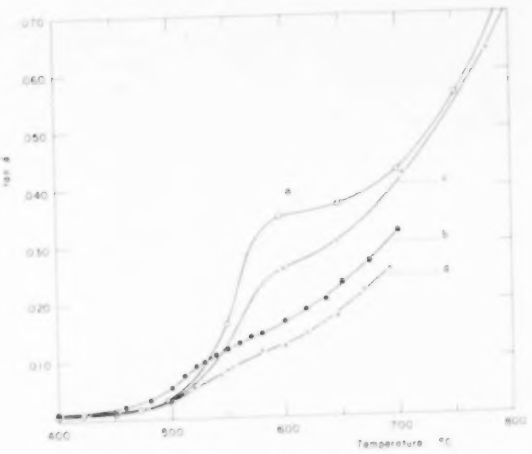

Fig. 9—Effect of oxygen distribution in the specimen on the grain boundary relaxation maximum is shown. Curves *a* and *c* represent the cases of more uniform distribution of solute, and *b* and *d* the cases of the preferential segregation at the grain boundaries.

boundaries by viscous flow and has contributed some evidence to refute it." He is, therefore, pleased that Bratina and Winegard, by omitting any reference to Kê, have tacitly repudiated his explanations. Under these circumstances, however, their use of the expression "relaxation across grain boundaries," may require some clarification. Their explanation for the internal-friction difference between coarse and fine grained zirconium, shown in Fig. 2, also appears to owe something to Kê. It is this point which the writer particularly wishes to discuss.

The features of internal friction which Kê presents as evidence of viscous grain boundaries are shown in Fig. 7, reproduced from his paper entitled *Stress Relaxation Across Grain Boundaries in Metals*. His argument is too involved to reproduce here, but he believes that increased grain size shifts the internal friction curve to higher temperatures because of viscous behavior of the grain boundaries. This is his explanation for the different positions of curves I, II, and III of Fig. 7. Curves IV and V are explained as follows: "Corresponding to curves IV and V, most of the grains are extended completely across the specimen and the internal friction maximum becomes much smaller."

Using aluminum of comparable purity, the writer was able to reproduce curve No. 1 of Fig. 7 in a number of experiments, with very little variation between tests except that the maximum occurred at a little higher temperature. He did not, however, obtain the same effect of grain size as that illustrated in Fig. 7; and the single crystal curve is valueless as evidence, since it was obtained by using very impure aluminum.

Fig. 8 shows the relationship between internal friction and temperature found by the writer in samples of different grain sizes. The figures attached to each curve indicate the average length of the grain for the sample represented by that curve. These figures give very little information about grain *diameters*, however. In the wire with the smallest grain size, one half of the grains occupied the full cross section of the wire. In the other wires the number of grains occupying the full cross section of the wires increased with grain size, and in the coarsest grained wire every grain occupied the full cross section of the wire. None of the wires contained more than two grains in a cross section at any point.

The curves shown in Fig. 8 do not confirm the relationship between grain size and internal friction indicated by Kê in Fig. 7, and they are quite inconsistent with the proposed mechanism of grain boundary viscosity. The reason for this discrepancy is not at all obvious, but it may be related to the annealing treatments. The grain sizes indicated in Fig. 8 were obtained by the strain-anneal method, annealed samples being strained between 1 and 2 pct and then reannealed for 16 hr at 550°C. The variation in grain size is fortuitous, and probably attributable to varying small temperature gradients during recrystallization in the 550°C annealing treatment. Kê's results were obtained by annealing at progressively higher temperatures and longer times. It may be that the systematic change in the curves of Fig. 7 is a result of the annealing treatments and that the apparent effect of grain size is only incidental. As for the almost complete absence of system in Fig. 8, that might be an orientation effect. Nash and Hall,[9] after making determinations of internal friction in gold wire, suggested that "grain boundary stability as determined by orientation, plays a role in the observed effects." The distribution of orientations in fine grained wire could be expected to be fairly constant from wire to wire, but in coarse grained wires the orientation distribution could vary considerably. The results recorded in Fig. 8, therefore, would be consistent with the suggestion advanced by Nash and Hall. In any case, it is evident that the difference between the two internal friction curves of Bratina and Winegard's Fig. 2 cannot confidently be ascribed to the difference in grain size.

W. J. Bratina and **W. C. Winegard** *(authors' reply)*—The authors greatly appreciate Dr. Forscher's comments and are pleased to notice that the results obtained by the workers at the Westinghouse Atomic Power Div. are in general agreement with those reported in the paper.

In the authors' case, the oxygen contamination of zirconium specimens took place during the experiments and was, of course, more appreciable the higher the temperature of the particular experiment, and the longer the time necessary to take the respective measurements. The oxygen and, as it is assumed, less significant amounts of nitrogen are picked up, despite the relatively high vacuum. It appears from the experiments that only a negligible amount of gas is absorbed below 700°C; therefore, the initial content of oxygen is expected to remain nearly constant if this temperature has not been exceeded in the experiments. In the case of the curve *a* in Fig. 4, the oxygen contamination took place during the experiment itself, mainly during the heating and cooling period when the temperature was in excess of 700°C.

The substantial drop in the internal friction values of curve *b* as compared to curve *a* (Fig. 4) was attributed to the preferential segregation of the interstitials to the grain boundaries, since the amount of solute is about the same in both cases, and since it is the so-called grain boundary relaxation maximum which is for the most part affected.

Some additional data is presented which appears to support the preferential segregation theory. In Fig. 9 data for a similar case as in Fig. 4 is shown. Curve *a* was obtained at falling temperature—a normal experimental procedure—after the specimen has been heated to 900°C. The characteristic grain boundary relaxation maximum is evident despite the high amount of 1.6 atomic pct of oxygen absorbed during the experiment. Curve *b* was obtained by reheating the same specimen to 700°C only and taking the measurements at falling temperature. The difference between curves *a* and *b* was thought to be due to a different distribution of interstitials in the specimen. A greater uniformity in solute distribution between the grains and the grain boundary regions in α phase was expected to occur by reheating the specimen above the allotropic transformation temperature. Curve *c* was obtained after the specimen was reheated to 900°C; the grain boundary relaxation maximum reappears although somewhat reduced in size. Curve *d* was then obtained by a similar procedure as curve *b* and failed to reveal the respective maximum.

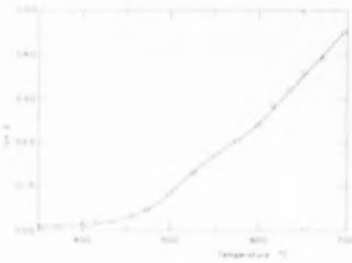

Fig. 10—Disappearance of the grain boundary relaxation maximum for a specimen with irregularly shaped grains is shown. The average grain diameter is 0.05 mm.

In general, a similarity exists between the curves *a* and *c*, which would correspond to the cases of more uniform distribution of solute. The same is true for the curves *b* and *d* where the preferential segregation of solute at the grain boundaries is expected.

The possible effects of a harder oxygen-enriched surface layer, as mentioned by Forscher, on the relaxation maximum have been considered.

In order to check the homogeneity of oxygen, microhardness measurements were made employing Tucon and Vickers microhardness indenters. No special attention was paid to the crystallographic orientations, although indentation hardness is undoubtedly a function of orientation in a close-packed-hexagonal metal. Surprisingly good uniformity of hardnesses across the specimens was observed, especially at lower oxygen content. On the basis of hardness data very little surface enrichment of solute was encountered in the specimen used in Fig. 4. Apparently this is the merit of the oxidation in situ technique where the oxidation is carried out in extremely reduced pressure, i.e., in virtual vacuum. In spite of this, the possible effects of an oxygen-rich surface layer on the grain boundary relaxation cannot be completely ignored.

However, the following considerations seem to rule out the possibility of the surface layer as the main contributing factor in the suppression of the grain boundary relaxation maximum in the authors' case. The surface layer apparently did not exist at the time curve *a* in Figs. 4 and 9 was taken, since the grain boundary relaxation maximum is evident. The layer could not form later during the reheating period, since the amount of additional oxygen absorbed by the specimen was negligible and the only oxygen available was that already in the specimen. Even if a slight enrichment of solute would occur at the surface, it is highly improbable that it should be able to influence in particular the grain boundary relaxation maximum so effectively.

The authors appreciate Mr. Bleakney's interest in and discussion of this paper. Bleakney's comments deal in particular with the relaxation across grain boundaries. It was not the intention of the authors to treat this type of relaxation in detail and therefore the term *relaxation across grain boundaries* was used without special explanations. After the original work by Kê,[11] many papers have been published on this subject. The stress relaxation across interfaces in general including grain boundaries has been reviewed by Nowick.[14] Recently Marsh[15] suggested certain modifications of Kê's theory by taking into consideration, for example, the grain boundary roughness. There are few doubts about the existence of the grain boundary relaxation phenomenon, but there is much controversy concerning Kê's mechanism which postulates viscous behavior of the grain boundaries. Very recently Rhines et al.[16] have raised serious objections with respect to this interpretation.

It appears quite difficult to deny that so-called relaxation across grain boundaries is actually related to the grain boundaries, although it might be difficult to establish the exact relationship between the average grain diameter and the relaxation maximum characteristics. In order to prove that the relaxation maximum in this investigation was caused by the relaxation across grain boundaries, the authors closely investigated two extremes in grain sizes, namely specimens with a fine grained structure and others consisting of extremely large grains, 10 mm or more in length. In such cases it seems difficult to ignore the effect of the grain boundary area completely.

The authors realize that it is possible to suppress the grain boundary relaxation maximum effectively even for fine grained specimens. Fig. 10 shows an internal friction curve for a zirconium specimen from the same high purity material which was annealed in vacuum at, and quenched from, 900°C. The grain boundary relaxation maximum is strikingly reduced despite an average grain diameter of 0.05 mm. In this case however the grains are irregular in size and shape.

[11] T. S. Kê: *Physical Review*, 1947, vol. 71, p. 533.
[14] H. H. Bleakney: An Evaluation of the Recovery Theory of Creep. *Canadian Journal of Technology*, 1955, vol. 33, pp. 56-66.
[15] D. R. Nash and L. D. Hall: *AIME Trans.*, 1953, vol. 197, p. 938; Journal of Metals, July 1953.
[16] A. S. Nowick: *Metal Interfaces*, 1952, p. 248. Cleveland. ASM.
[15] K. J. Marsh: *Acta Metallurgica*, 1954, vol. 2, p. 530.
[16] F. N. Rhines, W. E. Bond, and M. A. Kissel: *Trans.*, ASM, 1956, vol. 48, p. 919.

Phase Transformations in Titanium Rich Alloys of Nickel and Titanium

by D. H. Polonis and J. Gordon Parr

Journal of Metals, May 1956; *AIME Trans.*, 1956, vol. 206, pp. 531-536.

Harold Margolin and **R. F. Bunshah** *(New York University, New York)*—The discussers would like to compliment the authors on an interesting paper and present some related data and comments on the subject matter of their paper.

At New York University, we have carried out some *T-T-T* studies on sponge titanium base Ti-Ni alloy containing 4 and 6 pct Ni on work sponsored by Wright Patterson Air Force Base under contract AF33 (616)-2766. It was not possible to form martensite across the section of a ¼ in. cube* by water quenching. The specimen thickness was consequently reduced in stages to ⅛, 1/16, and 1/32 in. Specimens of 1/16 and 1/32 in. thickness, on quenching in an iced brine solution, yielded a martensite structure for the Ti-4 pct Ni alloy as shown in Fig. 11. It was impossible to form a martensite structure in the Ti-6 pct Ni alloy in any of the thicknesses used.

* The specimens were attached to a stainless steel rod and were annealed in flowing helium atmosphere. At the conclusion of the heat treatment, the specimens were quenched by plunging the rod into the quenching medium.

After a betatizing treatment of 1000°C, 30 min, followed by an ice brine quench, 1/16 in. thick samples showed a hardness of 440 Vpn for a 4 pct Ni alloy and 560 Vpn for a 6 pct Ni alloy. This suggests some ω formation.

The determination of the M_s temperature presented considerable difficulty. After some experimentation, the following technique was adopted: Samples 1/16 in. thick were betatized, then quenched into a molten-metal bath held at various temperatures from 700° to 300°C, held there for 5 sec and quenched into iced brine. After quenching from the reaction temperatures, the microstructure consists of α and martensite. As the reaction temperature is lowered, α disappears.

The entire specimens are carefully scrutinized for any signs of α, particularly at the prior β grain boundaries, and the temperature at which there are no signs

of α is taken to be the M_s temperature. From isothermal transformation specimens, it was known that some grain boundary α will form in 5 sec holding time. The M_s temperature may be too low because of the rapid transformation rate of Ti-Ni alloys thus requiring rapid cooling attainable only in a bath held at a sufficiently low temperature.

Based on this and other previous work with titanium alloys, an alternative explanation of the results reported in this paper is possible and we should appreciate the authors' comments on the interpretation advanced below.

The hardness of retained β in lump specimens is of the order of 300 Vpn. The authors' hardnness data for unalloyed iodide titanium indicated that the increased hardness due to the use of a small load, 10 g, is small. Thus, if β were retained, a hardness well below 390 Vpn reported by the authors would be expected. The inference consequently is that some β decomposition has taken place during the quench from the β field.

The presence of the ω phase has been reported in many titanium alloy systems including the Ti-Cu system and Ti-Ni systems. Robinson et al.[6] at Battelle Memorial Institute have reported the presence of the ω phase in β quenched and tempered 7.5 pct Ni alloy. The ω phase exists in the temperature range 400° to 800°F (204° to 427°C), coexisting with α + Ti_2Ni at the highest temperature.

The failure of the authors to detect the ω phase may be due to the fact that at any time only a very small amount is present and the X-ray techniques used are insensitive to this small amount.

Judging from the high hardness of the quenched samples, it is postulated that some $\beta \rightarrow \omega$ transformation occurs during quenching.

The following decomposition sequence is then proposed:

$$\beta \rightarrow \omega \rightarrow \text{supersaturated } \alpha \text{ (or } \alpha'') \rightarrow \text{equilibrium } \alpha + Ti_2Ni.$$

On this basis:

1) The high hardness of the as-quenched structure referred to by the authors as retained β may be β with some ω phase having formed during the quench.

2) The hardness peak and concurrent X-ray line breadth maxima may be caused by the coherency strains between β and ω and possibly between ω and saturated α.

3) α'' appears to form by nucleation and growth. Additional supporting evidence is that the substructure associated with the *retained* β disappears on transformation to α''. If α'' formed martensitically, this would not happen.

4) From the striking similarity of the behavior of α' and α'', they are both supersaturated α formed by nucleation and growth (i.e., α' in the Ti-6 pct Ni alloy is not martensite†), the morphological difference being accounted for by the difference in cooling rates from the β field. This further avoids the anomaly of the lack of a C-curve behavior because measurement of the rate of formation of α' morphology and α'' morphology would give the C-curve for the decomposition of $\beta \rightarrow$ saturated α.

† The structure shown in Fig. 2 of their paper for a Ti-1 pct Ni alloy is considered to be martensite. The as-quenched structure of the 6 pct Ni alloy is presumably similar to Fig. 1 of a paper by Polonis and Parr[5] and is not considered to be martensite.

Fig. 11—Ti-4 pct Ni alloy. Treated at 1000°C for 30 min, followed by an ice brine quench. X1500. Reduced approximately 10 pct for reproduction.

It might be added that the very rapid formation of α' morphology by nucleation and growth is not inconsistent with the very rapid transformation rates observed in this active eutectoid Ti-Ni system. Very rapid α formation has been observed in other alloys also. This also avoids the anomaly that the martensite formation is suppressed whereas a nucleation and growth product (ω phase) forms by higher cooling rates. (It is not intended to question the fact per se that in some alloys the martensite transformation can be suppressed.)

In passing, it might be pointed out that the Ti-Ni constitution diagram quoted by Polonis and Parr[1] placed the eutectoid composition about 6-7 pct Ni and, if correct, the 6 pct Ni alloy is not hypereutectoid as stated by the authors.

Douglas H. Polonis and **J. Gordon Parr** *(authors' reply)*—The authors wish to thank Drs. Margolin and Bunshah for submitting their interesting discussion and related data. It would appear in view of these additional results that there is some difference in behavior between finely divided material and larger lump specimens, as might be expected. The authors would be interested to know if X-ray techniques were used to detect any signs of transformation of retained β in the 6 pct Ni alloy quoted in the discussion. The determination of M_s temperatures in a fast eutectoid system such as Ti-Ni is difficult and we are inclined to favor the continuous cooling method in preference to the metallographic method quoted in the discussion. In addition we would like to offer the following comments:

1) The authors' work on this system was carried out on particles finer than 48 mesh (Tyler screen sizes). This particle size effect introduces a potential variable with respect to both M_s temperature and appearance of martensite under the microscope.

2) The authors believe that they were successful in retaining β although it is not inconceivable that very small traces of ω could be present and not detected. Attempts to reveal any ω by X-ray studies were unsuccessful. The hardness values do not seem high enough to indicate that ω is present in view of the Ni content of the specimens (6 atomic pct or 7.5 wt pct). Drs. Margolin and Bunshah have quoted a hardness of 300 Vpn for retained β but have not specified the corresponding nickel content. The 7.5 pct Ni alloy reported to contain ω by Robinson et al. corresponds approximately to our 6 pct (atomic) alloy. We would be interested to learn of any results of tempering treatments performed on their specimens for both 100 pct β and β + ω specimens following quenching.

3) The tempering treatments were performed high in the temperature range for ω formation (400° to 450°C). If ω did form during tempering, it is believed that there should be enough for X-ray detection, particularly since we were working with powders, which are generally more sensitive to X-ray studies than lumps. However, the hexagonal structure designated α'' in the paper was observed in increasing amounts with progressive tempering. Studies at lower temperatures than 400°C also revealed formation of α'' but at much lower rates.

4) The authors agree that α'' appears to form by nucleation and growth and may involve a mechanism similar to bainite formation. It is logical to consider this phase as a supersaturated α but it forms in a rather unique way. The structure we called α' is also a supersaturated α as verified by X-ray and by the incubation period prior to detection of Ti_2Ni in tempering this structure. Since our α' was produced by continuous cooling from the β field without precipitation of a second phase it has a similar structure to what other people refer to as martensite. True, it does appear to be different from the martensite which is shown

in the discussion, but this could be accounted for by the difference in specimen size. This does not exclude the possibility of a supersaturated α that is suggested for α' which in turn applies to the α' observed by others. The experimental observations appear to point quite directly to the relationship between the maximum hardness and the amount of α'' phase that has formed in tempering. It is interesting to note that the hardness maxima are not reached until much of the β has decomposed (approximately 50 pct β decomposition). It seems unlikely that a hardening mechanism involving ω would operate to this extent of decomposition without some ω phase being detected.

5) Regarding the alloy compositions, it has been stated in the paper that compositions are expressed in terms of atomic percent. Consequently the 6 pct (atomic) Ni alloy is equivalent to approximately 7.3 wt pct. This composition appears slightly hypereutectoid on the basis of the proposed phase diagram.

[9] H. A. Robinson, M. W. Purvis, A. E. Austin, C. M. Schwartz, and P. D. Frost: Precipitation Hardening and Embrittlement of High Strength Titanium Alloys. *WADC Technical Report* 54-355, December 1954, pp. 52-54.

[10] D. H. Polonis and J. G. Parr: *Acta Metallurgica*, 1955, vol. 3, No. 4, p. 397.

Primary Recrystallization Textures in Cold Rolled Si-Fe Crystals

by C. G. Dunn and P. K. Koh

JOURNAL OF METALS, August 1956; *AIME Trans.*, 1956, vol. 206, pp. 1017-1024.

Hsun Hu *(Westinghouse Electric Corp., Pittsburgh)*—The authors' results on the effect of adding a (001)[110] component to the (111)[112] deformation texture upon the subsequent recrystallization texture is interesting. In a cold rolled crystal with a single (111)[112] texture, they obtained a recrystallization texture predominantly (110)[001], which is related to the deformation texture by a rotation of 35° around the common (110) pole at the transverse direction (specimens D-1 and D-2, Figs. 6 and 8 in the authors' paper). The same recrystallization texture was observed in a crystal with a duplex deformation texture, consisting of both (111)[112] and (001)[110] components of approximately the same intensity (specimen A-3 and Fig. 2 in the authors' paper). In other words, the recrystallization texture developed in a crystal with a (111)[112] deformation texture appeared to have been little influenced by the addition of the (001)[110] component.

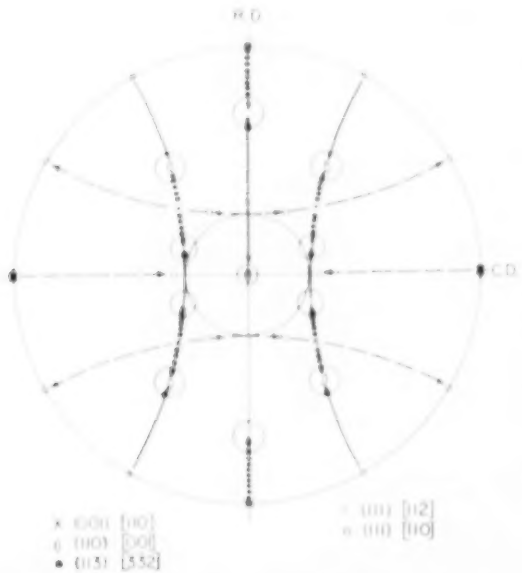

Fig. 14—(110) pole figure showing the rotational relationships among the orientations involved in the discussion. Small circles are drawn with a radius of 5°. Full line arrows indicate the 35° rotations from the (111)[112] orientation around the common (110) pole at *C.D.* Dotted line arrows indicate the 20° rotations from the (001)[110] orientation around the same common (110) pole at *C.D.* Dash line arrows indicate the 55° rotations from the (001)[110] orientation around the common (110) pole at *R.D.*

The authors used these results as an evidence unfavorable to the oriented growth theory. Since with a duplex deformation texture of (111)[112] and (001)[110], there is a (113)[332] orientation which is related to both texture components by [110] rotations of 25° to 30°. Therefore, nuclei of this orientation are favorably oriented for growth in both textures; hence, the recrystallization texture should be of the (113)[332] type if the oriented growth theory is valid. However, their experimental results showed that the recrystallization texture developed from a crystal with such a duplex deformation texture was still primarily (110)[001], which is favorably oriented for growth only with the (111)[112] component, but not with the (001)[110] component, of the deformation texture.

In a very recent work on the cross rolling and annealing textures of high purity iron at this laboratory,*

* Paper submitted for publication.

the discusser has found that the cross rolling texture consists of mainly (100)[011] plus minor components of (111)[110] or the (111)[112] type. Upon annealing, the minor texture components exhibited a much greater tendency for recrystallization than the main texture material of the (100)[011] orientation. It was found that while the minor texture components were completely replaced by recrystallized grains with new orientations, the main texture material had undergone only *polygonization* with no or very few recrystallized grains formed in these polygonized areas. The texture developed after complete recrystallization could be described as [110] rotations from the minor deformation texture components but not as well similarly related with the main deformation texture. The finding that the tendency for recrystallization appears to be different among different deformation textures is very well in accord with the authors' observations on Si-Fe single crystals. There is considerable evidence to suggest that the recrystallized grains formed earlier in the minor texture components have grown into the polygonized main deformation texture matrix before the latter has largely recrystallized by itself.

A close examination of the orientation relationships among the orientations involved in the authors' case reveals that the recrystallized grains of the (110)[001] orientation are fairly favorably oriented for growth with respect to a (001)[110] texture. As seen from Fig. 14, the pole positions of the (110)[001] orientation can be obtained by rotations of 20° around the common (110) pole at the cross direction from the (001)[110] orientation. From such rotations, some of the (110) poles of the resulting orientation are not inclusively accounted for by a simple (110)[001] orientation, but they do fall well within the weaker intensity areas of the recrystallization texture. Even the minor recrystallization texture components, which are approximately of the (111)[$\bar{1}$10] type orientations (*A* and *B* compo-

nents in the authors' Fig. 2), are related to the (001)[110] texture by [110] rotations around the common (110) pole at the rolling direction.

In view of these facts, the lack of noticeable influence in the recrystallization texture by adding a (001)[110] component to the (111)[112] deformation texture is probably due to the difference in the recrystallization tendency for the two deformation texture components. As a result, the recrystallized grains formed in the (111)[112] texture material grow finally at the expense of the (001)[110] texture material. In this respect, a comparison of the grain size and its distribution of two identically heat-treated specimens, of which one has a single (111)[112] deformation texture and the other has a duplex (111)[112] and (001)[110] deformation texture should be informative. Texture studies made at intermediate stages of the recrystallization process in a duplex textured specimen would be very helpful in understanding the reported phenomena.

C. G. Dunn and **P. K. Koh** *(authors' reply)*—Dr. Hu has presented some interesting information regarding rolling and annealing textures of high purity iron, which seems to correlate well with our data on Si-Fe. In particular there is good agreement on reorientation relationships and the effect of orientations on tendency to recrystallize. Dr. Hu's information from the study of annealing at intermediate temperatures is especially interesting; we certainly agree that similar studies on our cold rolled crystal with the duplex texture would be valuable. In connection with the duplex texture Dr. Hu's interpretation of what happens on annealing—namely, that nuclei for recrystallization come from the (111)[112] component and that these nuclei grow at the expense of material of the (001)[110] orientation—is, we believe, correct. The fact that one component can provide nuclei due to more rapid recrystallization is, in our opinion, completely in agreement with the oriented nucleation theory of recrystallization.

If a rotation of 25° to 30° about a <110> axis is selected as favorable for growth, then it has to be concluded that nuclei in the (110)[001] orientation are not favorably oriented for growth at the expense of the (001)[110] orientation. Dr. Hu's analysis giving a 20° rotation about the (110) pole in the cross direction is in error. Such a rotation applies only to one of the twins of the (110)[001] orientation. As far as we know the (110)[001] and (001)[110] orientations are as far apart as any two orientations can get. The rotation about the cross direction, which is a common (110) pole, is 90°. However, of the 24 possible rotations going from (110)[001] to (001)[110] or vice versa, the least rotation is close to 63° and the axis of rotation is not a (110) pole. On the other hand, if any large angle of rotation leads to good growth then the experimental conditions are favorable for (110)[001] nuclei growing at the expense of material in the (001)[110] orientation; but this is just another way of saying that oriented growth theory is not applicable.

Recovery of Cold Worked High Purity Al Mg Alloys

by E. C. W. Perryman

JOURNAL OF METALS, October 1956; *AIME Trans.*, 1956, vol. 206, pp. 1247-1252.

A. Berghezan *(European Research Associates, Brussels, Belgium)*—After his wonderful work on the recovery of pure aluminum, Dr. Perryman continued to study the influence of added atoms on this process. Using different methods, he tried to discover the relationship between the recovery of the physical properties and simultaneous changes in the structure. If some of the physical properties of the recovered metal were well known, the structural *changes* which the metal exhibits during the recovery process were completely ignored. In this matter, Dr. Perryman made a great contribution by showing the splitting of the initially deformed grains into subgrains and finding the relation between the structure and the physical properties.

In this paper, Dr. Perryman shows new evidence of the real structure of the recovered metal and raises a number of new questions about solute atoms in the matrix.

As is apparent, the most important evidence is the difference he found between the influence of these solute atoms on recrystallization and on recovery. Whereas a few magnesium atoms dissolved in an aluminum matrix *increase* the activation energy of recrystallization, they *decrease* the activation energy of recovery. It seems that this surprising experimental result is worth discussing.

The author gave an explanation of this unexpected result in terms of vacancies frozen in by a higher diameter of solute magnesium atoms which hasten the climbing process of dislocations in the subgrain boundaries during the recovery annealing.

On this hypothesis only, it is hard to understand other features closely connected; for example, the smaller subgrain size in the presence of magnesium atoms, or the little effect of magnesium on the size of the subgrains formed during high temperature deformation as was found by Rachinger and McLean and Former.

If during high temperature deformation vacancies are annealed out as fast as they are formed, the climb of dislocations will be delayed as will be recovery and, consequently, the subgrain size must be smaller.

Another explanation must be found and we think that a metallurgist some time ago, who was not accustomed to thinking in terms of dislocations and vacancies, would have said merely that this was a matter of stored energy, since it is well known that solute atoms greatly increase the energy stored during deformation. Pure aluminum deformed 20 pct will store less energy than does an aluminum alloy deformed to the same extent. Therefore, during annealing, the speed of the recovery process will be greater for the metal with higher stored energy.* That this is so is also shown by the following experiment: If a deformed metal is partially recovered at a very low temperature (T_1) and the same metal is then raised to a higher temperature (T_2), it will recover more slowly at the latter temperature, or even less than the same metal would if it were heated thus (T_2) directly after deformation.

* Instead of stored energy, work hardening can be expressed in terms of dislocations and vacancies, but it must be remembered that the part played by vacancies is small or else an opposite effect, by decreasing the strain energy around the magnesium atoms. In that case, the number, the kind, and the distribution of the dislocations and their interaction with the solute atoms are the important factors.

A series of other points are raised by the author: the large amount of X-ray line broadening due to the small particle size; the splitting of deformation bands after annealing; decrease of subgrain size with a decrease in the annealing temperature; and the absence of subgrains in some grains after recovery when examined under the microscope, but the exhibition of spotty X-ray rings in the same regions in which no subgrains were visible.

All these points were also found by us during similar work on aluminum with 3 pct Mg, the results of which were published last year.[1,2] This evidence provides welcome confirmation of our results and appears

more valuable, since it emanates from a completely different laboratory. Nevertheless, to make sure that the agreement is complete even in detail, we want to stress some other points:

1) It was found that a large amount of X-ray line broadening, due only to the small particle size, may occur in absence of any strain. Direct evidence of this was obtained with very small annealed particles.

2) The splitting of the grains and deformation bands happens during deformation and not during or after annealing.

3) The small subgrains resulting from deformation are not perfect elements. They become more and more perfect during annealing and they grow simultaneously. This can be seen by color microscopy where the subgrain boundaries appear—even after a length of annealing time—very broad and totally lacking sharpness. When they appear fine and sharp, a normal perfection[1] is achieved, equilibrium (at this temperature)

[1] The degree of perfection is related to the annealing temperature. The maximum perfection one can reach at a certain temperature is what we call normal perfection.

seems to be established at the interfaces, and thus growth is stopped. We think that the author has the same thing in mind when he says: "Once sharp subgrains have been formed, no signs of subgrain growth with increasing annealing time have been noticed."

At a higher temperature this equilibrium is not any more stable. The order (perfection) established on a certain scale (the lower the temperature, the smaller the scale) is no longer possible, new order at a larger scale will occur. New defects can be annealed out and greater perfection can be reached. Direct evidence has been obtained by microhardness testing on individual subgrains and by fine X-ray beams. Therefore, the final steady value of the half-peak line sharpening and the measured microhardness is greater than the lowest annealing temperature. The grain size which may account for these differences at different annealing temperatures cannot be separated from the relative perfection of the subgrains, because the subgrain growth is related to the degree of perfection of the entire volume of subgrains and not only to their interfacial energy. This is the reason for the large growth of subgrain size during the early stages of the recovery and the larger size (and subboundary mobility) with increasing annealing temperature. In this case, if the size of the particle is plotted in accordance with the annealing time, a curve similar to that of the softening (degree of recovery) must be found and this seems to be so.

E. C. W. Perryman *(author's reply)*—I would like to thank Dr. Berghezan for his most interesting discussion of my paper. I am familiar with his work on the recovery of Al-Mg alloys which unfortunately appeared after my paper was submitted for publication. It was indeed gratifying to see such good agreement between the two laboratories.

Dr. Berghezan considers that the equilibrium subgrain size is not only influenced by subgrain boundary energy but also by the perfection of the subgrains themselves. Assuming that recovery is due to the annealing out of crystal imperfections within the subgrains, it is difficult to reconcile the foregoing statement with the observed fact that the rate of recovery is markedly increased by the first small magnesium addition—increasing magnesium content having little further effect—whereas the subgrain size decreases continuously with magnesium content up to 3 pct.

As was suggested in the paper, it is possible that the effect of magnesium on subgrain size may, in fact, be due to magnesium concentrating at the subgrain boundaries, thereby decreasing the mobility of the subgrain boundaries. The question is, why doesn't this happen during plastic deformation at elevated temperatures? For both pure aluminum and Al-Mg alloys, I have shown that the subgrain size increases with decreasing amounts of cold work and have suggested that this is because the orientation difference between adjacent subgrains decreases with decreasing cold work. If this is so, then below some small amount of cold work magnesium may not segregate to the subgrain boundaries and hence would have no effect on the subgrain size. This may be the explanation as to why magnesium has no effect on the subgrain size after plastic deformation at elevated temperatures.

[9] A. Berghezan: Structure et propriétés du metal restauré. Métaux-Corrosion-Usure, 1955, Nos. 359-360, p. 1.

[10] A. Berghezan and J. Herenguel: *Comptes Rendus*, Paris, 1955, vol. 240, pp. 1343 and 1536.

Recrystallization and Grain Growth in Iodide Zirconium

by R. M. Treco

JOURNAL OF METALS, October 1956; *AIME Trans.*, 1956, vol. 206, pp. 1304-1311.

E. C. W. Perryman *(Atomic Energy of Canada Ltd., Chalk River, Ont., Canada)*—In the present work it would appear that even after heavy cold working recrystallization takes place by nucleation and growth whereas in the earlier work by McGeary and Lustman[9] it was concluded that softening was accompanied by the formation and growth of subgrains and that the formation of the recrystallization texture did not occur by the normal nucleation and growth process. Could the author comment on these apparent discrepancies?

Relative Interfacial Energies of Symmetrical Tilt Grain Boundaries in Silver

by K. T. Aust

JOURNAL OF METALS, August 1956; *AIME Trans.*, 1956, vol. 206, pp. 1026-1029.

N. A. Gjostein and **F. N. Rhines** *(Carnegie Institute of Technology, Pittsburgh)*—It does not seem likely that the inequality of angles d and b can be attributed to effects arising from the orientation of the boundaries unless the <001> directions of crystals B and C were markedly skewed. The author does not state the accuracy with which the <001> directions of crystals B and C could be grown parallel to one another, but experience in this laboratory has shown that such a misalignment would be at most ±2°. If this is true, in the case at hand, then boundary B-C should migrate to the energy cusp position parallel to the [001] direction in each crystal. Moreover, since crystals B and C have been oriented to make boundary B-C a symmetrical tilt boundary, boundaries A-B and A-C will necessarily have similar structures (provided a <112> or <110> type direction of crystal A is always kept vertical) for a given θ and axis of growth for crystal A. Hence at equilibrium they should have migrated into positions that are symmetrical with respect to an imaginary line

drawn from the triple point, parallel to boundary *B-C*, and extending into crystal *A*. In other words, the boundaries *A-B* and *A-C* should make an angle of $(e/2)$ with this imaginary line. Since the large angle incoherent boundaries are essentially of like structure, and since they would each be near equivalent boundary energy cusp positions (if they exist for these boundaries), their orientation derivatives would be nearly equal, and they would not be expected to produce a difference in the angles d and h.

Thus it would seem that boundary orientation effects should lead to d being equal to h and that the observed difference should be attributed to either, or both, 1) errors of measurement, and/or 2) lack of equilibrium at the triple point. In the latter case, impurity atoms or inclusions at the boundaries, or appreciable curvature of the boundaries near the triple point, may play an important role in preventing them from reaching their ideal positions. When the average of the measured values of d and h for each θ was used to recalculate $\gamma_{s.e}$ from Eq. 1, it was found that there were no significant differences in the values of $\gamma_{s.e}$ from those obtained by the author. Therefore, although the inequality of d and h indicates that there is a nonequilibrium condition present at the triple point, the calculation of $\gamma_{s.e}$ is fortunately insensitive to this factor.

It is assumed by the author in calculating $\gamma_{s.e}$ that the orientation derivatives of boundaries *A-B* and *A-C* are negligible because they have primarily an incoherent-type structure. With the exception of Hess,[1] and Friedel et al,[2] there have been no systematic attempts at measuring the effect of boundary orientation upon its energy reported in the literature. If the orientation derivative values obtained by Hess are of the right order of magnitude, considerable error could result in using Eq. 1 to calculate $\gamma_{s.e}$. On the other hand, as pointed out by Hess, his values are probably too high because of the presence of inclusions at the boundaries. At present, work is in progress in this laboratory to determine the effect of boundary orientation upon its energy for both large and small angles of misorientation.

K. T. Aust *(author's reply)*—It would be expected that the boundary angles d and h be equal on the basis of symmetry of the crystal orientations. However, three specimens in the present study showed marked divergence between the values of these angles, two of which were associated with relatively low angle grain boundaries. Three similar cases were observed previously,[3] each one corresponding to the presence of a low angle grain boundary. Therefore, it seemed possible to ascribe the asymmetry to the unknown effect of orientation of such a boundary on its energy. The anomaly might also be attributed, in part, to the difficulty of accurate observation of the boundary when it corresponds to a small orientation difference or low energy. The inequality of angles d and h is not sufficient, however, to invalidate the conclusions reached in this work since, as noted by Gjostein and Rhines, the calculation of $\gamma_{s.e}$ is insensitive to this variation.

Lomer and Nye[4] have indicated that the low mobility of small angle boundaries can seriously affect the equilibration process in tricrystals of the type used here. Consequently, migration kinetics as well as energy cusps may be involved. Similarly, Gjostein and Rhines suggest that a nonequilibrium condition is present at the triple point, at least in those specimens where angles d and h differ. Although boundaries in real crystals represent nonequilibrium structures, intersecting boundaries may attain local equilibrium through migration of atoms over relatively short distances. The good mobility of large angle boundaries may insure that in these experiments there are always two boundaries in each specimen which can move freely enough to produce local equilibrium. In fact, it was observed that the point of junction of the three boundaries frequently moved through a distance of several millimeters during the process of cooling from the freezing point. The specimens were then annealed at temperatures near the melting point for relatively long periods until constant boundary angles were obtained. It is assumed, therefore, that the angles under consideration are at their equilibrium values, and that metastable equilibrium states are not reached. An additional justification for this assumption was previously given in ref. 2.

Gjostein and Rhines mention the possibility of impurities playing an important role in preventing the boundaries from reaching equilibrium positions. Impurities in the boundary may be of more significance in their effect on the grain boundary energy itself. It is possible that impurity atoms in the vicinity of the dislocation lines of the boundary modify the boundary energy and thus control the boundary direction or orientation. The impurity factor may then lead to asymmetry of angles d and h for specimens containing a dislocation boundary, which would not be predicted by the dislocation model of the boundary based only on the presence of dislocations in a pure crystal lattice.

Since the energy of a large-angle incoherent boundary is nearly constant over wide ranges of orientation difference of the adjoining grains,[5,6] it appears likely that the orientation derivative of such a boundary is truly negligible within rather wide limits. However, a quantitative study of the magnitude of orientation derivatives for both large and small angle boundaries is certainly a needed approach in this field.

[1] J. B. Hess: Measurement of Solid: Solid Interfacial Energies. *Metal Interfaces*, p. 134. Cleveland, ASM.
[2] W. M. Lomer and J. F. Nye: *Proceedings*, Royal Soc., 1952, vol. A212, p. 576.
[3] B. Chalmers: *Proceedings*, Royal Soc., 1949, vol. A196, p. 64.
[4] J. Friedel, B. D. Cullity, and C. Crussard: *Acta Metallurgica*, 1953, vol. 1, p. 79.

Study of the Fe-Si Order-Disorder Transformation

by Frank W. Glaser and W. Ivanick

JOURNAL OF METALS, October 1956; *AIME Trans.*, 1956, vol. 206, pp. 1290-1295.

Hiroshi Sato *(Ford Motor Co., Dearborn)*—Several years ago, the behavior of the order-disorder transformation of the Fe-Al-Si system was investigated in the Research Institute for Iron, Steel and Other Metals, Tohoku University, Sendai, Japan, and a part of the result was published.[1,2] Since these results were not cited in this paper, it seems worthwhile to discuss some points of this paper together with the results.

The authors claim that the T_c-composition curve of Fe-Si alloy does not agree with the curve expected from the theory of AB_2-type alloy of Easthope[3] (also a similar calculation by Shockley[4]) but shows a maximum at the 3:1 composition. It should be noticed, however, that the calculation above should be applied only to the AB_3-type alloy of face-centered-cubic lattice and not to AB_2-type of body-centered-cubic lattice. If the problem of a body-centered-cubic lattice is treated in the usual manner, it is clear that at least the second nearest-neighbor interaction should be taken into account in order to have an AB_2-type superlattice as a stable phase. If the second nearest-neighbor interaction is taken into account, it is rather natural to expect from the theory that the T_c-composition curve of an AB_2-type alloy of body-centered-cubic lattice shows a maximum at the 3:1 composition. This was first pointed out by us during the investigation of the Fe-Al

superlattice.[7,8,9] Also, a detailed calculation was done using the Bragg-Williams approximation.[7]

As for the T_c-composition curve of Fe-Si system, Osawa and Murata investigated it along with the general phase diagram of the system obtained by measuring several physical properties at high temperatures. They published a similar result to the present one.[9] Since Osawa and Murata used a less direct method than that adopted by the present authors in determining T_c, it seems to me that their result may be less reliable. However, the Osawa-Murata result is higher in temperature than that of the present authors in spite of the fact that, in the latter experiment, T_c was obtained by measurements on quenched samples. Such a method of determining T_c might be expected to give a higher value if we consider the possibility of ordering during the quench. In this sense, the present authors' method should also be considered indirect. Also, these alloys are very likely to be cracked by severe quenching and it is difficult to expect highly accurate measurements for such samples. Since the figure indicating the dependence of the resistivity upon the quenching temperature is not shown in the text, the accuracy of determining T_c can not be judged by the reader.

The authors also claim that the stability characteristics of $Fe_3(SiAl)$ and Fe_3Si are very similar but very dissimilar to Fe_3Al. This expression seems rather vague to me. I investigated the behavior of the order-disorder transformation in the Fe-Al-Si system[10] by replacing aluminum atoms in Fe_3Al by silicon atoms on the composition line $Fe_3Al_xSi_{1-x}$ $(0 \leq x \leq 1)$. Such an investigation was made because Fe_3Al and Fe_3Si have many characteristics in common, especially in their relations between order-disorder and magnetic transformation. The Fe-Al-Si system gives very instructive information concerning the problem of the interaction of these two cooperative phenomena: the order-disorder of atomic arrangement and the ferro-paramagnetic transformation. From the measurement of specific heat-temperature curves of these alloys and other data, we could conclude as follows:

Silicon replaces aluminum randomly and, therefore, the type of superlattice in this range is $Fe_3(Al_xSi_{1-x})$ and is similar to Fe_3Al or Fe_3Si. No higher order superlattice is observed.

Replacing aluminum by silicon raises the T_c of the superlattice of $Fe_3(Al_xSi_{1-x})$ type more strongly than what would be expected from a simple replacement model where no interaction between aluminum and silicon atoms is assumed. In this case T_c would go up linearly with silicon along the line connecting the T_c's of Fe_3Al and Fe_3Si. This type of nonlinearity in the actual results means that there is a strong repulsion between aluminum and silicon atoms at the nearest-neighbor distance.

Although there is a complication in the behavior of physical properties measured near the Fe_3Al range because of the proximity of T_c to the Curie point, the essential behaviors of the order-disorder transformation and its effect on the spontaneous magnetization are found to be similar for both Fe_3Al and Fe_3Si.

In this sense, it does not seem to be reasonable to say that the stability characteristics of Fe_3Al and Fe_3Si or $Fe_3(SiAl)$ are very dissimilar.

When silicon is added to Fe_3Al, electrical resistivity at high temperature shows a negative temperature coefficient just like that observed in Fig. 8. However, by close examination of extremely accurate resistivity-temperature data, we could observe a slight bend of the curve at the critical temperature.[11] Probably the circumstances would be the same in the Fe-Si system.

Frank W. Glaser and **W. Ivanick** *(authors' reply)*—We sincerely regret that in reviewing pertinent literature, abstracts, and major references made to publications in connection with the Fe-Si order-disorder reaction, we have failed to uncover and thus include some of the studies made and referred to in his discussion by Mr. Sato. It appears, however, that Sato et al. have concerned themselves primarily with theoretical considerations of the order-disorder transformation while our paper dealt mainly with a description of experimentation designed to shed more light on the physical characteristics of Fe-Si alloys as a function of heat treatment. An attempt was made by us to correlate such experimental observations with certain studies made by others as cited in the article.

Regarding the relation of T_c vs composition, our experimental data were reported only for comparison with Easthope's theoretical curves, who made these calculations for structures with coordination numbers 6, 8, and ∞. He did not indicate a maximum at composition AB_3 for the body-centered-cubic case.

Since some of the studies cited by Sato have not been published or appeared in translation, we shall gladly accept his statements regarding similarities between our findings and those of Osawa and Murata[9] in connection with the relation of T_c vs composition. It appears possible that in quenching these brittle Fe-Si compositions, microcracks might be caused; however, we feel certain that this fact had very little influence, if any, on the order of magnitude of our results as reported.

Our suggestion regarding similarities in thermal stability characteristics of the Fe_3Si and $Fe_3(SiAl)$ superlattices was based on a comparison with results obtained by Garrod and Hogan.[4] As cited in our paper, these authors—like ourselves—have observed an extraordinary thermal stability of the superlattice, which was retained "in spite of rapid quenching from a temperature close to the melting point."

A similarity of thermal stability characteristics of the Fe_3Si and $Fe_3(SiAl)$ superlattices, and a corresponding dissimilarity of these two with the thermal stability characteristics as reported for the Fe_3Al superlattice, appeared to be a justifiable observation.

[7] H. Sato and R. Yamamoto: *Journal* Physical Soc., Japan, 1951, vol. 6, p. 65.
[8] H. Sato: *Science Reports*, Research Inst., Tohoku Univ., 1951, vol. A 3, p. 31; *Journal*, Japan. Inst. of Metals, 1948, vol. 13, No. 4, p. 3.
[9] W. Shockley: *Journal of Chemical Physics*, 1938, vol. 6, p. 130.
[10] H. Sato: *Science Reports*, Research Inst., Tohoku Univ., 1952, vol. A 4, p. 1.
[11] H. Sato: *Science Reports*, Research Inst., Tohoku Univ., 1951, vol. A 3, p. 25.
[12] K. Adachi: *Science Reports*, Tohoku Univ., 1951, Series I, vol. 35, p. 39.
[13] A. Osawa and T. Murata: *Journal*, Japan. Inst. of Metals, 1940, vol. 4, p. 228.
[14] H. Sato and R. Yamamoto: Unpublished work presented before the Physical Society of Japan, November 1948.

Temperature Dependence of Recovery Phenomena in a Cold Rolled Aluminum Single Crystal

by A. H. Lutts and P. A. Beck

JOURNAL OF METALS, October 1956; *AIME Trans.*, 1956, vol. 206, pp. 1226-1228.

E. C. W. Perryman *(Atomic Energy of Canada Ltd., Chalk River, Ont., Canada)*—I was very pleased to see that the results of this investigation have confirmed my results[1] obtained on polycrystalline superpurity aluminum. For heavy cold working (80 pct) at room temperature, I also found that the activation energy for the recovery of hardness and X-ray line breadth were similar and the actual values of $20{,}000 \pm 5{,}000$ cal per

mole for line breadth and 22,500 ± 2,400 cal per mole for softening agree very well with those reported by the authors. However with smaller amounts of cold work (20 pct), the activation energies for recovery of line breadth and hardness were not the same, being 22,400 ± 2,000 and 31,800 ± 2,600 cal per mole, respectively.

In view of the foregoing results, I cannot agree with the authors' tentative conclusion that the rate of line sharpening and the rate of initial softening are determined by related elementary processes. Since the activation energy for recovery of line broadening is independent of the amount of cold work it is not unreasonable to suppose that this is controlled by a single process such as dislocation climb. The activation energy for recovery of hardness is dependent on the amount of cold work which suggests that in addition to dislocation climb some other mechanism is operating. This is perhaps not surprising, for available evidence[2] indicates that subgrain growth occurs in the very early stages of recovery and also that the hardness or yield strength will be dependent on subgrain size and on the type of subgrain boundary present after recovery and the orientation difference between adjacent subgrains.

A. Berghezan *(European Research Associates, Brussels, Belgium)*—This paper is one of a long series focusing light on one of the most significant and currently important problems in the study of the physics of metals, that is, softening without recrystallization or the recovery of the cold worked metals by annealing at low temperatures.

Until now, the definition of recovery has been the softening of metal without observable structural changes.[4]

It is obvious that this definition contains a striking contradiction, since it is well known that softening of the metal during the recovery process brings its physical properties very near to those of recrystallized metal while still appearing to maintain the structure of the deformed metal.

As is also well known, there is a close relationship between structure and mechanical properties and vice versa. Thus, softened material after recovery, having mechanical properties approximating the recrystallized material, *cannot* have the structure of the deformed material. All methods used to reveal a change in the structure of deformed metals during the recovery process have failed to detect this until very recently.

It is greatly to Dr. Beck's credit that the problem of recovery is brought to the fore and that he shows how erroneous our ideas on this subject have been. Dr. Beck and A. H. Lutts raise a new and very interesting point: after the completion of line sharpening, there still remains a part of the total work hardening introduced by deformation.

In a recent paper on the structure and the properties of recovered metals,[5,6] we found the same feature in a homogeneous alloy of aluminum with 3 pct Mg, and showed by X-rays that, after the completion of line sharpening, imperfections still remained in subgrains which developed during recovery. These imperfections last for a long time at low temperatures. As an example, a strongly deformed metal shows the completion of line sharpening after 5 min at 250°C and after only 3 min at 280°C, whereas the nearly complete softening does not occur until after 3 hr at 250°C and 2 at 280°C. During the further softening, evolution of the structure can be followed not only by X-rays but also by color microscopy which provides evidence of the mechanism of this softening; the subgrains become more and more perfect and at the same time a continuous growth of the subgrains occurs.

It is thus evident that:

1) The subgrains appearing during recovery are not perfect; they become perfect only later after low temperature annealing. The numerous defects disappear progressively from their entire volume, before and during their growth.

2) When the subgrains achieve complete perfection, a thermodynamic equilibrium seems to be established at their interfaces and so growth is stopped.

3) These phenomena clearly suggest that their growth is related not only to the subboundary energy but equally, and possibly principally, to the defects which they contain in their entire volume.

Completion of line sharpening appears as soon as the size of the subgrains reaches about 0.5μ, even if there are still strains remaining in their volume. Direct powder evidence has been obtained in our work.[5,6] Further softening occurs, as was stated previously, by continuous growth and simultaneous perfection of the subgrains.

This is a confirmation of Dr. Beck's conclusion and we thank him and his coworkers for all their valuable and authoritative contributions to this important field.

Paul A. Beck *(author's reply)*—The agreement of our activation energies for line sharpening and for softening with those independently determined by Dr. Perryman for 80 pct rolled aluminum is encouraging. Which one of the two papers should be considered as a confirmation of the other is difficult to determine, since both manuscripts were received by AIME on the same day.

In regard to line sharpening, the agreement is all the more remarkable, since the kinetics were quite different. Dr. Perryman found a maximum of about 50 pct recovery only, with no further line sharpening beyond a certain annealing time, while we observed that line sharpening went to completion, e.g., after a sufficiently long period of recovery between 100° and 350°C it reached the value measured for fully recrystallized aluminum (i.e., a breadth at half intensity of about 4'). The reason for this discrepancy is not clear; among the differences in experimental conditions some of the most obvious are the use of polycrystalline material, a photographic method, and the (333) Kα reflection by Dr. Perryman, as compared with single crystal, quantitative diffractometer measurements by means of a G.M. counter and the (220) Kα reflection in our investigation. At any rate, the activation energy obtained in both investigations is significantly lower than that for self-diffusion and this fact would have to be accounted for, if an interpretation of the mechanism is attempted in terms of elementary processes.

As to the hardness data, it is not at all clear how a meaningful activation energy could possibly be derived from the time for *complete* recovery at various temperatures, when recovery resulted only in partial softening, the *final, steady* values *varying with the annealing temperature*. The activation energy (31.8 kcal per g mole) for the softening of the 20 pct rolled material was apparently determined by Dr. Perryman in this manner. It may be pointed out also that the scatter of the microhardness values, even in the case of the single crystals described in the present paper, is fairly large, so that no great accuracy can be claimed for the activation energy derived from them. The same is undoubtedly true even more for the polycrystalline specimens used by Dr. Perryman. Under the circumstances it might be safer not to draw far-reaching conclusions from the apparent difference observed by him between the activation energies for softening in 20 pct rolled and 80 pct rolled specimens. On the other hand, Dr. Perryman is probably correct in pointing out that the tentative conclusion derived in the present paper regarding the possible identity of the rate determining processes in line sharpening and in softening should be likewise not considered as a well established one.

Dr. Berghezan's interesting comments are greatly appreciated. His excellent paper should be certainly referred to in connection with our work. Perhaps it should be pointed out that recent, more accurate hardness measurements in our laboratory by B. G. Ricketts indicate that the initial hardness drop during recovery

at 350°C may be much larger than that indicated by the results of A. H. Lutts. Accordingly, the amount of work hardening that remains after complete line sharpening may be considerably smaller than previously thought. This work is still being continued.

[5] E. C. W. Perryman: *AIME Trans.*, 1955, vol. 203, p. 1053; JOURNAL OF METALS, September 1955.
[6] J. R. Murray: *Journal* Inst. of Metals, 1956, vol. 84, p. 93.
[7] A. Berghezan: Structure et propriétés du métal restauré. *Mélanx-Cornuaun-Usure*, 1955, Nos. 359-360, p. 1.
[8] A. Berghezan and J. Herenguel: *Comptes Rendus*, Paris, 1955, vol. 240, p. 1343.

X-Ray Diffraction Determination of the Coefficients of Expansion of Alpha Uranium

by J. R. Bridge, C. M. Schwartz, and D. A. Vaughan

JOURNAL OF METALS, October 1956; *AIME Trans.*, 1956, vol. 206, pp. 1282-1285.

Authors' Correction

Lowell T. Lloyd of the Argonne National Laboratory brought to the authors' attention a disagreement between the equation for the volume expansion of uranium reported by the authors and the experimental data given in Table I or the curve of Fig. 2 of the paper. A typographical error was made in reporting the coefficient of the third-power term of the equation for the volume expansion, which should read as follows:

$$V_t = V_o [1 + 45 \times 10^{-6} T - 3.4 \times 10^{-8} T^2 + 50.0 \times 10^{-11} T^3].$$

It should be noted that the continuous curve in Fig. 2 was plotted from the correct equation.

Discussion

L. T. Lloyd *(Argonne National Laboratory, Lemont, Ill.)*—While replotting the unit cell dimensions measured by the authors, it became evident that each set of data could be represented by a single curve over the entire temperature range of observations (20°K to 640°C). Equations for these have been calculated by the least squares method of curve fitting; the constants are given in Table III. Values are reported for three sets of the equations referred to 0°K, 0°C, and 27°C. The second and third sets were obtained from the 0°K equations by simple reference temperature transformations. In calculating the constants for a_t and unit cell volume the data at 20°K were considered as normal points; the possibility that there may be a sudden change in these dimensions in the low temperature region was disregarded.

Table III. Constants for Equations Relating Unit Cell Dimensions of α Uranium and Temperature[a]

	X_o	$\alpha \times 10^6$	$\beta \times 10^8$	$\gamma \times 10^{11}$	S_y[d]
Equations based on 0°K, $X_o = X$ at 0°K					
$[100]-a_t$	2.8353	19.37	−0.10	14.82	0.00203
$[010]-b_t$	5.8673	2.32	12.91	−18.41	0.00170
$[001]-c_t$	4.9277	21.57	−13.42	23.39	0.00235
V_t	81.98	38.19	1.09	19.00	0.081
Equations based on 0°C, $X_o = X$ at 0°C[e]					
$[100]-a_t$	2.8511	22.50	11.97	14.74	0.00172
$[010]-b_t$	5.8670	0.81	−2.17	−18.41	0.00184
$[001]-c_t$	4.9541	19.37	5.71	23.26	0.00252
V_t	82.87	42.57	16.48	18.80	0.079
Equations based on 27°C, $X_o = X$ at 27°C[e]					
a_t	2.8529	23.17	13.16	14.73	0.00172
b_t	5.8671	0.45	3.66	−18.41	0.00184
c_t	4.9567	19.72	7.59	23.25	0.00252
V_t	82.97	43.45	17.98	18.77	0.079
Equations reported by Bridge, Schwartz, and Vaughan, $X_o = X$ at 27°C[f]					
a_t	2.8541	17.2	30.8	0	0.00156
b_t	5.8677	9.2	40.4	−67.5	0.00224
c_t	4.9563	25.1	21.3	57.5	0.00264
V_t	83.00	45.0	−3.4	50.0	0.075

[a] Constants are for equations of the type:
$X_t = X_o (1 + \alpha T + \beta T^2 + \gamma T^3)$.
For the first set of equations T equals °K; for the second set T equals °C, and for the third and fourth sets $T = t°C - 27$.
[d] S_y is the root mean square of the observed unit cell dimension deviations about the respective fitted curves.
[e] Only the deviations of data points measured at 27° to 640°C are considered.
[f] The X_o values for this set of equations are taken as the average of the respective values observed at 27°C.

The mean coefficients of expansion calculated from the equations reported here agree well with those given in Table II of the paper; whereas those calculated for α_b from the authors' equations do not because of the drastic changes in slope near 27°C.

The discusser would like to acknowledge the assistance of J. L. Walker in carrying out the calculations related to the least mean square method of curve fitting.

J. R. Bridge, C. M. Schwartz, and **D. A. Vaughan** *(authors' reply)*—The authors wish to thank Dr. Lloyd for his contribution. His calculations provide equations that fit the observed data over the entire temperature range investigated. Addition of the low temperature data to the computation of the equations eliminates the uncertainty in the slope of the curves in the vicinity of room temperature. The authors did not use the low temperature data in their computation because of the larger spread in the observed cell dimensions for a given temperature and because of the limited number of observations at the lower temperatures. Although both the authors' and Dr. Lloyd's equations fit the observations equally well at the higher temperatures, his give a better fit of the data at and below room temperature. However, perhaps one should use caution in accepting the significance of the cell dimensions at 0°K from Lloyd's equations, considering the possibility of an abrupt change in this region.

Appreciation is gratefully acknowledged to the following organizations whose support has helped to make possible AIME's extensive publications program of metallurgical research:

Aerojet-General Corp.
Allis-Chalmers Mfg. Co.
Aluminum Co. of America
American Brake Shoe Co.
American Cast Iron Pipe Co.
American Iron & Steel Institute
American Metal Co. Ltd.
American Metallurgical Products Co.
American Smelting & Refining Co.
American Zinc, Lead & Smelting Co.
Anaconda Co.
Apex Smelting Co.
Arnold Engineering Co.
Atom Energy of Canada, Ltd.
Avco Manufacturing Corp.
Battelle Memorial Institute
Bridgeport Brass Co.
Budd Co.
Bunker Hill Co.
Calumet & Hecla, Inc.
Cerro de Pasco Corp.
Clevite Corp.
Climax Molybdenum Co.
Consolidated Coppermines Corp.
Consolidated Mining & Smelting Co. of Canada Ltd.
Copper Range Co.
Cornell Aeronautical Laboratory Inc.
Crane Co.
Cyprus Mines Corp.
Detroit Testing Laboratory Inc.
Dow Chemical Co.
Driver-Harris Co.
Wilbur B. Driver Co.
Eagle-Picher Co.
Eaton Mfg. Co.
Electro Metallurgical Co., Div. of Union Carbide & Carbon Corp.
Engineering Foundation
Esso Research and Engineering Co.
Ford Motor Co.
Freeport Sulphur Co.
General Electric Co.
General Motors Corp.
Handy & Harman
E. F. Houghton & Co.
Howe Sound Co.
Hudson Bay Mining & Smelting Co. Ltd.
International Nickel Co. Inc.
Janney Cylinder Co.
Kennecott Copper Corp.
Leeds & Northrup Co.
Magma Copper Co.
Mallinckrodt Chemical Works
P. R. Mallory & Co., Inc.
Mallory-Sharon Titanium Corp.
Metal Hydrides, Inc.
Miami Copper Co.
Molybdenum Corp. of America
Mueller Brass Co.
National Lead Co.
New Jersey Zinc Co.
Newmont Mining Corp.
Noranda Mines, Ltd.
Olin Mathieson Chemical Corp.
Owens-Corning Fiberglas Corp.
Owens-Illinois Co.
Phelps Dodge Corp.
Quigley Co. Inc.
Raytheon Mfg. Co.
Rem-Cru Titanium Inc.
Revere Copper & Brass Inc.
Reynolds Metals Co.
Richfield Oil Corp.
Scovill Mfg. Co.
Alfred P. Sloan Foundation, Inc.
Southwestern Engineering Co.
Steel Improvement & Forge Co.
St. Joseph Lead Co.
Superior Tube Co.
Texas Gulf Sulphur Co.
Thompson Products Inc.
Titanium Metals Corp. of America
U. S. Smelting, Refining & Mining Co.
Vanadium Corp. of America
S. K. Wellman Co.

Available ---

Order Now ---

A NEW LOOK AT THE NATURE OF THE OPEN-HEARTH PROCESS

by

B. M. LARSEN
Research Supervisor
United States Steel Corporation
Monroeville, Pennsylvania

NATIONAL OPEN HEARTH STEEL COMMITTEE
IRON AND STEEL DIVISION

$3.00

AIME Members: $2.00

American Institute of Mining, Metallurgical, and Petroleum Engineers
29 West 39th Street
New York 18, N.Y.

TABLE OF CONT

PREFACE
INTRODUCTION
Need for a Working Theory of the Process
I. FLOW OF HEAT INTO THE BATH
1. Mean Net Heat Flow over Whole Heat C
2. Flow Rate from Temperature Rise in M
3. Heat Flow Potential between Roof a
4. Total Available Heat Supply to Melt
5. Mechanism of Slag-Metal Heat Flo
6. Implications of This Theory of H
II. OXYGEN DIFFUSION AND CARBO
1. Mechanism and Rate of Mas
2. Origin of CO Bubbles in L
3. Sampling for Dissolved O
4. Basis for Diffusion Rat
5. Kinetics of Carbon Ox
6. Interpretation of Obs
III. SOME CHARACTERIST
1. Comparison of Bessemer,
2. Some Puzzles in Open Hearth
3. Distribution of Flame in Furnace Spa
4. Examples of Leakage and Excess Air—Ef
5. Factors Involved in Regenerator Efficiency.
6. Regenerator Efficiency and Cold Air Leakage Distri
7. Examples of High and Low Regenerator Efficiency.
8. Excess Air and Efficiency of Regeneration Related to Air Oxi
IV. AIR OXIDATION AND NET HEAT REQUIREMENT OF THE BATH
1. Oxygen Balances.
2. Mechanism of Air Oxidation.
3. Iron Burning and Scrap Melting.
4. Oxygen Absorbed from Air—Effects on Net Heat to Bath
5. Air Oxidation and Melt Carbon.
6. Excess Air and Combustion of Boil Gases.
7. Examples from Commercial Practices.
8. Summary of Relationships to Production Rate.
9. A Note on Furnace Design.
V. AVENUES FOR STUDY OR DEVELOPMENT
REFERENCES
37
38

AIME, 29 W. 39th St., New York 18, N. Y.
Please send me a copy: **A New Look at the Nature of the Open-Hearth Process**

Enclosed is Check ☐; Money Order ☐ for $
(AIME members may be billed.)

Name .....

Address .....

City and Zone ..... State .....

Nonmember Foreign Order, Add 50¢ for Mailing.

USE the Handy Order Form ---